HELMHOLTZ ZENTRUM
DRESDEN ROSSENDORF

# ANNUAL REPORT 2019

## Institute of Ion Beam Physics and Materials Research

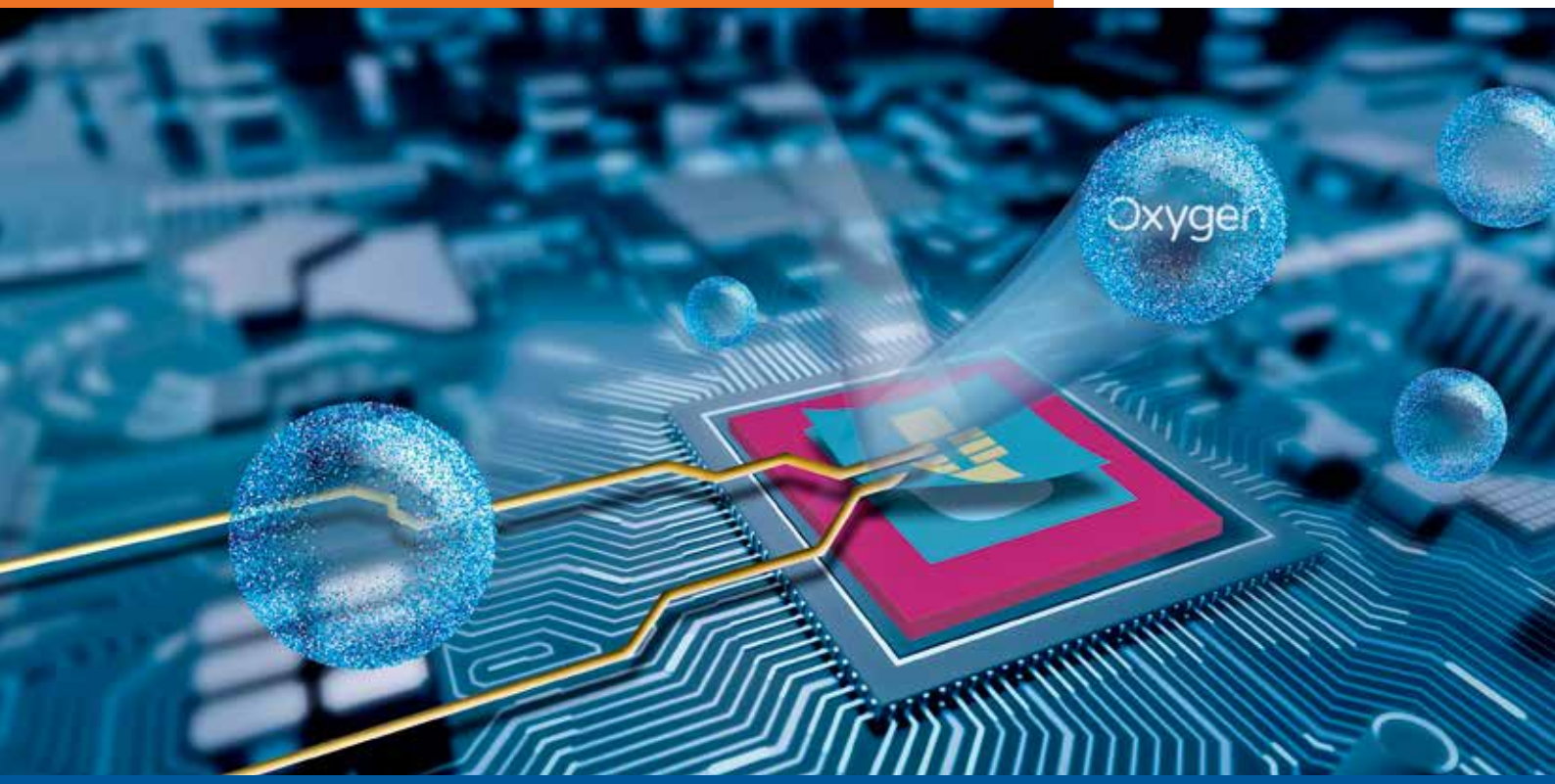


HZDR-109

Wissenschaftlich-Technische Berichte
HZDR–109

# Annual Report 2019

## Institute of Ion Beam Physics and Materials Research

Editors

J. Fassbender, M. Helm,
P. Zahn

HELMHOLTZ ZENTRUM
DRESDEN ROSSENDORF

## Cover Picture - Hermetically sealed 2D semiconductors

Two-dimensional (2D) materials have gained considerable attention in the last decade as potential candidates for carrying forward further miniaturization as per the Moore's law. While the investigations have revealed good transport properties, their instability in air yet limits their fundamental study as well as usage in technological applications.

The illustration demonstrates a new encapsulation method developed to protect 2D materials from air and moisture to facilitate long-term stability of the devices. The method involves sandwiching the 2D material between two layers of hexagonal boron nitride (hBN, blue in the illustration). The top hBN layer passivates the material from the environment and bottom hBN suppresses charge transfer from the substrate (pink in the illustration).

When the active channel is fully encapsulated between two hBN layers, how can the electrical connections be made? This can be achieved by using "via-contacts", which are metal electrodes embedded within the top hBN layer. With this technique, we could simultaneously achieve encapsulation and an electrical connection to the underlying 2D material without any direct lithographic patterning. As a result, the 2D material remains pristine, and devices with long-term stability as well as high performance could be realized. In the future, sensitive 2D materials could be integrated into electronic components, without impairing their performance.



For further information see:

Arora, H. et al., **Effective hexagonal boron nitride passivation of few-layered InSe and GaSe to enhance their electronic and optical properties**, ACS Appl. Mater. Interfaces **11**, 43480−43487 (2019), DOI: 10.1021/acsami.9b13442

Many thanks for providing material and for technical assistance to: S. Gebel, S. Kirch, S. Facsko, C. Schneider, and H. Arora.

Print edition: ISSN 2191-8708
Electronic edition: ISSN 2191-8716

urn:nbn:de:bsz:d120-qucosa2-708455
www.hzdr.de/publications/Publ-31045
Published by Helmholtz-Zentrum Dresden - Rossendorf e.V.

This report is also available at https://www.hzdr.de/FWI.

Helmholtz-Zentrum Dresden - Rossendorf e.V.
Institute of Ion Beam Physics and Materials Research
Bautzner Landstraße 400
01328 Dresden
Germany

| | | |
|---|---|---|
| Directors | Prof. Dr. M. Helm | Prof. Dr. J. Fassbender |
| Phone | +49 351 260 2260 | +49 351 260 3096 |
| Fax | +49 351 260 3285 | +49 351 260 3285 |
| Email | m.helm@hzdr.de | j.fassbender@hzdr.de |

www.hzdr.de/FWI

# Preface by the directors

The Institute of Ion Beam Physics and Materials Research (IIM) conducts materials research for future applications in, e.g., information technology. To this end, we make use of the various possibilities offered by our Ion Beam Center (IBC) for synthesis, modification, and analysis of thin films and nanostructures, as well as of the free-electron laser FELBE at HZDR for THz spectroscopy. The analyzed materials range from semiconductors and oxides to metals and magnetic materials. They are investigated with the goal to optimize their electronic, magnetic, optical as well as structural functionality. This research is embedded in the Helmholtz Association's programme "From Matter to Materials and Life". Seven publications from last year are highlighted in this Annual Report to illustrate the wide scientific spectrum of our institute.

After the scientific evaluation in the framework of the Helmholtz Programme-Oriented Funding (POF) in 2018 we had some time to concentrate on science again before end of the year a few of us again had to prepare for the strategic evaluation which took place in January 2020, which finally was also successful for the institute.

In 2019, there have been a number of organizational changes. First, and most prominently, we were able to hire Prof. Dr. Anton Wallner as new head of our department Accelerator Mass Spectrometry (AMS) and Isotope Research. This appointment is jointly with the TU Dresden where Toni has received a chair in the Institute of Nuclear and Particle Physics. Along with this employment, our scientific advisory board and board of trustees approved the acquisition of a dedicated 1 MV accelerator for AMS including a laser detachment system. With this move, we hope to widen the scope of the user facility Ion Beam Center to new user communities in the field of nuclear astrophysics, environmental and geosciences. Second, the department Ion Beam Center is now headed by Dr. Stefan Facsko, who took over the responsibility from Dr. Johannes von Borany who stepped down for partial retirement. Stefan has been working in the Ion Beam Center since 2003 in various functions and is one of our most established researchers. We wish him all the best for this responsible position. Third, after the successful evaluation of Dr. Denys Makarov we created a new department Intelligent Materials and Devices, which is now headed by Denys. For his outstanding work in the field of magnetic sensor technology he also received the HZDR Research Award 2019. In the same ceremony, Dr. Jacob König-Otto received the HZDR Doctoral Prize 2019 for his dissertation at our Institute. Fourth, in fall we struck a new path and created a young researcher group on "Immuno-oncology on a chip: nano-assisted screening for cancer therapy" across disciplines and Institutes headed by Dr. Larysa Baraban. Larysa heads a group in the Institute of Radiopharmaceutical Cancer Research and collaborates closely with our colleagues Dr. Artur Erbe on nanodevices and Dr. Denys Makarov on sensorics. We believe that this synergetic approach will pave the way to a fast and cost-efficient screening technology for personalized health care.

Again, in 2019, the level of newly received third-party funding was very good. In particular, we received the funding for two Helmholtz Innovation Laboratories (HIL); one on thermal treatment technology for defect engineering (UltraTherm) headed by Dr. Lars Rebohle and one on flexible sensors (FlexiSens) headed by Dr. Denys Makarov. The main emphasis of both HILs is to provide support of and technology transfer to small and medium enterprises in the respective technological areas. We are sure that in addition to our ion technology service provided via the HZDR Innovation GmbH both Innovation Labs will boost our technology transfer activities.

Several conferences and workshops were organized by scientists from our institute: the "Ion Beam Physics Workshop" as the annual meeting of the German Ion Beam Community was organized by Dr. Stefan Facsko and attracted around 50 participants to discuss the newest national developments

and research in the field of ion beam physics. In addition, the "3rd European Focused Ion Beam Network Workshop" was organized by Dr. Hans-Jürgen Engelmann and co-workers; 135 participants from 17 countries found their way to HZDR to discuss current research topics and exchange experience in Focused-Ion-Beam (FIB) and Scanning-Electron-Microscopy (SEM) work.

Finally, we would like to cordially thank all partners, friends, and organizations who supported our progress in 2019. Special thanks are due to the Executive Board of the Helmholtz-Zentrum Dresden-Rossendorf, the Minister of Science and Arts of the Free State of Saxony, and the Ministers of Education and Research, and of Economic Affairs and Energy of the Federal Government of Germany. Numerous partners from universities, industry and research institutes all around the world contributed essentially, and play a crucial role for the further development of the institute. Last but not least, the directors would like to thank again all members of our institute for their efforts and excellent contributions in 2019.

Prof. Manfred Helm

Prof. Jürgen Fassbender

# Contents

## Selected Publications



## Statistics

# Selected Publications

Image: HZDR / A. Kákay

# Copyright remarks

The following journal articles are reprinted with kind permission from:

**Effective Hexagonal Boron Nitride Passivation of Few-Layered InSe and GaSe to Enhance Their Electronic and Optical Properties**
Arora, H.; Jung, Y.; Venanzi, T.; Watanabe, K.; Taniguchi, T.; Hübner, R.; Schneider, H.; Helm, M.; Hone, J.C.; Erbe, A.
ACS Applied Materials and Interfaces **11**, 43480 (2019)

DOI: 10.1021/acsami.9b13442

**Widely tunable GaAs bandgap via strain engineering in core/shell nanowires with large lattice mismatch**
Balaghi, L.; Bussone, G.; Grifone, R.; Hübner, R.; Grenzer, J.; Ghorbani-Asl, M.; Krasheninnikov, A.V.; Schneider, H.; Helm, M.; Dimakis, E.
Nature Communications **10**, 2793 (2019)

DOI: 10.1038/s41467-019-10654-7

**A bimodal soft electronic skin for tactile and touchless interaction in real time**
Ge, J.; Wang, X.; Drack, M.; Volkov, O.; Liang, M.; Cañón Bermúdez, G.S.; Illing, R.; Wang, C.; Zhou, S.; Fassbender, J.; Kaltenbrunner, M.; Makarov, D.
Nature Communications **10**, 4405 (2019)

DOI: 10.1038/s41467-019-12303-5

**Nonstoichiometric Phases of Two-Dimensional Transition-Metal Dichalcogenides: From Chalcogen Vacancies to Pure Metal Membranes**
Joseph, T.; Ghorbani-Asl, M.; Kvashnin, A.G.; Larionov, K.V.; Popov, Z.I.; Sorokin, P.B.; Krasheninnikov, A.V.
Journal of Physical Chemistry Letters **10**, 6492 (2019)

DOI: 10.1021/acs.jpclett.9b02529

**Superconductivity in single-crystalline aluminum- and gallium-hyperdoped germanium**
Prucnal, S.; Heera, V.; Hübner, R.; Wang, M.; Mazur, G.P.; Grzybowski, M.J.; Qin, X.; Yuan, Y.; Voelskow, M.; Skorupa, W.; Rebohle, L.; Helm, M.; Sawicki, M.; Zhou, S.
Physical Review Materials **3**, 054802 (2019)

DOI: 10.1103/PhysRevMaterials.3.054802

**Excitation of Whispering Gallery Magnons in a Magnetic Vortex**
Schultheiss, K.; Verba, R.; Wehrmann, F.; Wagner, K.; Körber, L.; Hula, T.; Hache, T.; Kákay, A.; Awad, A.A.; Tiberkevich, V.; Slavin, A.N.; Fassbender, J.; Schultheiss, H.
Physical Review Letters **122**, 097202 (2019)

DOI: 10.1103/PhysRevLett.122.097202

**Emission and propagation of 1D and 2D spin waves with nanoscale wavelengths in anisotropic spin textures**
Sluka, V.; Schneider, T.; Gallardo, R.A.; Kákay, A.; Weigand, M.; Warnatz, T.; Mattheis, R.; Roldán-Molina, A.; Landeros, P.; Tiberkevich, V.; Slavin, A.; Schütz, G.; Erbe, A.; Deac, A.; Lindner, J.; Raabe, J.; Fassbender, J.; Wintz, S.
Nature Nanotechnology **14**, 328 (2019)

DOI: 10.1038/s41565-019-0383-4

ACS APPLIED MATERIALS & INTERFACES

Research Article

Cite This: ACS Appl. Mater. Interfaces 2019, 11, 43480−43487

www.acsami.org

# Effective Hexagonal Boron Nitride Passivation of Few-Layered InSe and GaSe to Enhance Their Electronic and Optical Properties

Himani Arora,[†,‡] Younghun Jung,[§] Tommaso Venanzi,[†,‡] Kenji Watanabe,[∥] Takashi Taniguchi,[∥] René Hübner,[†] Harald Schneider,[†] Manfred Helm,[†,‡] James C. Hone,*[,§] and Artur Erbe*[,†]

[†]Helmholtz-Zentrum Dresden-Rossendorf, 01328 Dresden, Saxony, Germany

[‡]Technische Universität Dresden, 01062 Dresden, Saxony, Germany

[§]Department of Mechanical Engineering, Columbia University, 10027 New York, New York, United States

[∥]National Institute for Materials Science, 1-1 Namiki, 305-0044 Tsukuba, Ibaraki, Japan

Supporting Information

**ABSTRACT:** Indium selenide (InSe) and gallium selenide (GaSe), members of the III−VI chalcogenide family, are emerging two-dimensional (2D) semiconductors with appealing electronic properties. However, their devices are still lagging behind because of their sensitivity to air and device fabrication processes which induce structural damage and hamper their intrinsic properties. Thus, in order to obtain high-performance and stable devices, effective passivation of these air-sensitive materials is strongly required. Here, we demonstrate a hexagonal boron nitride (hBN)-based encapsulation technique, where 2D layers of InSe and GaSe are covered entirely between two layers of hBN. To fabricate devices out of fully encapsulated 2D layers, we employ the lithography-free via-contacting scheme. We find that hBN acts as an excellent encapsulant and a near-ideal substrate for InSe and GaSe by passivating them from the environment and isolating them from the charge disorder at the $SiO_2$ surface. As a result, the encapsulated InSe devices are of high quality and ambient-stable for a long time and show an improved two-terminal mobility of 30−120 $cm^2\ V^{-1}\ s^{-1}$ as compared to mere ∼1 $cm^2\ V^{-1}\ s^{-1}$ for unencapsulated devices. On employing this technique to GaSe, we obtain a strong and reproducible photoresponse. In contrast to previous studies, where either good performance or long-term stability was achieved, we demonstrate a combination of both in our devices. This work thus provides a systematic study of fully encapsulated devices based on InSe and GaSe, which has not been reported until now. We believe that this technique can open ways for fundamental studies as well as toward the integration of these materials in technological applications.

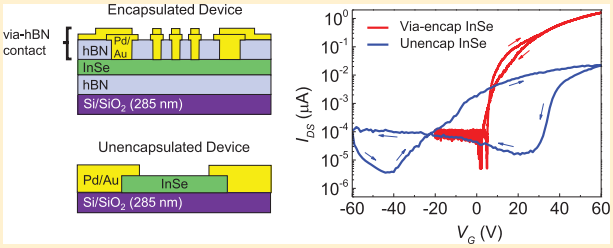


**KEYWORDS:** *indium selenide, gallium selenide, hexagonal boron nitride, encapsulation, photoluminescence, stable electronics, field-effect transistors, photodetectors*



The III−VI chalcogenide family (MX; M = Ga, In and X = S, Se, Te) has attracted considerable attention in recent years owing to its interesting properties and underlying physics at low dimensions. The two most prominent members of this family are indium selenide (InSe) and gallium selenide (GaSe), which are promising candidates for various applications such as high-speed electronics,[1−4] optoelectronics,[5−10] sensors,[11−13] and terahertz technology.[14] Recently, devices based on InSe have seen many advancements owing to its high electron mobility[1−3] resulting from its low electron effective mass ($m_e^*$ = 0.143 $m_o$)[15] and a direct band gap lying in the near-infrared range.[16] The electron mobility of ∼1000 $cm^2\ V^{-1}\ s^{-1}$ obtained at room temperature[1−3] in InSe devices is the highest value reported for an n-type two-dimensional (2D) material so far. GaSe, on the other hand, is a p-type material with a band gap of 2.11 eV in bulk and well known for its optical properties.[17−20] In terms of electronic transport, few-layered GaSe has revealed mobilities of 0.1−0.6 $cm^2\ V^{-1}\ s^{-1}$ when integrated as a channel into field-effect transistors (FETs).[8,11,20] Unlike InSe, GaSe is not a high-mobility material due to the presence of heavy holes, but it is still very appealing for optoelectronics,[8,21,22] single-photon emission,[23] nonlinear optics,[24] and terahertz applications.[14] Despite many promising properties of InSe and GaSe, limited work has been done exploiting them into devices because of their instability under ambient conditions.

Though GaSe has been demonstrated to degrade rapidly on interaction with ambient air,[21,25−27] the question whether InSe is air-sensitive or not is yet unclear within the scientific community. Some reports have claimed it to be relatively stable with no observable degradation over time[4,26,28,29] and extracted high mobilities under normal atmospheric con-

**Received:** July 29, 2019
**Accepted:** October 25, 2019
**Published:** October 25, 2019

  

DOI: 10.1021/acsami.9b13442
ACS Appl. Mater. Interfaces 2019, 11, 43480−43487

ditions,[2,3] while others observed that it degrades on contact with water and oxygen.[30−32] Even standard process steps of device fabrication involving lithographic patterning, resist spinning, and solvents' dips can cause considerable structural damage, degrading the quality of the material and resulting in poor performance of the devices.[7,33] It is worth mentioning that most previous reports which demonstrated high mobility on bare InSe used thicker layers (>30 nm) and shadow masks to fabricate their devices.[2−5] However, as InSe layer thickness approaches the quantum confinement limit, it becomes increasingly sensitive to environmental influences such as oxygen, moisture, charge traps in the dielectric and contaminations from chemical solvents, leading to fast and uncontrollable morphological changes and poor device performance. Therefore, in order to obtain high-performance and stable devices based on these materials, effective encapsulation techniques should be developed to protect InSe and GaSe layers against degradation.

Recently, the techniques of dry oxidation[32] and seeded atomic layer deposition (ALD)[34] have been demonstrated to overcome the instability of InSe. While both techniques use oxide-based encapsulation, they provide only top encapsulation, whereas the bottom surface of InSe rests on a $SiO_2$ substrate. $SiO_2$ has been revealed to be an unsuitable dielectric for 2D materials as it damages the material's quality and device performance by inducing the charge disorder at the interface due to scattering from charge traps, impurities, and surface roughness.[35,36] InSe-based FETs have previously shown substantial hysteresis and unreliability in their I−V characteristics due to charge trapping at the InSe−$SiO_2$ interface and hydration on the $SiO_2$ surface.[2] Moreover, ALD encapsulation requires lithography to fabricate devices, which as discussed above leads to further unreliability of the devices. For GaSe, hexagonal boron nitride (hBN) as top encapsulation has been recently reported, with a focus on its optoelectronic properties.[21] Though ambient-stable GaSe photodetectors were achieved, the performance was inferior to those reported on the $SiO_2$ substrate.[8,22,37]

Here, we report a hBN-based encapsulation, where 2D layers of InSe and GaSe are sandwiched between two layers of hBN; top hBN passivating the 2D layer from the environment and bottom hBN acting as a spacer and suppressing charge transfer to the 2D layer from the $SiO_2$ substrate. To fabricate the devices from fully encapsulated InSe and GaSe layers, we employ the technique of lithography-free via-contacts,[38] which are metal contacts embedded within hBN flakes and allow us to simultaneously achieve encapsulation and an electrical connection to the underlying 2D layer without any direct lithographic patterning. Based on our results, we find that full hBN encapsulation preserves InSe in its pristine form and suppresses its degradation with time under ambient conditions. Consequently, the electronic properties of encapsulated InSe are significantly improved, leading to a two-terminal field-effect mobility ($\mu_{FE}$) ranging 30−120 $cm^2\ V^{-1}\ s^{-1}$ and an on/off ratio of $10^4$ at room temperature as compared to $\mu_{FE}$ of mere ∼1 $cm^2\ V^{-1}\ s^{-1}$ obtained for unencapsulated devices. In addition, encapsulated InSe devices are stable for a prolonged period of time, overcoming their limitation to be air-sensitive. On employing full hBN encapsulation to GaSe, photoluminescence (PL) is dramatically improved and a high photoresponsivity of 84.2 A $W^{-1}$ at 405 nm is obtained.

This work advances previous efforts to encapsulate 2D layers of InSe and GaSe using hBN. The full hBN encapsulation technique passivates the air-sensitive layers from various degrading factors and preserves their unaltered properties. While previous studies have reported either good performance or long-term stability, we demonstrate a combination of both in our devices. The encapsulation technique we employ is robust and easily transferrable to other complex 2D materials which might not be compatible to the chemistry of ALD and dry oxidation techniques. Thus, this method opens up new avenues for the investigation of 2D materials which have been restricted so far in their fundamental study and applications due to environmental sensitivity.

## EXPERIMENTAL SECTION

The hBN/2D/hBN (here 2D: InSe and GaSe) heterostructures are fabricated by using the van der Waals (vdW) transfer technique as described by Wang et al.[39] In order to avoid exposing the 2D layers to air, the process steps from exfoliation of its bulk crystal until the 2D layers are fully covered between top and bottom hBN are performed inside a nitrogen-filled glovebox. Via-contacts used for the devices are fabricated as shown in the schematic of Figure 1a. hBN flakes (30−40 nm thick, crack- and residue-free) exfoliated onto a 285 nm $SiO_2$/Si substrate are identified using optical contrast and subsequently etched into desired electrode patterns using reactive-ion etching. The etched holes are then filled with 20 nm palladium (Pd)/40 nm gold (Au) by electron-beam evaporation. The via-contact is then picked up (Figure S1) and laminated onto the targeted 2D flake resting on a bottom hBN in a way that all via-metal electrodes cover the flake (Figure 1b). After full encapsulation, the whole assembly is moved out of the

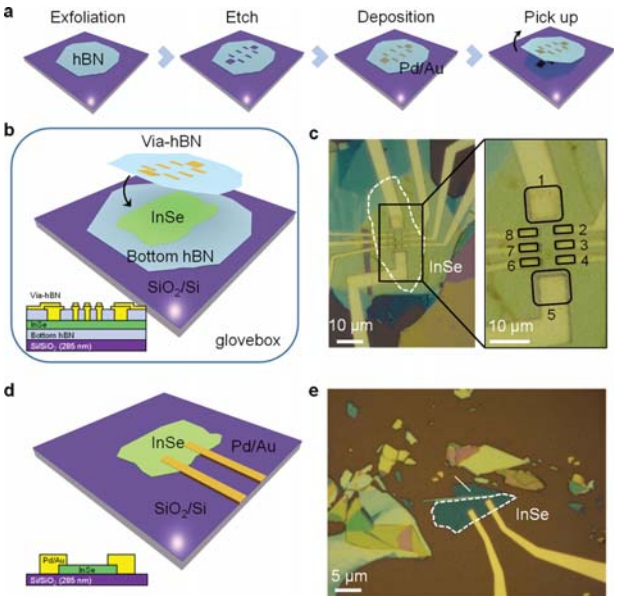


**Figure 1.** Fabrication of Pd/Au via-contacts and two configurations of InSe-based device geometries investigated in this work. (a) Step-wise illustration of the via-contact fabrication process. (b) Schematic of the InSe-via device when the via-contact hBN covers InSe in a glovebox to encapsulate it and to form an electrical connection. (c) Optical image of the InSe-via device measured in this work. ∼9.6 nm-thick InSe flake (white dashed line) is sandwiched between bottom hBN and top via-hBN. The black solid lines in the enlarged image highlight multiple Pd/Au metal contacts (numbered 1−8) embedded in hBN, which form a vdW contact with the underlying InSe layer. (d,e) Schematic and optical image of an unencapsulated device, respectively, white dashed line indicates the InSe flake on the $SiO_2$ substrate and metal electrodes fabricated by depositing Pd/Au metal.



DOI: 10.1021/acsami.9b13442
ACS Appl. Mater. Interfaces 2019, 11, 43480−43487

glovebox for fabricating metal extensions to the via-metals and contact pads, where the probes can be placed to carry out electrical measurements (see Methods and Supporting Information for details on the fabrication process). Figure 1b,c shows the schematic and the optical micrograph of one such InSe-via device, respectively, where black solid lines (in the enlarged image of Figure 1c) show the via-metal in intimate contact with the underlying InSe layer. The heterostructures are fabricated in a contamination-free environment, so that the layers have clean and impurity-free interfaces. Having multiple via-contacts in one hBN flake allows us to contact and measure multiple devices on one single InSe flake. Figure 1d,e shows the schematic and the optical image of an unencapsulated InSe device, respectively, fabricated by electron beam lithography and metal deposition on InSe layers exfoliated directly onto a 285 nm $SiO_2$/Si substrate. For a consistent comparison, both encapsulated and unencapsulated devices are fabricated with the same thickness of InSe that is ~9.6 nm or 12 layers (confirmed with atomic force microscopy, shown in Figure S2) and the same configuration of the metal contacts (Pd: 20 nm/Au: 40 nm) deposited by electron-beam evaporation.

## RESULTS AND DISCUSSION

The properties of the exfoliated thin layers depend strongly on the quality and composition of the bulk crystal. Figure 2a,b

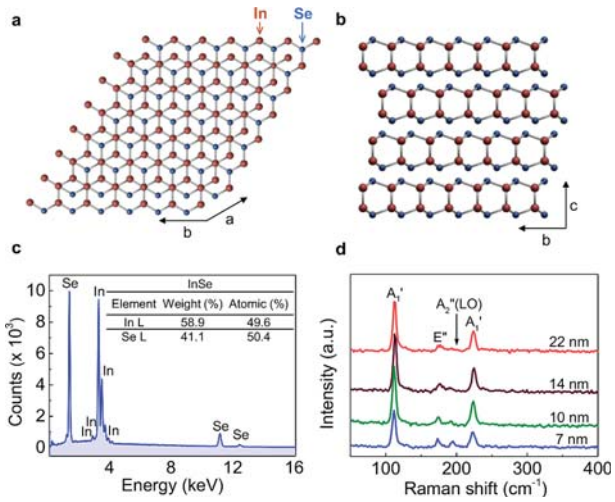


**Figure 2.** (a) Schematic of the top view of few-layered InSe showing the hexagonal lattice structure. (b) Side view of few-layered InSe showing the ABC stacking pattern of the $\gamma$-phase InSe (red balls: indium atoms, blue: selenium atoms). (c) EDS spectrum and compositional analysis of the InSe bulk crystal confirming an impurity-free crystal. (d) Raman spectra measured for various thicknesses of InSe at room temperature.

illustrates the schematics of top and side views of few-layered InSe. Energy-dispersive X-ray spectroscopy (EDS) and Raman spectroscopy are used to characterize the bulk and few layers of both InSe and GaSe. Figure 2c presents the EDS spectrum and compositional analysis of InSe bulk. The spectrum shows only indium and selenium peaks without any traces of impurities, which confirms high purity of the InSe crystals. The atomic ratio of In/Se is found to be 1:1. The Raman spectra measured at room temperature for various thicknesses ranging 7−22 nm of InSe are shown in Figure 2d. In all spectra, four major vibrational modes are recognized which are consistent with previously reported Raman spectra on thin films of InSe.[26,40] For the 10 nm thick InSe layer, the peaks at 113 and 223 $cm^{-1}$ correspond to the nonpolar $A_1$ mode and those at 176 and 193 $cm^{-1}$ to the polar E and $A_2$ (LO) modes, which are typical modes for $\gamma$-InSe. For GaSe, the EDS and Raman spectra are measured as well (Figure S3). The EDS analysis confirms that the crystal is impurity-free, while the Raman spectrum shows five prominent peaks at 57.3, 132.8, 211.5, 245, and 307.1 $cm^{-1}$ which are characteristic Raman modes for pristine 2H-GaSe.[20,22,27,41,42]

To demonstrate the effect of full hBN encapsulation on the stability of InSe, we employed micro-PL measurements to adjacent surfaces of exposed and protected InSe. Figure 3a,b

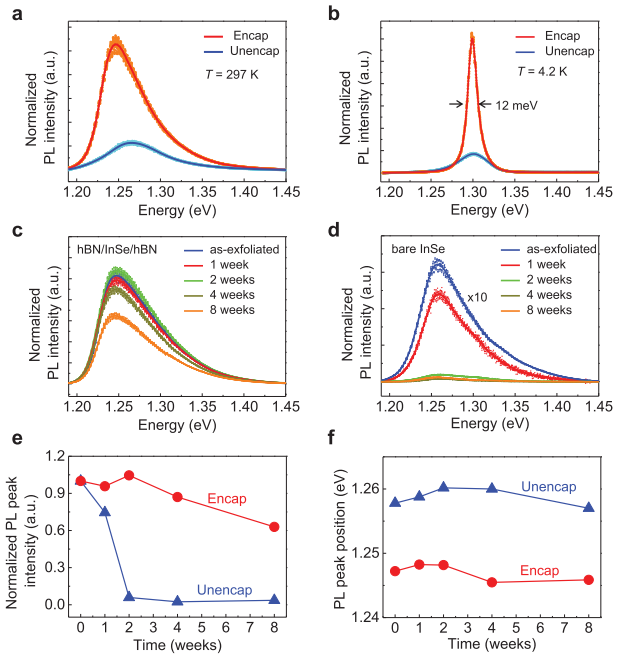


**Figure 3.** PL spectra measured for encapsulated and unencapsulated InSe, demonstrating high quality and ambient stability of fully hBN-encapsulated InSe. PL spectra measured for both samples, (a) at 297 K, showing higher intensity PL peak, and (b) at 4.2 K, showing a narrower linewidth with fwhm of 12 meV for encapsulated InSe. (c,d) Evolution of the PL spectra with time for both encapsulated and unencapsulated InSe at room temperature, respectively, stored under ambient conditions. (e,f) Normalized PL peak intensity and PL peak position measured over time, respectively, showing structural instability of InSe when exposed to air, whereas the encapsulated sample stays intact over 4 weeks.

shows the PL spectra obtained for both samples at 297 and 4.2 K, respectively. It is evident that at both temperatures, hBN encapsulation significantly enhances the PL spectra by yielding narrower and more intense peaks as compared to the unencapsulated InSe due to crystalline and atomically flat layers of hBN. The prominent effect of hBN encapsulation is seen at 4.2 K (Figure 3b), where the PL linewidth narrows down to give a full width at half maximum (fwhm) of ~12 meV in contrast to 36−38 meV obtained for the exposed InSe of the same thickness. The reduction of the PL linewidth and improved PL yield in the encapsulated sample indicates fabrication of a high-quality hBN/InSe/hBN vdW heterostructure. As compared to the PL at 4.2 K, the linewidth of both samples broadens at 297 K and shows a red shift (approx. 50 meV) from 1.30 (at 4.2 K) to ~1.25 eV (at 297 K) as seen in Figure 3a because of the interaction with acoustic and optical phonons.[43,44] Furthermore, the encapsulated InSe



DOI: 10.1021/acsami.9b13442
ACS Appl. Mater. Interfaces 2019, 11, 43480−43487

shows higher PL intensity, which further confirms the suppression of surface charge traps and defects by using the bottom hBN substrate.[36,43] On measuring multiple stacks, a mix of red and blue shifts in the PL peak position is obtained when full hBN encapsulation is used (Figure S4). The ambiguity in the shift direction is attributed to multilayered structures of InSe and GaSe employed in this study. Unlike monolayers of TMDCs where a reproducible red shift due to a strong effect of hBN dielectric is observed,[43−45] here, the effect is much less pronounced. While the red shift can be attributed to a stronger effect of the hBN dielectric, the blue shift may arise because of various reasons, such as the presence of shallow defect states, compositional fluctuations, and interface inhomogeneities and/or as demonstrated in TMDCs, the relative population of neutral and charged excitons.[46−49] A recent study shows that in multilayered InSe, hBN initiates stronger charge confinement than $SiO_2$, resulting in blue-shifting of the optical band gap.[50] Hence, the shift direction in the multilayers of InSe and GaSe is governed by several factors and cannot be associated only with the dielectric environment. Nevertheless, the superiority of full hBN encapsulation is evident in other PL features (intensity and fwhm). It is clearly seen that the PL yield is maximized when 2D layers are encapsulated in top and bottom hBN (Figures 3 and S4). A statistical analysis of multiple stacks (Figure S4c) confirms an overall narrowing down of the PL linewidth by 2−3 times when 2D layers are encapsulated between top and bottom hBN. These findings thus show that the best results are obtained when the bottom hBN layer which protects the InSe layers from the charge disorder at the $SiO_2$ surface is used in conjunction with top encapsulation which avoids exposure of the top surface to air.[49,51]

The same samples are measured over time to test their long-term stability under ambient conditions. Figure 3c,d reveals the PL spectra measured at room temperature under normal atmospheric conditions (see Methods for detailed PL specifications) for a time period of 8 weeks. Between consecutive measurements, both samples are stored in dark under ambient conditions, allowing the ambient exposure to affect both devices in the same manner. Figure 3e shows that the PL peak intensity of the encapsulated InSe is intact for almost 4 weeks, after which it starts to decline gradually, whereas for the unencapsulated sample, the PL intensity has almost vanished after 2 weeks. The PL peak position, however, is not significantly affected over time (Figure 3f). Balakrishnan et al.[28] have attributed the reduction in the PL intensity to the formation of $In_2O_3$ as InSe thin layers are exposed to air under high temperatures and focused lasers. The trend in Figure 3 indicates that the stability of the InSe layers is greatly enhanced by using hBN encapsulation which preserves InSe from the complex physical and chemical changes occurring when it comes in contact with air.

To investigate the quality of hBN encapsulated InSe FETs, electrical performance of both encapsulated and unencapsulated devices is measured in back-gate configuration. The transfer curves of both devices (Figure 4a) show an n-type FET behavior due to intrinsic doping of InSe layers as predicted previously.[2−4] The room-temperature two-terminal field-effect mobility ($\mu_{FE}$) is extracted using the following equation:

$$\mu_{FE} = \frac{dI_{DS}}{dV_G} \cdot \frac{L}{WC_iV_{DS}}$$

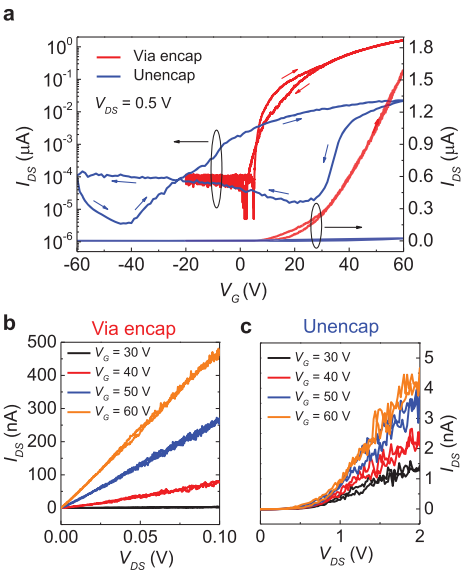


**Figure 4.** Electrical characterization of encapsulated InSe-via device and unencapsulated InSe device shown in Figure 1c,e, respectively. (a) Transfer characteristics (linear and semilog) of both devices at $V_{DS}$ = 0.5 V measured in back-gate configuration. The small arrows show the direction of the gate sweep. (b) Output characteristics of the InSe-via-encapsulated device for back-gate voltages from +30 to +60 V with steps of 10 V, showing linear characteristics, indicating ohmic behavior. (c) Output characteristics of the unencapsulated InSe device measured at back-gate voltages from +30 to +60 V with steps of 10 V, showing nonlinear behavior. Note that the current level in the unencapsulated device is significantly lower than the encapsulated device even in large $V_{DS}$ regimes.

where $L$ and $W$ are the length and width of the channel, $I_{DS}$ and $V_{DS}$ are source−drain current and voltage, $V_G$ is the back-gate voltage, and $C_i$ is the capacitance per unit area. $C_i$ estimated for the encapsulated device is $0.108 \times 10^{-7}$ F/cm$^2$ (full calculation provided in the Supporting Information). For the 9.6 nm InSe-via-encapsulated device shown in Figure 1c, the extracted $\mu_{FE}$ is 30 cm$^2$ V$^{-1}$ s$^{-1}$ with an on/off ratio of $10^4$. For other InSe-via devices with InSe thicknesses of 8−12 nm, mobility ranging 30−120 cm$^2$ V$^{-1}$ s$^{-1}$ is obtained (Figure S5). In addition, the hBN-encapsulated device shows negligible hysteresis in comparison to the unencapsulated device as well as to previously reported devices using ALD and dry oxidation as encapsulation, where substantial hysteresis was observed[32,34] because of trapped charge carriers at the InSe−$SiO_2$ interface.[2,36,52] Large hysteresis can give rise to further unreliability issues, for example, extraction of field-effect mobility which in a hysteric curve becomes strongly dependent on the gate sweep direction.[53] For this particular unencapsulated device, we extracted a mobility of ∼0.47 cm$^2$ V$^{-1}$ s$^{-1}$ (in forward sweep), which is the lower limit of the mobility due to large hysteresis (Figure S6b). On testing multiple unencapsulated devices, we obtained large hysteresis in all devices, poor mobility values of ∼1 cm$^2$ V$^{-1}$ s$^{-1}$, and on/off ratios of few hundreds. The output curve of the encapsulated device (Figure 4b) reveals linear characteristics indicating the formation of ohmic contacts between the Pd/Au metal used in the via-contact and the underlying InSe layer. However, we could not produce ohmic and reliable contacts for unencapsulated InSe FETs as revealed in Figure 4c, which might be due to degradation of InSe prior to the metal deposition, leading to tunnel barriers at the



DOI: 10.1021/acsami.9b13442
ACS Appl. Mater. Interfaces 2019, 11, 43480−43487

metal−InSe interface.[5] The InSe channel area, in addition, is continuously degrading due to air exposure. Thus, as evident from our results, full hBN encapsulation is a reliable and effective passivation technique for InSe and yields a stable charge transport, greatly enhanced $\mu_{FE}$ and larger on/off ratio as compared to the unencapsulated devices.

To investigate the long-term stability of InSe devices, the samples were stored and measured in air for 15 days. The transfer curve of the encapsulated device (Figure 5a) shows a

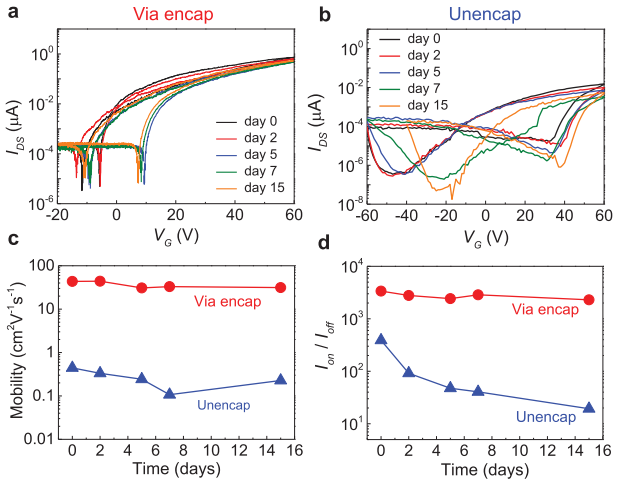


**Figure 5.** Transfer characteristics and FET parameters measured over time to investigate the stability of via-encapsulated and unencapsulated InSe devices. (a) Semilog transfer curve of via-encapsulated device at $V_{DS}$ = 0.5 V measured over 15 days. The on- and off-currents are highly reproducible with time indicating an ambient-stable device. (b) Semilog transfer curve of the unencapsulated device measured under same conditions as the encapsulated device. Large hysteresis and unstable current demonstrates unreliable device characteristics. Evolution of (c) mobility and (d) on/off ratio with time for both device configurations. Both parameters are intact for the encapsulated device, while the unencapsulated device degrades at a fast pace.

stable and consistent charge transport for over 2 weeks, whereas the unencapsulated device has a large hysteresis and low on-currents (Figure 5b). The large hysteresis and shift in the threshold voltage of the unencapsulated InSe device are attributed to the charge traps at the InSe−$SiO_2$ interface and to continuous adsorption/desorption of the gases because the samples are stored and measured in air. For the encapsulated sample, some changes in its transfer characteristics are observed after few days, which might be due to small amounts of moisture and gases getting trapped during the fabrication process. To completely mitigate these issues, fabrication of the devices can be carried out under stringent atmospheric conditions, for example, using an argon-filled glovebox instead of nitrogen. The evolution of the field-effect mobility and the on/off ratio for both devices over time is shown in Figure 5c,d, respectively. The unencapsulated device shows poor mobility and low on/off ratio as compared to the encapsulated device from the beginning and continues to deteriorate further with time. (Note that the unencapsulated device was fabricated and measured within a few hours from the time of exfoliation to minimize the degradation). The performance of the encapsulated device, on the other hand, stays intact throughout the measured time period. This indicates that InSe is susceptible to degradation in air and during standard process steps of device fabrication. During the whole process, InSe layers come in contact with various pre- and post-lithographic solvents, which may induce structural damage, tunnel barriers, and pinning of the Fermi level.[38] The presence of tunnel barriers and Fermi level pinning results in nonohmic contacts, low on-current, and poor mobility as seen in Figure 4c for the unencapsulated devices.[34,54] Wei et al.[31] have shown that adsorption of oxygen atoms into the InSe structure causes serious hampering of the electronic properties with mobility and other FET parameters to decrease 2−3 orders in magnitude. Therefore, it is essential to passivate InSe from air and at the same time from other detrimental processes where its structural integrity can be compromised. In this regard, the top and bottom hBN encapsulation scheme is extremely useful as it protects InSe from various forms of degradation and disorder and allows us to study its intrinsic properties.

Subsequently, we integrated the full hBN encapsulation technique into GaSe, another emerging 2D material belonging to the same family as InSe but far more sensitive under ambient conditions. The effectiveness of hBN encapsulation in suppressing GaSe degradation is supported by low-temperature PL measurements (Figure 6a,b) which show a significant

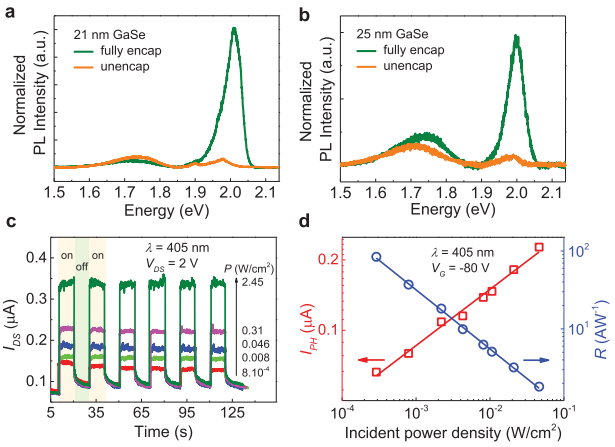


**Figure 6.** Optical characterization of fully encapsulated GaSe devices. PL spectra measured at 4.2 K for GaSe layers (a) 21 nm thick and (b) 25 nm thick. Fully encapsulated GaSe shows intense PL peaks at ∼2.0 eV, while unencapsulated GaSe shows PL reduction due to fast degradation. (c) Photoswitching response obtained for pulsed illumination of 405 nm at $V_G$ = −80 V, $V_{DS}$ = 2 V, and various laser power densities. (d) Photocurrent (red open squares) and responsivity (blue open dots) as a function of incident power density at $V_G$ = −80 V and $V_{DS}$ = 2 V. Red and blue straight lines are obtained by fitting the measured data.

improvement in the spectra of the encapsulated GaSe as compared to the unencapsulated layer. On measuring various thicknesses of GaSe layers, we observed 10 times higher PL peak intensity when it is encapsulated in top and bottom hBN, whereas unencapsulated GaSe shows significant PL reduction within 3 h from the time of exfoliation.

Because GaSe finds a majority of its applications in optics, the large band gap of hBN (∼5.7 eV)[55] is highly advantageous, as it stays transparent for the wavelengths where GaSe is optically active. The photoresponse obtained for the GaSe-via device under global illumination by a blue laser (405 nm) at various power settings is shown in Figure 6c,d. As the device is illuminated by higher laser power, $I_{DS}$ increases monotonically



DOI: 10.1021/acsami.9b13442
ACS Appl. Mater. Interfaces 2019, 11, 43480−43487

because of the increased number of electron-hole pairs generated. In response to pulsed illumination at 405 nm, the device shows a photoswitching behavior and maintains long-term stability of its photoresponse (Figure 6c). The rise in current from off- to steady-state on light illumination occurs within a 20 ms time interval, which is the resolution of the measurement setup. We believe that the photoresponse time should be less than 20 ms, which is comparable to the response times of 10−20 ms reported previously with top gold contacts.[22,37] The photocurrent ($I_{PH} = I_{light} - I_{dark}$) plotted in Figure 6d increases with increasing incident power densities. Responsivity, defined as the amount of the photocurrent generated per unit incident illumination and calculated as the ratio of the photocurrent density to the incident power density ($R = I_{PH}/PA$; $P$ is incident power density; $A$ is exposed device area),[56] is found to be decreasing as the incident power increases. At an incident power density of 0.3 mW/cm$^2$ ($V_G$ = −80 V and $V_{DS}$ = 2 V), we achieved a responsivity of 84.2 A W$^{-1}$, which is a major improvement over top-encapsulated GaSe photodetectors reported previously.[21]

## CONCLUSIONS

The sensitivity of few-layered InSe and GaSe toward air, bottom dielectrics, and lithography processes makes the assessment of their intrinsic properties difficult. We demonstrate that in order to obtain high-quality and stable devices, their full encapsulation in hBN layers is extremely advantageous as it protects the 2D layers from ambient degradation as well as from the charge disorder at the $SiO_2$ surface. The fully encapsulated InSe and GaSe devices show greatly enhanced and ambient-stable performance as compared to their unencapsulated counterparts. hBN, because of its inertness, atomically flat surface, and absence of charge traps, is an optimal encapsulation for fabricating reliable InSe- and GaSe-based devices. In the future, this technique can be applied to other sensitive 2D materials which might then supersede existing materials in terms of properties and performance.

## METHODS

Bulk crystals of InSe (3R phase with a purity of 99.999%) and GaSe (2H phase with a purity of 99.995%) are bought commercially from 2dSemiconductors and hqgraphene, respectively. The crystals are mechanically exfoliated using the adhesive tape (model BT-130E-SL bought from TELTEC GmBH) inside a nitrogen-filled glovebox and stacked between top and bottom hBN using the "vdW transfer" technique, described in detail in the Supporting Information. To fabricate via-contacts, holes are etched into hBN flakes using reactive-ion etching (Oxford RIE) with a gas mixture of $SF_6$ and $O_2$. The holes are deposited with Pd: 20 nm/Au: 40 nm using an e-beam evaporator. For lift-off process, the samples are dipped into acetone for at least 2 h followed by rinsing in isopropanol and nitrogen blow drying. The metal extensions to the hBN/InSe/via-hBN stack are fabricated by using e-beam lithography under a poly(methyl methacrylate) e-beam resist mask followed by metal deposition (Cr: 2 nm/Pd: 20 nm/Au: 40 nm) and standard lift-off process as described above. EDS is carried out at 20 kV by means of a conventional Si(Li) detector with the S-UTW window (Oxford Instruments) attached to a scanning electron microscope. EDS spectra are obtained with the INCA software by scanning a specimen area of about 3 × 5 $\mu$m$^2$ for a duration of 1 h and acquiring the data with an energy dispersion of 10 eV/channel in an energy range of 0−20 keV. Low-temperature micro-PL measurements are carried out using a LHe cryostat system. The excitation pump is a cw frequency-doubled Nd/YAG laser at a wavelength of 532 nm. The power is 10 $\mu$W focused on a spot diameter of 3 $\mu$m. The spectra are captured on a liquid nitrogen-cooled silicon CCD deep-depletion camera after being dispersed in a 300 lines/mm grating spectrometer. Electrical measurements are performed using a parameter analyzer (Agilent, 4155C) and photoresponse using Lake Shore probe station (Model CPX-VF) equipped with a cw blue laser diode at 405 nm wavelength. All electrical and photocurrent measurements are carried out in air and at room temperature.

## ASSOCIATED CONTENT

### Supporting Information

The Supporting Information is available free of charge on the ACS Publications website at DOI: 10.1021/acsami.9b13442.

Details on vdW heterostructure fabrication, EDS and Raman characterization of GaSe, low-temperature micro-PL measurements on InSe−hBN stacks, and electrical characterization of other InSe-via devices (PDF)

## AUTHOR INFORMATION


### Corresponding Authors

*E-mail: jh2228@columbia.edu (J.C.H.).
*E-mail: a.erbe@hzdr.de (A.E.).

### ORCID

Himani Arora: 0000-0003-3318-9877


### Author Contributions

H.A. and Y.J. contributed equally. H.A. exfoliated InSe and GaSe from bulk crystals and fabricated vdW heterostructures of hBN and InSe or GaSe. Y.J. fabricated via-contacts and prepared devices by electron-beam lithography. T.V., H.S., and H.A. performed PL measurements. H.A. measured charge transport and photoresponse in the devices. K.W and T.T. provided hBN crystals. All authors discussed the results and participated in the preparation of the manuscript. J.C.H. and A.E. supervised the project.

### Notes

The authors declare no competing financial interest.

## ACKNOWLEDGMENTS

We thank D. Rhodes, N. R. Finney, and G. Arefe for their help in device fabrication and subject matter discussion and F. Kilibarda and J. Franke for drawing the schematics. Growth of hBN crystals was supported by the Elemental Strategy Initiative conducted by the MEXT, Japan, A3 Foresight by JSPS and the CREST (JPMJCR15F3), JST. This work was kindly supported by the Initiative and Networking Fund of the Helmholtz Association of German Research Centers through the International Helmholtz Research School for Nanoelectronic Networks, IHRS NANONET (VH-KO-606) and INSPIRE grant from Center of Advancing Electronics Dresden (cfaed).

## REFERENCES

(1) Bandurin, D. A.; Tyurnina, A. V.; Yu, G. L.; Mishchenko, A.; Zólyomi, V.; Morozov, S. V.; Kumar, R. K.; Gorbachev, R. V.; Kudrynskyi, Z. R.; Pezzini, S.; Kovalyuk, Z. D.; Zeitler, U.; Novoselov, K. S.; Patanè, A.; Eaves, L.; Grigorieva, I. V.; Fal'Ko, V. I.; Geim, A. K.; Cao, Y. High Electron Mobility, Quantum Hall Effect and Anomalous Optical Response in Atomically Thin InSe. *Nat. Nanotechnol.* **2017**, *12*, 223−227.

(2) Sucharitakul, S.; Goble, N. J.; Kumar, U. R.; Sankar, R.; Bogorad, Z. A.; Chou, F.-C.; Chen, Y.-T.; Gao, X. P. A. Intrinsic Electron Mobility Exceeding 1000 cm$^2$/(Vs) in Multilayer InSe FETs. *Nano Lett.* **2015**, *15*, 3815−3819.



DOI: 10.1021/acsami.9b13442
ACS Appl. Mater. Interfaces 2019, 11, 43480−43487

(3) Feng, W.; Zheng, W.; Cao, W.; Hu, P. Back Gated Multilayer InSe Transistors with Enhanced Carrier Mobilities Via the Suppression of Carrier Scattering from a Dielectric Interface. *Adv. Mater.* **2014**, *26*, 6587−6593.
(4) Feng, W.; Zhou, X.; Tian, W. Q.; Zheng, W.; Hu, P. Performance Improvement of Multilayer InSe Transistors with Optimized Metal Contacts. *Phys. Chem. Chem. Phys.* **2015**, *17*, 3653−3658.
(5) Yang, H.-W.; Hsieh, H.-F.; Chen, R.-S.; Ho, C.-H.; Lee, K.-Y.; Chao, L.-C. Ultraefficient Ultraviolet and Visible Light Sensing and Ohmic Contacts in High-Mobility InSe Nanoflake Photodetectors Fabricated by the Focused Ion Beam Technique. *ACS Appl. Mater. Interfaces* **2018**, *10*, 5740−5749.
(6) Zheng, L.; Yu, P.; Hu, K.; Teng, F.; Chen, H.; Fang, X. Scalable-Production, Self-Powered $TiO_2$ Nanowell−Organic Hybrid UV Photodetectors with Tunable Performances. *ACS Appl. Mater. Interfaces* **2016**, *8*, 33924−33932.
(7) Tamalampudi, S. R.; Lu, Y.-Y.; Kumar, U.R.; Sankar, R.; Liao, C.-D.; Moorthy, B.K.; Cheng, C.-H.; Chou, F. C.; Chen, Y.-T. High Performance and Bendable Few-Layered InSe Photodetectors with Broad Spectral Response. *Nano Lett.* **2014**, *14*, 2800−2806.
(8) Abderrahmane, A.; Jung, P.-G.; Kim, N.-H.; Ko, P. J.; Sandhu, A. Gate-Tunable Optoelectronic Properties of a Nano-Layered GaSe Photodetector. *Opt. Mater. Express* **2017**, *7*, 587−592.
(9) Yang, Z.; Jie, W.; Mak, C.-H.; Lin, S.; Lin, H.; Yang, X.; Yan, F.; Lau, S. P.; Hao, J. Wafer-Scale Synthesis of High-Quality Semiconducting Two-Dimensional Layered InSe with Broadband Photoresponse. *ACS Nano* **2017**, *11*, 4225−4236.
(10) Yang, W.; Hu, K.; Teng, F.; Weng, J.; Zhang, Y.; Fang, X. High-Performance Silicon-Compatible Large-Area UV-to-Visible Broadband Photodetector Based on Integrated Lattice-Matched Type II Se/n-Si Heterojunctions. *Nano Lett.* **2018**, *18*, 4697−4703.
(11) Late, D. J.; Liu, B.; Luo, J.; Yan, A.; Matte, H. S. S. R.; Grayson, M.; Rao, C. N. R.; Dravid, V. P. GaS and GaSe Ultrathin Layer Transistors. *Adv. Mater.* **2012**, *24*, 3549−3554.
(12) Savchyn, V. P.; Kytsai, V. B. Photoelectric Properties of Heterostructures Based on Thermo-Oxidated GaSe and InSe Crystals. *Thin Solid Films* **2000**, *361*−*362*, 123−125.
(13) Li, Z.; Yang, Y.; Wang, X.; Shi, W.; Xue, D.-J.; Hu, J.-S. Three-Dimensional Optical Anisotropy of Low-Symmetry Layered GeS. *ACS Appl. Mater. Interfaces* **2019**, *11*, 24247−24253.
(14) Shi, W.; Ding, Y. J. A Monochromatic and High-Power Terahertz Source Tunable in the Ranges of 2.7−38.4 and 58.2−3540 $\mu$m for Variety of Potential Applications. *Appl. Phys. Lett.* **2004**, *84*, 1635−1637.
(15) Kuroda, N.; Nishina, Y. Resonance Raman Scattering Study on Exciton and Polaron Anisotropies in InSe. *Solid State Commun.* **1980**, *34*, 481−484.
(16) Mudd, G. W.; Svatek, S. A.; Ren, T.; Patanè, A.; Makarovsky, O.; Eaves, L.; Beton, P. H.; Kovalyuk, Z. D.; Lashkarev, G. V.; Kudrynskyi, Z. R.; Dmitriev, A. I. Tuning the Bandgap of Exfoliated InSe Nanosheets by Quantum Confinement. *Adv. Mater.* **2013**, *25*, 5714−5718.
(17) Le Toullec, R.; Balkanski, M.; Besson, J. M.; Kuhn, A. Optical Absorption Edge of a New GaSe Polytype. *Phys. Lett. A* **1975**, *55*, 245−246.
(18) Bube, R. H.; Lind, E. L. Photoconductivity of Gallium Selenide Crystals. *Phys. Rev.* **1959**, *115*, 1159−1164.
(19) Minder, R.; Ottaviani, G.; Canali, C. Charge Transport in Layer Semiconductors. *J. Phys. Chem. Solids* **1976**, *37*, 417−424.
(20) Jie, W.; Hao, J. Two-Dimensional Layered Gallium Selenide: Preparation, Properties, and Applications. In *Advanced 2D Materials*; Tiwari, A., Syvajarvi, M., Eds.; John Wiley & Sons: Hoboken, NJ, USA, 2016; Vol. *1*, pp 1−36.
(21) Zhao, Q.; Frisenda, R.; Gant, P.; Perez de Lara, D.; Munuera, C.; Garcia-Hernandez, M.; Niu, Y.; Wang, T.; Jie, W.; Castellanos-Gomez, A. Toward Air Stability of Thin GaSe Devices: Avoiding Environmental and Laser-Induced Degradation by Encapsulation. *Adv. Funct. Mater.* **2018**, *28*, 1805304.
(22) Hu, P.; Wen, Z.; Wang, L.; Tan, P.; Xiao, K. Synthesis of Few-Layer GaSe Nanosheets for High Performance Photodetectors. *ACS Nano* **2012**, *6*, 5988−5994.
(23) Tonndorf, P.; Schwarz, S.; Kern, J.; Niehues, I.; Del Pozo-Zamudio, O.; Dmitriev, A. I.; Bakhtinov, A. P.; Borisenko, D. N.; Kolesnikov, N. N.; Tartakovskii, A. I.; Michaelis de Vasconcellos, S.; Bratschitsch, R. Single-Photon Emitters in GaSe. *2D Mater.* **2017**, *4*, 021010.
(24) Jie, W.; Chen, X.; Li, D.; Xie, L.; Hui, Y. Y.; Lau, S. P.; Cui, X.; Hao, J. Layer-Dependent Nonlinear Optical Properties and Stability of Non-Centrosymmetric Modification in Few-Layer GaSe Sheets. *Angew. Chem. Int. Ed.* **2015**, *54*, 1185−1189.
(25) Rahaman, M.; Rodriguez, R. D.; Monecke, M.; Lopez-Rivera, S. A.; Zahn, D. R. T. GaSe Oxidation in Air: from Bulk to Monolayers. *Semicond. Sci. Technol.* **2017**, *32*, 105004.
(26) Del Pozo-Zamudio, O.; Schwarz, S.; Klein, J.; Schofield, R. C.; Chekhovich, E. A.; Ceylan, O.; Margapoti, E.; Dmitriev, A. I.; Lashkarev, G. V.; Borisenko, D. N.; Kolesnikov, N. N.; Finley, J. J.; Tartakovskii, A. I. Photoluminescence and Raman Investigation of Stability of InSe and GaSe Thin Films, **2015**, arXiv: 1506.05619 [cond-mat. mes-hall].
(27) Bergeron, A.; Ibrahim, J.; Leonelli, R.; Francoeur, S. Oxidation Dynamics of Ultrathin GaSe Probed Through Raman Spectroscopy. *Appl. Phys. Lett.* **2017**, *110*, 241901.
(28) Balakrishnan, N.; Kudrynskyi, Z. R.; Smith, E. F.; Fay, M. W.; Makarovsky, O.; Kovalyuk, Z. D.; Eaves, L.; Beton, P. H.; Patanè, A. Engineering P−N Junctions and Bandgap Tuning of InSe Nanolayers by Controlled Oxidation. *2D Mater.* **2017**, *4*, 025043.
(29) Politano, A.; Chiarello, G.; Samnakay, R.; Liu, G.; Gürbulak, B.; Duman, S.; Balandin, A. A.; Boukhvalov, D. W. The Influence of Chemical Reactivity of Surface Defects on Ambient-Stable InSe-Based Nanodevices. *Nanoscale* **2016**, *8*, 8474−8479.
(30) Shi, L.; Zhou, Q.; Zhao, Y.; Ouyang, Y.; Ling, C.; Li, Q.; Wang, J. Oxidation Mechanism and Protection Strategy of Ultrathin Indium Selenide: Insight from Theory. *J. Phys. Chem. Lett.* **2017**, *8*, 4368−4373.
(31) Wei, X.; Dong, C.; Xu, A.; Li, X.; Macdonald, D. D. Oxygen-Induced Degradation of the Electronic Properties of Thin-Layer InSe. *Phys. Chem. Chem. Phys.* **2018**, *20*, 2238−2250.
(32) Ho, P.-H.; Chang, Y.-R.; Chu, Y.-C.; Li, M.-K.; Tsai, C.-A.; Wang, W.-H.; Ho, C.-H.; Chen, C.-W.; Chiu, P.-W. High-Mobility InSe Transistors: the Role of Surface Oxides. *ACS Nano* **2017**, *11*, 7362−7370.
(33) Arora, H.; Schönherr, T.; Erbe, A. Electrical Characterization of Two-Dimensional Materials and Their Heterostructures. *IOP Conf. Ser. Mater. Sci. Eng.* **2017**, *198*, 012002.
(34) Wells, S. A.; Henning, A.; Gish, J. T.; Sangwan, V. K.; Lauhon, L. J.; Hersam, M. C. Supressing Ambient Degradation of Exfoliated InSe Nanosheet Devices Via Seeded Atomic Layer Deposition Encapsulation. *Nano Lett.* **2018**, *18*, 7876−7882.
(35) Dean, C. R.; Young, A. F.; Meric, I.; Lee, C.; Wang, L.; Sorgenfrei, S.; Watanabe, K.; Taniguchi, T.; Kim, P.; Shepard, K. L.; Hone, J. Boron Nitride Substrates for High-Quality Graphene Electronics. *Nat. Nanotechnol.* **2010**, *5*, 722−726.
(36) Lee, G.-H.; Cui, X.; Kim, Y. D.; Arefe, G.; Zhang, X.; Lee, C.-H.; Ye, F.; Watanabe, K.; Taniguchi, T.; Kim, P.; Hone, J. Highly Stable, Dual-Gated $MoS_2$ Transistors Encapsulated by Hexagonal Boron Nitride with Gate-Controllable Contact, Resistance, and Threshold Voltage. *ACS Nano* **2015**, *9*, 7019−7026.
(37) Cao, Y.; Cai, K.; Hu, P.; Zhao, L.; Yan, T.; Luo, W.; Zhang, X.; Wu, X.; Wang, K.; Zheng, H. Strong Enhancement of Photoresponsivity with Shrinking the Electrodes Spacing in Few Layer GaSe Photodetectors. *Sci. Rep.* **2015**, *5*, 8130.
(38) Telford, E. J.; Benyamini, A.; Rhodes, D.; Wang, D.; Jung, Y.; Zangiabadi, A.; Watanabe, K.; Taniguchi, T.; Jia, S.; Barmak, K.; Pasupathy, A. N.; Dean, C. R.; Hone, J. Via Method for Lithography Free Contact and Preservation of 2D Materials. *Nano Lett.* **2018**, *18*, 1416−1420.



DOI: 10.1021/acsami.9b13442
*ACS Appl. Mater. Interfaces* 2019, 11, 43480−43487

(39) Wang, L.; Meric, I.; Huang, P. Y.; Gao, Q.; Gao, Y.; Tran, H.; Taniguchi, T.; Watanabe, K.; Campos, L. M.; Muller, D. A.; Guo, J.; Kim, P.; Hone, J.; Shepard, K. L.; Dean, C. R. One-Dimensional Electrical Contact to a Two-Dimensional Material. *Science* **2013**, *342*, 614−617.
(40) Lei, S.; Ge, L.; Najmaei, S.; George, A.; Kappera, R.; Lou, J.; Chhowalla, M.; Yamaguchi, H.; Gupta, G.; Vajtai, R.; Mohite, A. D.; Ajayan, P. M. Evolution of the Electronic Band Structure and Efficient Photo-Detection in Atomic Layers of InSe. *ACS Nano* **2014**, *8*, 1263−1272.
(41) Li, X.; Lin, M.-W.; Puretzky, A. A.; Idrobo, J. C.; Ma, C.; Chi, M.; Yoon, M.; Rouleau, C. M.; Kravchenko, I. I.; Geohegan, D. B.; Xiao, K. Controlled Vapor Phase Growth of Single Crystalline, Two-Dimensional GaSe Crystals with High Photoresponse. *Sci. Rep.* **2015**, *4*, 5497.
(42) Zhang, X.; Tan, Q.-H.; Wu, J.-B.; Shi, W.; Tan, P.-H. Review on the Raman Spectroscopy of Different Types of Layered Materials. *Nanoscale* **2016**, *8*, 6435−6450.
(43) Cadiz, F.; Courtade, E.; Robert, C.; Wang, G.; Shen, Y.; Cai, H.; Taniguchi, T.; Watanabe, K.; Carrere, H.; Lagarde, D.; Manca, M.; Amand, T.; Renucci, P.; Tongay, S.; Marie, X.; Urbaszek, B. Excitonic Linewidth Approaching the Homogeneous Limit in $MoS_2$-Based Van Der Waals Heterostructures. *Phys. Rev. X* **2017**, *7*, 021026.
(44) Manca, M.; Glazov, M. M.; Robert, C.; Cadiz, F.; Taniguchi, T.; Watanabe, K.; Courtade, E.; Amand, T.; Renucci, P.; Marie, X.; Wang, G.; Urbaszek, B. Enabling Valley Selective Exciton Scattering in Monolayer $WSe_2$ Through Upconversion. *Nat. Commun.* **2017**, *8*, 14927.
(45) Ajayi, O. A.; Ardelean, J. V.; Shepard, G. D.; Wang, J.; Antony, A.; Taniguchi, T.; Watanabe, K.; Heinz, T. F.; Strauf, S.; Zhu, X.-Y.; Hone, J. C. Approaching the Intrinsic Photoluminescence Linewidth in Transition Metal Dichalcogenide Monolayers. *2D Mater* **2017**, *4*, 031011.
(46) Eliseev, P. G.; Perlin, P.; Lee, J.; Osiński, M. "Blue" Temperature-Induced Shift and Band-Tail Emission in InGaN-Based Light Sources. *Appl. Phys. Lett.* **1997**, *71*, 569−571.
(47) Cho, Y.-H.; Gainer, G. H.; Fischer, A. J.; Song, J. J.; Keller, S.; Mishra, U. K.; DenBaars, S. P. "S-Shaped" Temperature-Dependent Emission Shift and Carrier Dynamics in InGaN/GaN Multiple Quantum Wells. *Appl. Phys. Lett.* **1998**, *73*, 1370−1372.
(48) Buscema, M.; Steele, G. A.; van der Zant, H. S. J.; Castellanos-Gomez, A. The Effect of the Substrate on the Raman and Photoluminescence Emission of Single-Layer $MoS_2$. *Nano Res.* **2014**, *7*, 561−571.
(49) Wierzbowski, J.; Klein, J.; Sigger, F.; Straubinger, C.; Kremser, M.; Taniguchi, T.; Watanabe, K.; Wurstbauer, U.; Holleitner, A. W.; Kaniber, M.; Müller, K.; Finley, J. J. Direct Exciton Emission from Atomically Thin Transition Metal Dichalcogenide Heterostructures near the Lifetime Limit. *Sci. Rep.* **2017**, *7*, 12383.
(50) Makkawi, O.; Qiu, Y.; Feng, W.; Hu, P. A. The Modulation of Photoluminscences Band Gap of Two-Dimensional InSe Nanosheets on h-BN Substrate. *J. Nanosci. Nanotechnol.* **2016**, *16*, 9813−9819.
(51) Venanzi, T.; Arora, H.; Erbe, A.; Pashkin, A.; Winnerl, S.; Helm, M.; Schneider, H. Exciton Localization in $MoSe_2$ Monolayers Induced by Adsorbed Gas Molecules. *Appl. Phys. Lett.* **2019**, *114*, 172106.
(52) Doganov, R. A.; O'Farrell, E. C. T.; Koenig, S. P.; Yeo, Y.; Ziletti, A.; Carvalho, A.; Campbell, D. K.; Coker, D. F.; Watanabe, K.; Taniguchi, T.; Castro Neto, A. H.; Özyilmaz, B. Transport Properties of Pristine Few-Layer Black Phosphorus by Van Der Waals Passivation in an Inert Atmosphere. *Nat. Commun.* **2015**, *6*, 6647.
(53) Egginger, M.; Bauer, S.; Schwödiauer, R.; Neugebauer, H.; Sariciftci, N. S. Current Versus Gate Voltage Hysteresis in Organic Field Effect Transistors. *Monatsh. Chem.* **2009**, *140*, 735−750.
(54) Xiao, K. J.; Carvalho, A.; Castro Neto, A. H. Defects and Oxidation Resilience in InSe. *Phys. Rev. B* **2017**, *96*, 054112.
(55) Watanabe, K.; Taniguchi, T.; Kanda, H. Direct-Bandgap Properties and Evidence for Ultraviolet Lasing of Hexagonal Boron Nitride Single Crystal. *Nat. Mater.* **2004**, *3*, 404−409.
(56) Arora, H.; Malinowski, P. E.; Chasin, A.; Cheyns, D.; Steudel, S.; Schols, S.; Heremans, P. Amorphous Indium-Gallium-Zinc-Oxide as Electron Transport Layer in Organic Photodetectors. *Appl. Phys. Lett.* **2015**, *106*, 143301.



DOI: 10.1021/acsami.9b13442
*ACS Appl. Mater. Interfaces* 2019, 11, 43480−43487

nature COMMUNICATIONS

ARTICLE

https://doi.org/10.1038/s41467-019-10654-7 OPEN

# Widely tunable GaAs bandgap via strain engineering in core/shell nanowires with large lattice mismatch

Leila Balaghi [1,2], Genziana Bussone[3], Raphael Grifone[3], René Hübner[1], Jörg Grenzer[1], Mahdi Ghorbani-Asl [1], Arkady V. Krasheninnikov[1], Harald Schneider [1], Manfred Helm[1,2] & Emmanouil Dimakis [1]

The realisation of photonic devices for different energy ranges demands materials with different bandgaps, sometimes even within the same device. The optimal solution in terms of integration, device performance and device economics would be a simple material system with widely tunable bandgap and compatible with the mainstream silicon technology. Here, we show that gallium arsenide nanowires grown epitaxially on silicon substrates exhibit a sizeable reduction of their bandgap by up to 40% when overgrown with lattice-mismatched indium gallium arsenide or indium aluminium arsenide shells. Specifically, we demonstrate that the gallium arsenide core sustains unusually large tensile strain with hydrostatic character and its magnitude can be engineered via the composition and the thickness of the shell. The resulted bandgap reduction renders gallium arsenide nanowires suitable for photonic devices across the near-infrared range, including telecom photonics at 1.3 and potentially 1.55 μm, with the additional possibility of monolithic integration in silicon-CMOS chips.

[1] Institute of Ion Beam Physics and Materials Research, Helmholtz-Zentrum Dresden-Rossendorf, 01328 Dresden, Germany. [2] Center for Advancing Electronics Dresden (cfaed), Technische Universität Dresden, 01062 Dresden, Germany. [3] PETRA III, Deutsches Elektronen-Synchrotron (DESY), 22607 Hamburg, Germany. Correspondence and requests for materials should be addressed to E.D. (email: e.dimakis@hzdr.de)

III-V compound semiconductors have stimulated many breakthroughs in physics and technology owing to their direct bandgap and high electron mobility[1]. It has also been very important that these fundamental properties can be tailored, depending on the targeted device application or operation energy-range, by using (qua-) ternary alloys with selected chemical compositions. $In_xGa_{1-x}As$ is a representative example for applications in the near-infrared range, where the In-content $x$ can be chosen to provide appropriate bandgaps for multi-junction photovoltaics, light emitting diodes and photodiodes, or telecom photonics[2,3]. Nevertheless, not all compositions and corresponding bandgaps between the two endpoint binaries of a ternary alloy (e.g. GaAs and InAs for $In_xGa_{1-x}As$) are feasible because of the unavailability of lattice-matched substrates as well as the spinodal decomposition[4]. Furthermore, the alloy disorder is another factor that affects the performance of ternary alloys[5,6].

More recently, III–V semiconductors in the form of free-standing nanowires have shown new potentials for a wide range of future applications in nanotechnology, e.g., photovoltaic cells with enhanced light absorption[7], lasers with sub-wavelength size[8], tunnel field-effect transistors as energy-efficient electronic switches[9], and entangled photon-pair sources for quantum information technology[10]. Owing to their small footprint, nanowires can also be grown epitaxially without dislocations on lattice-mismatched substrates, enabling the monolithic integration of dissimilar materials with complementary properties, such as III–V semiconductors and Si[11–14] or graphene[15,16]. A distinct feature of the nanowire geometry is the possibility to create core/shell heterostructures of highly lattice-mismatched materials well beyond the limits for coherent growth in equivalent thin-film heterostructures[17]. The lattice mismatch can be accommodated via elastic deformation of not only the shell, but also the core, depending on the relative thicknesses and chemical compositions[18]. This increases the capabilities for engineering the strain and, thus, the electronic structure and properties of the heterostructure[19–23]. Unlike quantum-dot heterostructures, where elastic accommodation of large misfit stresses is also possible[24], the hetero-interface in nanowires can be several micrometres long, allowing for practical use in a wide variety of device concepts, e.g., in photovoltaics, lasers, thermoelectrics and electronics[25].

Strain-induced changes in the bandgap of the core in core/shell nanowires have been reported for GaAs/GaP[26], $GaAs/Al_xGa_{1-x}As$[27], $InAs/InAs_xP_{1-x}$[22], and $GaN/Al_xGa_{1-x}N$[20]. In all cases, the core was compressively strained and its bandgap increased, in the most extreme case by 260 meV[26]. Tensile strain and up to 150 meV smaller bandgap in the core have been reported only for $GaAs/Ga_xIn_{1-x}P$ nanowires[28]. Nevertheless, extending the same concept to higher strain values is not straightforward owing to limiting factors like plastic relaxation and/or morphological instabilities[29–32]. Alternatively, quantum confinement in thin nanowires[33] or post-growth external stress[34,35], which is less practical though for device applications, have also been suggested for tuning the GaAs bandgap.

Here, we exploit the unique opportunities for strain engineering in nanowires to achieve wide tuning of the bandgap in GaAs, a traditional III–V binary alloy. Specifically, we investigate the strain in highly-mismatched $GaAs/In_xGa_{1-x}As$ and $GaAs/In_xAl_{1-x}As$ core/shell nanowires, and its effects on the electronic properties of the GaAs core. The nanowires are grown epitaxially on Si substrates. Our work shows how to surmount strain-induced difficulties in the growth, how the misfit strain is distributed between the core and the shell depending on the design of the heterostructure and, most important, how to obtain highly strained cores with a sizeable change in their bandgap. After all, we demonstrate the possibility to reduce the bandgap of GaAs by up to 40% (≈600 meV) in a continuous manner (all intermediate values are possible), which renders GaAs nanowires a versatile material system for various photonic devices in the near-infrared range, including the 1.3 μm and potentially the 1.55 μm telecom windows, monolithically integrated on the same Si chip.

## Results

**Growth of strained core/shell nanowires**. Vertical $GaAs/In_xGa_{1-x}As$ and $GaAs/In_xAl_{1-x}As$ core/shell nanowires were grown on Si(111) substrates by molecular beam epitaxy (MBE). First, GaAs core nanowires with a diameter of 20–25 nm and a length of 2 μm were grown in self-catalysed mode[36] and then $In_xGa_{1-x}As$ or $In_xAl_{1-x}As$ shells were grown around the core nanowires (see Methods). The shell thickness ($L_S$) and composition ($x$) were varied independently according to the needs of our study. Figure 1a, b depict side-view scanning electron microscopy (SEM) images of bare GaAs core nanowires (without shell) and $GaAs/In_xGa_{1-x}As$ core/shell nanowires ($x = 0.20$, $L_S = 40$ nm), respectively. The growth conditions for the shell were tuned to obtain a homogeneous thickness and composition around the core nanowires. Specifically, the growth of the shell was performed at a considerably low substrate temperature (370 °C) with a continuous substrate-rotation of 20 rpm and relatively high growth rates (≈ 0.6 Å/s). Apart from the nanowires, a continuous planar layer with polycrystalline structure and similar composition to that of the nanowire shells also grew on the substrate.

The structure and composition of the nanowires were evaluated with transmission electron microscopy (TEM). The nanowires grew along the $[\bar{1}\bar{1}\bar{1}]$ crystallographic direction and have six $\{1\bar{1}0\}$ sidewalls. Figure 1c, d show element maps along and perpendicular to the nanowire axis as measured with energy-dispersive X-ray spectroscopy (EDXS; see Methods). The incorporation of In into the shell was found very homogeneous except for the nanowire corners (Fig. 1d), where the incorporation was reduced, giving rise to six $<11\bar{2}>$ lines of lower $x$ (the same occurs in $In_xAl_{1-x}As$ shells). Similar phenomena have been observed by others in various material systems and have been attributed to self-ordering effects that occur during heteroepitaxy on nonplanar substrates[37]. The shell adopted the crystal structure of the core (see Supplementary Fig. 1 and Supplementary Note 1), i.e., both the core and the shell grew in the zinc blende structure and only the two ends of the nanowires contain a high number of rotational twins around the [111] nanowire axis and stacking faults that were formed in the beginning and the end of the GaAs growth (owing to transient changes of the droplet contact angle). Small wurtzite segments (i.e. continuous formation of twins) could be found by high-resolution TEM only occasionally and only at the two ends of the nanowires, but their volume was negligible compared to the total volume of the nanowires. Finally, the coherent growth along the $\langle 11\bar{2}\rangle$ crystallographic directions of the core/shell interface was evidenced by the absence of misfit dislocations as shown in Fig. 1e (high-resolution TEM image of the region shown with the yellow square in Fig. 1d).

We obtained similar results also for $In_xGa_{1-x}As$ shells with higher $x$ and larger $L_S$ or for $In_xAl_{1-x}As$ shells. For example, cross-sectional EDXS element maps for $In_{0.45}Ga_{0.55}As$ and $In_{0.49}Al_{0.51}As$ shells ($L_S = 80$ nm) are shown in Fig. 1f, g, respectively. The absence of misfit dislocations at the core/shell interface across the whole nanowire length was confirmed with TEM weak-beam dark-field measurements using the 220 reflection and the so-called (g, 3 g) condition. The example of a $GaAs/In_{0.49}Al_{0.51}As$ nanowire, of the same type like the one in Fig. 1g, is shown in Fig. 1h. Finally, we found that the highest possible $x$ for coherent growth of $GaAs/In_xGa_{1-x}As$ nanowires

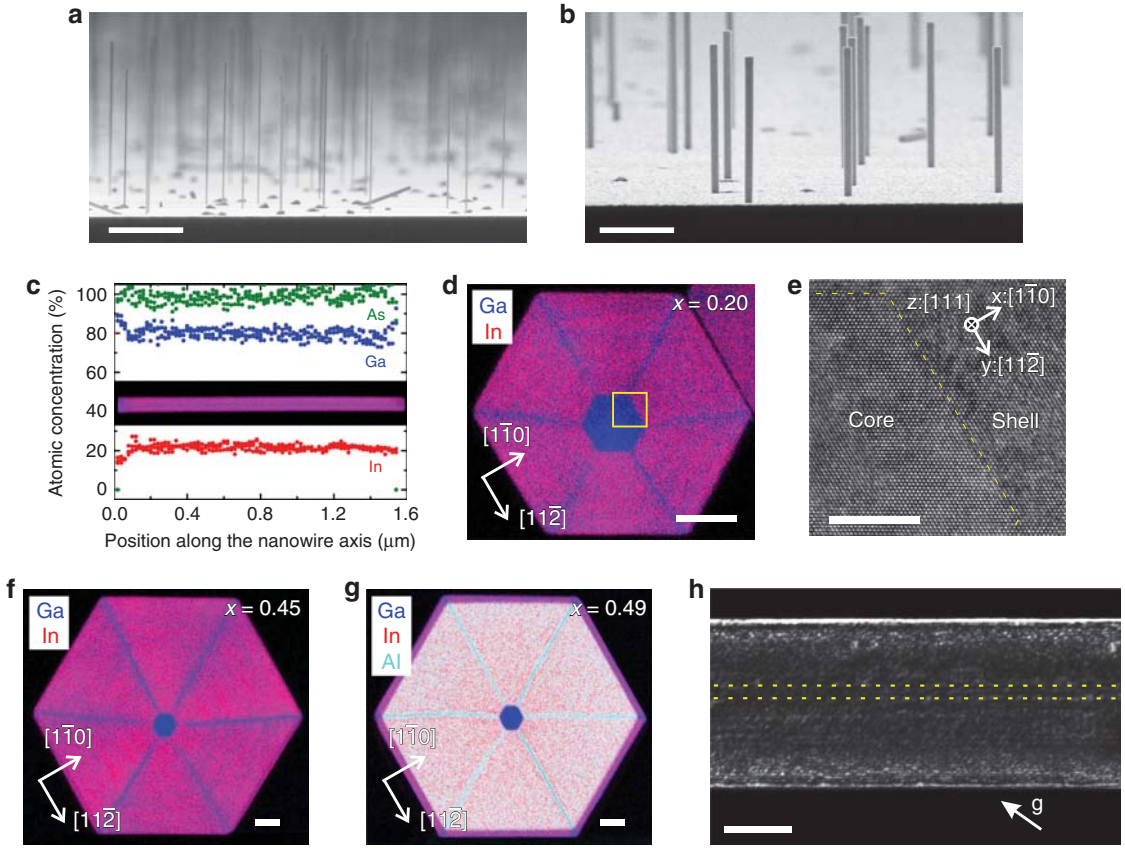


**Fig. 1** Morphological, compositional and structural analysis of GaAs/$In_xGa_{1-x}As$ and GaAs/$In_xAl_{1-x}As$ core/shell nanowires grown on Si(111) substrates. **a** Side-view scanning electron microscopy (SEM) image of as-grown bare GaAs core nanowires and (**b**) GaAs/$In_xGa_{1-x}As$ core/shell nanowires ($x = 0.20$, shell thickness $L_S = 40$ nm). **c** Energy-dispersive X-ray spectroscopy (EDXS) compositional analysis of the shell along the axis of one nanowire from the sample shown in (**b**). The zero position corresponds to the tip of the nanowire. The inset depicts the corresponding compositional map. **d** EDXS compositional map perpendicular to the axis of one nanowire from the sample shown in (**b**). **e** High-resolution transmission electron microscopy (TEM) micrograph of the core/shell interface region shown in (**d**) with a yellow square. The dotted line indicates the core/shell interface. The [1$\bar{1}$0], [11$\bar{2}$] and [111] crystallographic directions are indicated as *x*-, *y*- and *z*- axes, respectively. **f** EDXS compositional map perpendicular to the axis of a GaAs/$In_xGa_{1-x}As$ core/shell nanowire with $x = 0.45$ and $L_S = 80$ nm. **g** EDXS compositional map perpendicular to the axis of a GaAs/$In_xAl_{1-x}As$ core/shell nanowire with $x = 0.49$ and $L_S = 80$ nm. **h** (220) weak-beam dark-field TEM image of a GaAs/$In_xAl_{1-x}As$ nanowire like in (**g**) that shows no misfit dislocations in the region of the core (between the yellow dotted lines). The scale bars correspond to 1 μm in (**a**, **b**), 30 nm in (**d**, **f**, **g**), 5 nm in (**e**), and 100 nm in (**h**)

with $L_S = 80$ nm resides between 0.55 (no misfit dislocations were observed) and 0.70 (misfit dislocations were observed).

It is worth to mention that we identified a tendency for preferential growth of the shells with high *x* on one side of the core, similar to Day et al.[38] for highly strained Si/Ge core/shell nanowires. This effect imposed anisotropic misfit stress to the core and, thus, the nanowires bent towards the thinner shell side[21,30,38,39]. However, it was possible to minimise this tendency by performing the shell growth at sufficiently low temperatures with high growth rates, which imposed strong kinetic limitations. In contrast, the nanowires were bent permanently at higher growth temperatures and lower growth rates, even for *x* as low as 0.20.

**Analysis of strain in core/shell nanowires**. The strain in core/shell nanowires was measured by micro-Raman scattering spectroscopy at 300 K ($\lambda = 532$ nm, beam spot size = 800 nm). The measurements were performed in back-scattering configuration with normal incidence excitation on single nanowires (see Methods), which had been transferred previously on an Au-coated Si wafer. The removal of nanowires from their original substrate did not affect their strain state because of the small nanowire/substrate interface area (see Supplementary Fig. 2d and Supplementary Note 2). An example of a GaAs/$In_xGa_{1-x}As$ core/shell nanowire with $x = 0.20$ and $L_S = 40$ nm is shown in Fig. 2a in comparison with a bare GaAs nanowire (without shell). The spectrum of the bare GaAs nanowire is dominated by scattering from transverse optical (TO) phonons, with the peak position at 268.6 $cm^{-1}$ in good agreement with reported values for strain-free bulk GaAs in zinc blende phase[40,41] (longitudinal optical (LO) phonon transitions are forbidden in the particular measurement geometry, but a weak signal is still present). In contrast, the spectrum of the core/shell nanowire shows a more complex structure. Using Lorentzian curves for the fitting of the line shape, we identified three scattering contributions, i.e. scattering in the core from GaAs TO phonons and scattering in the shell from GaAs-like and InAs-like TO phonons (see Methods). Measuring the relative peak shift ($\Delta\omega/\omega$) with respect to the strain-free position for GaAs and GaAs-like TO phonons (268.6 $cm^{-1}$ and 268.6–30·*x* $cm^{-1}$, respectively[42,43]), we deduced the amount of hydrostatic strain $\Delta V/V$ in the core and in the shell, respectively, using the following equation:

$$\Delta V/V = 1/\gamma_{TO} \cdot \Delta\omega/\omega, \quad (1)$$

where $\gamma_{TO} = 1.39$ is the hydrostatic deformation potential (or Grüneisen parameter) of GaAs TO phonons[40]. Here, the shift of

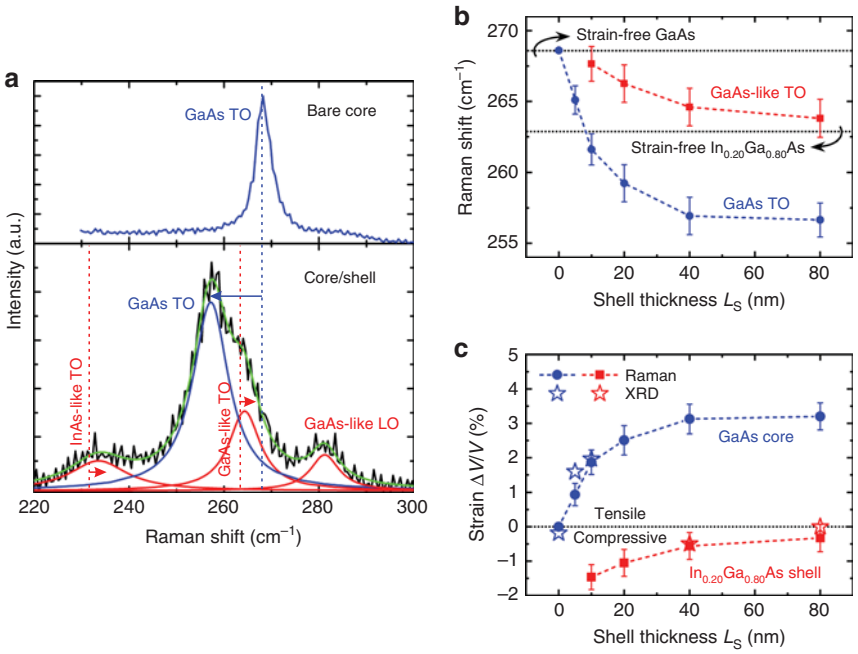


**Fig. 2** Strain analysis of GaAs/$In_{0.20}Ga_{0.80}As$ core/shell nanowires as a function of shell thickness $L_S$. **a** Raman scattering spectra at 300 K from a single core nanowire without shell ("bare core") and a single core/shell nanowire with $L_S = 40$ nm ("core/shell"). Phonon peaks in blue are attributed to the core, whereas the ones in red belong to the shell. The cumulative fit curve is shown in green and the strain-free values of phonons with vertical dashed lines. The arrows indicate the strain-induced shift of the various transverse optical (TO) phonons. **b** Raman shift of the GaAs (blue data points) and the GaAs-like (red data points) TO phonons as a function of $L_S$. The dashed lines are guides to the eye, whereas the horizontal dotted lines show the expected Raman shift of GaAs and GaAs-like TO phonons in strain-free GaAs and strain-free $In_{0.20}Ga_{0.80}As$, respectively. The error bars represent the standard deviation and the instrument error. **c** The hydrostatic strain in the core (blue data points) and the shell (red data points) as a function of $L_S$. The dashed lines are guides to the eye. The error bars originate from the error bars in Raman shift. The star symbols correspond to X-ray diffraction (XRD) results

GaAs TO phonons has been attributed exclusively to strain, neglecting any other potential contributions (e.g., phonon confinement or zone-folding)[44,45]. This means that our $\Delta V/V$ values for the GaAs core correspond to the highest possible strain. Given the large size of the laser beam compared to the nanowire length, the potential existence of alloy disorder in the shell (below the resolution of our EDXS analysis) or any other type of local structural disorder is expected to affect the width of the phonon lines rather than their peak positions.

Figure 2b, c summarise the measured Raman shifts and the corresponding strain, respectively, in GaAs/$In_xGa_{1-x}As$ core/shell nanowires as a function of $L_S$ for $x = 0.20$ (see all Raman spectra in Supplementary Fig. 3a). For the smallest $L_S$, both the shell and the core are strained, i.e., the shell is compressively strained, whereas the core is tensile-strained. With increasing $L_S$, though, the shell becomes less strained and the core more strained. In other words, the compressive misfit strain that exists in thin shells is elastically relaxed with increasing $L_S$ by stretching the core (later we will show that this is not the only mechanism of strain relaxation in the shell). Eventually, for $L_S \geq 40$ nm the shell becomes almost strain-free, whereas the strain in the core saturates at 3.2%. These results already show that thin enough nanowires can be used as flexible substrates for overgrowth with lattice-mismatched shells, going far beyond what is possible in equivalent thin-film heterostructures[46].

The strain state of the GaAs core and the $In_{0.20}Ga_{0.80}As$ shell was verified using high-resolution X-ray diffraction (XRD) at synchrotron light sources. The lattice parameters of the core and the shell were measured along the three orthogonal crystallographic directions x, y, z defined in Fig. 1e (*z*-axis is parallel to the nanowire axis, whereas *x*- and *y*- axes are perpendicular to it). For this purpose, three-dimensional reciprocal space maps were recorded for nanowire ensembles around the $20\bar{2}$, $22\bar{4}$ and $\bar{1}1\bar{1}$ Bragg reflections, respectively (see Methods). As an example, the reciprocal space map around the $22\bar{4}$ reflection, projected on the $(Q_{[11\bar{2}]}, Q_{[1\bar{1}0]})$ plane, for nanowires with $L_S = 10$ nm is depicted in Fig. 3a. The contributions from the core and the shell are indicated with dashed rectangles. The corresponding 1D plot along $Q_{[11\bar{2}]}$, after integration of the intensity along $Q_{[1\bar{1}0]}$, is also shown in Fig. 3a. The comparison of the 1D plot (continuous curve) with simulations (dashed curve) based on elasticity theory (see Methods) shows a reasonable agreement. Measurements and simulations were also performed on nanowires with $L_S = 0$, 5, 40, and 80 nm (see Supplementary Fig. 5). The diffraction signal from the core was strong enough and, thus, could be unambiguously identified only for $L_S = 0$, 5, and 10 nm. On the other hand, the complexity of the radial strain profile in thin shells (see Supplementary Fig. 6) allowed for extracting single lattice parameters for the shell along x or y direction only for $L_S = 40$ and 80 nm. The extracted average lattice parameters of the core ($\alpha_x^c$, $\alpha_y^c$, $\alpha_z^c$) and the shell ($\alpha_x^s$, $\alpha_y^s$, $\alpha_z^s$) are plotted in Fig. 3b as a function of $L_S$.

The fact that all three lattice parameters of the core increased with $L_S$ is a manifestation of the hydrostatic character of strain in the core. $\alpha_z^c$, which was found equal to $\alpha_z^s$, increased gradually with $L_S$ from the value of strain-free GaAs to that of strain-free $In_{0.20}Ga_{0.80}As$. This means that for thick enough shells, the misfit along the nanowire axis was elastically accommodated exclusively by stretching the core. The situation is not the same in the x–y plane. $\alpha_x^c$ and $\alpha_y^c$ also increased with $L_S$, but they showed a tendency to saturate well below the value of strain-free $In_{0.20}Ga_{0.80}As$. Nevertheless, $\alpha_x^s$ and $\alpha_y^s$ reached almost strain-free values, which suggests that the misfit perpendicular to the

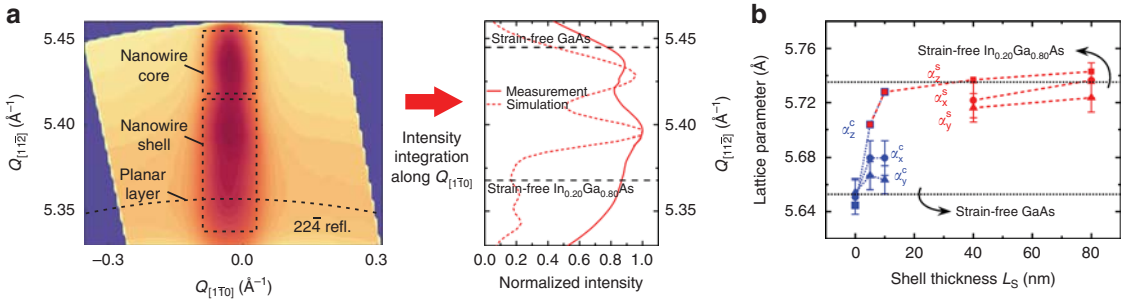


**Fig. 3** Measurements of the lattice parameters in GaAs/$In_{0.20}Ga_{0.80}As$ core/shell nanowires as a function of shell thickness $L_S$ by high-resolution X-ray diffraction (XRD). The measurements were performed on ensembles of as-grown nanowires. **a** Left: An example of a 2D reciprocal space map of the $22\bar{4}$ reflection for nanowires with $L_S = 10$ nm. The contributions from the core and the shell are indicated with dashed rectangles. The weak contribution from the planar polycrystalline layer is indicated with a curved dashed line. Right: the corresponding 1D plot after integration of the 2D map intensity along $Q_{[1\bar{1}0]}$. The identification of the core and shell contributions was based on the comparison of the measurement (continuous curve) with the theoretical simulation (dashed curve). The multiple peaks from the shell in the range of 5.33–5.40 $Å^{-1}$ indicate the complex strain distribution in thin shells. The horizontal dashed lines indicate the strain-free values of the $22\bar{4}$ reflection for GaAs and $In_{0.20}Ga_{0.80}As$. **b** XRD-measured average lattice parameters of the core (blue data points) and the shell (red data points) as a function of $L_S$. $\alpha_z$ is the lattice parameter parallel to the nanowire axis, extracted from the $\bar{1}\bar{1}\bar{1}$ reflection. $\alpha_x$ and $\alpha_y$ are two orthogonal lattice parameters perpendicular to the nanowire axis, extracted from the $20\bar{2}$ and the $22\bar{4}$ reflections, respectively. The dashed lines are guides to the eye, whereas the horizontal dotted lines show the strain-free lattice parameters for GaAs and $In_{0.20}Ga_{0.80}As$. The error bars originate from the fitting error of the corresponding 1D XRD spectra

nanowire axis was only partly accommodated by stretching the core. We speculate that the reason for that is the continuously increasing width of the nanowire sidewalls during shell growth, which also enables the elastic accommodation of misfit.

The strain components along ($\varepsilon_{zz}$) and perpendicular ($\varepsilon_{xx}$, $\varepsilon_{yy}$) to the nanowire axis were calculated for the GaAs core as $\varepsilon_n = (\alpha_n^c - \alpha_0)/\alpha_0$ (where $n$ = xx, yy, zz, and $\alpha_0 = 5.6533$ Å is the lattice parameter of strain-free GaAs), whereas the corresponding hydrostatic strain was calculated as $\Delta V/V = \varepsilon_{xx} + \varepsilon_{yy} + \varepsilon_{zz}$. As shown in Fig. 2c, the results for $\Delta V/V$ (star symbols) are in good agreement with the strain measured by Raman scattering. Thus, it is two independent experimental techniques that verify the unusually large strain in the GaAs core.

The amount of tensile strain in the GaAs core depends also on the core/shell misfit $f$ (relative difference in lattice constants) or, in other words, the shell composition $x$. Figure 4a summarises the Raman shift and Fig. 4b the corresponding strain in GaAs/$In_xGa_{1-x}As$ core/shell nanowires with different values of $x$, from 0.10 to 0.55 (the nominal values of $x$ were confirmed for a selected number of samples by EDXS analysis in the TEM), and $L_S = 40$–$80$ nm (see all Raman spectra in Supplementary Fig. 3b). The tensile strain in the core was found to increase linearly with $x$ (i.e. $\Delta V/V = 1.7f$), whereas the shell remained approximately strain-free. The tensile strain in the core was also measured for GaAs/$In_xAl_{1-x}As$ nanowires with different $x$ and $L_S = 80$ nm (see all Raman spectra in Supplementary Fig. 4). The results (open symbols in Fig. 4; $\Delta V/V = 1.8f$) are similar to those for GaAs/$In_xGa_{1-x}As$ nanowires because of the similar lattice parameters of $In_xGa_{1-x}As$ and $In_xAl_{1-x}As$ for the same $x$. Assuming $\varepsilon_{zz} \approx f$, we estimate that the strain in the core is 2.5 times larger along the nanowire axis than perpendicular to it (i.e. $\varepsilon_{zz} = 2.5\,\varepsilon_{xx} = 2.5\,\varepsilon_{yy}$).

For the highest misfit in this work, i.e. $f = 4\%$ for $In_{0.55}Ga_{0.45}As$ or $In_{0.54}Al_{0.46}As$ shells, the tensile hydrostatic strain in the core reached the remarkably large value of 7%. The linear increase of strain in the core with $x$ suggests that no apparent plastic relaxation occurred, in accordance with our TEM analysis. These results are in agreement with theoretical predictions of growth coherency in core/shell nanowires with $f$ up to 4% and core radii of about 10 nm or less[47]. We point out that it would have been impossible to grow such highly lattice-mismatched heterostructures in conventional thin-film geometry without forming dislocations.

**Effect of strain on the electronic properties of the GaAs core.** The effect of strain on the bandgap of the GaAs core was studied by means of photoluminescence (PL) spectroscopy. The existence of tensile strain with hydrostatic character in the core is expected to reduce the bandgap. In fact, the bandgaps of the tensile-strained GaAs core and the strain-free $In_xGa_{1-x}As$ shell are expected to be similar[1,48], which makes their distinction in optical spectra difficult. To avoid any ambiguities, we used GaAs/$In_xAl_{1-x}As$ core/shell nanowires, where the larger bandgap of strain-free $In_xAl_{1-x}As$ (larger than 1.38 eV at 12 K for $x \le 0.54$) cannot be confused with that of the tensile-strained GaAs. PL measurements were performed at 12 and 300 K (laser excitation at 532 nm) on ensembles of GaAs/$In_xAl_{1-x}As$ nanowires, which had been transferred previously on amorphized Ge wafers (to quench the photoluminescence from crystalline Ge). The spectra for different values of $x$ ($L_S$ = 80 nm) are plotted in Fig. 5a. Emission was obtained only in the 0.8–1.2 eV range, which is suggestive of radiative recombination of electron-hole pairs only inside the tensile-strained GaAs core. The emission shifts to lower energies with increasing $x$, in agreement with the expected effect of increasing tensile strain in the core.

The energy of the emission peak ($E_1$) at 12 K is plotted in Fig. 5b as a function of the hydrostatic strain ($\Delta V/V$) in the core and the corresponding In-content $x$ in the shell. The linear dependence was fitted (blue dashed line) with an equation of the form:

$$E_1 = E^0 + a \cdot \frac{\Delta V}{V}, \qquad (2)$$

where $E^0$ is the strain-free value of $E_1$ and $a$ is the hydrostatic deformation potential of $E_1$. The fitting parameters ($E^0 = 1.55 \pm 0.03$ eV and $a = -9.0 \pm 0.5$ eV) are in good agreement with the strain-free bandgap energy (1.52 eV) and the hydrostatic deformation potential (−8.5 eV) of bulk GaAs[1,49,50]. Thus, $E_1$ can be attributed to band-edge transitions in the tensile-strained GaAs core.

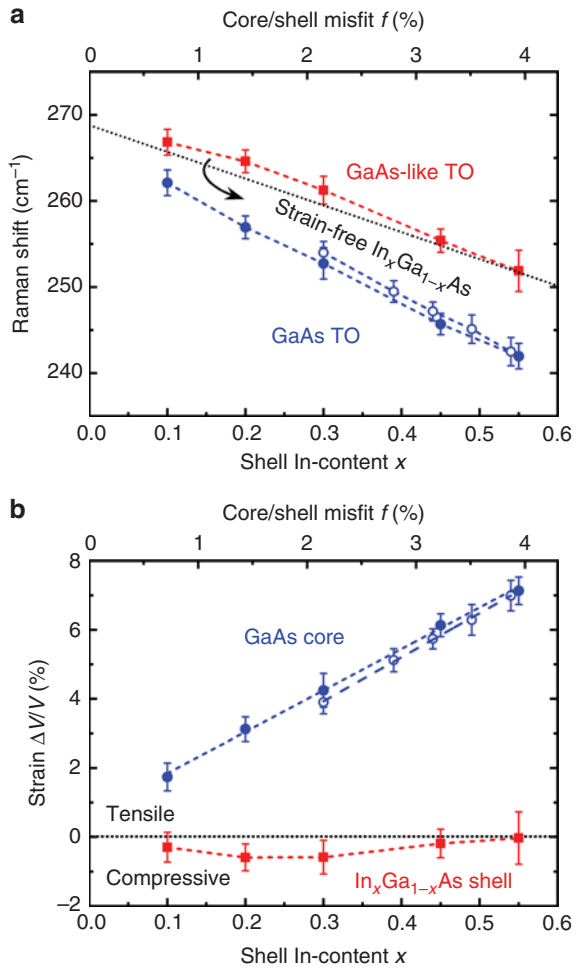


**Fig. 4** Strain analysis of GaAs/$In_xGa_{1-x}As$ (shell thickness $L_S = 40$–$80$ nm; closed symbols) and GaAs/$In_xAl_{1-x}As$ ($L_S = 80$ nm; open symbols) core/shell nanowires as a function of In-content $x$ in the shell (bottom $x$-axis) and the corresponding core/shell misfit $f$ (top $x$-axis). **a** Raman shift of the GaAs (blue data points) and the GaAs-like (red data points) transverse optical (TO) phonons as a function of $x$ and $f$. The dashed lines are guides to the eye, whereas the dotted line shows the expected Raman shift of GaAs-like TO phonons in strain-free $In_xGa_{1-x}As$. The error bars represent the standard deviation and the instrument error. GaAs-like TO phonons do not exist in $In_xAl_{1-x}As$ shells. **b** The hydrostatic strain in the core (blue data points) and the shell (red data points) as a function of $x$ and $f$. The blue dashed lines are linear fits, whereas the red one is a guide to the eye. The error bars originate from the error bars in Raman shift

Our results are compared in Fig. 5b with the bandgap of strained GaAs calculated either from first-principles (a combination of density-functional theory, DFT, with GW approximation; black dash-dotted line) or with the band-edge deformation potential (DP) theory (black short-dashed line)[49,51]. The theoretical bandgap here is defined as the energy difference between the electron conduction band minimum and the heavy-hole valence band maximum at the Γ-point of the Brillouin zone (the heavy-hole/light-hole degeneracy of the valence band is lifted owing to the strain anisotropy; see Methods). The agreement between experiment and theory is reasonably good, whereas the energy offset of 40 meV between PL and DP in Fig. 5b could be attributed to quantum confinement owing to the small diameter of the GaAs core. The heavy-hole character of the valence band was also tested with polarisation-resolved PL measurements on oriented nanowires. The polar graph in Fig. 5c shows that $E_1$ is polarised perpendicular to the nanowire axis, as expected for recombination of electrons with heavy holes[52].

An empirical relation that describes the change of GaAs bandgap ($\Delta E_g$) at 12 K as a function of $x$ is extracted from the linear dependence of $E_1$ on $x$ in Fig. 5b:

$$\Delta E_g = (-1.124 \pm 0.008)\, x\, \mathrm{eV} \quad (3)$$

We emphasise that the bandgap of GaAs at 12 K was reduced from the strain-free value of 1.52 eV to 0.91 eV for the highest strain (obtained for $x = 0.54$), i.e. a striking reduction by 40%. The same behaviour was observed at 300 K, where the bandgap energy of strained GaAs (indicated with blue arrows in Fig. 5a) was reduced to 0.87 eV with increasing $x$ to 0.54. This is particularly important for applications in optical fibre telecommunications because the emission from strained GaAs nanowires can now cover the 1.3 µm (O-band) and potentially the 1.55 µm (C-band) of telecommunication wavelengths. This is better illustrated in Fig. 6a, where our results (blue data points) are also compared to the bandgap of strain-free ternary alloys[1] (continuous curves). Although our experiments and discussion are focusing on the narrowest achievable bandgap for GaAs, all intermediate values should also be feasible by using shells with lower $L_S$ and/or lower $x$.

A secondary PL peak ($E_2$) was observed at 300 K (indicated with black arrows in Fig. 5a), ~40–50 meV higher in energy compared to $E_1$. Its origin is unclear, but could be associated either with the complex radial profile of strain inside the core, which leads to complex localisation patterns of carriers[53], or with unintentional composition/strain inhomogeneity. We also note that $E_2$ appears even at 12 K if optical excitation power is high enough.

The reduction of the bandgap of GaAs with increasing tensile strain should be accompanied by a reduction of the effective mass of electrons at the Γ-point of the Brillouin zone. If we assume that the strain in GaAs is purely hydrostatic, the corresponding effective mass of electrons ($m_e^*$) can be estimated using the following pressure coefficients[48]:

$$\frac{dE_g}{dP} = 12.02\ \mathrm{eV/Mbar} \quad (4)$$

$$\frac{1}{m_e^*}\frac{dm_e^*}{dP} = 6.8\ \mathrm{Mbar}^{-1}, \quad (5)$$

where $dE_g$ is the change of the bandgap energy induced by a relative pressure $dP$. In our case, $m_e^*$ in GaAs core is expected to decrease with increasing $x$ in the shell, reaching a value of $m_e^* = 0.0448\, m_0$ at 300 K for the highest $x$ here. This is equivalent to a reduction by ~30% from the strain-free value of $0.065\, m_0$. In fact, this lowest value of $m_e^*$ is comparable to that for bulk $In_xGa_{1-x}As$ in the range of $x = 0.53$[1] that is typically used in high electron mobility transistors (HEMTs) on lattice-matched InP substrates (Fig. 6b). This means that high-frequency photonics as well as high-mobility transistors could now be possible with strained GaAs nanowires and without the need for lattice-matched substrates.

## Discussion

Our results show that the GaAs core in GaAs/$In_xGa_{1-x}As$ or GaAs/$In_xAl_{1-x}As$ core/shell nanowires can sustain unusually large misfit strains that would have been impossible in equivalent thin-film heterostructures. The strain of GaAs is tensile, can be engineered via the shell thickness and composition, and exhibits a predominantly hydrostatic character that is similar only to quantum-dot heterostructures. As a result, the electronic

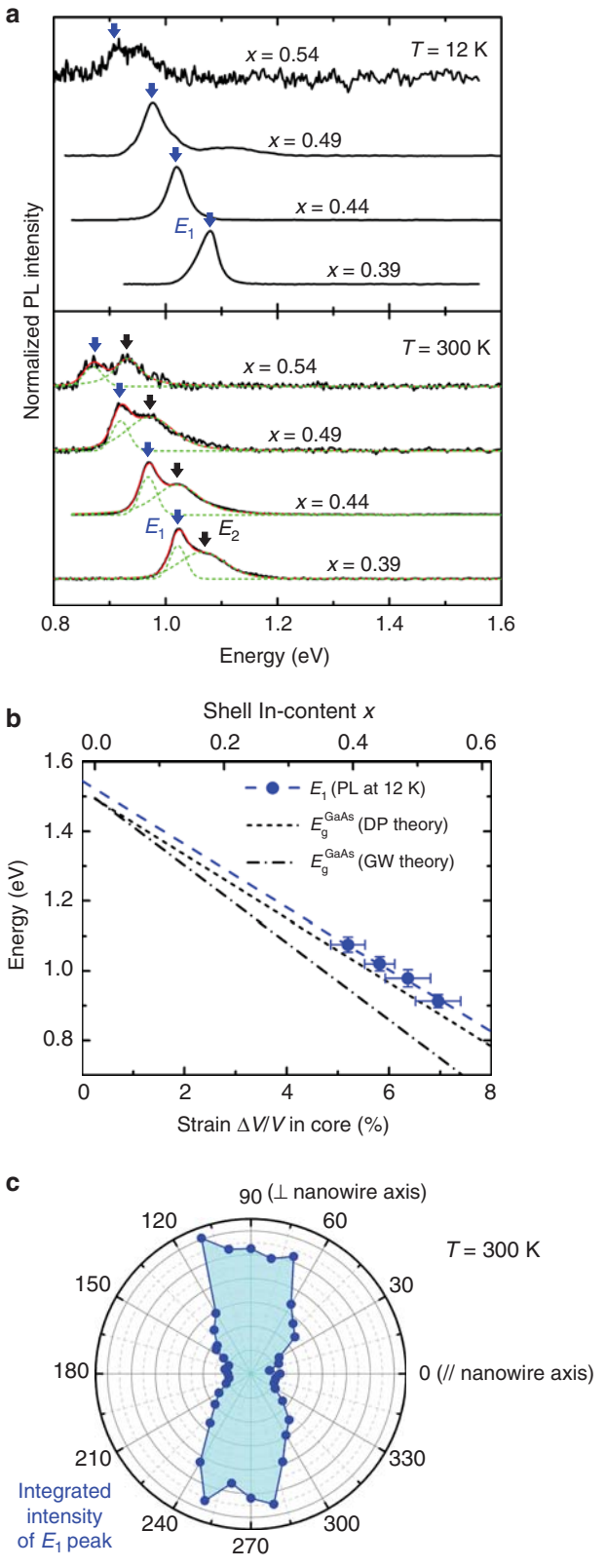


**Fig. 5** Effect of strain on the bandgap energy of the core in GaAs/$In_xAl_{1-x}As$ core/shell nanowires with shell thickness $L_S = 80$ nm. **a** Photoluminescence (PL) spectra as measured on ensembles of nanowires with different $x$ at 12 and 300 K. The spectra have been shifted vertically for the sake of clarity. Fit curves (Voigt) are shown in green (contributing peaks) and red (cumulative curves). Primary ($E_1$) and secondary ($E_2$) emissions are indicated with blue and black arrows, respectively. **b** $E_1$ peak energy at 12 K (blue data points) as a function of the hydrostatic strain in the core (bottom $x$-axis) and the corresponding In-content $x$ in the shell (top $x$-axis). The energy error bars correspond to the full-width at half-maximum of the PL fit curves, whereas the strain error bars originate from the error bars in Raman scattering measurements. The blue dashed line is a linear fit of the PL data. The black lines correspond to the bandgap energy of bulk GaAs as a function of strain, calculated with deformation potential theory (DP; dashed line) or from first-principles (GW; dash-dotted line). **c** Integrated intensity of the $E_1$ peak in polarisation-resolved PL at 300 K. The polarisation of the excitation light was parallel to the nanowire axis (0° and 180°)

properties of GaAs can be widely tuned as if we had changed its chemical composition by adding In, but without the limitations of ternary alloys. $In_xGa_{1-x}As$ or $In_xAl_{1-x}As$ shells are still necessary in order to regulate the strain in the GaAs core, but phenomena like phase separation or alloy disorder, which typically exist in ternary alloys and limit the device performance, become less critical. For the highest strain in this work, the bandgap of GaAs is reduced by 40%, making it possible to reach the 1.3 µm and potentially the 1.55 µm telecom wavelengths. A corresponding reduction of the electron effective mass by 30% is also expected. Extrapolation of our results suggests that tuning of the bandgap towards the visible range should also be possible using this time compressively strained GaAs nanowires, e.g., with $GaAs_xN_{1-x}$ or $B_xGa_{1-x}As$ shells[54,55]. Furthermore, we anticipate that the aforementioned concepts can also be adopted for other III–V binary/ternary material systems. All in all, our findings open up new possibilities for monolithically integrated III-V photonics (as well as electronics) in Si-CMOS circuits. With an advanced method of position-controlled growth, different devices (lasers, photodiodes, photovoltaic cells, etc.) could be made of the same material system on the same Si chip. The use of the same material for all devices would ensure process compatibility (e.g. no issues with cross-contamination, different processing temperatures or different thermal budget limits) and minimisation of the fabrication costs.

## Methods

**Growth of core/shell nanowires**. All nanowire samples were grown by solid-source MBE. Si(111) substrates covered with a native oxide layer were subjected to an in situ surface modification process with Ga droplets to create nano-sized holes in the oxide layer for the subsequent nucleation of GaAs nanowires directly on Si[36]. The GaAs core nanowires were grown for 10 min at a substrate temperature of 615 °C using Ga and $As_4$ beam fluxes equal to $6 \times 10^{13}$ $cm^{-2}$ $s^{-1}$ and $2 \times 10^{15}$ $cm^{-2}$ $s^{-1}$, respectively. The core growth was interrupted by closing the Ga shutter and the substrate temperature was ramped down to 370 °C under continuous exposure to the As beam. During that stage, the Ga droplets at the nanowire tips were converted to GaAs[56]. The shell growth was performed at 370 °C using In and Ga or Al beams with a total flux of $5 \times 10^{14}$ $cm^{-2}$ $s^{-1}$ and an $As_4$ or $As_2$ beam flux of $4–5 \times 10^{15}$ $cm^{-2}$ $s^{-1}$. The shell In-content $x$ was controlled via the ratio of In and Ga or Al fluxes, whereas the shell thickness was controlled via the shell growth duration. The $In_xAl_{1-x}As$ shells were capped with a 5-nm-thick $In_xGa_{1-x}As$ shell to avoid oxidation of the Al-containing shells in air.

**Chemical analysis**. Chemical analysis based on EDXS was performed in scanning TEM mode. In particular, spectrum imaging analysis based on EDXS was used to obtain the element distributions along or perpendicular to the axis of single nanowires. Figure 1c, d, f, g show two-dimensional element distributions. Quantification of the recorded element maps including Bremsstrahlung background correction based on the physical TEM model, series fit peak deconvolution, and application of tabulated theoretical Cliff-Lorimer factors as well as absorption correction was done for the elements In (Lα line), Ga (Kα line), and As (Kα line) using the ESPRIT software version 1.9 (Bruker). The line scan plotted in Fig. 1c shows the chemical composition of the shell along the nanowire axis. The data have been extracted from the complete two-dimensional element map shown in the inset by selecting the data along a line (line width = 10 nm) parallel to the nanowire axis and in a distance of ~20 nm from the nanowire core (to exclude any contribution

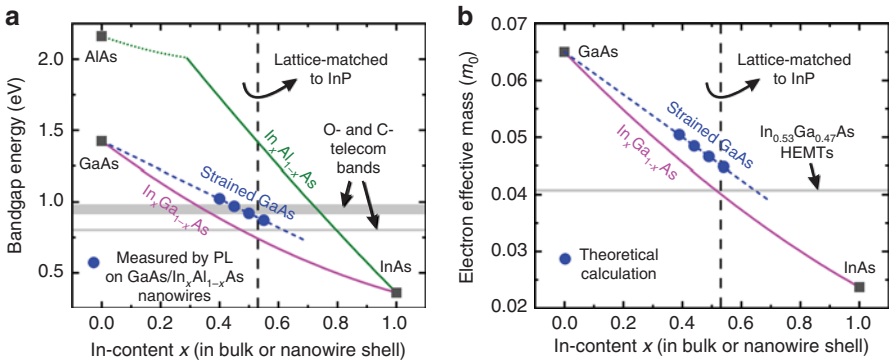


**Fig. 6** Comparison of electronic properties at the Γ-point of the Brillouin zone, at 300 K, between strained GaAs in GaAs/$In_xAl_{1-x}As$ core/shell nanowires (our results) and strain-free III-As ternary alloys (ref. [1]), as a function of In-content $x$ in the shell or the bulk. **a** Bandgap energy. The values for strained GaAs (blue data points) are the ones for $E_1$ measured by photoluminescence (PL) at 300 K in Fig. 5a. The blue dashed line is a linear fit. The magenta and green curves correspond to strain-free $In_xGa_{1-x}As$ and strain-free $In_xAl_{1-x}As$, respectively. **b** Electron effective mass. The values for strained GaAs (blue data points) were calculated using Eqs. (3), (4) and (5). The blue dashed line is a linear fit. The magenta curve corresponds to strain-free $In_xGa_{1-x}As$. The grey bands in (**a**, **b**) indicate regimes relevant to specific device applications (telecom photonics and high electron mobility transistors-HEMTs), where typically $In_xGa_{1-x}As$ thin films with $x = 0.53$ (indicated with a vertical dashed line) are employed because they are lattice-matched to commercial InP substrates

from the core). For the statistical confirmation of the results, we performed multiple line scans within the shell of the same or different nanowires.

**Raman scattering spectroscopy**. Micro-Raman scattering measurements were performed using a frequency-doubled Nd:YAG laser with $\lambda = 532$ nm and 0.08 mW (the laser spot size was approximately 800 nm). Nanowires were transferred from the original substrate onto an Au-coated Si wafer. Single nanowires lying on their $\{1\bar{1}0\}$ sidewall were selected and measured using an objective lens ×100 in back scattering and normal incidence configuration. The nanowire axis was oriented parallel to the linear polarisation of the laser, whereas the measurement was polarisation-unresolved. Different polarisation configurations were also tested and found to be in agreement with the selection rules for zinc blende nanowires[41] (see Supplementary Fig. 2b and Supplementary Note 2). Furthermore, no signal related to wurtzite phase could be detected within the resolution of our setup (see also Supplementary Fig. 2c and Supplementary Note 2). The identification of the GaAs TO phonon peak in a Raman spectrum of a GaAs/$In_xAl_{1-x}As$ nanowire is simple because no other peaks exist in the same range of wavenumbers (see Supplementary Fig. 4). In contrast, the close proximity of GaAs and GaAs-like TO phonons in GaAs/$In_xGa_{1-x}As$ nanowires (as shown in Fig. 2a) makes their distinction difficult. To overcome this problem, we used the peak position of GaAs TO phonon in GaAs/$In_xAl_{1-x}As$ nanowires as a reference for the identification of the corresponding peak in GaAs/$In_xGa_{1-x}As$ nanowires with the same In-content $x$ (a similar peak position is expected). This methodology was eventually validated via the successful comparison to XRD and PL results (Figs. 2c and 5b). Raman spectra from GaAs/$In_xAl_{1-x}As$ nanowires also showed the existence of only one peak for GaAs TO phonons within the resolution of our scans. This means that the triple degeneracy of TO phonons was not clearly lifted, which is in agreement with the predominantly hydrostatic character of the strain inside the GaAs core. The peak fitting was performed with Lorentzian profiles. The error bars in Raman shift measurements (Figs. 2b and 4a) represent the standard deviation of measurements on several nanowires from the same sample (≈0.5 $cm^{-1}$) and the instrument error (≈1.0 $cm^{-1}$).

**Photoluminescence spectroscopy**. Photoluminescence measurements were performed with a frequency-doubled Nd:YAG laser with $\lambda = 532$ nm and a liquid-nitrogen-cooled InGaAs detector with a response up to 1.5 µm. The excitation power was 10 mW at 12 K (to avoid heating effects) and 20 mW at 300 K for all samples in Fig. 5a (the laser spot size was ~1 mm). Nanowires were transferred from the original substrate onto a Ge wafer, which was previously implanted with Ge-ions to quench its luminescence. The measurements were performed on ensembles of a few hundreds of nanowires at various temperatures using a closed-cycle He-cryostat. Due to technical restrictions of the setup, it was not possible to perform the measurements at 12 K and 300 K at exactly the same position on the sample. Thus, the number of probed nanowires was probably different for the two temperatures. The peak fitting was performed with Voigt profiles and the full-width at half-maximum (FWHM) is shown as error bars in Fig. 5b. For polarisation-resolved measurements, a $\lambda/2$ plate and a polarizer were placed in the light path before and after the sample, respectively.

**High-resolution X-ray diffraction**. The high-resolution X-ray diffraction characterisation was carried out at beamline P08, at the PETRA III synchrotron in Hamburg (Germany), and at beamline I07, at the Diamond Light Source in Didcot (United Kingdom). The out-of-plane symmetric reflection $\bar{1}\bar{1}\bar{1}$ and the asymmetric reflections $\bar{3}3\bar{1}$, $4\bar{2}\bar{2}$ (cubic) and $\bar{1}01\bar{5}$ (hexagonal) were measured in coplanar geometry at beamline P08. Here, a set of Be focusing lenses (two lenses with 0.2 mm radius), 33 m upstream from the sample, was used to define a beam size of 200 µm (vertical) × 300 µm (horizontal) at an energy of 10 keV. A two-dimensional detector Pilatus 300 K was used to collect full 3D reciprocal space maps of the signals under investigation. The in-plane $20\bar{2}$ and $22\bar{4}$ reflections (about 30° apart from each other) were measured in non-coplanar grazing incidence X-ray geometry at beamline I07. Here an incident angle of 0.2° was chosen close to the critical angle of total external reflection. According to the penetration depth profile of X-rays for the material under investigation, this choice ensures a depth sensitivity of only a few nanometres below the surface, and reduces significantly the diffracted contribution from the growth substrate. Also for those measurements, an X-ray beam with energy of 9 keV was similarly focused to hundreds of µm size. We optimised these parameters to be able to separate the different contributions of the core and shell in the diffraction patterns. However, the final beam size in the vertical direction corresponded to the large footprint of the X-ray beam impinging on the substrate surface, a footprint which was several mm long. Therefore, due to the given experimental conditions, the in-plane reflections show a different resolution in reciprocal space, which is mainly influenced by the illuminated sample area. Furthermore, a small thickness fluctuation of the nanowire affects much more strongly the in-plane $20\bar{2}$ than the in-plane $22\bar{4}$ reflections. 3D reciprocal space maps were collected using a 100 K Pilatus detector. For all samples, a constant He flux was blown around the sample within a Kapton® dome to limit possible radiation damage.

The three components of the wave vector transfer are defined as: $Q_{[\bar{1}\bar{1}\bar{1}]}$ out-of-plane component parallel to the surface normal; $Q_{[1\bar{1}0]}$ and $Q_{[11\bar{2}]}$ perpendicular in-plane components. For all Bragg signals originating from the nanowires, the corresponding signal from the Si substrate was collected and it constitutes the reference of our measurements. As a last qualitative evaluation, the polytype sensitive reflections $\bar{3}3\bar{1}$, $4\bar{2}\bar{2}$ and $\bar{1}01\bar{5}$, sensitive to zinc blende, twinned zinc blende and wurtzite, respectively, reveal twinning together with an insignificant presence of the wurtzite polytype.

2D reciprocal space maps were calculated by integrating the 3D maps along $Q_{[11\bar{2}]}$ for the out-of-plane $\bar{1}\bar{1}\bar{1}$ reflection or along $Q_{[\bar{1}\bar{1}\bar{1}]}$ for the in-plane $20\bar{2}$ and $22\bar{4}$ ones. A further integration within a range of 0.03 1/Å perpendicular to the aforementioned directions provided 1D plots of integrated intensity vs $Q_{[\bar{1}\bar{1}\bar{1}]}$ for the out-of-plane reflection or integrated intensity vs $Q_{[10\bar{1}]}$ or $Q_{[11\bar{2}]}$ for the in-plane ones. The extracted line profiles reveal multiple diffracted contributions from nanowires and parasitic layer. In the symmetric out-of-plane reflection, nanowire core and shell appear convoluted in a common signal, while the in-plane data reveal both signals from the nanowire core and shell in a multiple peak configuration. All curves have been fitted with the help of multiple Lorentzian functions, with the intent to separate the contribution from core, shell and parasitic layer to the diffracted signal. The extracted out-of-plane and in-plane values were used to calculate the corresponding average lattice parameters shown in Fig. 3b.

We have selected the $22\bar{4}$ in-plane reflection to compare calculated and experimental 1D diffraction curves. A simple kinematical approximation was used for the calculations, mainly paying attention to the effect of strain (as calculated by continuum elasticity theory) and the behaviour of the core and the shell peak positions as a function of the shell thickness. The intensity of the scattered signal can be evaluated using the following kinematical approach

$$I(\mathbf{Q}) = \left| \sum_j f_j(\mathbf{Q}) e^{-i\mathbf{Q}(\mathbf{r}_j - \mathbf{u}_j)} \right|^2 \quad (6)$$

The sum is carried out over all nodes (all atoms in all unit cells of the nanowire) of the simulated strain profile, $\mathbf{r}_j$ is the initial unstrained positional vector of the j-th node and $\mathbf{u}_j$ is the corresponding displacement vector. For a nanowire of infinite length, the calculation for the in-plane $20\bar{2}$ and $22\bar{4}$ reflections collapses into the following one-dimensional equation:

$$I(Q_{hkl}) = \left| \sum_j f_j(Q_{hkl}) e^{-iQ_{hkl}(r_j - u_j)} \right|^2 \text{ with hkl} = 20\bar{2},\ 22\bar{4} \quad (7)$$

Figure 3a shows that both the experimental data and the theoretically calculated curve exhibit the same trend. With increasing the shell thickness, the $In_{0.20}Ga_{0.80}As$ peak gets more intense and shifts toward the $In_{0.20}Ga_{0.80}As$ strain-free position, whereas the GaAs peak moves away from the GaAs strain-free position and becomes weaker, until it almost disappears.

**Theoretical calculations**. The distribution of strain in core/shell nanowires (with infinite length) was calculated with the finite-element continuum elasticity model featured in the commercial software "nextnano". A description of the model is given in ref. [18]. The results were used as a reference for the analysis of the XRD data.

For the calculation of the effect of strain on the bandgap of GaAs, we used the band-edge deformation potential theory as explained in refs. [49,51]. The effect of hydrostatic strain on the bandgap energy of GaAs was calculated with equations similar to Eq. (2). The additional change of the bandgap ($\Delta E_v$) due to strain anisotropy, which lifts the degeneracy of the valence band at the Γ-point of the Brillouin zone, was calculated according to ref. [49]:

$$\Delta E_{v(hh)} = -\frac{1}{2}\delta E_{111} \quad \text{, for heavy holes} \quad (8)$$

$$\Delta E_{v(lh)} = -\frac{1}{2}\Delta_0 + \frac{1}{4}\delta E_{111} + \frac{1}{2}\left[\Delta_0^2 + \Delta_0 \delta E_{111} + \frac{9}{4}(\delta E_{111})^2\right]^{1/2} \text{, for light holes} \quad (9)$$

and

$$\delta E_{111} = 2\sqrt{3} d \frac{\varepsilon_{zz} - \varepsilon_{xx}}{3}, \quad (10)$$

where $\Delta_0 = 0.34$ eV is the spin-orbit splitting at the top of the valence band of bulk GaAs and $d = -4.5$ eV is the deformation potential of GaAs.

Electronic structure calculations have been performed using density-functional theory (DFT), as implemented in the ABINIT code[57]. We used the local density approximation (LDA) and Hartwigsen-Goedecker-Hutter (HGH) pseudopotentials[58], and the results were consistent with a previous report on GaAs[59]. The results are obtained using an energy cut-off of 20 Ha and a force convergence threshold of $10^{-6}$ Ha/Bohr. The irreducible Brillouin zone was sampled using a set of $8 \times 8 \times 8$ k points. The effect of spin-orbit coupling (SOC) was taken into account in the electronic structure calculations. The GW calculations are performed using self-consistent quasiparticle (QP) method on both energies and wave functions. Our QP calculations include self-consistent screened exchange approximation to the self-energy[60]. The computational details for obtaining the imaginary part of the self-energy are the same as in DFT calculations.

## Data availability

All data are available from the corresponding author upon reasonable request.

Received: 19 October 2018 Accepted: 20 May 2019
Published online: 26 June 2019

## References

1. Vurgaftman, I., Meyer, J. R. & Ram-Mohan, L. R. Band parameters for III-V compound semiconductors and their alloys. *J. Appl. Phys.* **89**, 5815–5875 (2001).
2. Green, M. A. et al. Solar cell efficiency tables (version 52). *Prog. Photovolt.* **26**, 427–436 (2018).
3. Eng, P. C., Song, S. & Ping, B. State-of-the-art photodetectors for optoelectronic integration at telecommunication wavelength. *Nanophotonics* **4**, 277–302 (2015).
4. Ning, C. Z., Dou, L. T. & Yang, P. D. Bandgap engineering in semiconductor alloy nanomaterials with widely tunable compositions. *Nat. Rev. Mater.* **2**, 17070 (2017).
5. Glas, F., Gors, C. & Henoc, P. Diffuse-scattering, size effect and alloy disorder in ternary and quaternary-III-V compounds. *Philos. Mag. B* **62**, 373–394 (1990).
6. Dimoulas, A., Derekis, A., Kyriakidis, G. & Christou, A. Alloy disorder effects in III-V ternaries studied by modulation spectroscopy. *Appl. Surf. Sci.* **50**, 353–358 (1991).
7. Krogstrup, P. et al. Single-nanowire solar cells beyond the Shockley-Queisser limit. *Nat. Photon.* **7**, 306–310 (2013).
8. Saxena, D. et al. Optically pumped room-temperature GaAs nanowire lasers. *Nat. Photon.* **7**, 963–968 (2013).
9. Ionescu, A. M. & Riel, H. Tunnel field-effect transistors as energy-efficient electronic switches. *Nature* **479**, 329–337 (2011).
10. Versteegh, M. A. M. et al. Observation of strongly entangled photon pairs from a nanowire quantum dot. *Nat. Commun.* **5**, 5298 (2014).
11. Tomioka, K., Yoshimura, M. & Fukui, T. A III-V nanowire channel on silicon for high-performance vertical transistors. *Nature* **488**, 189–193 (2012).
12. Dimakis, E. et al. Coaxial multishell (In,Ga)As/GaAs nanowires for near-infrared emission on Si substrates. *Nano Lett.* **14**, 2604–2609 (2014).
13. Balaghi, L. et al. Droplet-confined alternate pulsed epitaxy of GaAs nanowires on Si substrates down to CMOS-compatible temperatures. *Nano Lett.* **16**, 4032–4039 (2016).
14. Borg, M. et al. Vertical III-V nanowire device integration on Si(100). *Nano Lett.* **14**, 1914–1920 (2014).
15. Munshi, A. M. et al. Vertically aligned GaAs nanowires on graphite and few-layer graphene: generic model and epitaxial growth. *Nano Lett.* **12**, 4570–4576 (2012).
16. Hong, Y. J. et al. Van der Waals epitaxial double heterostructure: InAs/single-layer graphene/InAs. *Adv. Mater.* **25**, 6847–6853 (2013).
17. Glas, F. Strain in nanowires and nanowire heterostructures. *Semiconduct. Semimet.* **93**, 79–123 (2015).
18. Gronqvist, J. et al. Strain in semiconductor core-shell nanowires. *J. Appl Phys.* **106**, 053508 (2009).
19. Conesa-Boj, S. et al. Boosting hole mobility in coherently strained [110]-oriented Ge-Si core-shell nanowires. *Nano Lett.* **17**, 2259–2264 (2017).
20. Hetzl, M. et al. Strain-induced bandgap engineering in selectively grown GaN-(Al,Ga)N core-shell nanowire heterostructures. *Nano Lett.* **16**, 7098–7106 (2016).
21. Lewis, R. B. et al. Nanowires bending over backward from strain partitioning in asymmetric core-shell heterostructures. *Nano Lett.* **18**, 2343–2350 (2018).
22. Treu, J. et al. Enhanced luminescence properties of InAs-InAsP core-shell nanowires. *Nano Lett.* **13**, 6070–6077 (2013).
23. Wen, F. & Tutuc, E. Enhanced electron mobility in nonplanar tensile strained Si epitaxially grown on SixGe1-x nanowires. *Nano Lett.* **18**, 94–100 (2018).
24. Simmonds, P. J. et al. Tuning quantum dot luminescence below the bulk bandgap using tensile strain. *ACS Nano* **7**, 5017–5023 (2013).
25. Royo, M., De Luca, M., Rurali, R. & Zardo, I. A review on III-V core-multishell nanowires: growth, properties, and applications. *J. Phys. D Appl Phys.* **50**, 143001 (2017).
26. Montazeri, M. et al. Direct measure of strain and electronic structure in GaAs/GaP core-shell nanowires. *Nano Lett.* **10**, 880–886 (2010).
27. Hocevar, M. et al. Residual strain and piezoelectric effects in passivated GaAs/AlGaAs core-shell nanowires. *Appl. Phys. Lett.* **102**, 191103 (2013).
28. Skold, N. et al. Growth and optical properties of strained GaAs-GaxIn1-xP core-shell nanowires. *Nano Lett.* **5**, 1943–1947 (2005).
29. Lewis, R. B. et al. Anomalous strain relaxation in core-shell nanowire heterostructures via simultaneous coherent and incoherent growth. *Nano Lett.* **17**, 136–142 (2017).
30. Wallentin, J., Jacobsson, D., Osterhoff, M., Borgström, M. T. & Salditt, T. Bending and twisting lattice tilt in strained core-shell nanowires revealed by nanofocused X-ray diffraction. *Nano Lett.* **17**, 4143–4150 (2017).
31. Gagliano, L., Albani, M., Verheijen, M. A., Bakkers, E. P. A. M. & Miglio, L. Twofold origin of strain-induced bending in core-shell nanowires: the GaP/InGaP case. *Nanotechnology* **29**, 315703 (2018).
32. Dayeh, S. A. et al. Direct measurement of coherency limits for strain relaxation in heteroepitaxial core/shell nanowires. *Nano Lett.* **13**, 1869–1876 (2013).
33. Loitsch, B. et al. Tunable quantum confinement in ultrathin, optically active semiconductor nanowires via reverse-reaction growth. *Adv. Mater.* **27**, 2195–2202 (2015).
34. Zardo, I. et al. Pressure tuning of the optical properties of GaAs nanowires. *ACS Nano* **6**, 3284–3291 (2012).

35. Signorello, G., Karg, S., Bjork, M. T., Gotsmann, B. & Riel, H. Tuning the light emission from GaAs nanowires over 290 meV with uniaxial strain. *Nano Lett.* **13**, 917–924 (2013).
36. Tauchnitz, T. et al. Decoupling the two roles of Ga droplets in the self-catalyzed growth of GaAs nanowires on SiOx/Si(111) substrates. *Cryst. Growth Des.* **17**, 5276–5282 (2017).
37. Biasiol, G., Gustafsson, A., Leifer, K. & Kapon, E. Mechanisms of self-ordering in nonplanar epitaxy of semiconductor nanostructures. *Phys. Rev. B* **65**, 205306 (2002).
38. Day, R. W., Mankin, M. N. & Lieber, C. M. Plateau-Rayleigh crystal growth of nanowire heterostructures: strain-modified surface chemistry and morphological control in one, two, and three dimensions. *Nano Lett.* **16**, 2830–2836 (2016).
39. Hetzl, M. et al. Surface passivation and self-regulated shell growth in selective area-grown GaN-(Al,Ga)N core-shell nanowires. *Nanoscale* **9**, 7179–7188 (2017).
40. Wickboldt, P., Anastassakis, E., Sauer, R. & Cardona, M. Raman phonon piezospectroscopy in GaAs - infrared measurements. *Phys. Rev. B* **35**, 1362–1368 (1987).
41. Zardo, I. et al. Raman spectroscopy of wurtzite and zinc-blende GaAs nanowires: Polarization dependence, selection rules, and strain effects. *Phy Rev. B* **80**, 245324 (2009).
42. Groenen, J. et al. Optical-phonon behavior in Ga1-xInxAs: the role of microscopic strains and ionic plasmon coupling. *Phys. Rev. B* **58**, 10452–10462 (1998).
43. Islam, M. R., Verma, P., Yamada, M., Tatsumi, M. & Kinoshita, K. Micro-Raman characterization of starting material for traveling liquidus zone growth method. *Jpn J. Appl Phys.* **41**, 991–995 (2002).
44. Arora, A. K., Rajalakshmi, M., Ravindran, T. R. & Sivasubramanian, V. Raman spectroscopy of optical phonon confinement in nanostructured materials. *J. Raman Spectrosc.* **38**, 604–617 (2007).
45. Colvard, C. et al. Folded acoustic and quantized optic phonons in (GaAl)As superlattices. *Phys. Rev. B* **31**, 2080–2091 (1985).
46. Zou, J., Cockayne, D. J. H. & Usher, B. F. Misfit dislocations and critical thickness in InGaAs/GaAs heterostructure systems. *J. Appl. Phys.* **73**, 619–626 (1993).
47. Salehzadeh, O., Kavanagh, K. L. & Watkins, S. P. Geometric limits of coherent III-V core/shell nanowires. *J. Appl. Phys.* **114**, 054301 (2013).
48. Christensen, N. E. Electronic-structure of GaAs under strain. *Phys. Rev. B* **30**, 5753–5765 (1984).
49. Van De Walle, C. G. Band lineups and deformation potentials in the model-solid theory. *Phys. Rev. B* **39**, 1871–1883 (1989).
50. Wei, S. H. & Zunger, A. Predicted band-gap pressure coefficients of all diamond and zinc-blende semiconductors: chemical trends. *Phys. Rev. B* **60**, 5404–5411 (1999).
51. Pollak, F. H. & Cardona, M. Piezo-electroreflectance in Ge GaAs and Si. *Phys. Rev.* **172**, 816–837 (1968).
52. Pollak, F. H., Cardona, M. & Shaklee, K. L. Piezoelectroreflectance in GaAs. *Phys. Rev. Lett.* **16**, 942–944 (1966).
53. Sitek, A. et al. Excitons in core-shell nanowires with polygonal cross sections. *Nano Lett.* **18**, 2581–2589 (2018).
54. Wang, S. Z. et al. The role of nitrogen-nitrogen pairs in the deviation of the GaAsN lattice parameter from Vegard's law. *J. Appl. Phys.* **96**, 2010–2014 (2004).
55. Detz, H. et al. Growth rate dependence of boron incorporation into BxGa1-xAs layers. *J. Cryst. Growth* **477**, 77–81 (2017).
56. Dimakis, E., Ramsteiner, M., Tahraoui, A., Riechert, H. & Geelhaar, L. Shell-doping of GaAs nanowires with Si for n-type conductivity. *Nano Res.* **5**, 796–804 (2012).
57. Gonze, X. et al. First-principles computation of material properties: the ABINIT software project. *Comp. Mater. Sci.* **25**, 478–492 (2002).
58. Hartwigsen, C., Goedecker, S. & Hutter, J. Relativistic separable dual-space Gaussian pseudopotentials from H to Rn. *Phys. Rev. B* **58**, 3641–3662 (1998).
59. Petrova, N. V. & Yakovkin, I. N. DFT calculations of phonons in GaAs with zinc blende and wurtzite structures. *Phys. Status Solidi B* **250**, 2141–2144 (2013).
60. Bruneval, F., Vast, N. & Reining, L. Effect of self-consistency on quasiparticles in solids. *Phys. Rev. B* **74**, 045102 (2006).

## Acknowledgements

We express our gratitude for the granted beam time and financial support at the Diamond light source (beamline I07; allocated beam time: SI15923), as well as for the granted beam time at the German Synchrotron DESY, PETRA III (beamline P08; allocated beam time: I-20160337). In particular, G.B. and R.G. thank the beamline staff for their support during the experiments. We also thank J. Wagner for the technical maintenance of the molecular beam epitaxy laboratory, L. Bischoff and A. Kunz for the preparation of TEM specimens, G. Hlawacek for Helium Ion Microscopy, M. Krause and U. Lucchesi for assistance with Raman spectroscopy, and S. Prucnal for assistance with PL spectroscopy. M.G. and A.K. thank Silvan Kretschmer for helping in DFT calculations. Finally, support by the Structural Characterization Facilities Rossendorf at Ion Beam Center, computational support from the HZDR Computing Cluster, and funding of TEM Talos by the German Federal Ministry of Education of Research (BMBF), Grant No. 03SF0451 in the framework of HEMCP, are gratefully acknowledged.

## Author contributions

L.B. performed the SEM, the Raman scattering and the PL measurements, as well as the strain calculations. E.D. and L.B. designed the core/shell structures and analysed the Raman and the PL measurements. H.S. and M.H. contributed to PL analyses. R.H. performed the TEM and EDXS measurements and analyses. G.B. and R.G. performed the XRD measurements and analyses. J.G. and E.D. contributed to the XRD analyses. J.G. performed the XRD simulations. M.G.A. and A.V.K. performed the first-principles calculations. E.D. directed and coordinated the research, performed the growth experiments, and wrote the manuscript with the contribution of L.B. All authors discussed the results and commented on the manuscript.

## Additional information

**Supplementary Information** accompanies this paper at https://doi.org/10.1038/s41467-019-10654-7.

**Competing interests:** The authors declare no competing interests.

**Reprints and permission** information is available online at http://npg.nature.com/reprintsandpermissions/

**Peer review information:** *Nature Communications* thanks Katsuhiro Tomioka and other anonymous reviewer(s) for their contribution to the peer review of this work.

**Publisher's note:** Springer Nature remains neutral with regard to jurisdictional claims in published maps and institutional affiliations.

nature COMMUNICATIONS

ARTICLE

https://doi.org/10.1038/s41467-019-12303-5 OPEN

# A bimodal soft electronic skin for tactile and touchless interaction in real time

Jin Ge [1], Xu Wang[1], Michael Drack[2], Oleksii Volkov[1], Mo Liang[1], Gilbert Santiago Cañón Bermúdez[1], Rico Illing[1], Changan Wang[1], Shengqiang Zhou [1], Jürgen Fassbender[1], Martin Kaltenbrunner [2,3] & Denys Makarov [1]

The emergence of smart electronics, human friendly robotics and supplemented or virtual reality demands electronic skins with both tactile and touchless perceptions for the manipulation of real and virtual objects. Here, we realize bifunctional electronic skins equipped with a compliant magnetic microelectromechanical system able to transduce both tactile—via mechanical pressure—and touchless—via magnetic fields—stimulations simultaneously. The magnetic microelectromechanical system separates electric signals from tactile and touchless interactions into two different regions, allowing the electronic skins to unambiguously distinguish the two modes in real time. Besides, its inherent magnetic specificity overcomes the interference from non-relevant objects and enables signal-programmable interactions. Ultimately, the magnetic microelectromechanical system enables complex interplay with physical objects enhanced with virtual content data in augmented reality, robotics, and medical applications.

[1] Helmholtz-Zentrum Dresden-Rossendorf e.V., Institute of Ion Beam Physics and Materials Research, Bautzner Landstrasse 400, 01328 Dresden, Germany. [2] Soft Materials Lab, Linz Institute of Technology, Johannes Kepler University Linz, Altenberger Strasse 69, 4040 Linz, Austria. [3] Soft Matter Physics, Johannes Kepler University Linz, Altenberger Strasse 69, 4040 Linz, Austria. Correspondence and requests for materials should be addressed to J.G. (email: j.ge@hzdr.de) or to M.K. (email: martin.kaltenbrunner@jku.at) or to D.M. (email: d.makarov@hzdr.de)

Electronic skins (e-skins) will revolutionize the way we interact with each other, with machines, electronics, and our surrounding environment[1–9]. Current systems here predominantly rely on interfacing either through physically touching (tactile interaction) or through tracking and monitoring of objects without approaching them (touchless interaction). The ever-increasing complexity that is involved in the manipulation of objects however calls for e-skins that are capable of simultaneously perceiving both tactile and touchless inputs[10–12]. Emerging technologies such as augmented reality (AR) appliances entail new requirements on the process of interaction that dissolve the now-common separation between tactile and touchless operation modes[11]. This paradigm shift will remove the barriers between handling virtual and physical objects and enable even complex interactions in a natural and intuitive way without the need for numerous regulation knobs and different sensory systems[10,13,14].

Assuring the best user experience when manipulating objects places several requirements on e-skins and their multimodal sensors. These forms of interactive electronics are ideally soft and mechanically compliant, selective in their response to objects of interest only and most importantly are able to unambiguously discriminate the desired interaction modes in real time. Presently, there are exciting demonstrations of compliant tactile[15–20] and touchless sensorics including humidity[21,22], magnetic[23–25], temperature[26], optical[27], and capacitive[28,29] sensors. Flexible capacitive structures[28,29] with both pressure and proximity detection are promising candidates for bimodal sensors. However, interference from irrelevant objects and difficulties in discriminating the signal source are fundamental challenges for capacitive systems. Combining individual tactile and touchless sensors on one flexible support is another appealing route. Yet, this requires significantly higher design efforts and often cumbersome and complex fabrication processes[27] that may hamper widespread permeation.

Here, we introduce a compliant magnetic microelectromechanical system (m-MEMS) enabling tactile and touchless interaction modes simultaneously in a single wearable sensor platform. The m-MEMS relies on a genuine, distinguishable bimodal sensing principle. It allows separating the signals from tactile and touchless interactions into two non-overlapping regions, realizing the challenging task of unambiguous discriminating the two interaction modes without knowing the history of the signal. The single sensing unit design of the m-MEMS not only simplifies sensor architecture for fabrication, but also avoids the interference from non-relevant objects. The magnetic touchless sensing mode of the m-MEMS is ready to specify the magnetic objects out of the irrelevant nonmagnetic objects and enables signal-programmable manipulation of the objects by adjusting the magnetic properties of objects of interest. Natural skin not only readily distinguishes different types of stimuli; it is also sensitive over a wide range of signal intensity. Implementations of tactile transducers are often optimized for a high-pressure sensitivity. Practical electronic embodiments would benefit from a high signal-to-noise ratio since only this readily allows for appropriate signal amplification and post processing. We thus optimized our m-MEMS to have a very high signal-to-noise ratio of above 100 in the pressure range from 0.72 to 11.6 kPa. Our m-MEMS e-skins enable complex interactions with a magnetically functionalized physical object that is supplemented with content data appearing in the virtual reality. We design and fabricate a demonstrator where our compliant m-MEMS skin is used not only to identify an object of interest but also to activate a pop-up menu and interact with its content relying on a combination of gestures and physical pressing. This intrinsically bimodal magnetosensitive smart skin allows reducing the number of physical "clicks" needed to activate the same functionality of the device to one, instead of at least three as up to now required when using state-of-the-art gadgets. The demonstrated enhanced —yet intuitive—interaction and manipulation ability enabled by our m-MEMS platform is an important milestone toward multifunctional, highly compliant human-machine interfaces. Beyond the field of AR, e-skins with multimodal interaction abilities are expected to bring benefits for healthcare, e.g., to ease surgery operations and manipulation of medical equipment[30,31], as well as for humanoid robots to overcome the challenging task of grasping[32,33].

## Results

**Compliant m-MEMS platform**. The m-MEMS platform is realized by packaging a flexible magnetic field sensor and a compliant permanent magnet with a pyramid-shaped extrusion at its top surface into a single architecture (Fig. 1a). The magnetic field sensor of the m-MEMS changes its electrical resistance when exposed to an external magnetic field of a magnetically functionalized object for touchless interaction and by mechanical deformation of the m-MEMS package upon application of pressure for tactile interaction (Fig. 1b). The signals of electrical resistance from tactile and touchless interactions separate into two non-overlapping regions by adjusting the field of the magnetic beacons in polarity and strength (Fig. 1c). The compliant m-MEMS platform consists of two major components. The first one is a soft frame based on a 335-µm-thick Polydimethylsiloxane (PDMS) rubber support with a central blind hole (Fig. 1d). The opening in the PDMS frame accommodates a 75-µm-thin compliant permanent magnet (NdFeB microparticles embedded in PDMS rubber) with 28-µm-high pyramid-shaped extrusions at its top surface (Fig. 1e–i). The second component is a high-performance magnetic field sensor, relying on the giant magnetoresistive (GMR) effect, which is hosted on a 20-µm-thin flexible polymeric foil (Fig. 1f). The thin foil seals the opening of the PDMS frame, resulting in a packaged flexible m-MEMS platform. Details on the fabrication are provided in Supplementary Figs. 1 and 2.

Applying a perpendicular directed pressure to the m-MEMS platform changes the distance between the permanent magnet and the GMR sensor through deformation of the 112-µm-thick air gap (Fig. 1g), which causes an altered field at the sensor location. The NdFeB microparticles inside the compliant permanent magnet (Fig. 1j and Supplementary Fig. 3) generate a magnetic stray field (Fig. 1k, Supplementary Figs. 4 and 5), which is adjusted to deliver a field strength in the range from about 2.1 to 1.7 mT at the location of the GMR sensor, depending on the magnet-to-sensor separation distance (Fig. 1l). This field range is selected to assure that the GMR sensor operates at its maximum sensitivity (Fig. 1m).

**Tactile and touchless operation modes**. The entire soft m-MEMS platform is thin and compliant (Fig. 2a), can be bent (Fig. 2b) and applied to curved surfaces such as a model finger (Fig. 2c). Worn as e-skin, our m-MEMS platform readily enables interaction with surrounding magnetic objects in both tactile and touchless modes (Fig. 2c). We demonstrate the capabilities with a delicate daisy flower to interact with (Supplementary Movie 1). One petal of the flower is decorated with a piece of thin and compliant permanent magnet (Fig. 2d) with a small field of <0.6 mT (Supplementary Fig. 6). The direction of the magnetic stray field generated by this patch is opposite to the polarity of the built-in magnetic field at the location of the GMR sensor that stems from the compliant permanent magnet of the m-MEMS platform. Figure 2e shows the time evolution of the change in

NATURE COMMUNICATIONS | https://doi.org/10.1038/s41467-019-12303-5 ARTICLE

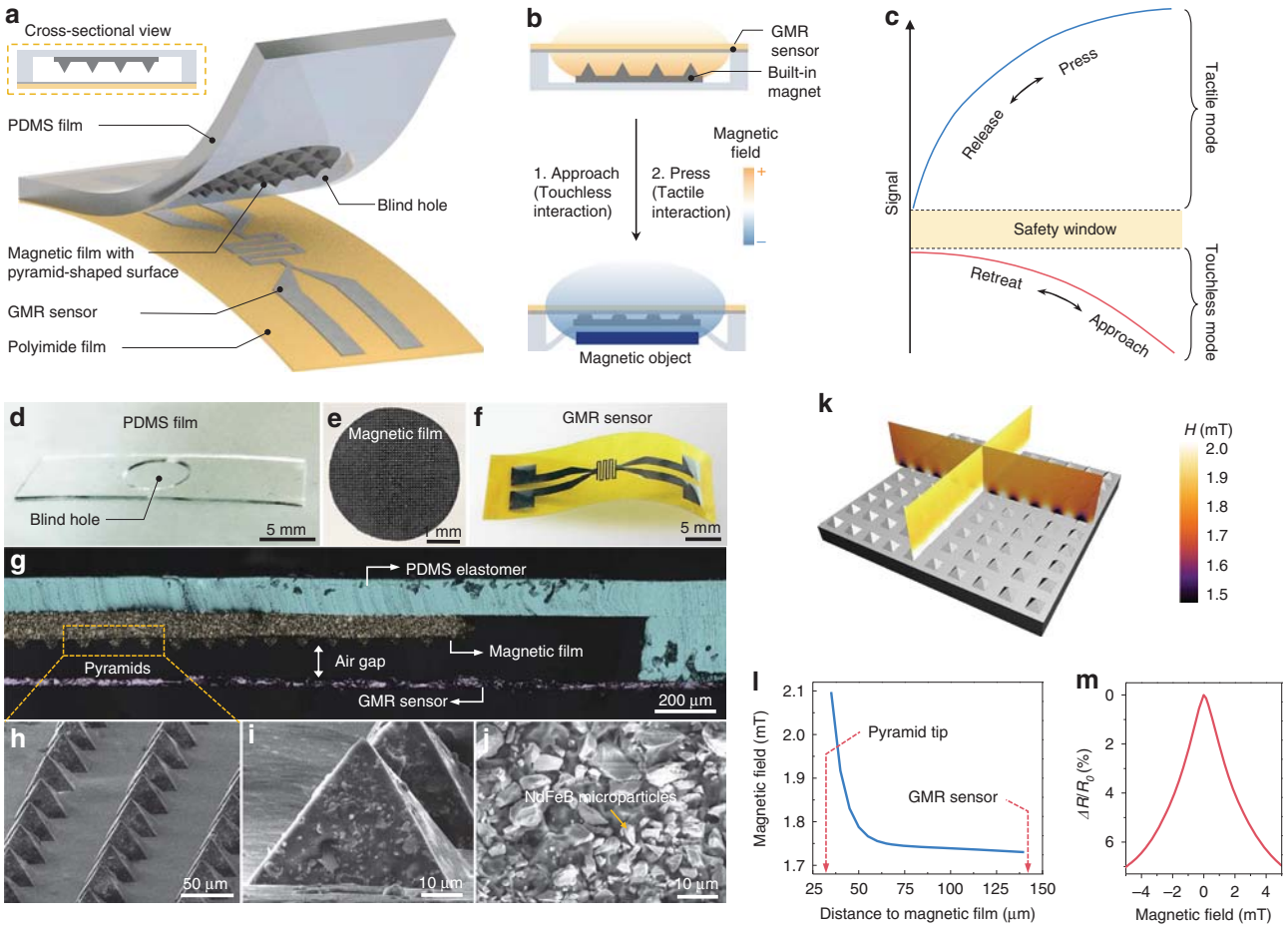


**Fig. 1** Assembly and sensing mechanisms of the compliant m-MEMS platform. **a** Schematic structure of the m-MEMS platform. **b** Mechanisms of the touchless (proximity) and tactile (pressure) sensing modes. The GMR sensor is biased by the built-in magnetic field (yellow cloud; only the field on the sensor side is sketched) of a compliant permanent magnet with pyramid-shaped extrusions. The m-MEMS is exposed to an external magnetic field with the opposite polarity (blue cloud) to the one of the built-in magnet. **c** The m-MEMS platform unambiguously discriminates touchless and tactile interaction modes, as the corresponding signals are located at different ranges with respect to a safety window (orange-shaded stripe). Since the signals are not overlapping, this method does not depend on the history of the interaction process (Supplementary Figs. 7 and 11). Optical images of (**d**) a PDMS frame with a blind hole, (**e**) a compliant permanent magnet with pyramid-shaped extrusions on its top surface, and (**f**) a GMR sensor on a polymeric foil. (**g**) Optical microscopy image (with false color) of the cross-section of the m-MEMS platform. SEM images of the pyramid-shaped extrusions in (**h**) low and (**i**) high magnification. **j** Cross-sectional SEM image of a compliant permanent magnet. **k** Simulated magnetic field profile above the compliant permanent magnet with pyramid-shaped extrusions (magnetized in a field of 1.5 T, Supplementary Fig. 5). **l** Simulated magnetic field profile between a pyramid tip and the GMR sensor. **m** The experimentally measured change of the electrical resistance ($\Delta R/R_0$) of the GMR sensor in response to an applied external magnetic field. $\Delta R = R_0 - R$, $R_0$ and $R$ are the initial and real-time resistance of the GMR, respectively

electrical resistance of the GMR sensor ($\Delta R/R_0$) upon approaching the petal, touching it and retracting the finger from the petal. The signal of the GMR sensor decreases when the fingertip approaches the petal (independent of the manipulation in the touchless mode, the signal remains negative; see discussion for the Supplementary Fig. 7). We note that the sensing responses might be different if the finger approaches the flower petal (Fig. 2a–e) from the back or from the front side. However, for in-plane isotropic magnetic stray fields varying with the distance to the object only, the readout will still be the same. As soon as the fingertip touches the petal and presses it, the signal rapidly increases and changes in sign to positive values where it remains during tactile interaction. Since the petal is very soft, the pressure applied on the petal is imperceptible by human skin and is estimated to be <1 kPa. Typically, the pressure used by humans for the manipulation of objects in the tactile mode is above 1 kPa (colloquially referred to as the softest human touch[34]). This qualitative signal change upon transition from touchless (negative signal) to tactile (positive signal) interaction mode intrinsically renders discrimination between the modes unambiguous. Furthermore, in contrast to state-of-the-art reports, our m-MEMS skins sense the current interaction mode without the need to know the history of the signal change to interpret the state. This eases signal post processing and in turn speeds up response time.

The entire interaction process is illustrated in Fig. 2f. When the m-MEMS platform approaches the magnet on the petal, its field starts to compensate the built-in field of the compliant permanent magnet (Supplementary Fig. 7), resulting in the increase of the electrical resistance of the GMR sensor. The magnetic field will be compensated further until the m-MEMS platform is in touch with the magnetic object (the petal in this case). Applying pressure then moves the GMR sensor toward the pyramidal shaped built-in magnet. Here, the magnetic field at the location of the GMR sensor starts to increase, in turn leading to a decrease of the resistance of the GMR sensor. The processes illustrated in Fig. 2f are confirmed by the simulated change of the magnetic field at the

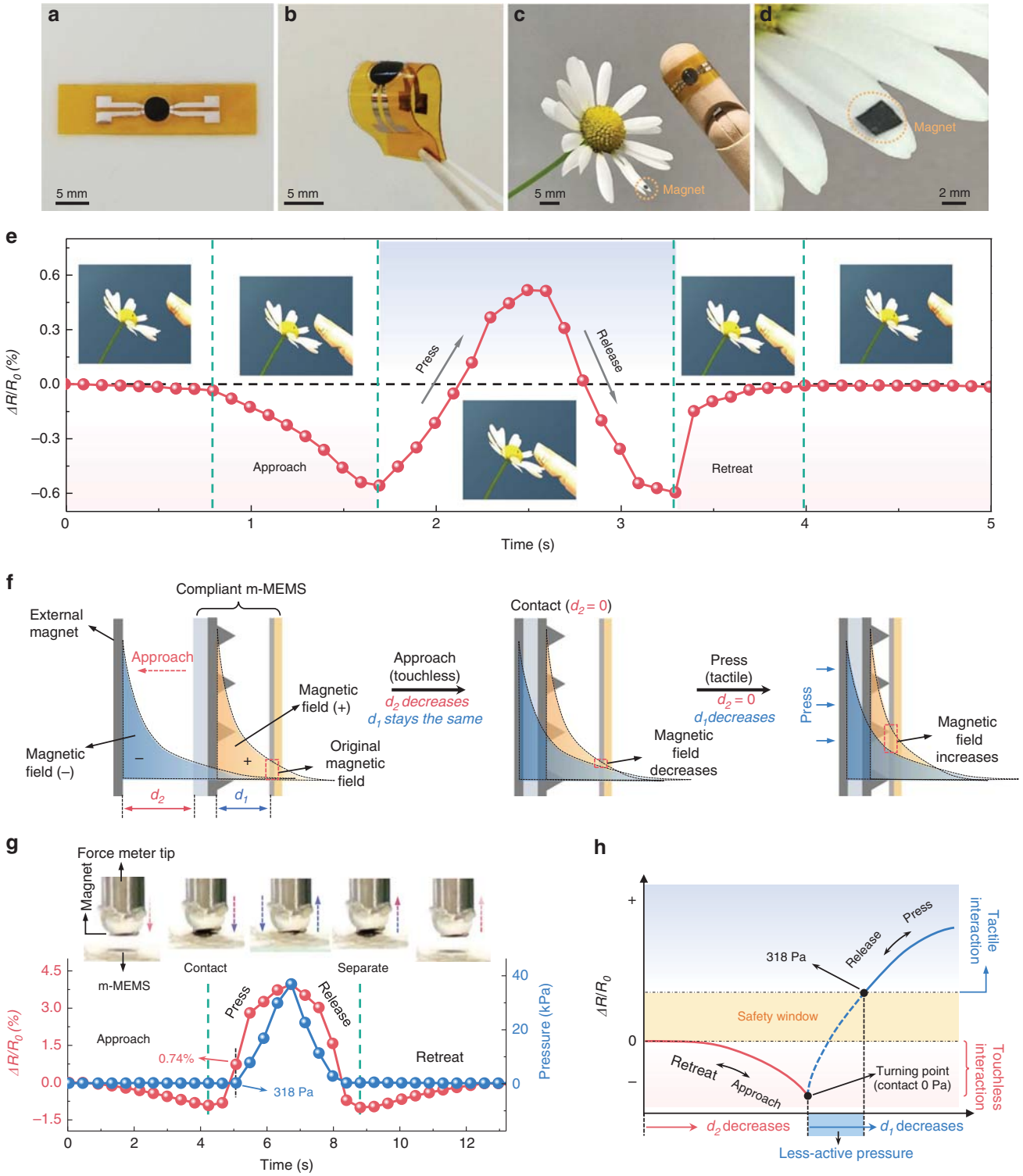


**Fig. 2** Tactile and touchless sensing with the compliant m-MEMS platform. Photographs of our m-MEMS platform in (**a**) a flat and (**b**) bent state. **c** A photograph of the MEMS platform wrapped around a wooden model finger. **d** A petal of a daisy flower decorated with a 20-μm-thin compliant permanent magnet (magnetized by 2.3 T, Supplementary Fig. 5). **e** Change of the electrical resistance ($\Delta R/R_0$) upon an interaction event where the finger bearing the m-MEMS platform approaches, touches and retreats from the magnet-decorated flower petal. The distance between the m-MEMS platform and the external permanent magnet is 4 mm. **f** Schematic illustration of the evolution of the strength of the magnetic field at the sensor location: superposition of the built-in magnetic field provided by the compliant permanent magnet (orange-shaded region) and an external magnetic field source (blue-shaded region). **g** Change of the electrical resistance (red dots) and the corresponding mechanical force (blue dots) applied to the m-MEMS during approaching, touching, pressing, releasing and retracting. **h** Schematic illustration of the safety window that separates the signal of the touchless interaction from the one of the tactile interaction

location of the GMR sensor during the interaction process (Supplementary Fig. 8).

We experimentally determine the applied pressure during tactile interaction and correlate it to the change of the electrical resistance of the GMR sensor ($\Delta R/R_0$) right after switching from touchless to tactile mode with a custom-built setup that simultaneously measures the change of the electrical resistance and the corresponding mechanical force applied on the m-MEMS platform (Supplementary Fig. 9 and Supplementary Movie 2). Here, the m-MEMS is moved upward to approach a permanent magnet (of same thickness and magnetization as the one on the flower petal, 4 mm in diameter) fixed at the tip of a force meter, followed by bringing them into contact and further pressing them together. When a predefined pressure is reached, we move the m-MEMS back to its original position. We evidence that the turning points in the resistance change are consistent with the ones of the force change (Fig. 2g). The small offset observed between the turning points in the force and relative resistance curves is due to the limited sensitivity of the force sensor (gentle pressure of <79 Pa at the beginning and end of the mechanical contact cannot be detected, Supplementary Fig. 10). Bringing the m-MEMS platform into contact with the magnet causes $\Delta R/R_0$ to jump from −0.92% (negative value, characteristic of touchless mode) to +0.74% (positive value, characteristic of the tactile mode) with a pressure increase of only 318 Pa, which is much smaller than the softest human touch (1 kPa).

The essence of manipulating magnetic objects with our m-MEMS platform is based on the algorithm that correlates the signal of the sensor $\Delta R/R_0$ to the commands for manipulation (Supplementary Fig. 11). As the signals specific to touchless and tactile manipulation modes do not overlap, the compliant m-MEMS is able to unambiguously discriminate between the two interaction types. In more detail (Fig. 2h), the value of $\Delta R/R_0$ upon touchless interaction is always negative, but $\Delta R/R_0$ at the initial stage of the tactile interaction (from the very event of touching to a certain degree of subsequent pressing) is also negative and thus in theory briefly overlaps in this region with the signal of the touchless interaction mode. However, in practical settings, especially such ones that involve manipulation processes with (human) fingers, the minimum pressure required to switch the signal polarity (here determined to be <318 Pa) is overcome immediately upon a pressing event. In addition, this transition to the positive signal range is achieved during <0.8 s when moving the finger even at a slow speed of 1 mm/s (Fig. 2g). We demonstrated that the evolution of the signal during the touchless and tactile interaction process is highly repeatable (Supplementary Fig. 12), which endows the m-MEMS platform with a safety window for reliably manipulating objects in both interaction modes.

**Enhancement of the m-MEMS performance**. The presence of the air gap between the GMR sensor and the compliant permanent magnet as well as the pyramid-shaped extrusions drastically enhance the performance of the compliant m-MEMS platform in terms of the pressure sensitivity and sensing speed. The pressure sensitivity is determined by the change of the magnetic field at the location of the GMR sensor, which is realized through relative displacement of the soft magnet in the blind hole (Fig. 1g). We simulate the mechanical deformation of the individual components (Fig. 3a) under low and high applied pressures. We extract the simulated change of air gap height versus pressure (Fig. 3b) from these calculations. Due to the cantilever-like structure of the m-MEMS package, the air gap height can be substantially reduced even at a low pressure of <764 Pa (Fig. 3a, upper panel), resulting in a sharp increase of $\Delta R/R_0$ for pressures over 318 Pa (see also transition region in Fig. 2g, dashed blue line). At higher pressures (>764 Pa), the pyramid-shaped extrusions are brought into mechanical contact with the GMR sensor. Elastic deformation of the soft pyramids (Fig. 3a, lower panel) then brings the compliant permanent magnet still closer to the GMR sensor. This elastic shape change of the magnetic pyramids provokes a signal change $\Delta R/R_0$ in regions of higher pressures and significantly expands the sensitivity range of our m-MEMS platform (corresponds to the solid blue line in Fig. 2h) for object manipulation in the tactile mode. The dynamic shape deformation of the compliant m-MEMS platform under pressure is shown in Supplementary Movie 3.

To demonstrate the effectiveness of the air gap with pyramid-shaped soft magnet design, we compare the finite element mechanical simulations of the m-MEMS platforms possessing either only an air gap, or only pyramid-shaped extrusions (Fig. 3b). The displacement of the compliant permanent magnet towards the GMR sensor for the device with an air gap only (without pyramids) completes solely in the low-pressure range. In contrast, the displacement of the compliant permanent magnet towards the GMR sensor for the structure with pyramids only (no air gap) is very small in the low-pressure range. The simulated data are in agreement with the experimental results (Fig. 3c). The $\Delta R/R_0$ of the structure with air gap only and with both air gap and pyramids below 1 kPa is much higher than that of the structure with pyramids only, demonstrating the contribution of the air gap to the sharp increase of $\Delta R/R_0$ for pressures below the softest human touch. The change of $\Delta R/R_0$ for the structure with air gap only is higher than that of the structure with both air gap and pyramids for pressures below 1 kPa, but $\Delta R/R_0$ gradually saturates in the higher-pressure region rather than continuously increasing as in the case of structures with pyramids. This further corroborates the importance of pyramidal structures in improving the pressure sensitivity at high pressures.

Pyramidal extrusions in addition avoid sticking of the compliant permanent magnet to the PI foil of the GMR sensor. This anti-sticking effect significantly increases the dynamic range of the sensor, and ensures fast switching between touchless and tactile interaction modes in less than 75 µs (Fig. 3d, e). Without the pyramid-shaped extrusions, the compliant permanent magnet sticks to the surface of the PI foil and the electrical resistance of the m-MEMS recovers rather slowly after releasing the pressure (Supplementary Fig. 13).

Our m-MEMS platform exhibits an exceptionally high signal-to-noise ratio (SNR) of above 80 at the small pressure of 240 Pa, and above 100 in the entire pressure range from 0.72 to 11.6 kPa due to its small noise floor of only 0.01% (Fig. 3f). Our approach of optimizing the SNR rather than the pressure sensitivity is motivated by practical considerations of signal amplification. Indeed, from an electrical engineering point of view it is rather straightforward to amplify even small signals given that the SNR is large. We here outperform state-of-the-art reports[35–37] (Supplementary Fig. 14), rendering our m-MEMS concept highly promising even for pressure transducers only. With high SNR, our m-MEMS are able to detect different levels of pressure in a highly repeatable way (Fig. 3g). Even after 5000 pressure-release cycles (with a maximum pressure of 42.5 kPa), no degradation in the sensor response is observed (Fig. 3h).

**Array of compliant m-MEMS**. The compliant m-MEMS platform is readily scaled into a sensor array (Fig. 4a, b) for mapping the spatial distributions of magnetic fields and pressure. A PDMS frame is modified to have four openings (diameter of each opening, Ø, is 4 mm) accommodating four compliant permanent magnets (Ø = 3 mm, magnetized in an in-plane field of 1.5 T).

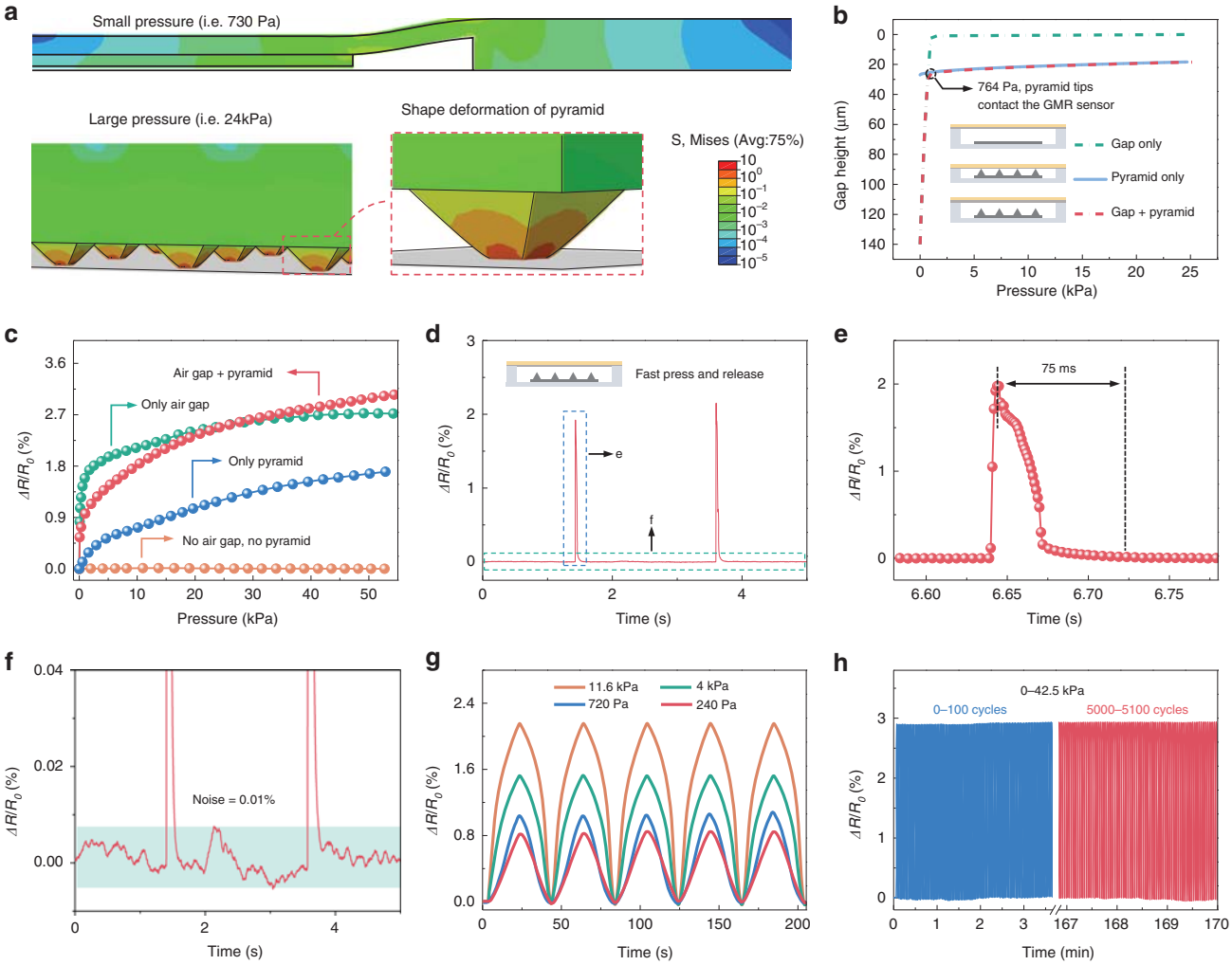


**Fig. 3** Impact of the m-MEMS structure on the pressure sensing performance. **a** Finite element mechanical simulations of the shape deformation and stress distribution of a compliant m-MEMS platform under high and low applied pressure. **b** The simulated change of the air gap height as a function of the applied pressure for the case of the m-MEMS platform possessing pyramids only, air gap only as well as a combination of air gap and pyramids. **c** The experimentally measured change of the electrical resistance of the compliant m-MEMS platform as well as the devices with pyramids only, with air gap only, and without air gap and pyramids, versus the applied pressure. **d** The experimentally measured change of the resistance of the compliant m-MEMS platform under a fast pressure stimulus. **e** The close-up of the area indicated with a dash square in **d**. **f** The close-up of the baseline in panel **d**, highlighting the excellent signal-to-noise ratio of over 100. **g** The experimentally measured change of the electrical resistance of the compliant m-MEMS platform during the press-release cycles. The device is exposed to a pressure of different magnitude of 240 Pa, 720 Pa, 4 kPa, and 11.6 kPa. **h** Durability test of the compliant m-MEMS platform by applying more than 5000 press-release cycles without signs of fatigue. Maximum pressure is 42.5 kPa

The PDMS frame is encapsulated with a polyimide foil hosting an array of four GMR sensors consisting of Py/Cu multilayers. Such packaged compliant m-MEMS arrays, here consisting of four functional elements (four-pixel array), intimately conform to curved surfaces such as a model finger (Fig. 4c). The four sensors are connected in series and driven with a constant current. The voltages of each m-MEMS are simultaneously recorded with a data acquisition box. The resistance of each pixel is calculated by dividing the measured voltage by the applied current. Based on the change of the resistance of each m-MEMS element upon applying a pressure or an external magnetic field, the distribution of both pressure and magnetic field can be uniquely recognized. We are thus able to map of the resistance changes of the m-MEMS in the array at every spatial position when activated by gently pressing (Fig. 4d). Here, a non-magnetic cotton swab is used to press one of the pixels in the array, leaving the others unaffected. Similarly, when an external magnetic object approaches each of the four m-MEMS pixels, the one closest to the external magnet reveals the most pronounced change in resistance (Fig. 4e), thus enabling spatial mapping and contributing to the improved spatial resolution of the m-MEMS in touchless mode. Downscaling lateral dimensions of individual sensor elements can achieve further improvement of the spatial resolution.

**Multichoice 3D touch in AR**. AR allows to complement real objects with features and properties evident in virtual reality only. The possibility to interact with the virtual content and thus manipulate the properties of the real object is one of the major promises of future AR devices (Supplementary Fig. 15). We here realize an interactive e-skin with tactile and touchless sensing functionalities that allows us to perform complex interactions with a physical object (e.g., a region of a glass plate) supplemented with content data appearing in the virtual reality (e.g., virtual knobs superimposed on the glass plate). The data can be selected and manipulated using our compliant m-MEMS

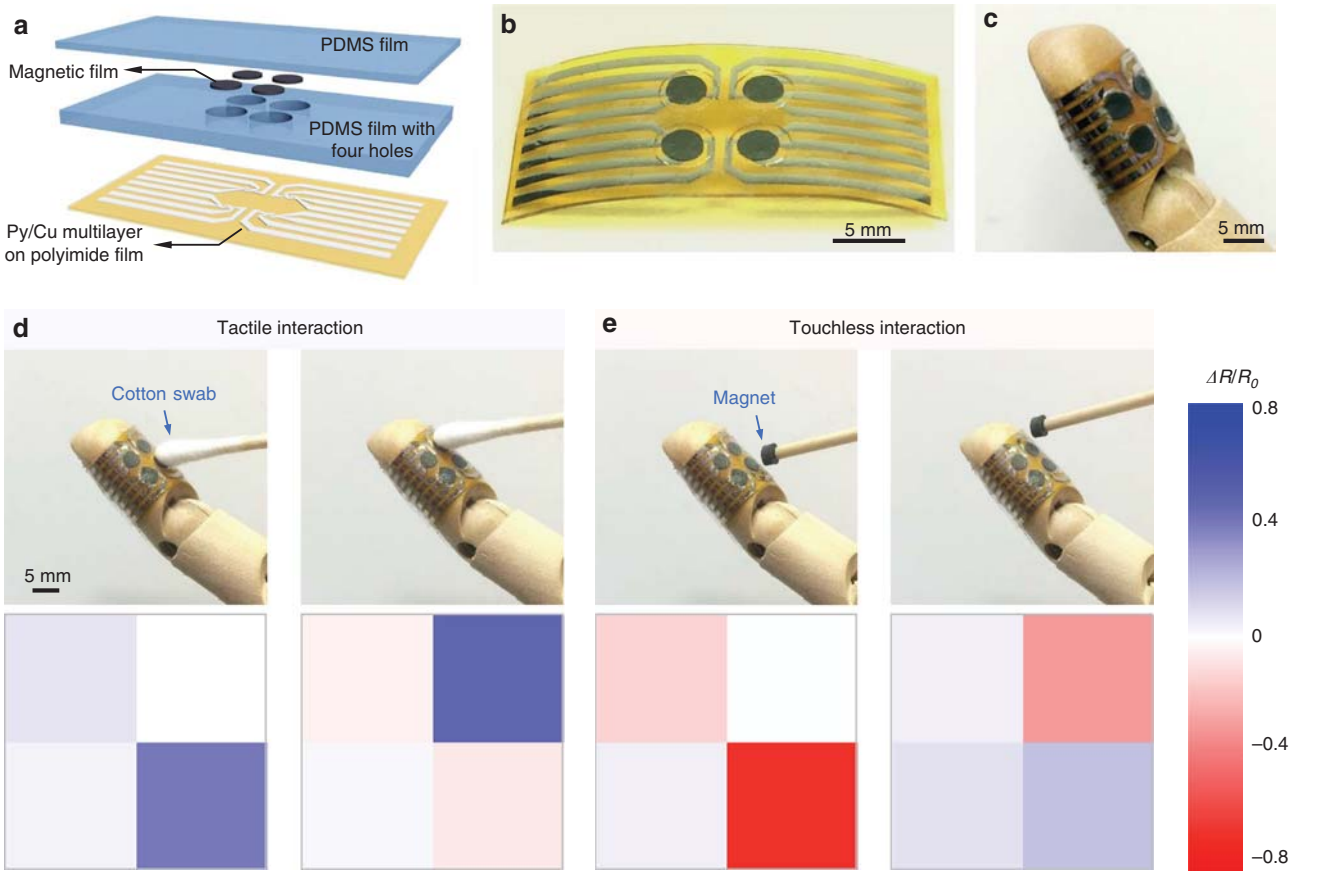


**Fig. 4** Array of compliant m-MEMS. **a** Schematic illustration of a 2 × 2 array of compliant m-MEMS. The PDMS frame is encapsulated with a polymeric foil hosting an array of four GMR sensors. **b** Photograph of a freestanding m-MEMS array. **c** A multi-pixel m-MEMS conformally adhered onto a model finger. **d** Resistance change $\Delta R/R_0$ of the four pixels when consecutively pressed with a cotton swab. **e** $\Delta R/R_0$ of the four pixels on the array when approached individually by a cylindrical soft magnet

platform in the form of multiple choices (Fig. 5, Supplementary Movie 4). Those pop-up at a (virtual) screen upon approaching the object, can be chosen by swiping the finger to the function of interest and can be manipulated by pressing. Finger-motion-correlated manipulation of multichoice in a touchless manner requires a sufficiently large interaction distance and thus sensitivity of the e-skin. Here, the real-world object (the glass plate) is equipped with a strong magnetic field source to improve the proximity sensitivity even at larger distances (Supplementary Figs. 16 and 17).

To demonstrate the concept, we adhere a compliant m-MEMS platform conformably to a wooden fingertip (inset in Fig. 5f) that then interacts with a glass plate with a permanent magnet located behind. Since the distance of the touchless interaction increases with a decreasing gradient of the magnetic field in the front region of the glass plate, we fix a permanent magnet with a strong magnetic stray field 1-cm-far behind the glass plate in order to have a long touchless interaction distance (Supplementary Fig. 18). We here arrange four GMR sensors into a Wheatstone bridge and package one of them into the m-MEMS platform to cancel unwanted thermoresistive effects of the GMR sensors (Supplementary Fig. 19 and Supplementary Note 1). Although this translates the output signal into voltage changes ($\Delta V/V_0$) rather than a change of resistance ($\Delta R/R_0$), the signal $\Delta V/V_0$ generated through touchless manipulation and tactile manipulation is still separated by a safety window and can be unambiguously discriminated (Supplementary Fig. 20). Upon approaching the glass plate, the $\Delta V/V_0$ of the m-MEMS platform increases. Once the m-MEMS sensor contacts the glass plate and pressure is applied, the $\Delta V/V_0$ starts to decrease. Our m-MEMS e-skin is able to select a virtual item (i.e., room temperature, Fig. 5b–d, g–i, l–n) from a multichoice list on a virtual display in touchless mode, and then adjust the value of this option using tactile interactions between the finger and the glass plate (Fig. 5e, j, o). For example, the room temperature can be decreased by firmly pressing or increased by gently pressing.

The manipulation of virtual objects is realized by coding different execution sequences triggered by electrically read signals ($\Delta V/V_0$) from the m-MEMS. Figure 5p shows the evolution of the electrical signal during the interaction process between a wooden finger and a glass plate decorated with a piece of permanent magnet (Fig. 5a–o). We define distinct voltage thresholds and motion patterns of the finger and correlate them with switching events of data elements shown on a virtual screen. The option of interest (here, room temperature) is selected for further manipulation by pointing to a proper location for a while. When $\Delta V/V_0$ passes the safety window, the tactile interaction mode is activated and $\Delta V/V_0$ is used to adjust the value of the visual item of choice. For example, by firmly pressing, the temperature is changed from 21.0 °C to 19.6 °C. Our e-skin here enables us to manipulate virtual objects in a way we usually do with physical objects.

The field of a magnetic object can be adjusted to the requirement in terms of its strength and gradient (Figs. 2 and 5). Thus, the electrical signal of the touchless interaction can be defined for easily coding the manipulation of the objects of choice, which enables intrinsic selectivity upon interaction with irrelevant objects. Our multichoice 3D touch demonstrator (Fig. 5, Supplementary Movie 4), may enable a broad range of applications. Beyond

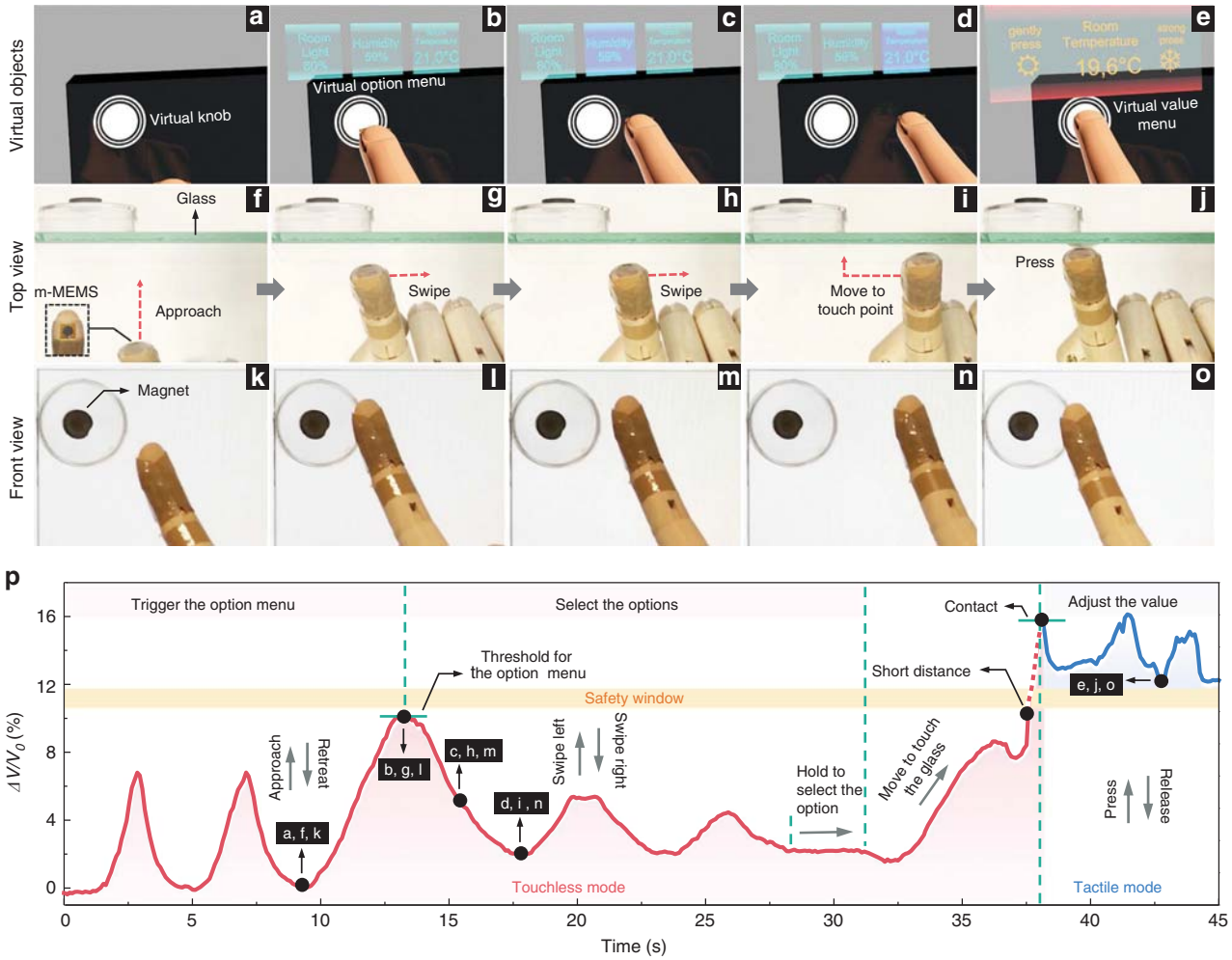


**Fig. 5** Multichoice 3D touch in augmented reality. **a**–**e** The interactive on-skin device with tactile and touchless sensing functionalities allows us to perform complex interactions with a physical object (e.g., a functionalized region on a glass plate) supplemented with a content data appearing in the virtual reality (a virtual knob). The actual realization of the concept is shown with snapshots of the Supplementary Movie 4 shown in **f**–**j** top view and **k**–**o** front view where an m-MEMS applied to a fingertip approaches the virtual knob, swipes over it and proceeds with pressing. As the first step (**a**, **f**, **k**), the e-skin interacts with the knob in a touchless way upon approach. At a certain distance to the object, a selection of options appears on a virtual display (**b**, **g**, **l**). The options are pre-assigned to this object, e.g., room light on/off, humidity, room temperature. The corresponding option (e.g., temperature) can be chosen by a gesture, e.g. motion of a finger towards the object of choice (**c**, **h**, **m** and **d**, **i**, **n**). Its value can be further manipulated using conventional tactile interaction by pressing the knob with a finger (**e**, **j**, **o**). **p** Evolution of the electrical readout upon the interaction process between the compliant m-MEMS platform applied to a wood finger and a glass plate, decorated with a permanent magnet. $\Delta V = V_0 - V$ with $V_0$ and $V$ denoting the initial voltage and real-time voltage, respectively

proximity sensing, our m-MEMS platform also features an angle sensing functionality (Supplementary Fig. 21, Supplementary Note 2, Supplementary Movie 5), which is of advantage for rotation-based manipulations in AR settings[25,38] and medical applications. Generally, we envision that surgeons wearing e-skins equipped with an m-MEMS platform will acquire the ability to quantitatively sense mechanical properties of tissues upon a regular palpation. At the same time, the touchless interaction functionality may enable surgeons to manipulate medical equipment in a touchless manner, helping them to avoid unwanted contamination. Furthermore, touchless perception through our m-MEMS platform may enable robots to navigate their grippers to a desired position in a touchless way, while the tactile perception guarantees a suitable force for grasping objects without dropping or breaking them. Although the demonstrations here are done with the m-MEMS platform positioned on a fingertip of a wooden finger, the same performance is achieved when the device is positioned on a human finger (Supplementary Fig. 22, Supplementary Movie 6).

## Discussion

We put forth a concept of e-skins equipped with a compliant magnetic microelectromechanical system (m-MEMS) that synergistically combines tactile and touchless interaction modes in a single sensor unit. The unambiguous discrimination between the interaction modes is aided by the rational design of the structure (air gap and pyramid-shaped extrusions) and the magnetic stray field inside the m-MEMS as well as the one around an object of interest. The m-MEMS architecture in this work is of a general design. Albeit already highly functional, further performance optimization is expected through adjusting size and number of the pyramids, the gap height, the thickness of the PDMS film, the diameter of the circular opening and the magnetic moment of the compliant magnet.

We showcase the usability of our bimodal e-skin in AR settings, where a sensor-functionalized hand performs complex selection and manipulation of virtual objects by simultaneously using the two sensing modes. Our concept provides a fertile base

for a cornucopia of applications in interactive electronics, supplemented reality, human-machine interfaces, but also for the realization of smart soft robotics with highly compliant integrated feedback systems as well as in medicine for physicians and surgeons.

Our here-developed m-MEMS platform is very general and can be realized based on magnetic field sensors other than those relying on the GMR effect. Concepts including compliant Hall effect[24,39] (sensitive to out-of-plane magnetic fields) and compliant planar Hall effect[40] (sensitive to in-plane magnetic fields) sensors might offer further advantages to m-MEMS platforms. They are linear sensors of magnetic field and also possess high sensitivity to small magnetic fields. Considering that generic stray fields of magnetized objects contain three components (two in-plane and one out-of-plane), we envision that the m-MEMS would benefit from three-axial compliant magnetic field sensors.

The wearable m-MEMS platform supports interaction with multiple magnetic objects. If the functionality of objects is encoded in a different magnetic field profile (different field strength, different symmetry of the magnetic field, different field gradients), then our sensing platform can be trained to recognize these objects. This is the case demonstrated in Figs. 2 and 5. In the first case when a thin magnetic patch is used, the field is weak and interaction starts at close distance. In the second case (standard permanent magnet), the field is rather strong and interaction starts at a larger distance to the object. The spatio-temporal variation of the signal will be different when approaching these two objects. These differences are unique fingerprints of each magnetic object, allowing constructing spatio-temporal maps for their unique identification.

## Methods

**Preparation of the silicon mold**. Thermally oxidized $SiO_2$ (1000 nm)/Si(100) wafers were coated with a grid photoresist pattern relying on a regular photolithography processing. The exposed $SiO_2$ patterns were etched by HF solutions. After this, the samples were anisotropically etched in the solution of KOH and isopropanol (35%wt KOH in $H_2O$: Isopropanol = 4:1, v/v) at 80°C. When the etching process was finished, the samples were cleaned in water and ethanol, and further modified with 1 H,1 H,2 H,2H-perfluorodecyltrichlorosilane (Sigma-Aldrich) by gas phase silanization to prevent adhesion.

**Preparation of the GMR sensor based on Py/Cu multilayers**. Polyimide (PI) resin (PI2545, MicroSystem, USA) was drop casted on Polyethylene terephthalate (PET) sheet (125 µm thick) fixed to a film applicator (TOC AB3400). Then, a wet PI coating was fabricated by the film applicator. The wet polymeric film was dried at 80 °C. After drying, the sample was heated at 200 °C for 1 h to crosslink the PI film. Here, PI films with a thickness of 20 µm were used as a substrate for the deposition of GMR sensors. GMR multilayers with a stack [substrate//Ta(5 nm)/$[Py(1.5\ nm)/Cu(2.3\ nm)]_{30}$/Py(1.5 nm)] were grown by magnetron sputter deposition (BESTEC, Germany) at room temperature.

**Characterizations**. Scanning electron microscopy (SEM) images and elemental mappings were taken using a Hitachi S-4800 microscope. Magnetic hysteresis loops were measured at 300 K using a superconducting quantum interference device vibrating sample magnetometer (SQUID-VSM, Quantum Design). Compliant permanent magnets (NdFeB microparticles embedded in PDMS) were magnetized in a 1.5 T magnetic field of an electromagnet. Confocal microscopy images were taken using a confocal microscope (Zeiss, Smartproof 5). Giant magnetoresistive performance of Py/Cu multilayers (Py: $Ni_{80}Fe_{20}$) was measured at room temperature in an in-plane magnetic field generated by an electromagnet. The force was measured by a universal digital force gauge (Sauter FH-5). Electrical resistance of the compliant m-MEMS platform was measured using a Keysight B2902A or Keysight 34461 A device.

**Magnetic field simulation**. Here, we describe our calculation of the spatial distribution of a magnetic field $\vec{\mathbf{B}}$ outside a disk-shaped compliant permanent magnet with pyramid-shaped extrusions, which is homogeneously filled with magnetic NdFeB microparticles. To simplify numerical calculations, we assume that each microparticle is (i) of spherical shape with a radius, $R$, of 2.5 µm and (ii) magnetized along $\vec{y}$-axis. In this case, the magnetic field, which is generated outside each magnetic particle, has a following form:

$$\vec{\mathbf{B}}_i(\vec{\mathbf{r}}_i) = \frac{\mu_0}{4\pi}\frac{3\vec{\mathbf{n}}_i\left(\vec{\mathbf{n}}_i\vec{\mathbf{M}}\right) - \vec{\mathbf{M}}}{r_i^3}$$

where $\mu_0$ is a vacuum permeability, $\vec{\mathbf{n}}_i = \vec{\mathbf{r}}_i/r_i$ with $r_i = \sqrt{(x-x_i)^2 + (y-y_i)^2 + (z-z_i)^2}$ being a distance from the center of a magnetic particle $(x_i,y_i,z_i)$ to any other point $(x, y, z)$, $\vec{\mathbf{M}} = \frac{4}{3}\pi R^3 M_s \vec{\mathbf{y}}$ is the total magnetic moment of a spherical particle, with $M_s$ being the saturation magnetization.

Due to the big density of magnetic microparticles inside the polymeric disk-shaped film and their random distribution, we consider the magnetic disk as a homogeneously magnetized body with a reduced saturation magnetization compared with an individual microparticle. We calculate numerically the spatial distribution of the magnetic field generated by a disk and sum it with a field distribution, which is generated by magnetic microparticles located in pyramids. The resulting field distribution is presented in Fig. 1k.

**Mechanical simulations**. The mechanical simulation has been calculated in Abaqus Standard. It is split into the deformation of the sensor enclosure with rotational symmetry and the deformation of the NdFeB permanent magnet pyramids. The sensor geometry as shown in Supplementary Fig. 9 is indented in perpendicular direction by a rigid stamp of 4-mm diameter that is loaded by a certain pressure. The two cases of a non-sealed inner sensor volume with unhampered air exchange as well as a perfectly sealed volume with adiabatic compression of the air content have been simulated. For the compression of the permanent magnet, a single unit cell of an infinite array of the pyramid-structured disk has been simulated. For both cases the displacement versus the applied pressure was calculated.

**Discrimination of the two interaction modes**. Upon approaching or retreating the finger with a m-MEMS to or from an external magnetic object (blue object), the electrical resistance of the magnetic field sensor integrated in the m-MEMS platform will change (Supplementary Fig. 7). In the touchless mode, the signal change remains negative (Fig. 2 and Supplementary Fig. 11). The software decides that the interaction mode is switched from the touchless to the tactile one as soon as the signal $\Delta R/R_0$ reached the contact point (0 Pa; highest negative signal change) and subsequently raised up to the value corresponding to 318 Pa of applied pressure. As soon as these two conditions are detected by the electronics, the signal analysis is paused for a certain user-defined time. After this waiting time, the signal level is analyzed further. If $\Delta R/R_0$ is positive (negative), the interaction mode is assigned to be tactile (touchless) (Supplementary Fig. 11).

We note that the compliant m-MEMS platform can provide a reliable and unambiguous separation between the two interaction modes even if the settings are sub-optimal. One of the examples is when the strength of the external magnetic field is chosen to be large enough that the resulting resistance change upon touchless interaction is very large and positive values of the resistance change cannot be achieved upon tactile interaction. Still, by properly choosing the logic behind the interaction process, touchless and tactile modes can be readily separated (Fig. 5 and Supplementary Fig. 20).

## Data availability

The datasets generated during and/or analysed during the current study are available from the corresponding author on reasonable request.

Received: 9 March 2019 Accepted: 3 September 2019
Published online: 27 September 2019

## References

1. Wang, S. et al. Skin electronics from scalable fabrication of an intrinsically stretchable transistor array. *Nature* **555**, 83–88 (2018).
2. Kim, Y. et al. A bioinspired flexible organic artificial afferent nerve. *Science* **360**, 998–1003 (2018).
3. Miyamoto, A. et al. Inflammation-free, gas-permeable, lightweight, stretchable on-skin electronics with nanomeshes. *Nat. Nanotechnol.* **12**, 907–913 (2017).
4. Larson, C. et al. Highly stretchable electroluminescent skin for optical signaling and tactile sensing. *Science* **351**, 1071–1074 (2016).
5. Kang, S.-K. et al. Bioresorbable silicon electronic sensors for the brain. *Nature* **530**, 71–76 (2016).
6. Gao, W. et al. Fully integrated wearable sensor arrays for multiplexed in situ perspiration analysis. *Nature* **529**, 509–514 (2016).
7. Chortos, A., Liu, J. & Bao, Z. Pursuing prosthetic electronic skin. *Nat. Mater.* **15**, 937 (2016).

8. Kaltenbrunner, M. et al. An ultra-lightweight design for imperceptible plastic electronics. *Nature* **499**, 458–463 (2013).
9. Hammock, M. L. et al. 25th anniversary article: the evolution of electronic skin (E-Skin): a brief history, design considerations, and recent progress. *Adv. Mater.* **25**, 5997–6038 (2013).
10. Maisto, M. et al. Evaluation of wearable haptic systems for the fingers in augmented reality applications. *IEEE Trans. Haptics* **10**, 511–522 (2017).
11. Giordano, M. et al. Mid-air haptics for control interfaces. In *Extended Abstracts of the 2018 CHI Conference on Human Factors in Computing Systems* p.W15, (ACM, 2018).
12. Lee, L. H. & Hui, P. Interaction methods for smart glasses: a survey. *IEEE Access* **6**, 28712–28732 (2018).
13. Cantón, P., González, Á. L., Mariscal, G. & Ruiz, C. Applying new interaction paradigms to the education of children with special educational needs. In *International Conference on Computers for Handicapped Persons* 65–72 (Springer, Berlin, Heidelberg, 2012).
14. Huang, D.-Y. et al. DigitSpace: designing thumb-to-fingers touch interfaces for one-handed and eyes-free interactions. In *Proc. 2016 CHI Conference on Human Factors in Computing Systems* 1526–1537 (ACM, 2016).
15. Pan, L. et al. An ultra-sensitive resistive pressure sensor based on hollow-sphere microstructure induced elasticity in conducting polymer film. *Nat. Commun.* **5**, 3002 (2014).
16. Jin, G. et al. A stretchable electronic fabric artificial skin with pressure-, lateral strain-, and flexion-sensitive properties. *Adv. Mater.* **28**, 722–728 (2016).
17. Lee, S. et al. A transparent bending-insensitive pressure sensor. *Nat. Nanotechnol.* **11**, 472–478 (2016).
18. Dagdeviren, C. et al. Conformable amplified lead zirconate titanate sensors with enhanced piezoelectric response for cutaneous pressure monitoring. *Nat. Commun.* **5**, 4496 (2014).
19. Wu, W., Wen, X. & Wang, Z. L. Taxel-addressable matrix of vertical-nanowire piezotronic transistors for active/adaptive tactile imaging. *Science* **340**, 952–957 (2013).
20. Sungmook, J. et al. Reverse-micelle-induced porous pressure-sensitive rubber for wearable human–machine interfaces. *Adv. Mater.* **26**, 4825–4830 (2014).
21. Jun, F. et al. Giant moisture responsiveness of VS2 ultrathin nanosheets for novel touchless positioning interface. *Adv. Mater.* **24**, 1969–1974 (2012).
22. Katalin, S. et al. Touchless optical finger motion tracking based on 2D nanosheets with giant moisture responsiveness. *Adv. Mater.* **27**, 6341–6348 (2015).
23. Melzer, M. et al. Imperceptible magnetoelectronics. *Nat. Commun.* **6**, 6080 (2015).
24. Michael, M. et al. Wearable magnetic field sensors for flexible electronics. *Adv. Mater.* **27**, 1274–1280 (2015).
25. Cañón Bermúdez, G. S. et al. Magnetosensitive e-skins with directional perception for augmented reality. *Sci. Adv.* **4**, eaao2623 (2018).
26. Martin, Z. et al. An all-printed ferroelectric active matrix sensor network based on only five functional materials forming a touchless control interface. *Adv. Mater.* **23**, 2069–2074 (2011).
27. Oh, N. et al. Double-heterojunction nanorod light-responsive LEDs for display applications. *Science* **355**, 616–619 (2017).
28. Zhang, B. et al. Dual functional transparent film for proximity and pressure sensing. *Nano Res.* **7**, 1488–1496 (2014).
29. Sarwar, M. S. et al. Bend, stretch, and touch: Locating a finger on an actively deformed transparent sensor array. *Sci. Adv.* **3**, e1602200 (2017).
30. Black, D. et al. Auditory display as feedback for a novel eye-tracking system for sterile operating room interaction. *Int. J. Comput. Assist. Radiol. Surg.* **13**, 37–45 (2018).
31. Ming, Y. et al. Silicon nanomembranes for fingertip electronics. *Nanotechnology* **23**, 344004 (2012).
32. Bartolozzi, C., Natale, L., Nori, F. & Metta, G. Robots with a sense of touch. *Nat. Mater.* **15**, 921–925 (2016).
33. Tai, K., El-Sayed, A.-R., Shahriari, M., Biglarbegian, M. & Mahmud, S. State of the art robotic grippers and applications. *Robotics* **5**, 11 (2016).
34. Boland, J. J. Within touch of artificial skin. *Nat. Mater.* **9**, 790–792 (2010).
35. Park, S. et al. Stretchable energy-harvesting tactile electronic skin capable of differentiating multiple mechanical stimuli modes. *Adv. Mater.* **26**, 7324–7332 (2014).
36. Pang, C. et al. A flexible and highly sensitive strain-gauge sensor using reversible interlocking of nanofibres. *Nat. Mater.* **11**, 795–801 (2012).
37. Wang, X., Gu, Y., Xiong, Z., Cui, Z. & Zhang, T. Silk-molded flexible, ultrasensitive, and highly stable electronic skin for monitoring human physiological signals. *Adv. Mater.* **26**, 1336–1342 (2014).
38. Cañón Bermúdez, G. S. et al. Electronic-skin compasses for geomagnetic field-driven artificial magnetoreception and interactive electronics. *Nat. Electron.* **1**, 589–595 (2018).
39. Wang, Z., Shaygan, M., Otto, M., Schall, D. & Neumaier, D. Flexible Hall sensors based on graphene. *Nanoscale* **8**, 7683–7687 (2016).
40. Granell, P. N. et al. Highly compliant planar Hall effect sensor with sub 200 nT sensitivity. *npj Flex. Electron.* **3**, 3 (2019).

## Acknowledgements

We acknowledge T. Voitsekhivska, R. Kaltofen, Dr I. Mönch, B. Scheumann, G. Schnabel (Helmholtz-Zentrum Dresden-Rossendorf e.V.) for their assistance in the sample preparation; Dr T. Kosub (HZDR) for the support with the magnetotransport characterization; E. Christalle and Dr R. Hübner (HZDR) for the SEM and EDX measurements; Z. Zhang for the assistance in preparing the software for the data acquisition. Support by the Structural Characterization Facilities Rossendorf at the Ion Beam Center (IBC) at the HZDR is greatly appreciated. This work was financed in part via the German Research Foundation (DFG) grants MA 5144/9-1 and MA 5144/13-1, the European Research Council Starting Grant "GEL-SYS" (grant agreement no. 757931) and a startup grant of the Linz Institute of Technology (grant agreement no. LIT013144001SEL).

## Author contributions

J.G. conceived the idea, designed, and carried out the experiments. J.G., M.K., and D.M. analyzed the results and wrote the paper with contributions from all authors. O.V. performed magnetic simulations. M.D. performed mechanical simulations. X.W. and M.L. performed the optimization of compliant permanent magnets. J.G. and G.S.C.B prepared the software and hardware for the data acquisition. J.G., R.I., and D.M. designed multichoice 3D touch demonstrator. C.A.W. and S.Q.Z. measured the integral magnetic properties of the samples. All co-authors discussed the results and edited the manuscript. D.M., M.K. and J.F. supervised the project.

## Additional information

**Supplementary Information** accompanies this paper at https://doi.org/10.1038/s41467-019-12303-5.

**Competing interests:** The authors declare no competing interests.

**Reprints and permission** information is available online at http://npg.nature.com/reprintsandpermissions/

**Peer review information** *Nature Communications* thanks Iain Anderson and the other, anonymous, reviewer(s) for their contribution to the peer review of this work. Peer reviewer reports are available.

**Publisher's note** Springer Nature remains neutral with regard to jurisdictional claims in published maps and institutional affiliations.

THE JOURNAL OF PHYSICAL CHEMISTRY Letters
Cite This: J. Phys. Chem. Lett. 2019, 10, 6492−6498
Letter
pubs.acs.org/JPCL

# Nonstoichiometric Phases of Two-Dimensional Transition-Metal Dichalcogenides: From Chalcogen Vacancies to Pure Metal Membranes

T. Joseph,[*,†] M. Ghorbani-Asl,[†] A. G. Kvashnin,[‡] K. V. Larionov,[¶,§] Z. I. Popov,[¶,∥] P. B. Sorokin,[¶,§,∥] and Arkady V. Krasheninnikov[*,†,⊥]

[†]Institute of Ion Beam Physics and Materials Research, Helmholtz-Zentrum Dresden-Rossendorf, 01328 Dresden, Germany
[‡]Skolkovo Institute of Science and Technology, Skolkovo Innovation Center, 3 Nobel Street, Moscow 121205, Russia
[¶]National University of Science and Technology "MISIS", Leninsky prospect 4, Moscow 119049, Russia
[§]Moscow Institute of Physics and Technology, Institutsky lane 9, Dolgoprudny, Moscow region, 141700, Russian Federation
[∥]Emanuel Institute of Biochemical Physics RAS, Moscow 119334, Russia
[⊥]Department of Applied Physics, Aalto University, P.O. Box 11100, 00076 Aalto, Finland

**ABSTRACT:** Two-dimensional (2D) membranes consisting of a single layer of Mo atoms were recently manufactured [*Adv. Mater.* **2018**, *30*, 1707281] from $MoSe_2$ sheets by sputtering Se atoms using an electron beam in a transmission electron microscope. This is an unexpected result as formation of Mo clusters should energetically be more favorable. To get microscopic insights into the energetics of realistic Mo membranes and nonstoichiometric phases of transition-metal dichalcogenides (TMDs) $M_aX_b$, where M = Mo and W and X = S, Se, and Te, we carry out first-principles calculations and demonstrate that the membranes, which can be referred to as metallic quantum dots embedded into a semiconducting matrix, can be stabilized by charge transfer. We also show that an ideal neutral 2D Mo or W sheet is not flat but a corrugated structure, with a square lattice being the lowest-energy configuration. We further demonstrate that several intermediate nonstoichiometric phases of TMDs are possible as they have lower formation energies than pure metal membranes. Among them, the orthorhombic metallic 2D $M_4X_4$ phase is particularly stable. Finally, we study the properties of this phase in detail and discuss how it can be manufactured by the top-down approaches.

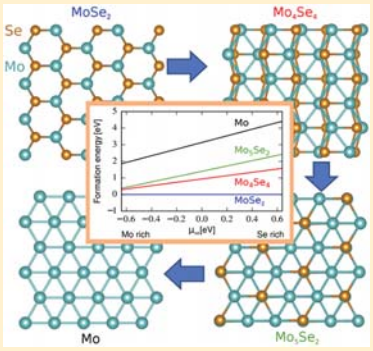


Recent progress in the mechanical[1] and liquid[2] exfoliation of two-dimensional (2D) systems from layered bulk solids bonded by weak van der Waals (vdW) forces, as well as their direct synthesis by chemical methods,[3] made it possible to manufacture dozens of 2D materials with unique and diverse characteristics. In addition to tailoring their properties for particular applications, the investigations of 2D systems gave rise to a fundamental question: Is it possible to synthesize free-standing 2D counterparts of solids, which normally have bulk isotropic, but not layered, structure? Recent experiments indicated that this is indeed possible as hematene layers were produced[4] from bulk $\alpha$-$Fe_2O_3$, which is a non-vdW solid.

Owing to the exotic properties such as highly active surface charge carriers with fast kinetics and surface plasmon resonance, 2D metals offer potential applications for catalysts, battery devices, and optical sensors.[5] In that context, a lot of attention has also been paid to free-standing 2D metals. Specifically, patches of 2D iron were reported to appear inside of graphene nanopores in the transmission electron microscopy (TEM) experiments.[6] Likewise, suspended one-atom-thick Mo membranes were recently fabricated from monolayer $MoSe_2$ sheets via complete sputtering of Se atoms in a scanning TEM.[7] As for the theoretical efforts, the trends in the stability and properties of perfectly flat 2D metals have been studied using first-principles calculations,[8] along with the energetics of small 2D metallic patches embedded in graphene and stabilized by the strong covalent bonds at the metal−graphene interface.[9,10] It should be pointed out, though, that the experimental observations of 2D systems, which were interpreted as pure metal membranes, could also be explained through the formation of mixed 2D phases, e.g., carbides or oxide, as reported for gold,[11] iron,[10,12] or copper,[13] which hints that mixed phases may also be present in the case of 2D Mo embedded into $MoSe_2$ sheets.[7]

Specifically, taking into account that Mo sheets were produced by the electron beam by removal of Se atoms from 2D $MoSe_2$, there are several contradictions or points that should be clarified. The membranes were reported to have a hexagonal structure, but the calculated and experimentally measured bond lengths did not match. This may be due to the mechanical strain present in the system, but, as we show below,

**Received:** August 29, 2019
**Accepted:** October 7, 2019
**Published:** October 7, 2019







DOI: 10.1021/acs.jpclett.9b02529
J. Phys. Chem. Lett. 2019, 10, 6492−6498

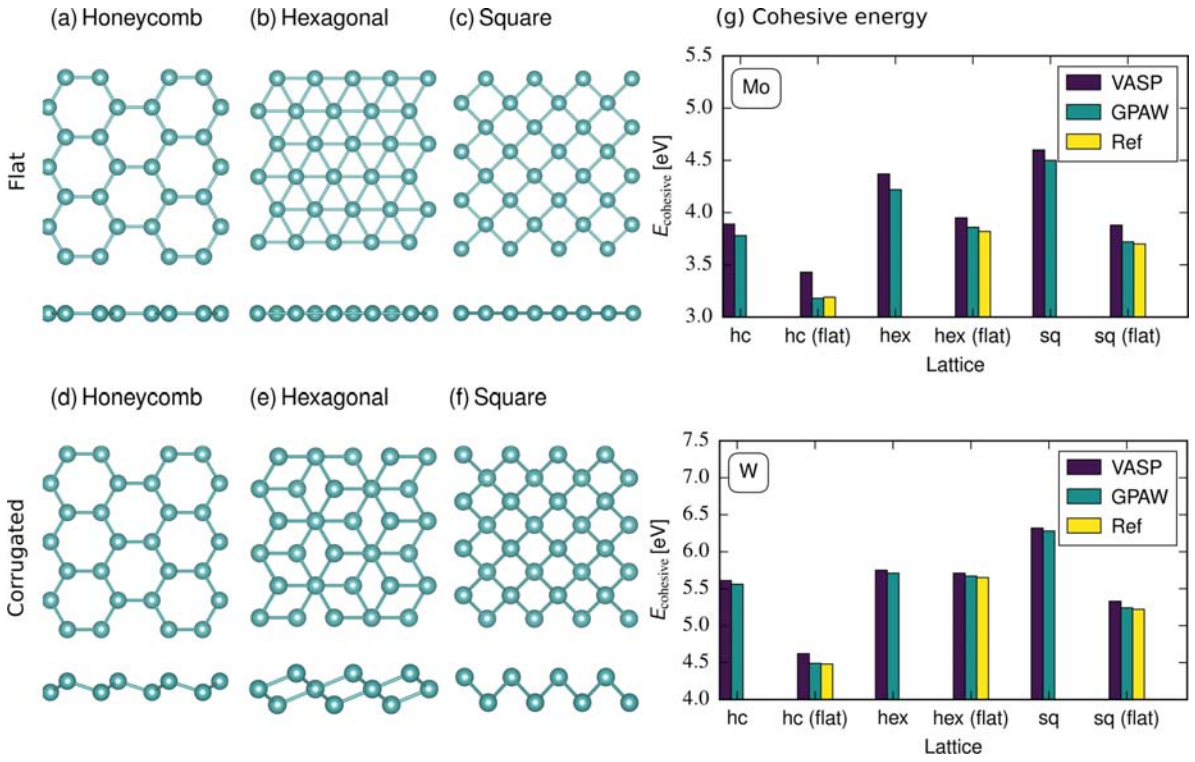


**Figure 1.** Atomic structures of 2D phases of Mo and W, top and side views, for the constrained (flat) atomic network (a–c), and those obtained without any constraints (d–f). (g) Comparison of the cohesive energy of the 2D phase of Mo and W as calculated using VASP and GPAW codes. The data represented by yellow bars are taken from ref 8.

a hexagonal lattice does not correspond to the lowest-energy 2D configuration of Mo. Besides, as Se atoms were gradually (over a time of a few minutes) removed by the electron beam, similar to other experiments on the exposure of TMDs to electron-beam irradiation,[14−18] a natural question is why other phases with intermediate stoichiometry were not observed, contrary to, e.g., tin dichalcogenides.[19] This problem is not only of fundamental importance but also directly relevant to the electron-beam engineering of 2D materials.[20−24]

In this work, we use extensive first-principles calculations to study the structure and energetics of 2D metals and nonstoichiometric phases of $MoSe_2$ and some other most common 2D transition-metal dichalcogenides (TMDs). The 2D phases were assumed to appear by the formation and aggregation of vacancies in the pristine system. The energetics of the 2D materials with different stoichiometries is analyzed for a wide range of chemical potentials. We further calculate the electronic structure of the most stable nonstoichiometric phase.

Specifically, we employed density functional theory (DFT) as implemented in the VASP code,[25,26] with the PBE exchange and correlation functional.[27] A plane-wave cutoff of 600 eV was used in all of the calculations. The geometry optimization was carried out based on minimization of the forces acting on the atoms in the structure, with the force tolerance being set to 0.01 eV $Å^{-1}$. The Brillouin zone of the primitive cells of the materials was sampled with a 12 × 12 × 1 Monkhorst−Pack k-mesh. We also carried out test calculations using GPAW code[28] and got similar results.

We simulated both finite metallic patches inside of a sheet of the parent TMD and infinite nonstoichiometric sheets assuming that they are also embedded into the 2D TMDs. In the latter case, we used two approaches: "manual" search for the metastable nonstoichiometric phases and "automatic" search using the evolutionary algorithm USPEX,[29,30] which is a powerful tool for predicting stable compounds of various dimensionalities of given elements. USPEX was successfully extended to 2D materials.[31,32] First, the variable-composition search for stable 2D-$Mo_xSe_y$ was performed using the algorithm described in ref 33. There were two searches with the initial thickness of the layer equal to 3 and 5 Å because $Mo_xSe_y$ may prefer nonplanar structures. Both calculations showed similar results. There were three stable structures predicted, namely, $Mo_5Se_2$, MoSe, and $MoSe_2$. After that, for each stable composition, the fixed-composition search was performed in order to predict the most thermodynamically stable structure of each composition. Computational search for free-standing two-dimensional $Mo_5Se_2$ and MoSe layers was performed with 2, 3, 4, 8, and 12 formula units in the considered unit cell. The first generation of 160 structures was created using a plane group symmetry generator, while all subsequent generations contained 20% random structures, and 80% were created using heredity, soft mutation, and transmutation variation operators. The newly produced structures were all relaxed, and the energies were used for selecting structures as parents for the new generation of structures. Structure relaxations were performed with the same DFT method with the exception that the plane-wave kinetic energy cutoff was set to 500 eV and the Brillouin zone was samples by Γ-centered k-point meshes with a resolution of $2\pi \times 0.05$ $Å^{-1}$. The phonon density of states of predicted MoSe was calculated



DOI: 10.1021/acs.jpclett.9b02529
J. Phys. Chem. Lett. 2019, 10, 6492−6498

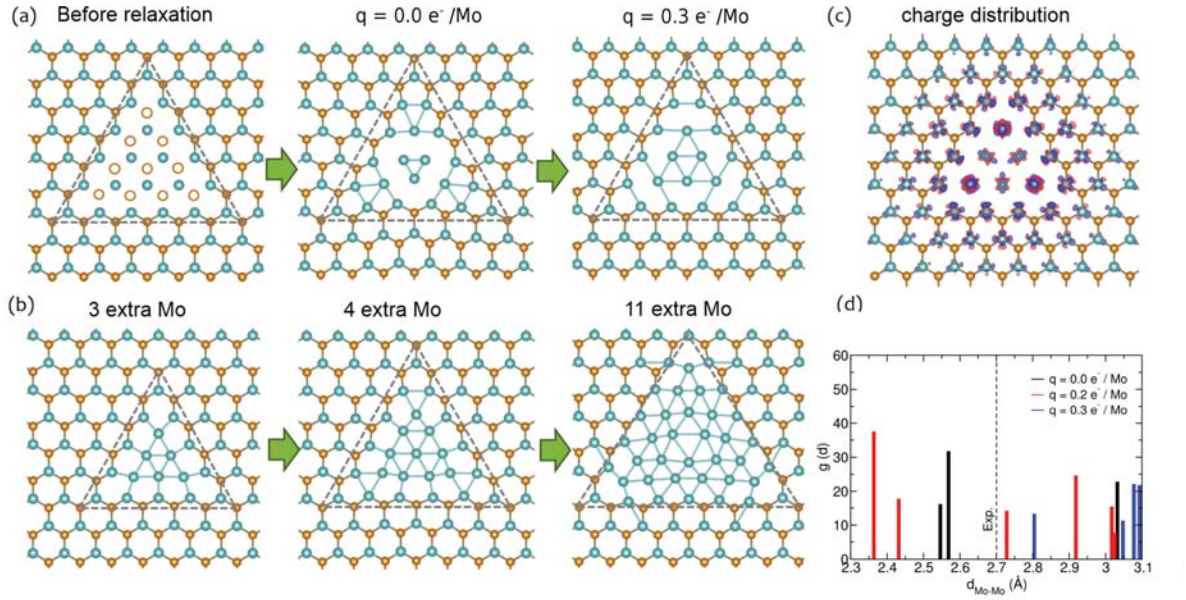


**Figure 2.** (a) Illustration of the evolution of the atomic structure of the metal membrane upon introduction of additional charge. It is evident that extra charge increases interatomic distances. (b) Optimized structure of the membrane with extra Mo atoms. (c) Charge density distribution with extra 0.3 e charge in the system. (d) Radial distribution function for the neutral and charged system.

using the finite displacement method as implemented in the PHONOPY code.[34]

The annular dark field scanning TEM (ADF-STEM) image simulations were carried out with the Dr. Probe[35] code assuming an aberration-free probe and 5 Å source size to give a focus spread of 3.0 nm. The STEM simulations were performed at 80 kV with a 30 mrad illumination half-angle and 20 mrad outer detection angle.

We studied first the energetics of the periodic 2D phases of transition metals, which are present in the most common TMDs: Mo and W. To assess the stability of 2D metals, the atomic structure of various 2D infinite periodic systems was fully optimized without any constraints, and cohesive energy $E_{\text{cohesive}}$ was calculated. It was defined as usual as $E_{\text{cohesive}} = E_{\text{atom}} - \frac{E(N)}{N}$, where $E_{\text{atom}}$ is the energy of an isolated atom, $E$ is the energy of the structure, and $N$ the total number of atoms in the unit cell. Note that $E_{\text{cohesive}}$ is positive, and larger values indicate a higher stability of the system.

The atomic structures of transition metal membranes and the associated cohesive energies are presented in Figure 1. Contrary to the simulation setup employed in ref 8, where perfectly flat structures were studied to get insights into the trends in the geometry and bonding, we allowed out-of-plane relaxation. Our results for flat structures proved to be in good agreement with those presented in ref 8, and the hexagonal (flat) phase was found to have the highest cohesive energy for both Mo and W. However, our simulations indicate that when out-of-plane relaxation is allowed the most energetically favorable phase is the square one. This stresses the importance of the out-of-plane degrees of freedom for the realistic 2D materials in the three-dimensional space.

However, a Mo hexagonal lattice was observed in the experiment,[7] contrary to the most energetically favorable square lattice. The experimental bond length was found to be 2.7 Å. From our simulations, the apparent separation between the atoms (projected into the plane) in the corrugated hexagonal lattice and the planar hexagonal lattice is 2.47 and 2.57 Å, respectively, in the case of Mo. Because the Mo domains are formed by sputtering of Se atoms from $MoSe_2$, the islands may be subjected to tensile strain, but to match the experiment, strain must be rather high, nearly 10%. Moreover, careful analysis of the TEM images shown in Figures 1−3 in ref 7 using the scale bar of 5 Å indicates that many bonds are much longer, nearly 3 Å. The same conclusion also can be drawn from the analysis of the atomically perfect interface between $MoSe_2$ and the new phase, which suggests close lattice constants of both phases. The tensile strain of 20% is unrealistically high, especially with account for migration of Mo atoms into the membrane areas, as observed in the experiment,[7] and in general, it is unclear why hexagonal lattice is preferred.

To understand the reason for large separations between the atoms, we considered possible charging of Mo membranes. A Mo island in a $MoSe_2$ sheet is essentially a quantum dot embedded into a semiconductor matrix. If the sample is n-type doped, it may give rise to negative charge accumulation. The additional charge may also come from other defects created in $MoSe_2$ by the electron beam[36−38] or adsorption of impurities[39] on these defects, which gives rise to the occupied or partially occupied defect-induced states in the gap.

Simulations for the neutral and charged systems were conducted, and the results are presented in Figure 2. In the neutral system considered, a small cluster of metal atoms is formed, and the cluster moves then to one of the edges. The behavior of the charged system is different. As evident from Figure 2c, the extra charge is localized in the membrane area, giving rise to longer bonds between the metal atoms. From the radial distribution function shown in Figure 2d, it is clear that charging of the system improves the agreement between theory and experiment.[7] With a charge of 0.2 e, the bond length of the structure matches well the experimental value of 2.7 Å, with some distortions at the edges at the interface to $MoSe_2$. Moreover, calculations for infinite free-standing metals showed



DOI: 10.1021/acs.jpclett.9b02529
J. Phys. Chem. Lett. 2019, 10, 6492−6498

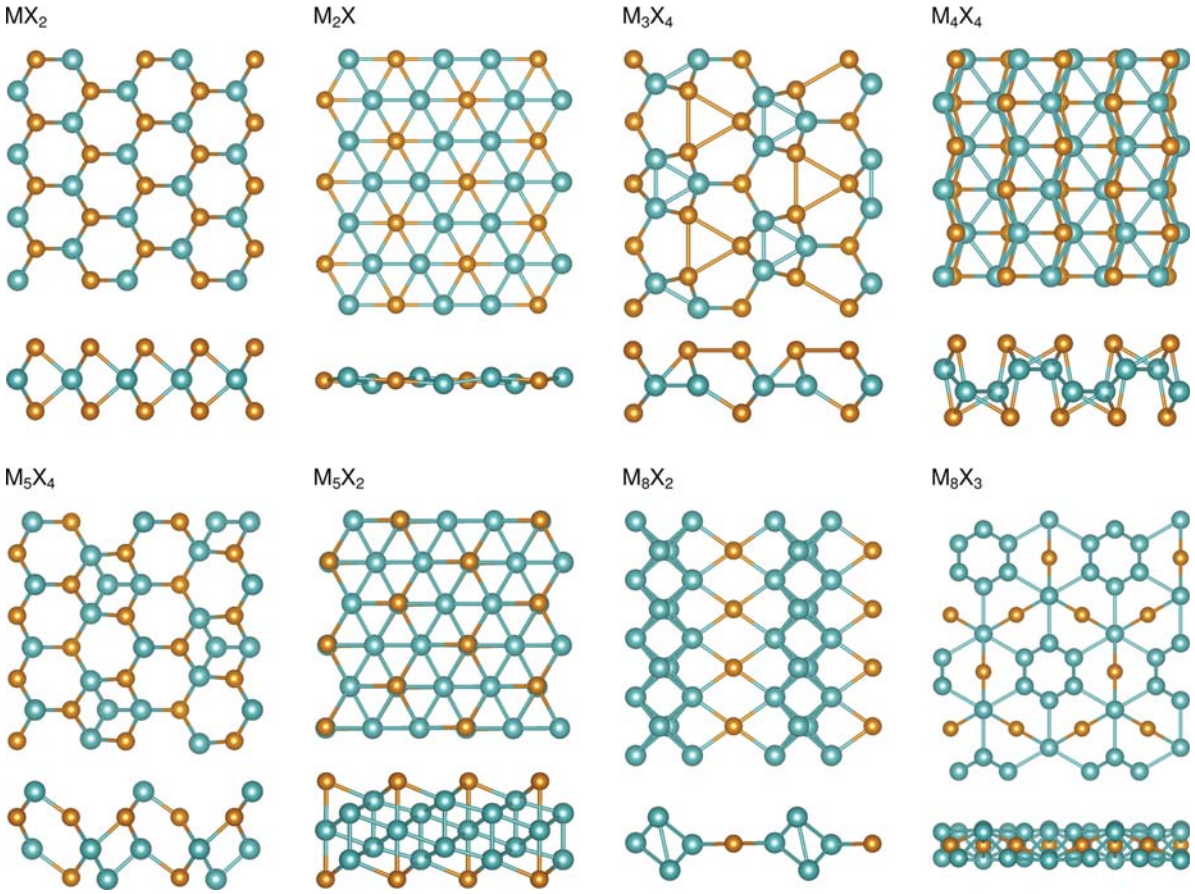


**Figure 3.** Atomic structures of nonstoichiometric phases of binary compounds formed from transition metal (M = Mo, W) and chalcogen (X = S, Se, Te) atoms, top and side views.

that the hexagonal phase is energetically preferable over the square lattice when an additional charge is added.

As an alternative scenario, we also investigated the changes in the atomic structure of the membrane when extra Mo atoms are added to the system, Figure 2b. Extra atoms do stabilize the membrane, but interatomic distances are smaller than those in the experiment, as follows from Figure 2b and the analysis of the radial distribution function. On the basis of these results, it appears that accumulation of the extra charge is the main reason for the stabilization of the membrane and rather a long separation between the Mo atoms.

As in the experiment, Se atoms were gradually (over a time of a few minutes) sputtered by the electron beam before patches of pure metals were produced; we also studied phases with intermediate stoichiometry, which hypothetically can also appear in the chalcogen-deficient material. We considered various nonstoichiometric binary compounds $M_yX_{2(1-y)}$, where M = Mo and W and X = S, Se, and Te. Mimicking the experimental situation, the phases were created by adding vacancies to the pristine structure and optimizing the geometry. Some of the structures that we studied are shown in Figure 3. The stability of these phases, which should naturally depend on the chemical potentials of the atoms, was evaluated by calculating the formation energies of the structures. Assuming that the nonstoichiometric phase is embedded into the pristine stoichiometric phase, the energetics (formation energy $E_f$ per formula unit) of the phase $M_aX_b$ consisting of $a$ transition metal atoms and $b$ chalcogen atoms was calculated as a function of chalcogen atom chemical potential $\mu_X$ as

$$E_f = \frac{E(M_aX_b)}{a} - E(MX_2) + \frac{2a - b}{a}\mu_X \quad (1)$$

where $E(M_aX_b)$ and $E(MX_2)$ are the total energies of the primitive cells of the nonstoichiometric and stoichiometric phases, respectively. Correspondingly, for any value of $\mu_X$, the formation energy $E_f$ of the $MX_2$ phase is zero. Equation 1 is essentially the formation energy of a defect in the pristine material normalized to the defect area. We stress that in these calculations we do not take into account the actual structure of the interface between the stoichiometric and nonstoichiometric phases, assuming that the structure is large enough, so that the interfaces can be neglected. It can also be used to assess the energy loss for removing all chalcogen atoms from the system and forming a pure metal membrane. As the phase is embedded into the stoichiometric phase, it is assumed that for any stoichiometry

$$\mu_M + 2\mu_X = \mu_{MX_2} \quad (2)$$

where the value of $\mu_M$ and $\mu_X$ are limited by the lowest-energy phases.

The formation energies for nonstoichiometric phases and for pure metal membranes are shown in Figure 4. It is seen that there are nonstoichiometric phases that are more stable than



DOI: 10.1021/acs.jpclett.9b02529
J. Phys. Chem. Lett. 2019, 10, 6492−6498

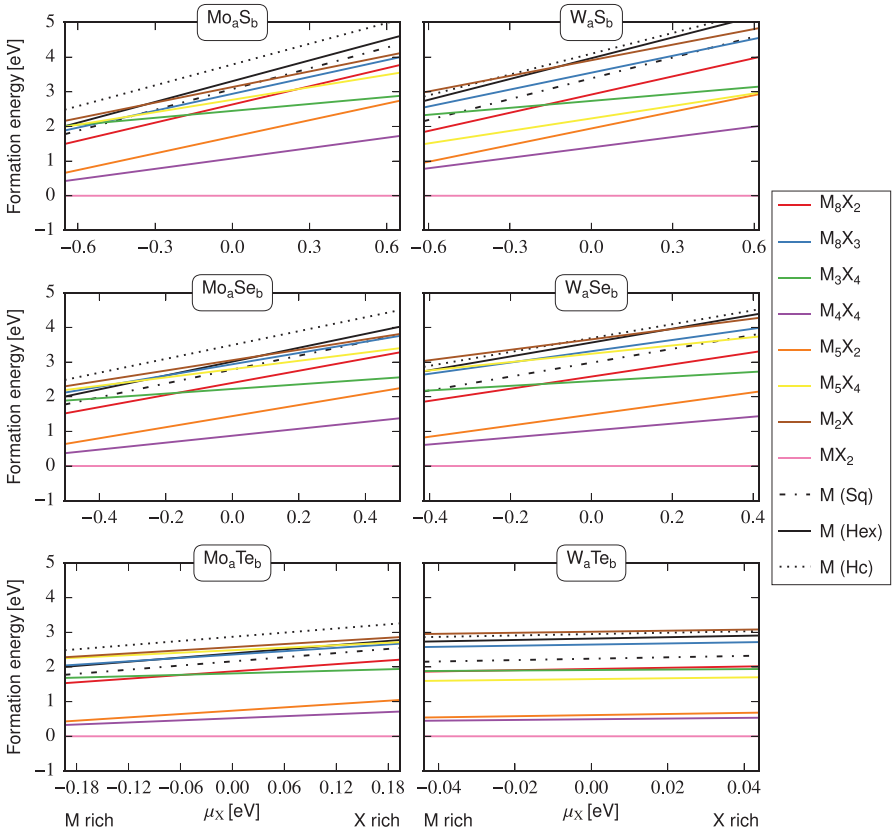


**Figure 4.** Formation energies of nonstoichiometric phases and pure metal membranes embedded into pristine material as functions of chalcogen atom chemical potentials.

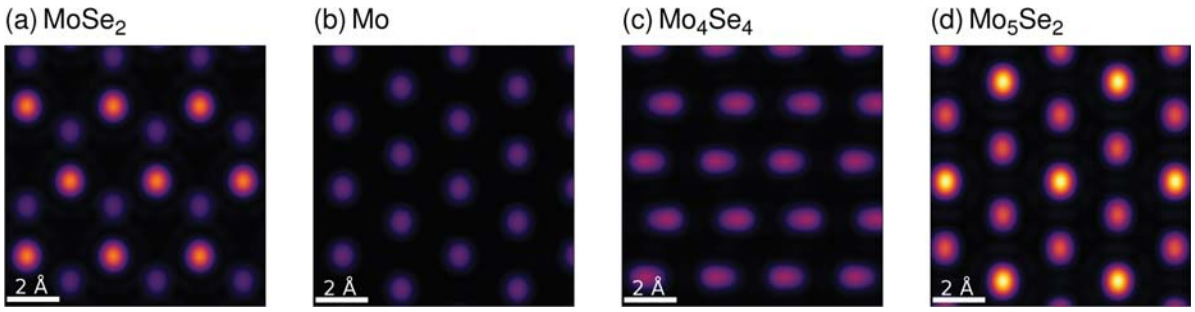


**Figure 5.** Simulated annular dark field scanning transmission electron microscopy images of the $Mo_4Se_4$ and $Mo_5Se_2$ phases in comparison to a pure Mo membrane and $MoSe_2$ at 80 kV. The intensity scale is the same for all of the images.

pure 2D metals. The most stable nonstoichiometric phase from the simulation is $M_4X_4$, with the energy difference between the hexagonal metal phase and $M_4X_4$ being over 1 eV. As evident from Figure 4, the energy difference between this and the stoichiometric phase is 0.3−0.6 eV in the metal-rich limit, which indicates that the phase can potentially be synthesized or manufactured using an electron beam by sputtering chalcogen atoms, e.g., by using moderate heating during irradiation. Another nonstoichiometric phase of interest is $M_5X_2$, which, unlike $M_4X_4$, has a hexagonal lattice with a formation energy comparable to the lowest-energy $M_4X_4$ at the metal-rich end. The phase can be referred to as a corrugated Mo sheet with attached chalcogen atoms, and it is a likely candidate for forming domains when chalcogen atoms are sputtered away by the electron beam.

Although we considered single-layer structures, the vdW interaction is known to affect the cohesive energies of nonlayered materials by up to 0.3 eV per atom, especially when defects are present (for an overview, see ref 40). To address this issue, we repeated the calculations of the total energies and geometries of all of the phases of the MoSe system that we considered with the Tkatchenko−Scheffler vdW exchange and correlation functional.[41] The primitive cell size of every phase was carefully optimized. The account for the vdW interaction decreased the energy difference between the nonstoichiometric phases and MoSe by 0.1−0.3 eV but did not change the qualitative picture. The geometry of the systems remained the same, and the Mo membrane was still corrugated.



DOI: 10.1021/acs.jpclett.9b02529
J. Phys. Chem. Lett. 2019, 10, 6492−6498

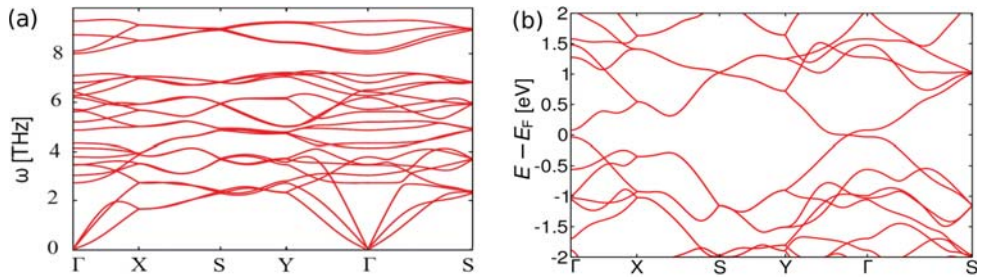


**Figure 6.** (a) Phonon dispersion and (b) electronic structure of the $Mo_4Se_4$ phase.

To further facilitate a comparison with the experimental results,[7] we simulated STEM images of the phases with the lowest energies, along with those for a pure Mo membrane and pristine $MoSe_2$. Figure 5 presents the simulated STEM images of the $Mo_4Se_4$ and $Mo_5Se_2$ phases in comparison to a pure Mo membrane and $MoSe_2$. The intensity scale is the same for all of the images. Interestingly, the $Mo_5Se_2$ has a slightly distorted hexagonal lattice with a lattice constant of ∼2.7 Å, close to the experimental result reported in ref 7. On the other hand, the simulated metallic Mo membrane has a lattice constant of only 2.57 Å. Thus, some areas in the irradiated $MoSe_2$ sheets may not be a purely metallic phase but one of the mixed phases.

Independently, we also carried out a global minimum search of nonstoichiometric 2D structures by the evolutionary algorithm. The simulation yielded the same 2D molybdenum monoselenide with a distorted puckered honeycomb lattice of orthorhombic symmetry, Figures 3 and 5c. Such a phase has lattice parameters $a$ = 5.455 Å and $b$ = 4.449 Å (*Pbcm* space group) with one Mo atom (0.402, 0.250, 0.477) and one Se atom (−0.016, 0.250, 0.425). The dynamical stability of a predicted monolayer was studied by the phonon calculations, shown in Figure 6a. One can see no imaginary phonon modes, Figure 6a, so that even the free-standing structure should be stable. The presence of a substrate will further stabilize this phase. The elastic constants of the $Mo_4Se_4$ phase were found to be $C_{11}$ = 87.1 N/m, $C_{22}$ = 204.7 N/m, $C_{12}$ = 46.4 N/m, and $C_{66}$ = 53.7 N/m. One elastic constant of uniaxial deformation ($C_{22}$) is almost 2 times larger than the corresponding value for $MoSe_2$ (110.5 N/m), whereas another constant ($C_{11}$) is slightly lower.

We further calculated the electronic structure of the $Mo_4Se_4$ phase. The PBE band structure of $Mo_4Se_4$ is shown in Figure 6b. It is evident that the phase is metallic. We obtained similar results for other $M_4X_4$ systems. The metallic nature of these compounds was also confirmed by the $G_0W_0$ calculations.

To sum up, using first-principles calculations, we demonstrated that the lowest-energy configuration of a neutral 2D membrane composed of Mo atoms only is not the hexagonal one, as previously assumed,[8] but the square lattice. The structure is not flat but develops out-of-plane corrugation. However, when a finite-size Mo membrane embedded into a semiconducting $MoSe_2$ material is negatively charged, the lowest-energy configuration corresponds to the hexagonal lattice, which has experimentally been observed,[7] provided that indeed no other chemical element (e.g., carbon, oxygen) is present, as confirmed by EELS. We further showed that the extra charge also gives rise to increased separations between the atoms, which may explain the apparent contradiction between the bond lengths obtained in the calculations and those experimentally measured in Mo membranes derived from $MoSe_2$ sheets by sputtering Se atoms using the electron beam in the scanning TEM.[7] We also provide evidence that other nonstoichiometric 2D phases of $MoSe_2$ and other TMDs $MX_2$(M = Mo, W; X = S, Se, Te) with low formation energies can exist. Among these 2D phases, the 2D $M_4X_4$ and $M_5X_2$ phases are particularly stable, especially in the Mo-rich limit, which corresponds to the conditions in the TEM experiments. This indicates that, although the formation of the pure Mo/W phase may be related to the dynamical effects and preferential sputtering of chalcogen atoms, it should in principle be possible to quench the system into this configuration by, e.g., moderate heating of the sample during exposure to the electron beam. The lowest-energy $M_4X_4$ phase is metallic, contrary to the original material, which is a semiconductor. This potentially opens new avenues for patterning and atomic-scale engineering of the properties of 2D TMDs with high miniaturization and integration. As exposure to chalcogen atoms combined with annealing will likely lead to the restoration of the original structure, the system can be used in rewritable electronics.

## AUTHOR INFORMATION


### Corresponding Authors

*E-mail: t.joseph@hzdr.de.
*E-mail: a.krasheninnikov@hzdr.de.

### ORCID

T. Joseph: 0000-0002-1985-1222
M. Ghorbani-Asl: 0000-0003-3060-4369
A. G. Kvashnin: 0000-0002-0718-6691
K. V. Larionov: 0000-0003-4771-7220
P. B. Sorokin: 0000-0001-5248-1799
Arkady V. Krasheninnikov: 0000-0003-0074-7588


### Notes

The authors declare no competing financial interest.

## ACKNOWLEDGMENTS

We thank J. Nevalaita, P. Koskinen, and A. Oganov for discussions. We acknowledge funding from the German Research Foundation (DFG), Projects KR 48661/1 and KR 48661/2, and the Academy of Finland under Project No. 286279. We also acknowledge the financial support of the Ministry of Education and Science of the Russian Federation in the framework of Increase Competitiveness Program of NUST "MISiS" (No. K2-2019-016) and a Grant of President of Russian Federation for government support of young DSc (MD-1046.2019.2). Study of the $Mo_4Se_4$ monolayer was supported by the Russian Science Foundation (Project Identifier: 17-72-20223). We further thank CSC Finland,



DOI: 10.1021/acs.jpclett.9b02529
J. Phys. Chem. Lett. 2019, 10, 6492−6498

PRACE (HLRS, Stuttgart, Germany), and TUD (Taurus cluster) for generous grants of CPU time.

## REFERENCES


(1) Radisavljevic, B.; Radenovic, A.; Brivio, J.; Giacometti, V.; Kis, A. Single-layer MoS2 transistors. *Nat. Nanotechnol.* **2011**, *6*, 147−150.

(2) Coleman, J. N.; Lotya, M.; O'Neill, A. O.; Bergin, S. D.; King, P. J.; Khan, U.; Young, K.; Gaucher, A.; De, S.; Smith, R. J.; et al. Two-dimensional nanosheets produced by Liquid Exfoliation of Layered Materials. *Science* **2011**, *331*, 568−571.

(3) Zhan, Y.; Liu, Z.; Najmaei, S.; Ajayan, P. M.; Lou, J. Large-Area Vapor-Phase Growth and Characterization of $MoS_2$ Atomic Layers on a $SiO_2$ Substrate. *Small* **2012**, *8*, 966−971.

(4) Puthirath Balan, A.; Radhakrishnan, S.; Woellner, C. F.; Sinha, S. K.; Deng, L.; Reyes, C. D. L.; Rao, B. M.; Paulose, M.; Neupane, R.; Apte, A.; et al. Exfoliation of a non-van der Waals material from iron ore hematite. *Nat. Nanotechnol.* **2018**, *13*, 602−609.

(5) Ma, Y.; Li, B.; Yang, S. Ultrathin two-dimensional metallic nanomaterials. *Mater. Chem. Front.* **2018**, *2*, 456−467.

(6) Zhao, J.; Deng, Q.; Bachmatiuk, A.; Sandeep, G.; Popov, A.; Eckert, J.; Rümmeli, M. H. Free-Standing Single-Atom-Thick Iron Membranes Suspended in Graphene Pores. *Science* **2014**, *343*, 1228−1232.

(7) Zhao, X.; Dan, J.; Chen, J.; Ding, Z.; Zhou, W.; Loh, K. P.; Pennycook, S. J. Atom-by-Atom Fabrication of Monolayer Molybdenum Membranes. *Adv. Mater.* **2018**, *30*, 1707281.

(8) Nevalaita, J.; Koskinen, P. Atlas for the properties of elemental two-dimensional metals. *Phys. Rev. B: Condens. Matter Mater. Phys.* **2018**, *97*, 035411.

(9) Chen, S.; Zeng, X. C. Interaction between Iron and Graphene Nanocavity: Formation of Iron Membranes, Iron Clusters, or Iron Carbides. *ACS Appl. Mater. Interfaces* **2017**, *9*, 12100−12108.

(10) Larionov, K. V.; Kvashnin, D. G.; Sorokin, P. B. 2D FeO: A New Member in 2D Metal Oxide Family. *J. Phys. Chem. C* **2018**, *122*, 17389−17394.

(11) Westenfelder, B.; Biskupek, J.; Meyer, J. C.; Kurasch, S.; Lin, X.; Scholz, F.; Gross, A.; Kaiser, U. Bottom-up formation of robust gold carbide. *Sci. Rep.* **2015**, *5*, 8891.

(12) Shao, Y.; Pang, R.; Shi, X. Stability of Two-Dimensional Iron Carbides Suspended across Graphene Pores: First-Principles Particle Swarm Optimization. *J. Phys. Chem. C* **2015**, *119*, 22954−22960.

(13) Kano, E.; Kvashnin, D. G.; Sakai, S.; Chernozatonskii, L. A.; Sorokin, P. B.; Hashimoto, A.; Takeguchi, M. One-atom-thick 2D copper oxide clusters on graphene. *Nanoscale* **2017**, *9*, 3980−3985.

(14) Zhou, W.; Zou, X.; Najmaei, S.; Liu, Z.; Shi, Y.; Kong, J.; Lou, J.; Ajayan, P. M.; Yakobson, B. I.; Idrobo, J.-C. Intrinsic Structural Defects in Monolayer Molybdenum Disulfide. *Nano Lett.* **2013**, *13*, 2615−2622.

(15) Parkin, W. M.; Balan, A.; Liang, L.; Das, P. M.; Lamparski, M.; Naylor, C. H.; Rodríguez-Manzo, J. A.; Johnson, A. T.; Meunier, V.; Drndić, M. Raman Shifts in Electron-Irradiated Monolayer MoS2. *ACS Nano* **2016**, *10*, 4134−4142.

(16) Lehnert, T.; Ghorbani-Asl, M.; Köster, J.; Lee, Z.; Krasheninnikov, A. V.; Kaiser, U. Electron-Beam-Driven Structure Evolution of Single-Layer MoTe2 for Quantum Devices. *ACS Appl. Nano Mater.* **2019**, *2*, 3262−3270.

(17) Lin, J.; Pantelides, S. T.; Zhou, W. Vacancy-Induced Formation and Growth of Inversion Domains in Transition-Metal Dichalcogenide Monolayer. *ACS Nano* **2015**, *9*, 5189−5197.

(18) Wang, S.; Lee, G.-D.; Lee, S.; Yoon, E.; Warner, J. Detailed Atomic Reconstruction of Extended Line Defects in Monolayer MoS 2. *ACS Nano* **2016**, *10*, 5419−5430.

(19) Sutter, E.; Huang, Y.; Komsa, H.-P.; Ghorbani-Asl, M.; Krasheninnikov, A. V.; Sutter, P. Electron-Beam Induced Transformations of Layered Tin Dichalcogenides. *Nano Lett.* **2016**, *16*, 4410−4416.

(20) Krasheninnikov, A. V.; Banhart, F. Engineering of Nanostructured Carbon Materials with Electron or Ion Beams. *Nat. Mater.* **2007**, *6*, 723−733.

(21) Kalinin, S. V.; Borisevich, A.; Jesse, S. Fire up the atom forge. *Nature* **2016**, *539*, 485−487.

(22) Lin, Z.; Carvalho, B. R.; Kahn, E.; Lv, R.; Rao, R.; Terrones, H.; Pimenta, M. A.; Terrones, M. Defect Engineering of Two-Dimensional Transition Metal Dichalcogenides. *2D Mater.* **2016**, *3*, 022002.

(23) Krasheninnikov, A. V.; Nordlund, K. Ion and Electron Irradiation-Induced Effects in Nanostructured Materials. *J. Appl. Phys.* **2010**, *107*, 071301.

(24) Zhao, X.; Kotakoski, J.; Meyer, J. C.; Sutter, E.; Sutter, P.; Krasheninnikov, A. V.; Kaiser, U.; Zhou, W. Engineering and modifying two-dimensional materials by electron beams. *MRS Bull.* **2017**, *42*, 667−676.

(25) Kresse, G.; Furthmüller, Efficiency of Ab-Initio Total Energy Calculations for Metals and Semiconductors Using a Plane-Wave Basis Set *J. Comput. Mater. Sci.* **1996**, *6*, 15−50.

(26) Kresse, G.; Furthmüller, J. Efficient iterative schemes for ab initio total-energy calculations using a plane-wave basis set. *Phys. Rev. B: Condens. Matter Mater. Phys.* **1996**, *54*, 11169−11186.

(27) Perdew, J. P.; Burke, K.; Ernzerhof, M. Generalized Gradient Approximation Made Simple. *Phys. Rev. Lett.* **1996**, *77*, 3865−3868.

(28) Enkovaara, J.; Rostgaard, C.; Mortensen, J. J.; Chen, J.; Dułak, M.; Ferrighi, L.; Gavnholt, J.; Glinsvad, C.; Haikola, V.; Hansen, H. A.; et al. Electronic structure calculations with GPAW: a real-space implementation of the projector augmented-wave method. *J. Phys.: Condens. Matter* **2010**, *22*, 253202.

(29) Oganov, A. R.; Glass, C. W. Crystal structure prediction using ab initio evolutionary techniques: Principles and applications. *J. Chem. Phys.* **2006**, *124*, 244704.

(30) Lyakhov, A. O.; Oganov, A. R.; Stokes, H. T.; Zhu, Q. New developments in evolutionary structure prediction algorithm USPEX. *Comput. Phys. Commun.* **2013**, *184*, 1172−1182.

(31) Zhou, X.-F.; Dong, X.; Oganov, A. R.; Zhu, Q.; Tian, Y.; Wang, H.-T. Semimetallic Two-Dimensional Boron Allotrope with Massless Dirac Fermions. *Phys. Rev. Lett.* **2014**, *112*, 085502.

(32) Wang, Z.; Zhou, X.-F.; Zhang, X.; Zhu, Q.; Dong, H.; Zhao, M.; Oganov, A. R. Phagraphene: A Low-Energy Graphene Allotrope Composed of 5−6-7 Carbon Rings with Distorted Dirac Cones. *Nano Lett.* **2015**, *15*, 6182−6186.

(33) Revard, B. C.; Tipton, W. W.; Yesypenko, A.; Hennig, R. G. Grand-canonical evolutionary algorithm for the prediction of two-dimensional materials. *Phys. Rev. B: Condens. Matter Mater. Phys.* **2016**, *93*, 054117.

(34) Togo, A.; Tanaka, I. First principles phonon calculations in materials science. *Scr. Mater.* **2015**, *108*, 1−5.

(35) Barthel, J. Dr. Probe: A software for high-resolution STEM image simulation. *Ultramicroscopy* **2018**, *193*, 1−11.

(36) Shafqat, A.; Iqbal, T.; Majid, A. A DFT study of intrinsic point defects in monolayer MoSe2. *AIP Adv.* **2017**, *7*, 105306.

(37) Lehtinen, O.; Komsa, H. P.; Pulkin, A.; Whitwick, M. B.; Chen, M. W.; Lehnert, T.; Mohn, M. J.; Yazyev, O. V.; Kis, A.; Kaiser, U.; et al. Atomic scale microstructure and properties of Se-deficient two-dimensional MoSe2. *ACS Nano* **2015**, *9*, 3274−3283.

(38) Komsa, H.-P.; Krasheninnikov, A. V. Engineering the Electronic Properties of Two-Dimensional Transition Metal Dichalcogenides by Introducing Mirror Twin Boundaries. *Adv. El. Mater.* **2017**, *3*, 1600468.

(39) Guo, Y.; Ji, Y.; Dong, H.; Wang, L.; Li, Y. Electronic and optical properties of defective MoSe2 repaired by halogen atoms from first-principles study. *AIP Adv.* **2019**, *9*, 025202.

(40) Tkatchenko, A. Current Understanding of Van der Waals Effects in Realistic Materials. *Adv. Funct. Mater.* **2015**, *25*, 2054−2061.

(41) Tkatchenko, A.; Scheffler, M. Accurate Molecular Van Der Waals Interactions from Ground-State Electron Density and Free-Atom Reference Data. *Phys. Rev. Lett.* **2009**, *102*, 073005.




DOI: 10.1021/acs.jpclett.9b02529
*J. Phys. Chem. Lett.* 2019, 10, 6492−6498

PHYSICAL REVIEW MATERIALS **3**, 054802 (2019)

# Superconductivity in single-crystalline aluminum- and gallium-hyperdoped germanium

Slawomir Prucnal,[1,*] Viton Heera,[1] René Hübner,[1] Mao Wang,[1] Grzegorz P. Mazur,[2,3] Michał J. Grzybowski,[2,3] Xin Qin,[4] Ye Yuan,[1,5] Matthias Voelskow,[1] Wolfgang Skorupa,[1] Lars Rebohle,[1] Manfred Helm,[1] Maciej Sawicki,[2] and Shengqiang Zhou[1]

[1]*Helmholtz-Zentrum Dresden-Rossendorf, Institute of Ion Beam Physics and Materials Research, Bautzner Landstraße 400, D-01328 Dresden, Germany*

[2]*Institute of Physics, Polish Academy of Sciences, Aleja Lotnikow 32/46, PL-02668 Warsaw, Poland*

[3]*International Research Center MagTop, Institute of Physics, Polish Academy of Sciences, Aleja Lotnikow 32/46, PL-02668 Warsaw, Poland*

[4]*Hefei National Laboratory for Physical Sciences at the Microscale, University of Science and Technology of China, Hefei, Anhui 230026, China*

[5]*Physical Science and Engineering Division, King Abdullah University of Science and Technology, 23955-6900 Thuwal, Saudi Arabia*

(Received 18 December 2018; revised manuscript received 15 March 2019; published 9 May 2019)

Superconductivity in group IV semiconductors is desired for hybrid devices combining both semiconducting and superconducting properties. Following boron-doped diamond and Si, superconductivity has been observed in gallium-doped Ge; however, the obtained specimen is in polycrystalline form [Phys. Rev. Lett. **102**, 217003 (2009)]. Here we present superconducting single-crystalline Ge hyperdoped with gallium or aluminum by ion implantation and rear-side flash lamp annealing. The maximum concentration of Al and Ga incorporated into substitutional positions in Ge is 8 times higher than the equilibrium solid solubility. This corresponds to a hole concentration above $10^{21}\,\mathrm{cm}^{-3}$. Using density functional theory in the local-density approximation and pseudopotential plane-wave approach, we show that the superconductivity in *p*-type Ge is phonon mediated. According to the *ab initio* calculations, the critical superconducting temperature for Al- and Ga-doped Ge is in the range of 0.45 K for 6.25 at.% of dopant concentration, being in qualitative agreement with experimentally obtained values.

DOI: 10.1103/PhysRevMaterials.3.054802

## I. INTRODUCTION

Since the discovery of superconductivity in diamond [1] with a boron content above the equilibrium solid solubility (ESS), many studies have been performed to find new "superconducting semiconductors." Such a materials class would enable the monolithic integration of quantum and conventional electronics [2]. Indeed, several groups found superconductivity, even in the technologically more relevant semiconductors such as Si [3], Ge [4], or SiC [5], after a heavy hole doping. A brief introduction into the research field of superconducting semiconductors was given in recent review articles [6–9].

The term "superconducting semiconductor" is a bit misleading, since in a semiconductor, the carriers necessary for the Cooper pair condensate freeze out at low temperatures, and superconductivity is impossible. Therefore, the semiconductor has to be heavily doped above the metal-insulator transition (MIT). It turned out that an acceptor concentration in excess of 1 at.% (i.e., above $5\times10^{20}\,\mathrm{cm}^{-3}$) is required to induce the superconductivity in germanium. Such concentration is higher than the ESS of typical acceptors in Ge. Hyperdoping, however, is difficult to achieve and requires nonequilibrium doping techniques, such as a high-pressure high-temperature synthesis [1] or chemical vapor deposition [8] in the case of diamond, gas immersion laser doping [3,10,11], and high-fluence ion implantation combined with rapid thermal annealing (RTA) or flash lamp annealing (FLA) [4,12–15] for Si and Ge. Among these doping schemes, ion implantation followed by FLA is best adopted to the current semiconductor technology.

Despite advanced nonequilibrium doping techniques, hyperdoped semiconductors are in most cases inhomogeneous materials with dopant concentration fluctuations [16] up to cluster or nanoprecipitate formation [13]. Moreover, dopant segregation at grain boundaries in polycrystalline materials or at interfaces to technologically relevant capping layers is a next serious problem [17]. There is experimental evidence that in some semiconductor-acceptor systems, Si:Ga, for example, amorphous acceptor-rich nanoprecipitates ($c_{\mathrm{Ga}} > 20$ at.%) are vital for superconductivity [13]. Granularities of the superconducting condensates have been also obtained in boron-doped diamond [18,19]. Such granular superconductors can be modeled by a random network of Josephson junctions and exhibit a superconductor-insulator transition [20], as observed, e.g., in Si:Ga [21,22]. The presence of the superconductor-insulator transition clearly reveals the inhomogeneous character of the superconductor. Due to local superconducting regions, even in the insulating state such hyperdoped semiconductors demonstrate nonlinear transport phenomena [22] and anomalous large magnetoresistance [23].

However, for a perfect monolithic integration of superconducting nanocircuits in semiconductor devices, a homogeneous and single-crystalline structure is desirable. It remains an unresolved question whether superconducting semiconductor films of sufficient quality can be fabricated at all

*Corresponding author: s.prucnal@hzdr.de

 

by today's top-down selective doping technologies and which semiconductor-acceptor combination is most promising. Since the tendency for disorder and cluster formation by hyperdoping increases with the covalent bond strength of the semiconductor and decreases with growing acceptor solid solubility, the Ge:Ga system appears to be favorable compared to diamond:B and Si:B [14]. Previous studies demonstrated that conventional implantation doping of Ge with Ga enables a maximum hole concentration of $6.6\times10^{20}\,\mathrm{cm}^{-3}$ after annealing at 450°C for 1 h [24]. Higher temperatures of conventional long-term annealing led to Ga clustering. In order to reduce acceptor diffusion and clustering, FLA in the millisecond range without layer melting is an appropriate method [25–28]. With this method hole concentrations up to $1.4\times10^{21}\,\mathrm{cm}^{-3}$ and superconductivity at critical temperatures below 0.5 [4,15] and 2.0 K [29] have been achieved in Ge layers with about 6 and 8 at.% Ga content, respectively. Unfortunately, the layers are nanocrystalline [4,15], and the activation level of the Ga acceptors varies from sample to sample up to a factor of 2, which is due to the formation of Ga-rich nanoprecipitates [29]. Single-crystalline Ge:Ga has been obtained by RTA [14]. However, in this case, a large amount of the Ga atoms accumulates as an amorphous film at the $SiO_2$/Ge interface. This interface layer becomes superconducting below 6 K, which is similar to the critical temperature of Ga clusters.

In this paper we show that an optimized FLA process can be used to fabricate single-crystalline, superconducting layers of hyperdoped *p*-type Ge. In addition to Ga doping, we also investigate Al doping. Similar to Ga, Al has high ESS but a higher diffusivity than Ga and is more difficult to activate. As shown recently, ion implantation of Al into Ge followed by conventional thermal annealing results in a maximum hole concentration of only $1\times10^{20}\,\mathrm{cm}^{-3}$ [30]. Here we show that the maximum carrier concentration in Ga- and Al-implanted Ge followed by FLA exceeds $10^{21}\,\mathrm{cm}^{-3}$. FLA suppresses the dopant diffusion and segregation. The recrystallized Ge is single crystalline with critical temperatures of $T_C \sim 0.5\,\mathrm{K}$. Moreover, first-principles investigation of superconductivity in Al-doped and Ga-doped Ge using *ab initio* calculations within the Eliashberg-McMillan theory reveals that the Ga:Al system behaves similar to a Ge:Ga covalent superconductor, where the critical temperature can be tuned by the carrier concentration.

## II. EXPERIMENTAL

### A. Sample fabrication

*N*-type (Sb-doped, $\rho > 10\,\Omega\mathrm{cm}$), (100)-oriented Ge wafers are used as substrates for acceptor implantation in order to electrically isolate the processed layer from the substrate by formation of a *p-n* junction. First, a 30-nm-thick $SiO_2$ cover layer is sputter-deposited to protect the Ge surface during ion implantation and annealing. Then the wafers are implanted with Ga or Al ions with different fluencies of 1, 2, and $4\times10^{16}\,\mathrm{cm}^{-2}$ and energies of 100 keV for $Ga^+$ and 50 keV for $Al^+$ ions. The implantation energies are chosen in such a way that the acceptor profiles are similar, with a maximum acceptor concentration at a depth of 60 nm, as predicted by the SRIM simulation code [31]. Figure 1(a) shows the calculated Ga and Al distributions implanted into the $SiO_2$/Ge wafers for an ion fluence of $2\times10^{16}\,\mathrm{cm}^{-2}$. The peak concentration and the depth distribution of Al and Ga within Ge are different for the same ion fluence and similar projected ion range $R_p$. After implantation, a heavily doped amorphous surface layer of about 120 nm width with a relatively sharp interface to the single-crystalline Ge substrate was formed (see Supplemental Material, Fig. S1a) [15,32]. The presence of a sharp amorphous/crystalline interface is an important precondition for the explosive solid-phase epitaxy process which appears during millisecond-range FLA of the implanted layer [29].

The Al peak concentration is about 6 at.%, whereas the Ga concentration exceeds 10 at.%. This is due to different interactions of light (Al) and heavy (Ga) elements with germanium during the ion-implantation process. This is due to different stopping power and energy loss straggling for different ions within the solid. For heavier ions the stopping power and the energy loss straggling are higher, causing a smaller FWHM of the depth distribution of the implanted ions and, in consequence, a higher peak concentration for the same ion fluence.

In order to activate the dopants and recrystallize the implanted layer, we have used a strongly nonequilibrium thermal processing, i.e., flash lamp annealing. Implanted samples were annealed either from the front side (f-FLA) or from the rear side (r-FLA) with an energy density deposited to the sample surface in the range of $50-130\,\mathrm{J\,cm}^{-2}$. The annealing time was 3, 6, or 20 ms. The influence of the annealing time on the recrystallization process of the implanted layer is presented in Supplemental Material (see Fig. S1b [15,32]). Figure 1(b) shows the temperature distribution within the implanted layer after front- and rear-side FLA for 20 ms. The f-FLA leads to a partial epitaxial regrowth of the implanted layer and to the formation of polycrystalline hyperdoped Ge at the surface [15]. Taking into account the wavelength spectrum of the Xe lamps in the FLA system (300–800 nm) and the optical properties of Ge, the main part of the flash light is absorbed by implanted Ge within 50 nm from the surface. This causes a temperature gradient within the implanted layer. For a short moment (in the submicrosecond range), the surface is much hotter than the amorphous/crystalline interface. Also, the threshold energy needed for crystalline seed nucleation is lower than the energy needed for the epitaxial regrowth [33]. Therefore, during f-FLA, the recrystallization of the implanted layer starts from the surface and a polycrystalline layer is formed. In order to avoid the formation of such a polycrystalline layer at the top of implanted Ge, we developed the rear-side FLA process [28]. In this case, the implanted sample is annealed from the rear side and the heat is transferred through the wafer to the implanted surface. Using r-FLA, the amorphous/crystalline interface is heated first. Therefore, before the surface temperature reaches the level needed for crystalline seed nucleation, the whole implanted layer is recrystallized due to the explosive solid-phase epitaxy [28]. We have found that using a 400-$\mu$m-thick Ge layer the optimal annealing time for rear-side annealing is 20 ms. RTA and pulsed laser annealing (PLA) are alternatives to FLA annealing techniques. During RTA, similar to the r-FLA process,

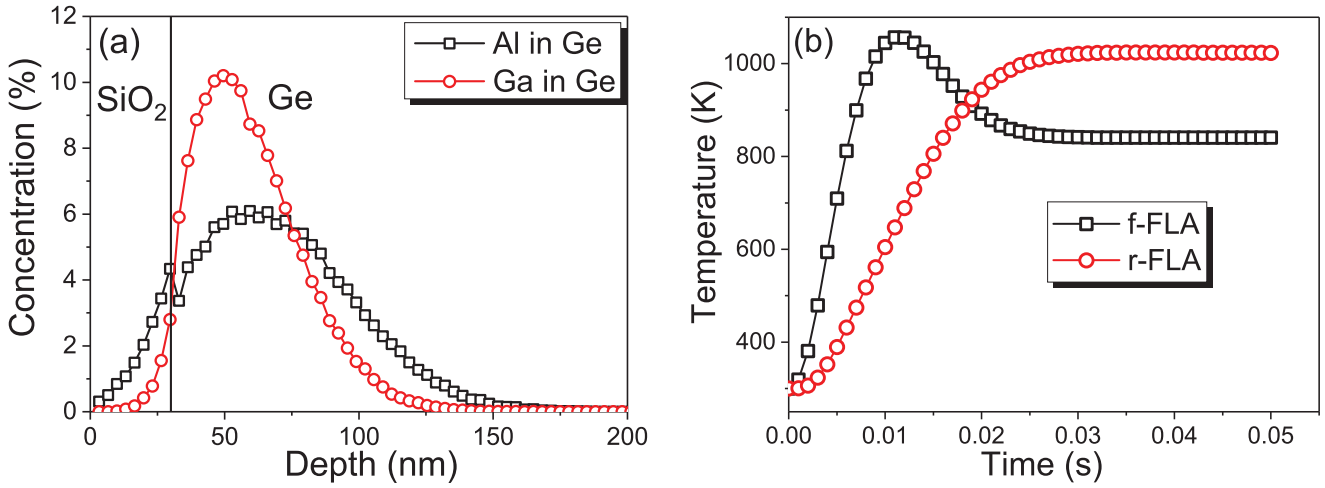


FIG. 1. The Ga and Al depth distribution in Ge obtained by the SRIM code for an ion-implantation fluence of $2\times10^{16}$ cm$^{-2}$ (a) and simulated temperature distribution at the implanted surface during 20 ms FLA from the front side (f-FLA, black curve) and from the rear side (r-FLA, red curve) (b).

the implanted layer recrystallizes via solid-phase epitaxy. But due to much smaller heating rate the recrystallization speed of the implanted layer is significantly slower than the diffusion of dopants. As a consequence, the implanted elements with concentration higher than the solid solubility are only partially incorporated into the crystal lattice and form clusters. In contrast to FLA and RTA, during PLA the annealing layer recrystallizes via liquid phase epitaxy. The typical pulse length for PLA is in the nanosecond range, and the total annealing time is in the range of tens of microseconds. The solidification/recrystallization speed observed during PLA is similar to the explosive solid-phase epitaxy after FLA. But the diffusion coefficient of dopants in the liquid phase is a few orders of magnitude higher than in the solids. Hence, during PLA dopants often diffuse towards the surface and form a dopant-rich but nonactivated layer. According to our experience, only the millisecond-range annealing provides enough energy to activate explosive solid-phase epitaxy, which is crucial for the formation of single-crystalline hyperdoped germanium.

### B. Characterization techniques

The crystallization process of the Al- and Ga-implanted and annealed samples is studied using Rutherford backscattering-channeling spectrometry (RBS/C). The RBS/C measurements are performed on the samples before and after annealing using the 1.7 MeV $He^+$ beam. To investigate the microstructural properties of the implanted Ge layer, cross-sectional bright-field transmission electron microscopy (TEM) investigations are performed in a Titan 80-300 (FEI) microscope operated at an accelerating voltage of 300 kV. High-angle annular dark-field scanning transmission electron microscopy (HAADF-STEM) imaging and spectrum imaging based on energy-dispersive X-ray spectroscopy (EDXS) are performed at 200 kV with a Talos F200X microscope equipped with a Super-X EDXS detector system (FEI). Prior to TEM analysis, the specimen mounted in a high-visibility low-background holder was placed for 10 s into a model 1020 Plasma Cleaner (Fischione) to remove contaminations. The optical properties are investigated by micro-Raman spectroscopy. The phonon spectra were obtained in backscattering geometry in the range of $100-600\,\mathrm{cm}^{-1}$ using a 532-nm Nd:YAG laser with a liquid-nitrogen-cooled CCD camera.

The concentration of carriers in the implanted and annealed samples was estimated from temperature-dependent Hall-effect measurements in van der Pauw configuration. The thickness of the doped layer was extracted from the RBS data under the assumption that the diffusion of implanted elements during 20-ms pulse annealing can be neglected. The electrical properties of the annealed samples are measured at millikelvin temperatures in a dry dilution refrigerator (Triton 400 by Oxford Instruments), which allows sweeping temperature in the range from 10 mK to 30 K. Four-probe ac measurements were taken using the ac lock-in method with an excitation current of 10 nA and frequency 127 Hz. The existence of superconducting states in hyperdoped *p*-type Ge was predicted by *ab initio* calculations within the Eliashberg/McMillan theory.

## III. RESULTS AND DISCUSSION

### A. Microstructure

The recrystallization process of ion-implanted and flash-lamp-annealed Ge is investigated using RBS random (RBS/R) and channeling (RBS/C) spectrometry. Since Al and Ga are lighter than Ge, they unfortunately cannot be measured directly by RBS. However, the ratio between the yields of the RBS/C and RBS/R spectra ($\chi_{\mathrm{min}}$) is a measure of the crystalline quality of the sample. In our case, $\chi_{\mathrm{min}}$ for Al- and Ga-hyperdoped Ge after FLA is in the range of $(5\pm1)\%$ (see Fig. 5), which is slightly higher than $\chi_{\mathrm{min}}$ for the virgin Ge. Moreover, the RBS/C spectra recorded from the as-implanted samples provide information about the thickness of the amorphized layer, which is needed to calculate the carrier density using Hall-effect measurements.

Figure 2 shows the RBS/R and RBS/C spectra obtained from the Al-doped sample before and after r-FLA, from the Ga-doped sample after r-FLA and from virgin Ge. As

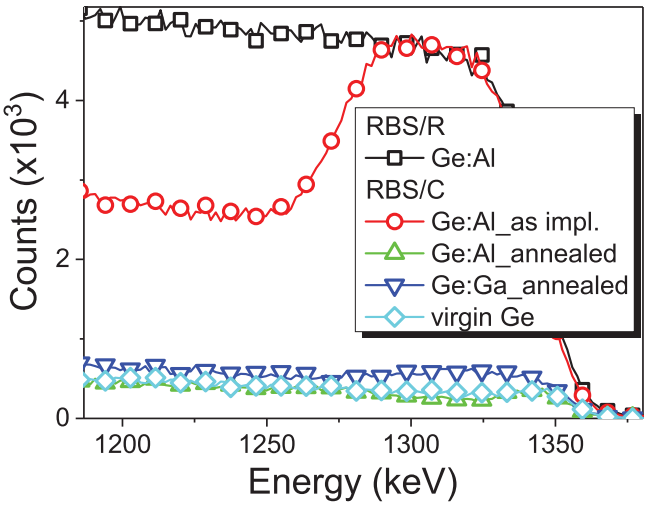


FIG. 2. The RBS/R and RBS/C spectra obtained from Al- and Ga-hyperdoped Ge. The RBS/C spectrum recorded from virgin Ge is shown as well. The concentrations of Al and Ga in Ge are at the level of $2\times10^{21}$ cm$^{-3}$.

expected, the RBS/C spectrum obtained from the as-implanted sample reveals the formation about a 120-nm-thick amorphous surface layer. The thickness of the amorphous layer is calculated based on the RBS data using the RUMP Software. After 20-ms r-FLA with an energy density of 120 J cm$^{-2}$, the yield of RBS/C spectrum drops down to the level registered from the virgin Ge wafer. This behavior points to an epitaxial regrowth of the implanted layer during r-FLA. Moreover, we can conclude that Al atoms are incorporated into the lattice of Ge. Taking into account that the solid solubility of Al in Ge is in the range of $5\times10^{20}$ cm$^{-3}$, the investigated sample contains 4 times more Al in substitutional positions than the solid solubility limit. Such a gain is only possible due to the strongly nonequilibrium character of the process. The absence of significant dechanneling suggests that the formation of Al clusters is also suppressed by the millisecond-range r-FLA.

In the case of Ga-hyperdoped Ge after r-FLA, the RBS/C spectrum also reveals full incorporation of Ga into the Ge lattice. The yield of the RBS/C spectrum obtained from virgin Ge and the Ga-doped sample is at the same level, meaning that the Ga-implanted sample behaves the same way as Al-doped Ge after r-FLA. In both cases, the ESS limit has been overcome by 4 times.

In order to clarify the lattice position of Al and Ga within Ge, we performed particle-induced x-ray emission (PIXE) spectroscopy in the random and channeling direction. Figures 3(a) and 3(b) show the PIXE spectra obtained from the Al- and Ga-doped samples, respectively. The peaks are identified as the characteristic x-ray emissions of the $Al_{K\alpha}$(1.78 keV), $Ga_{K\alpha}$(9.27 keV), $Ge_{K\alpha}$(9.85 keV), and $Ge_{K\beta}$(10.98 keV) lines. Since in the PIXE channeling spectra the $Al_{K\alpha}$ and $Ga_{K\alpha}$ intensities drop down to the noise level, it can be concluded that both Al and Ga atoms are fully incorporated into Ge lattice sites, even with a concentration being 4 times higher than the ESS.

More insight into the microstructure is provided by TEM. Please note that the $SiO_2$ capping layer is still present for these samples. Figure 4(a) displays a cross-sectional bright-field TEM image taken from Al-doped Ge after annealing. In this case, both single dislocations within the implanted layer and end-of-range defects are detected [34]. Figure 4(b) shows the Ge, Al, and O distributions based on EDXS analysis from a representative surface region, as exemplarily marked by the white square in Fig. 4(a). Aluminum is quite evenly distributed within Ge, showing only few small agglomerates over the implantation depth, which is in good agreement with RBS and PIXE data.

Figures 4(c) and 4(d) show a cross-sectional bright-field TEM micrograph and the corresponding superimposed Ge, Ga, and O element distributions obtained from Ga-hyperdoped Ge. Here, the Ga is completely homogeneously distributed within the implanted layer. Moreover, in the case of the Ga-doped sample, even the end-of-range defects are not detected. For Al as well as Ga, the recrystallized Ge is single-crystalline. This is in contrast to our previous results, where front-side flash lamp annealing was used [15]. Applying

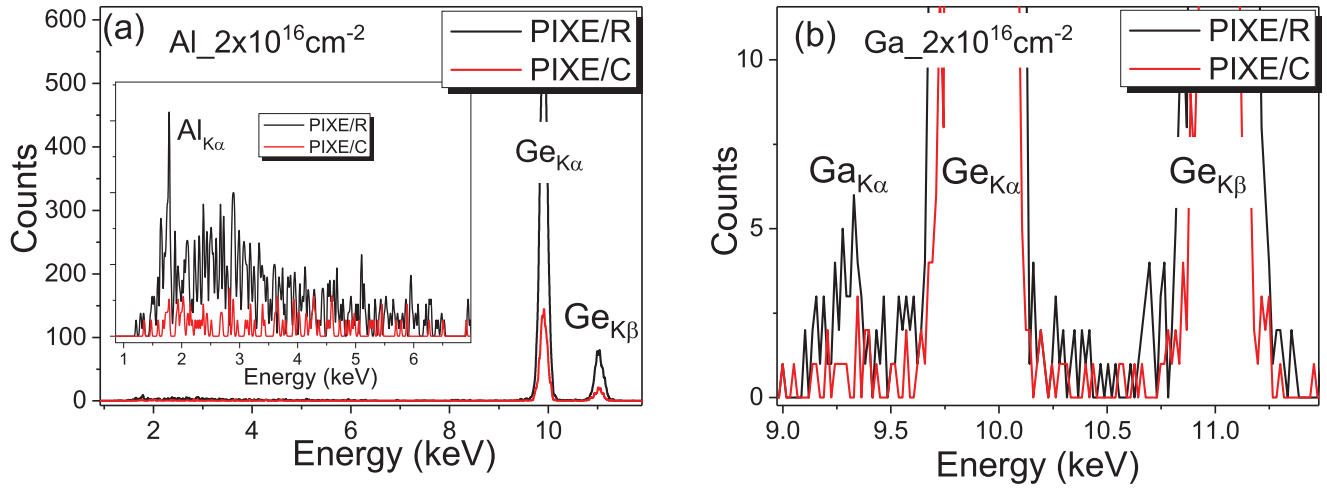


FIG. 3. PIXE spectra of Al- (a) and Ga-hyperdoped Ge (b) followed by rear-side FLA for 20 ms.

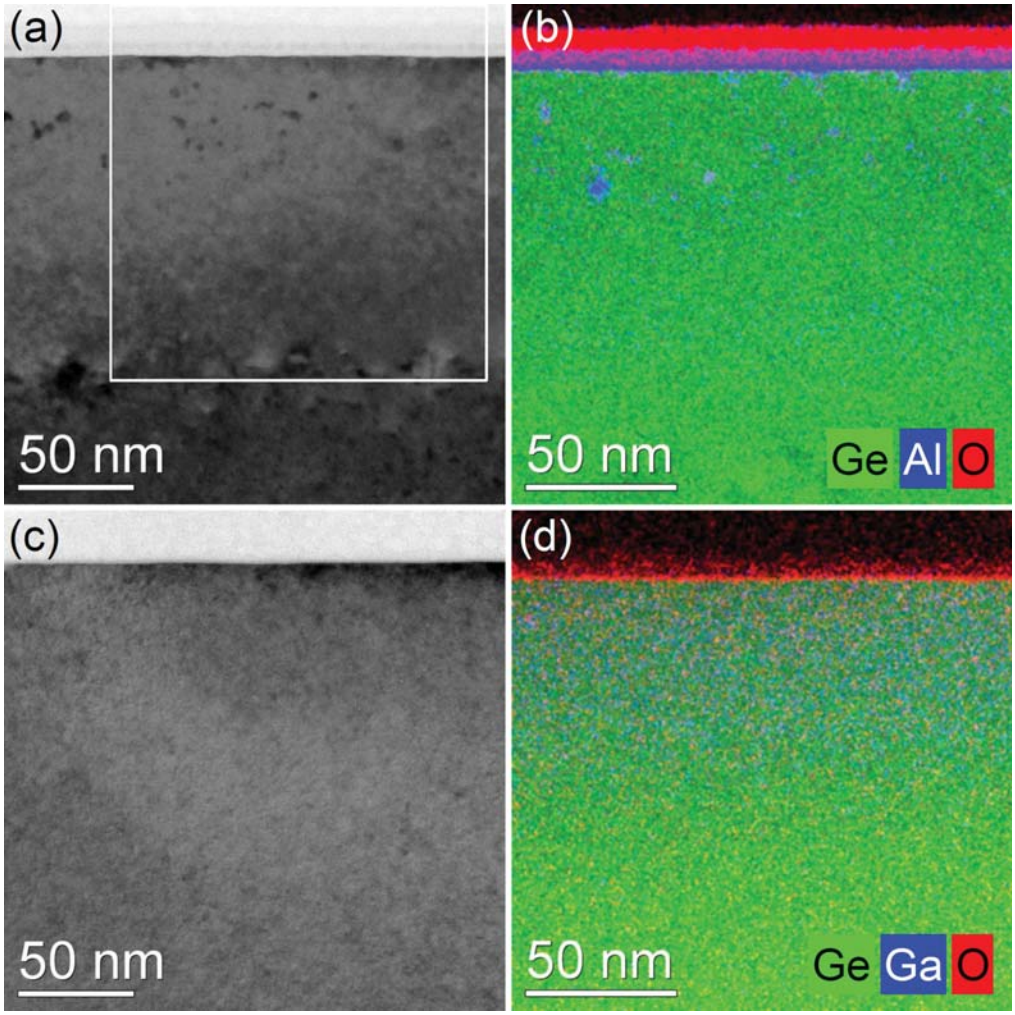


FIG. 4. (a), (c) Cross-sectional bright-field TEM images obtained from Al- and Ga-hyperdoped Ge, respectively, (b), (d) superimposed Ge (green), O (red), and Al or Ga (blue), respectively, element distributions obtained by spectrum imaging analysis based on EDXS in scanning TEM mode for a representative surface region of each sample, as exemplarily marked by the white square in (a).

f-FLA, the implanted layer is composed of polycrystalline Ge with Ga clusters and an epitaxial layer which has a thickness of about 70% of the thickness of the implanted layer. Using r-FLA, we can fully suppress the formation of poly-Ge and Ga clusters for dopant concnetrations much above the ESS.

### B. Superconductivity

The established electrical parameters of the studied doped layers are summarized in Table I. The carrier concentration was estimated from the Hall-effect measurements. The thickness of the doped layer was determined by RBS measurements. The presented activation efficiency is a ratio between the total acceptor concentration and the carrier concertation estimated from the Hall-effect measurement at 3 K. The presented critical temperatures are taken from Fig. 5. We find that for diluted hyperdoped Ge the minimum carrier concentration needed for superconductivity is in the range of $1\times10^{21}$ cm$^{-3}$. If we assume that the superconductivity in *p*-type Ge is phonon mediated, for the same doping level the critical temperature should be slightly higher for Al-doped Ge

TABLE I. Summary of the doping level and carrier concentration in hyperdoped Ge obtained for Al- and Ga-doped samples annealed with optimized parameters.

| Sample | Dopant concentration | Carrier concentration at 3 K | Activation efficiency | Critical temperature |
|---|---|---|---|---|
| Ge:Al | ∼6% | $10.7\times10^{20}$ cm$^{-3}$ | 44.5% | $T_C \sim 0.15$ K |
| Ge:Ga | ∼10% | $12.6\times10^{20}$ cm$^{-3}$ | 31.5% | $T_C \sim 0.45$ K |

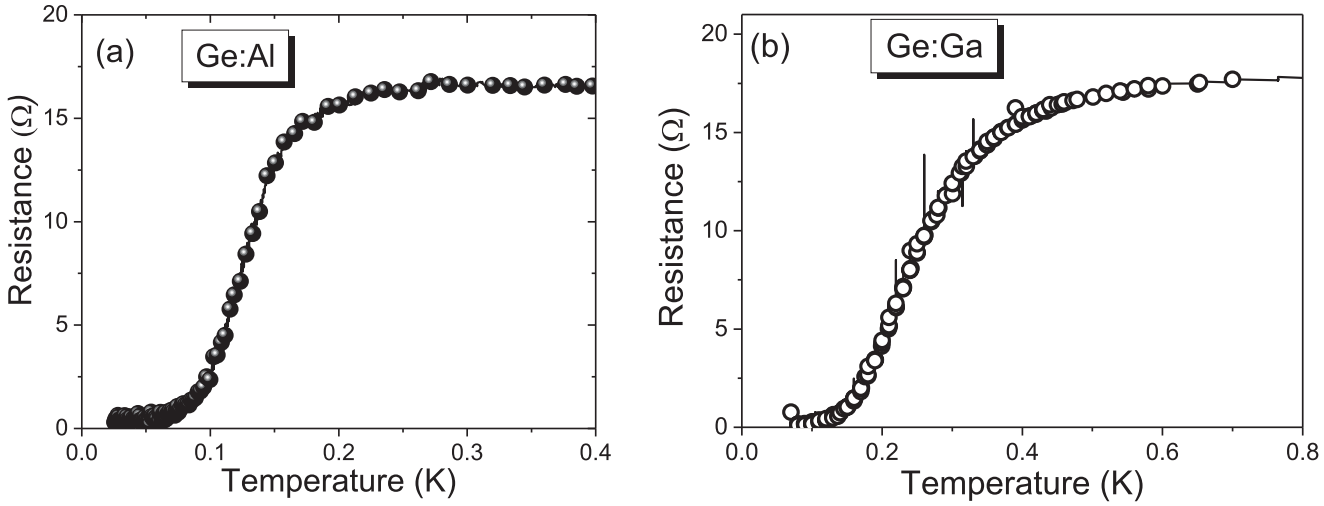


FIG. 5. Temperature dependence of the longitudinal resistance for different samples: (a) low-temperature part of $R_{xx}$ vs $T$ of superconducting Ge with 6% Al (a) and Ga (b).

than for the Ga-doped sample due to a stronger phonon coupling. Unfortunately, in hyperdoped Ge it is very challenging to control the carrier concentration keeping the same dopant concentration. In fact, for the doping level above the solid solubility, we are not able to activate 100% of the implanted element. Therefore experimental verification of theoretical predictions is very challenging. Here we decided to compare samples with similar hole concentrations.

It is worthy to note that we are able to show superconducting Ge hyperdoped with Al. The achieved hole concentration is the highest ever published for Al-doped samples. Figure 5(a) shows the temperature dependence of resistance for Al-hyperdoped Ge. The superconducting temperature is about 150 mK. This is much lower than that predicted by calculation ($T_C \sim 480$ mK, shown later) but also much below the critical superconducting temperature for Al thin film or Al clusters [35]. If we take into account the carrier concentration, which is roughly half of the Al concentration, the obtained $T_C$ is at a reasonable level. The temperature dependence of the resistance for the Ga-doped sample is shown in Fig. 5(b). In Ga-hyperdoped Ge, $T_C$ is about 400 mK. Presented critical temperatures are obtained from samples annealed from the rear side with a flash energy density of 120 J cm$^{-2}$. The annealing at lower energy densities is not sufficient to recrystallize the implanted layer (no superconductivity), while annealing at higher energy densities activates the dopant diffusion and cluster formation, leading to the superconductivity driven by metallic clusters (see Supplemental Material Figs. 1(b) and 2) [15]. Consequently, the fraction of electrically active dopants, both Al and Ga, in the substitutional position is much smaller.

### C. Model calculations for the electron-phonon coupling

According to the BCS theory the critical temperature of a homogeneous superconductor grows with increasing electron-phonon coupling strength and Debye temperature. Theoretical calculations demonstrate that in homogeneously doped semiconductors the critical temperature scales with their hole concentration [36,37]. The critical temperature in diamond can exceed 20 K for a hole concentration of 10%($\sim 10^{22}$ cm$^{-3}$). Much lower critical temperatures ($<1$ K) have been predicted for Si and Ge. We used the supercell technique to model the hyperdoped Ge. For simulation we have used Ge doped with Al or Ga with the concentration of 6.25%, corresponding to the $2\times2\times2$ supercell with one Ge atom substituted by an Al(Ga) atom. All calculations were performed within the plane-wave implementation of the local-density approximation (LDA) [38] to density functional theory (DFT) [38–40] in the QUANTUM-ESPRESSO package [41]. Norm-conserving pseudopotentials with a kinetic energy cutoff of 45 Ry were used to represent electron-ion interactions. The $k$-point sampling of the Brillouin zone was set to $6\times6\times6$ during the structural relaxation and electronic structure calculations, while a dense $12\times12\times12$ Monkhorst-Pack grid [32] was used for the phonon linewidth calculations. Phonon spectra and electron-phonon coupling constants were calculated using density functional perturbation theory [42] with a $3\times3\times1$ mesh of $q$ points. For all calculations we have used an optimized lattice constant of Ge supercell of 11.234 Å. The hyperdoping of Ge with Al or Ga will lead to a lattice expansion by 0.2% (11.259 Å for Al-doped Ge) or lattice compression by 0.1% (11.226 Å for Ga doped Ge), respectively.

Figure 6 shows the electronic structure of Al- and Ga-hyperdoped Ge. According to our calculations for the same dopant concentration, the density of states $N(E_F)$ in Al-hyperdoped Ge ($\sim$2.82 [states/eV/(supercell)]) is slightly higher than in Ga-hyperdoped Ge ($\sim$2.67 [states/eV/(supercell)]). In both cases the hyperdoped Ge is strongly degenerate, with the Fermi level ($E_F$) located deep in the valence band ($\sim$0.67 eV below the top of the valence-band maximum). The electronic states near the $E_F$ of Al- and Ga-hyperdoped Ge are very similar, and they originate from $p$ states of Ge and acceptor dopants. The hyperdoped Ge is an $sp3$ covalent metal.

In a similar way to the electronic structure of hyperdoped Ge, we have calculated the phonon band structure of Al- and Ga-hyperdoped Ge (see Fig. 7). By solid blue circles we

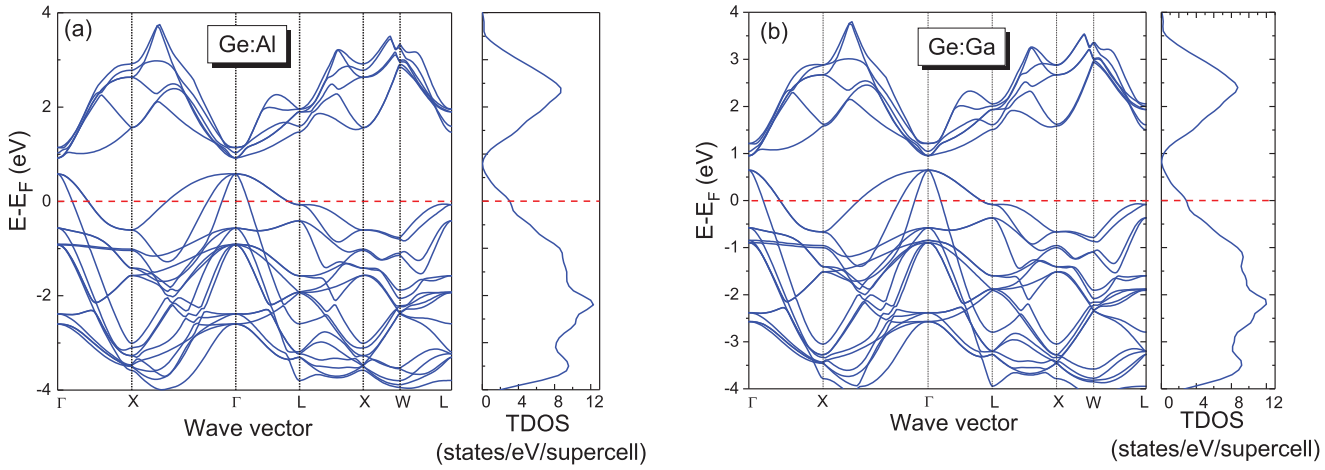


FIG. 6. The electronic structure of Al- (a) and Ga-hyperdoped (b) Ge with the corresponding total density of electronic states $N(E_F)$.

have marked the highest optical phonons at the Γ point. In the case of Al-hyperdoped Ge we have found three optical $T_2$ modes located at 256, 267, and 364 $cm^{-1}$ and one $A_1$ optical mode with frequency around 188 $cm^{-1}$. The strongest electron-phonon coupling strength $\lambda_{vq}$ at the Γ point is at $A_1$ with $\lambda_{vq} \sim 0.16$. The triple degeneracy also produces

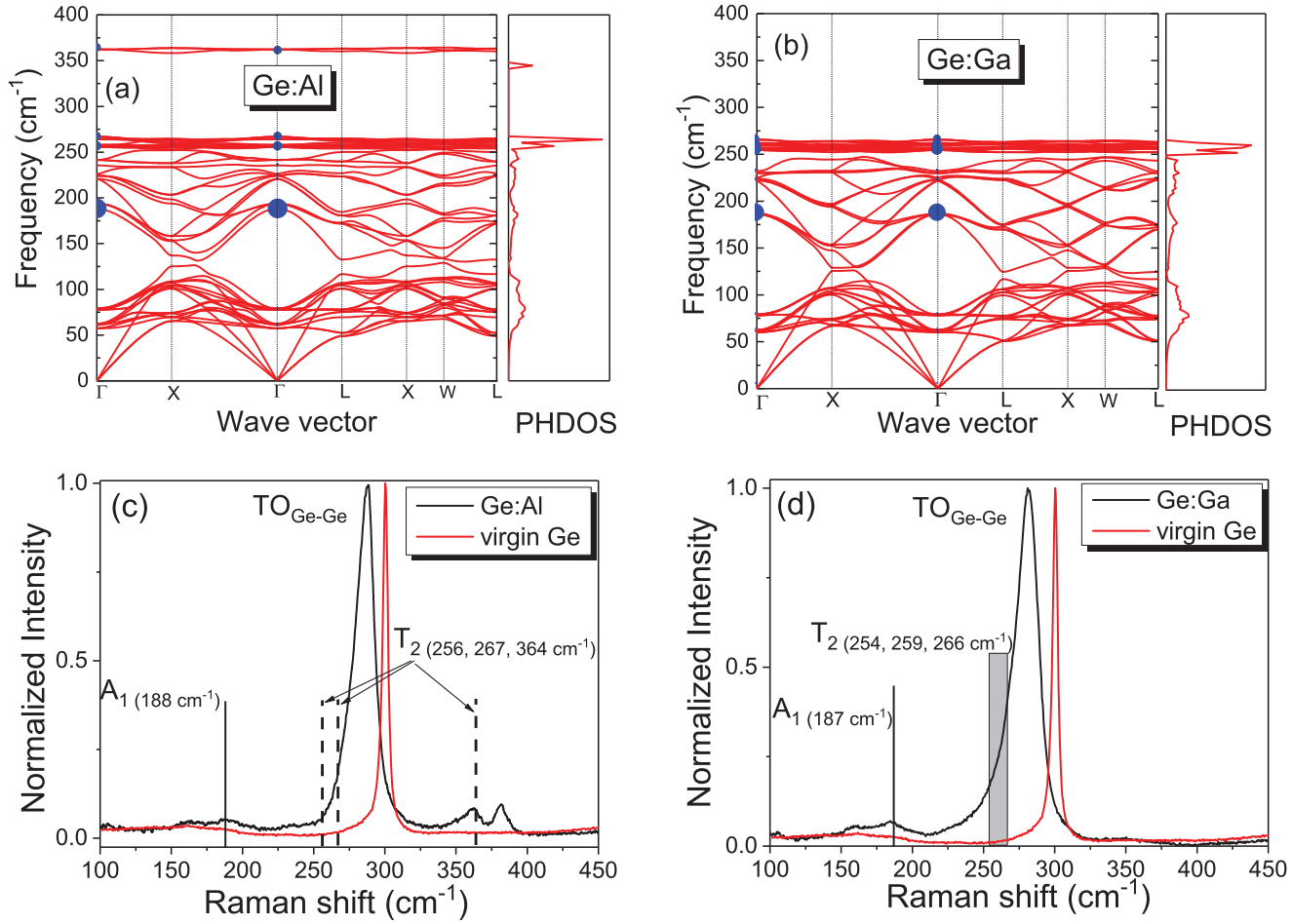


FIG. 7. Phonon band structure with corresponding phonon DOS for Al-hyperdoped Ge (a) and for Ga-hyperdoped Ge (b). The unit of phonon DOS (PHDOS) is states/($cm^{-1}$ × supercell). Blue solid circles indicate the partial electron-phonon coupling strength $\lambda_{vq}$ at the Γ point. (c, d) show the Raman spectra obtained from Al- and Ga-hyperdoped Ge, respectively. The Raman spectrum of virgin undoped Ge is shown for comparison.

electron-phonon coupling strength of about $\lambda_{vq(q=\Gamma)} \sim 0.05 - 0.06$. The phonon structure of Ga-hyperdoped Ge is very similar to Al-hyperdoped Ge. The $A_1$ optical mode should be located at 187 $cm^{-1}$, with maximum electron-phonon coupling of about 0.12. The optical $T_2$ modes in Ga-hyperdoped Ge are located at 254, 259, and 266 $cm^{-1}$, and the $\lambda_{vq(q=\Gamma)}$ is in the range of 0.04–0.07. The theoretical calculated phonon structure of hyperdoped Ge was verified using micro-Raman spectroscopy. The micro-Raman spectra were collected under 532-nm laser excitation, with a laser power of 3.2 mW and a focal diameter of about 1 $\mu$m. Figures 7(c) and 7(d) show the Raman spectra obtained from Al- and Ga-hyperdoped Ge, respectively. The transverse-optical phonon mode of Ge-Ge in intrinsic Ge is located at 300.5 $cm^{-1}$. After hyperdoping the TO phonon mode of the Ge-Ge vibrational is shifted down to 288.2 $cm^{-1}$ for the Al-doped sample and down to 281.9 $cm^{-1}$ for the Ga-doped Ge. This is very close to the theoretically predicted values for the high frequency of the zone-center optical mode in hyperdoped Ge (about 278 $cm^{-1}$). The shift of the TO phonon mode in ultrahigh-doped Ge and the peak asymmetry is due to the phonon softening and the Fano effect [43–45]. Besides the TO phonon mode we can easily distinguish the $A_1$ phonon mode in both samples. The measured peak position of the $A_1$ mode located at about 188 $cm^{-1}$ fits well to the theoretically predicted phonon energy using density of states (DOS) calculation.

Due to the fact that the $T_2$ phonon mode positions are close to the strongest zone-center TO phonon mode it is difficult to distinguish them. But in the case of Al-hyperdoped Ge, the $T_2$ mode at 364 $cm^{-1}$ is well visible [see Fig. 7(c)]. In Ga-hyperdoped Ge all three $T_2$ modes are overlapped with the TO phonon mode. Next we analyze the electron-phonon coupling. Figures 8(a) and 8(b) show the Eliashberg spectral function and the integrated electron-phonon coupling constant $\lambda(\omega)$. The total $\lambda$ calculated for Al- and Ga-doped Ge are similar and equal to 0.355 and 0.350, respectively. The calculated logarithmic phonon frequency $\omega_{log}$ is about 243.6 K for Al-doped Ge and about 245.1 K for Ga-doped Ge, which is much smaller than the $\omega_{log}$ in other group IV superconductors—for example, about 700 K for Si:B and about 1287 K for boron-doped diamond [45]. Finally, we have calculated the superconducting critical temperature for both samples. We found that the expected $T_C$ for Al-doped Ge should be slightly higher than that for the Ga-doped sample, mainly due to slightly higher phonon-carrier coupling. The $T_C$ for Ge:Al is 0.48 K and for the Ge:Ga system the $T_C$ should be about 0.43 K. According to our calculation(s), the superconductivity in diluted *p*-type hyperdoped Ge should be phonon mediated.

Note that there is significant discrepancy between calculated $T_C$ and the experimental values shown in Table I. The theoretical calculation cannot take into account all phenomena which may exist in real samples. In fact, we have a Gaussian distribution of the implanted elements introducing a kind of inhomogeneity into the doped layer which is not accounted for in our calculations and modeling. Next, although the thermal treatment is very short and we were not able to detect big metallic clusters within the implanted Ge layer, we cannot exclude the formation of Ga clusters with a diameter below the resolution limit of our TEM system. Moreover, the effective carrier concentration is lower than the nominal dopant concentration, which is not taken into account for simulation.

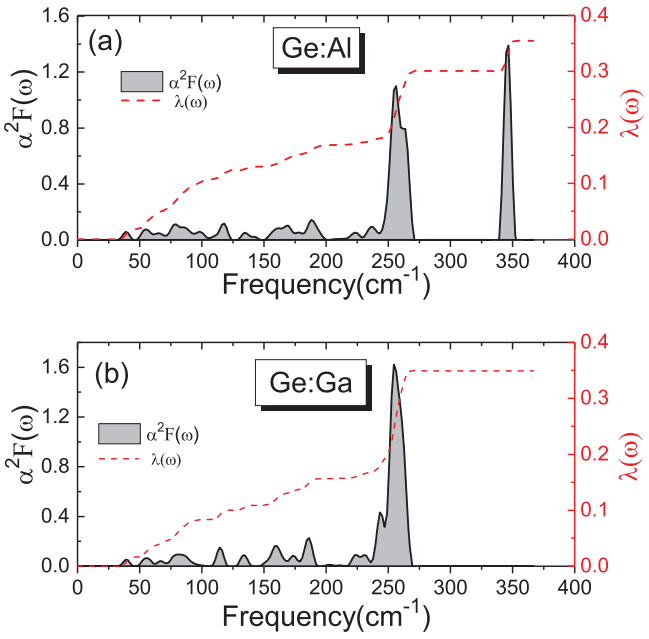


FIG. 8. The total and projected Eliashberg spectral function [$\alpha^2F(\omega)$] for Al-hyperdoped Ge (a) and for Ga-hyperdoped Ge (b). The red dashed curves represent the integrated electron-phonon coupling constant $\lambda$ ($\omega$).

## IV. CONCLUSIONS

We have fabricated single-crystalline Al- and Ga-doped superconducting Ge where the diffusion and clustering of dopants are suppressed by utilization of strongly nonequilibrium thermal processing. Using rear-side FLA, the implanted Ge layers recrystallize epitaxially due to the explosive solid-phase epitaxy. The theoretically predicted critical temperatures qualitatively agree with experimental values. With further optimizing dopant concentrations and annealing parameters, our work will pave the way for monolithic integration of superconducting nanocircuits in semiconductor devices.

## ACKNOWLEDGMENTS

Support by the Ion Beam Center (IBC) at HZDR and the funding of TEM Talos by the German Federal Ministry of Education of Research (BMBF) through Grant No. 03SF0451, in the framework of HEMCP, is gratefully acknowledged. We would like to thank Andrea Scholz for XRD measurements and Romy Aniol for TEM specimen preparation. This work was partially supported by the German Academic Exchange Service (DAAD, Project-ID:57216326) and National Science Center, Poland, under Grant No. 2016/23/B/ST7/03451. Partial support by the EU 7th Framework Program, Project No. REGPOT-CT-2013-316014 ("EAgLE") and by the Foundation for Polish Science through the IRA Program cofinanced by the EU within SG OP is also acknowledged.

[1] E. A. Ekimov, V. A. Sidorov, E. D. Bauer, N. N. Mel'nik, N. J. Curro, J. D. Thompson, and S. M. Stishov, Superconductivity in diamond, Nature (London) **428**, 542 (2004).

[2] Y.-P. Shim and Ch. Tahan, Bottom-up superconducting and Josephson junction devices inside a group-IV semiconductor, Nat. Commun. **5**, 4225 (2014).

[3] E. Bustarret, C. Marcenat, P. Achatz, J. Kacmarcik, F. Lévy, A. Huxley, L. Ortéga, E. Bourgeois, X. Blasé, D. Débarre *et al.*, Superconductivity in doped cubic silicon, Nature (London) **444**, 465 (2006).

[4] T. Herrmannsdörfer, V. Heera, O. Ignatchik, M. Uhlarz, A. Mücklich, M. Posselt, H. Reuther, B. Schmidt, K.-H. Heinig, W. Skorupa *et al.*, Superconducting State in a Gallium-Doped Germanium Layer at Low Temperatures, Phys. Rev. Lett. **102**, 217003 (2009).

[5] T. Muranaka, Y. Kikuchi, T. Yoshizawa, N. Shirakawa, and J. Akimitsu, Superconductivity in carrier-doped silicon carbide, Sci. Technol. Adv. Mater., **9**, 044204 (2008).

[6] X. Blase, E. Bustarret, C. Chapelier, T. Klein, and C. Marcenat, Superconducting group-IV semiconductors, Nat. Mater. **8**, 375 (2009).

[7] K. Iakoubovskii, Recent advances in superconductivity of covalent superconductors, Physica C **469**, 675 (2009).

[8] Y. Takano, Superconductivity in CVD diamond films, J. Phys.: Condens. Matter **21**, 253201 (2009).

[9] E. Bustarret, Superconductivity in doped semiconductors, Physica C **514**, 36 (2015).

[10] D. Cammilleri, F. Fossard, D. Débarre, C. Tran Manh, C. Dubois, E. Bustarret, C. Marcenat, P. Achatz, D. Bouchier, and J. Boulmer, Highly doped Si and Ge formed by GILD (gas immersion laser doping), From GILD to superconducting silicon, Thin Solid Films **517**, 75 (2008).

[11] C. Marcenat, J. Kačmarčík, R. Piquerel, P. Achatz, G. Prudon, C. Dubois, B. Gautier, J. C. Dupuy, E. Bustarret, L. Ortega *et al.*, Low-temperature transition to a superconducting phase in boron-doped silicon films grown on (001)-oriented silicon wafers, Phys. Rev. B **81**, 020501(R) (2010).

[12] A. Grockowiak, T. Klein, E. Bustarret, J. Kačmarčík, C. Dubois, G. Prudon, K. Hoummada, D. Mangelinck, T. Kociniewski, D. Débarre *et al.*, Superconducting properties of laser annealed implanted Si:B epilayers, Supercond. Sci. Technol. **26**, 045009 (2013).

[13] J. Fiedler, V. Heera, R. Skrotzki, T. Herrmannsdörfer, M. Voelskow, A. Mücklich, S. Oswald, B. Schmidt, W. Skorupa, G. Gobsch *et al.*, Superconducting films fabricated by high-fluence Ga implantation in Si, Phys. Rev. B **83**, 214504 (2011).

[14] J. Fiedler, V. Heera, R. Skrotzki, T. Herrmannsdörfer, M. Voelskow, A. Mücklich, S. Facsko, H. Reuther, M. Perego, K.-H. Heinig *et al.*, Superconducting Ga-overdoped Ge layers capped with$SiO_2$: Structural and transport investigations, Phys. Rev. B **85**, 134530 (2012).

[15] R. Skrotzki, T. Herrmannsdörfer, V. Heera, J. Fiedler, A. Mücklich, M. Helm, and J. Wosnitza, The impact of heavy Ga doping on superconductivity in germanium, Low Temp. Phys. **37**, 877 (2011).

[16] K. Hoummada, F. Dahlem, T. Kociniewski, J. Boulmer, C. Dubois, G. Prudon, E. Bustarret, H. Courtois, and D. M. Débarre, Absence of boron aggregates in superconducting silicon confirmed by atom probe tomography, Appl. Phys. Lett. **101**, 182602 (2012).

[17] J. Fiedler, V. Heera, R. Hübner, M. Voelskow, S. Germer, B. Schmidt, and W. Skorupa, High-fluence Ga-implanted silicon—The effect of annealing and cover layers, J. Appl. Phys. **116**, 024502 (2014).

[18] F. Dahlem, P. Achatz, O. A. Williams, D. Araujo, E. Bustarret, and H. Courtois, Spatially correlated microstructure and superconductivity in polycrystalline boron-doped diamond, Phys. Rev. B **82**, 033306 (2010).

[19] G. Zhang, T. Samuely, J. Kačmarčík, E. A. Ekimov, J. Li, J. Vanacken, P. Szabó, J. Huang, P. J. Pereira, D. Cerbu *et al.*, Bosonic Anomalies in Boron-Doped Polycrystalline Diamond, Phys. Rev. Appl. **6**, 064011 (2016).

[20] V. F. Gantmakher and V. T. Dolgopolov, Superconductor—insulator quantum phase transition, Phys. Usp. **53**, 1 (2010).

[21] V. Heera, J. Fiedler, M. Voelskow, A. Mücklich, R. Skrotzki, T. Herrmannsdörfer, and W. Skorupa, Superconductor-insulator transition controlled by annealing in Ga implanted Si, Appl. Phys. Lett. **100**, 262602 (2012).

[22] V. Heera, J. Fiedler, R. Hübner, B. Schmidt, M. Voelskow, W. Skorupa, R. Skrotzki, T. Herrmannsdörfer, J. Wosnitza, and M. Helm, Silicon films with gallium-rich nanoinclusions: From superconductor to insulator, New J. Phys. **15**, 083022 (2013).

[23] V. Heera, J. Fiedler, and W. Skorupa, Large magnetoresistance of insulating silicon films with superconducting nanoprecipitates, AIP Adv. **6**, 105203 (2016).

[24] G. Impellizzeri, S. Mirabella, A. Irrera, M. G. Grimaldi, and E. Napolitani, Ga-implantation in Ge: Electrical activation and clustering, J. Appl. Phys. **106**, 013518 (2009).

[25] V. Heera, A. Mücklich, M. Posselt, M. Voelskow, C. Wündisch, B. Schmidt, R. Skrotzki, K. H. Heinig, T. Herrmannsdörfer, and W. Skorupa, Heavily Ga-doped germanium layers produced by ion implantation and flash lamp annealing: Structure and electrical activation, J. Appl. Phys. **107**, 053508 (2010).

[26] L. Rebohle, S. Prucnal, and W. Skorupa, A review of thermal processing in the subsecond range: Semiconductors and beyond, Semicond. Sci. Technol. **31**, 103001 (2016).

[27] S. Prucnal, L. Rebohle, and W. Skorupa, Doping by flash lamp annealing, Mater. Sci. Semicond. Process., **62**, 115-127 (2017).

[28] S. Prucnal, F. Liu, M. Voelskow, L. Vines, L. Rebohle, D. Lang, Y. Berencén, S. Andric, R. Boettger, M. Helm *et al.*, Ultra-doped n-type germanium thin films for sensing in the mid-infrared, Sci. Rep. **6**, 27643 (2016)

[29] V. Heera, J. Fiedler, M. Naumann, R. Skrotzki, S Kölling, L. Wilde, T. Herrmannsdörfer, W. Skorupa, J. Wosnitza, and M. Helm, Depth-resolved transport measurements and atom-probe tomography of heterogeneous, superconducting Ge:Ga films, Supercond. Sci. Technol. **27**, 055025 (2014).

[30] G. Impellizzeri, E. Napolitani, S. Boninelli, V. Privitera, T. Clarysse, W. Vandervorst, and F. Priolo, Aluminium implantation in germanium: Uphill diffusion, electrical activation, and trapping, Appl. Phys. Express **5**, 021301 (2012).

[31] J. F. Ziegler, J. P. Biersack, and U. Littmark, *The Stopping and Range of Ions in Matter* (Pergamon Press, New York, 1985).

[32] See Supplemental Material at http://link.aps.org/supplemental/10.1103/PhysRevMaterials.3.054802 for more details about samples fabrication and an influence of the dopant concentration on the superconducting states in Ge.

[33] M. Posselt and A. Gabriel, Atomistic simulation of amorphous germanium and its solid phase epitaxial recrystallization, Phys. Rev. B **80**, 045202 (2009).

[34] A. Claverie, S. Koffel, N. Cherkashin, G. Benassayag, and P. Scheiblin, Amorphization, recrystallization and end of range defects in germanium, Thin Solid Films **518**, 2307 (2010).

[35] A. Bezryadin and B. Pannetier, Nucleation of superconductivity in a thin film with a lattice of circular holes, J. Low Temp. Phys. **98**, 251 (1995).

[36] L. Boeri, J. Kortus, and O. K. Andersen, Three-Dimensional MgB2-Type Superconductivity in Hole-Doped Diamond, Phys. Rev. Lett. **93**, 237002 (2004).

[37] L. Boeri, J. Kortus, and O. K. Andersen, Electron-phonon superconductivity in hole doped diamond: A first principles study, J. Phys. Chem. Solids **67**, 552 (2006).

[38] D. M. Ceperley and B. J. Alder, Ground State of the Electron Gas by a Stochastic Method, Phys. Rev. Lett. **45**, 566 (1980).

[39] P. Hohenberg and W. Kohn, Inhomogeneous electron gas, Phys. Rev. **136**, B864 (1964).

[40] W. Kohn and L. J. Sham, Self-consistent equations including exchange and correlation effects, Phys. Rev. **140**, A1133 (1965).

[41] P. Giannozzi *et al.*, QUANTUM EXPRESSO: A modular and open-source software project for quantum simulations of materials, J. Phys.: Condens. Matter **21**, 395502 (2009).

[42] S. Baroni, S. de Gironcoli, A. Dal Corso, and P. Giannozzi, Phonons and related crystal properties from density-functional perturbation theory, Rev. Mod. Phys. **73**, 515 (2001).

[43] X. Blase, C. Adessi, and D. Connetable, Role of the Dopant in the Superconductivity of Diamond, Phys. Rev. Lett. **93**, 237004 (2004).

[44] H. J. Xiang, Zhenyu Li, Jinlong Yang, J. G. Hou, and Qingshi Zhu, Electron-phonon coupling in a boron-doped diamond superconductor, Phys. Rev. B **70**, 212504 (2004).

[45] J. Dai, Z.-Y. Li, and J.-L. Yang, Electron-phonon coupling in gallium-doped germanium, Chin. Phys. Lett. **27**, 086102 (2010).

PHYSICAL REVIEW LETTERS **122,** 097202 (2019)

# Excitation of Whispering Gallery Magnons in a Magnetic Vortex

K. Schultheiss,[1,*] R. Verba,[2] F. Wehrmann,[1] K. Wagner,[1,3] L. Körber,[1,3] T. Hula,[1,4] T. Hache,[1,5] A. Kákay,[1] A. A. Awad,[6] V. Tiberkevich,[7] A. N. Slavin,[7] J. Fassbender,[1,3] and H. Schultheiss[1,3]

[1]*Helmholtz-Zentrum Dresden–Rossendorf, Institute of Ion Beam Physics and Materials Research, Bautzner Landstraße 400, 01328 Dresden, Germany*

[2]*Institute of Magnetism, National Academy of Sciences of Ukraine, Kyiv 03680, Ukraine*

[3]*Technische Universität Dresden, 01062 Dresden, Germany*

[4]*Westsächsische Hochschule Zwickau, 08056 Zwickau, Germany*

[5]*Institut für Physik, Technische Universität Chemnitz, 09107 Chemnitz, Germany*

[6]*Department of Physics, University of Gothenburg, 412 96 Gothenburg, Sweden*

[7]*Department of Physics, Oakland University, Rochester, Michigan 48309, USA*

(Received 2 September 2018; published 5 March 2019)

We present the generation of whispering gallery magnons with unprecedented high wave vectors via nonlinear 3-magnon scattering in a $\mu$m-sized magnetic $Ni_{81}Fe_{19}$ disc which is in the vortex state. These modes exhibit a strong localization at the perimeter of the disc and practically zero amplitude in an extended area around the vortex core. They originate from the splitting of the fundamental radial magnon modes, which can be resonantly excited in a vortex texture by an out-of-plane microwave field. We shed light on the basics of this nonlinear scattering mechanism from an experimental and theoretical point of view. Using Brillouin light scattering microscopy, we investigated the frequency and power dependence of the 3-magnon splitting. The spatially resolved mode profiles give evidence for the localization at the boundaries of the disc and allow for a direct determination of the modes wave number.

DOI: 10.1103/PhysRevLett.122.097202

One of the most fascinating topics in current quantum physics are hybridized systems, in which different quantum resonators are strongly coupled. Prominent examples are circular cavities that allow the coupling of optical whispering gallery modes [1–5] to microwave cavities [6] or magnetic resonances [7–10]. Whispering gallery modes play a special role in this endeavor because of their high quality factor and strong localization, which ultimately increases the overlap of the wave functions of quantum particles in hybridized systems. In optomagnonics the hybridization with magnons, the collective quantum excitations of the electron spins in a magnetically ordered material, is of particular interest because magnons can take over two functionalities: due to their collective nature they are robust and can serve as a quantum memory [11] and, moreover, they can act as a wavelength converter between microwave and terahertz photons [9]. However, the observation of whispering gallery magnons has not yet been achieved due to the lack of efficient excitation schemes for magnons with large wave vectors in a circular geometry. To tackle this problem, we studied nonlinear 3-magnon scattering [12–15] as a means to generate whispering gallery magnons. This Letter discusses the basics of this nonlinear mechanism in a confined, circular geometry from an experimental and theoretical point of view.

Whispering gallery magnons are eigenmodes in systems with rotational symmetry. This not only applies to the geometry of the magnetic element but also to the magnetization texture therein. For that reason, we study a $Ni_{81}Fe_{19}$ disc that inherently exhibits a magnetic vortex structure [16–20]. The red arrows in Fig. 1(a) schematically depict the generic features of such a vortex in a 50-nm thick $Ni_{81}Fe_{19}$ disc with 5.1 $\mu$m diameter: the magnetic moments curl in plane along circular lines around the vortex core, a nanoscopic region in the center of the disc where the magnetization tilts out of plane. According to this rotational symmetry, the magnon eigenmodes in a vortex are characterized by mode numbers $(n, m)$, with $n = 0, 1, 2, \ldots$ counting the number of nodes across the disc radius and $m = 0, \pm 1, \pm 2, \ldots$ counting the number of nodes in azimuthal direction over half the disc [21,22].

Other than commonly known waves, like sound, water, or electromagnetic waves, magnons exhibit a strongly anisotropic dispersion relation in in-plane magnetized thin films [23]. In a vortex, this results in increasing (decreasing) mode energies for increasing $n$ $(m)$ as shown by our analytic calculations in Fig. 1(b). An introduction to these calculations is given in the Supplemental Material [24], which includes Refs. [20,22,25–29]. The four exemplary intensity profiles for the eigenmodes (0,0), (0,10), (0,20), and (0,30), that are shown in Fig. 1(c), reveal the character of whispering gallery magnons: the larger $m$, the more the magnon intensity is pushed toward the perimeter of the disc. This can be understood intuitively by the reduction of

 

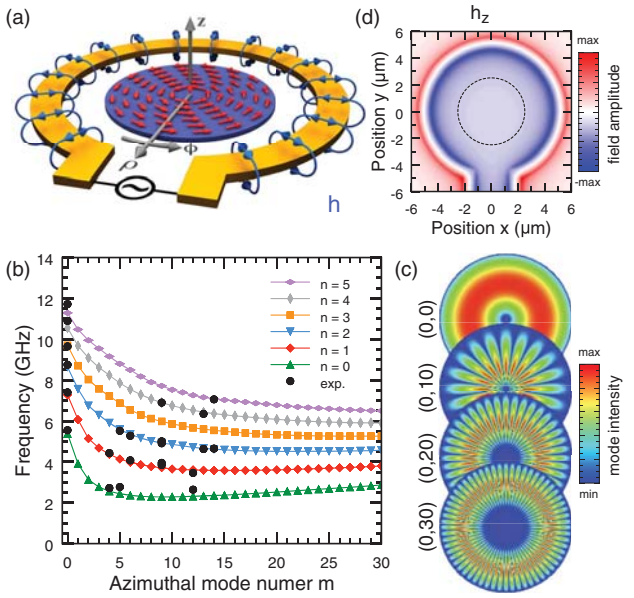


FIG. 1. (a) A $Ni_{81}Fe_{19}$ disc with 50 nm thickness and 5.1 $\mu$m diameter is patterned inside an Ω-shaped Au antenna (for fabrication details please see Supplemental Material [24]). Red arrows depict the magnetization configuration of the magnetic vortex structure and the blue lines represent the dynamic magnetic field generated by the loop-shaped microwave antenna. (b) Analytical calculation of the magnon mode frequencies as a function of the radial and azimuthal mode numbers $n$, $m$ (see Supplemental Material [24]). Black dots show experimental results. (c) Four exemplary mode profiles resulting from analytical calculations. The larger $m$, the more pronounced the character of the whispering gallery magnons is revealed. (d) COMSOL simulation of the $z$ component of exciting magnetic field **h** generated by the Ω-shaped antenna. The dashed circle indicates the size and position of the disc.

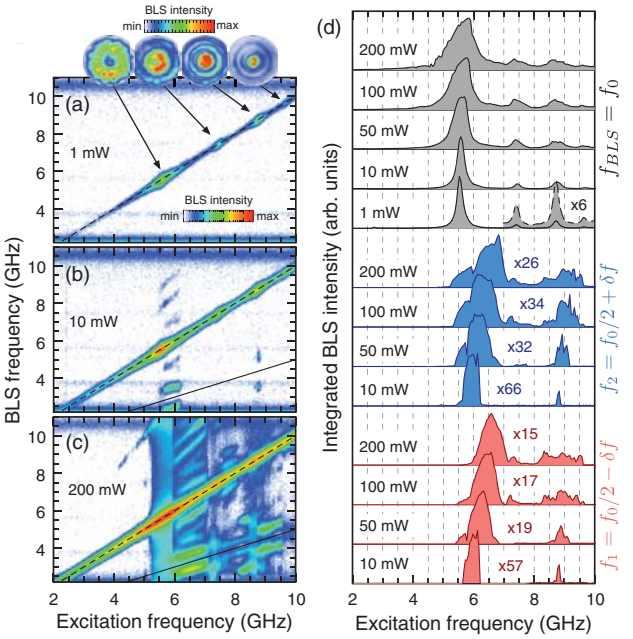


FIG. 2. (a)–(c) BLS spectra for excitation frequencies $f_0$ between 2 and 10 GHz and excitation powers of 1, 10, and 200 mW, respectively. The diagonal dashed lines indicate the directly excited magnetic oscillations at $f_{\mathrm{BLS}} = f_0$. The solid lines indicate frequencies measured at half the excitation frequency $f_{\mathrm{BLS}} = f_0/2$. At 10 and 200 mW, off-diagonal signals associated with multimagnon scattering processes are detected. (d) Black data show the BLS intensity integrated in 800-MHz wide windows around the direct excitation for 1, 10, 50, 100, and 200 mW (bottom to top). At 1 mW, the intensity integrated for excitation frequencies between 7 and 10 GHz was multiplied by a factor of 6 to better visualize the resonances of the higher order radial modes. Blue (red) data show the intensities of the split modes integrated in 1.4-GHz wide windows around $f_1 = f_0/2 + \delta f$ ($f_2 = f_0/2 - \delta f$) with $\delta f = 800$ MHz.

exchange energy: Leaving an extended area around the vortex core with zero amplitude avoids a strong tilt of neighboring spins close to the vortex core and, therefore, reduces the total energy.

Even though magnon spectra in magnetic vortices have been intensively studied in the past [20,21,30,31], magnons with large azimuthal wave vectors have not yet been measured experimentally and were only observed in micromagnetic simulations [32]. The challenge to generate such magnons and, thereby, to reach out to whispering gallery magnons is finding an efficient excitation mechanism. Here, we tackle this problem via nonlinear 3-magnon scattering. In this process, one magnon splits in two magnons under conservation of energy and momentum. The rotational symmetry of the vortex texture implies specific selection rules for the scattering process which we will describe in context with the experimental data.

In order to selectively excite magnetization dynamics, we apply microwave currents to an Ω-shaped gold antenna that encloses the vortex [Fig. 1(a)]. Inside the Ω loop, a spatially uniform magnetic field is generated that is oriented perpendicularly to the disc as shown in Fig. 1(d). The rotational symmetry of this magnetic field prohibits direct coupling to magnons with $m \neq 0$. However, because of the small diameter of the antenna, strong magnetic fields can be generated so that these magnons can be indirectly excited in the nonlinear regime via multimagnon scattering processes.

We track these nonlinear processes by measuring magnon spectra as a function of the applied microwave frequency using Brillouin light scattering (BLS) microscopy [33]. We would like to emphasize that even though the system is driven with one particular microwave frequency, the BLS technique allows us to detect the dynamic magnetic response in a broad frequency range. In Figs. 2(a)–2(c) we plot the BLS spectra measured between 2 and 11 GHz ($y$ axis) for each excitation frequency ($x$ axis) at microwave powers of 1, 10, and 200 mW. The magnon intensity is encoded using the same logarithmic scale shown as an inset in Fig. 2(a).

At the lowest microwave power of 1 mW [Fig. 2(a)], magnons are excited in the linear regime, which is corroborated by the fact that magnons are only observed at the BLS frequency that matches the applied microwave frequency $f_{\mathrm{BLS}} = f_0$. Hence, the measured intensities strictly follow the diagonal, dashed line. Four distinct resonances emerge at 5.55, 7.40, 8.75, and 9.65 GHz, which we identify as the well-known first four radial modes [21,34] by spatially resolved BLS microscopy [insets in Fig. 2(a)].

At a power of 10 mW [Fig. 2(b)], the excitation field is strong enough to generate magnons in the nonlinear regime. Hence, we observe strong off-diagonal signals that appear at BLS frequencies symmetrically spaced around half the excitation frequency $f_0/2$ (straight line with slope 0.5). These satellite peaks are the result of 3-magnon splitting processes. In order to conserve energy the initial magnon with frequency $f_0$ splits in two magnons with frequencies $f_1 = f_0/2 - \delta f$ and $f_2 = f_0/2 + \delta f$. Moreover, the rotational symmetry of the vortex requires conservation of the momentum component in azimuthal direction. For an initial magnon with $m = 0$ this implies that the split modes have azimuthal mode numbers with the same modulus but opposite sign: $m_1 = -m_2$. Our analytic calculations further show that the split modes must not share the same radial index, i.e., $n_1 \neq n_2$ (see Supplemental Material [24]). All three selection rules drastically restrict the possible scattering channels within the discrete eigenmode spectrum of the vortex [see Fig. 1(b)].

Besides the magnons with frequencies $f_1$ and $f_2$, we observe integer multiples thereof. We attribute these signals to higher harmonics giving evidence to large amplitude resonances with a high $q$ factor.

At the maximum applied microwave power of 200 mW, the number of off-diagonal signals increases further [Fig. 2(c)]. Especially, for excitation frequencies between 6 and 7 GHz, we do not just measure two satellite peaks with frequencies $f_1$ and $f_2$ but a total number of ten additional modes. Their presence is attributed to avalanche processes of higher order multimagnon scattering. Their frequencies are given by combinations of the three initial magnons, e.g., $2f_1$, $2f_2$, $f_0 + f_1$. Furthermore, the significant line broadening of the directly excited mode and of the split modes in the frequency range between 5.3 and 5.9 GHz can be attributed to 4-magnon scattering [35]. However, this Letter solely focusses on the study of the initial 3-magnon scattering processes which dominate in intensity due to the lower threshold compared to 4-magnon scattering.

To better illustrate the power dependence of the observed modes, we plot the BLS intensity integrated over different frequency windows as a function of the excitation frequency in Fig. 2(d). The black data resemble the BLS intensity of the direct excitation. With increasing power the initially sharp resonances become broader and show the characteristic nonlinear foldover to higher frequencies [36,37]. The red and blue data in Fig. 2(d) show the intensities of the split modes below (red data) and above $f_0/2$ (blue data), which overall broaden in range and shift to higher frequencies with increasing power.

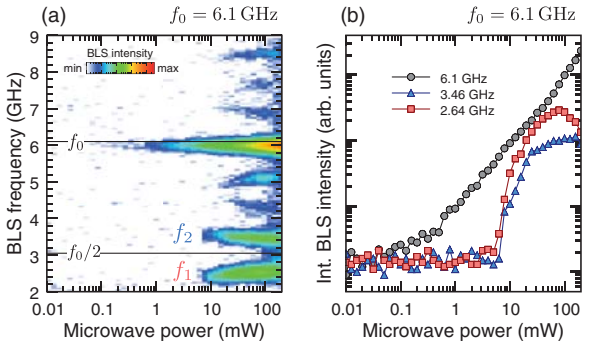


FIG. 3. (a) Power dependence of the BLS spectra excited at $f_0 = 6.1$ GHz. (b) BLS intensity integrated in 800-MHz wide frequency windows around the BLS frequencies $f_0 = 6.1$, $f_1 = 2.64$, and $f_2 = 3.46$ GHz as a function of the microwave power. In the double-logarithmic plot, the direct excitation at 6.1 GHz follows a linear trend, whereas the split modes at 3.46 and 2.64 GHz show a clear threshold behavior.

To further elucidate the threshold character of the 3-magnon splitting, we plot a more detailed power dependence of the magnon intensities in Fig. 3(a) for $f_0 = 6.1$ GHz. While the mode at 6.1 GHz can be observed over a large power range, it is evident that the split modes $f_1$ and $f_2$ only appear above a certain threshold power. Furthermore, we observe a pronounced frequency shift of these two split modes with increasing microwave power. For a quantitative comparison, we integrate the BLS intensity in narrow frequency windows around the directly and indirectly excited modes, respectively, and plot them in Fig. 3(b). The double logarithmic scale reveals the linear growth of the direct excitation at 6.1 GHz starting at 0.1 mW. However, the intensities of the satellite peaks around $f_1 = 2.65$ and $f_2 = 3.48$ GHz abruptly increase above 10 mW which demonstrates the threshold character of the splitting process.

In order to reveal the spatial structure of the modes that are generated via 3-magnon scattering, we simultaneously mapped the profiles of the directly excited mode and the split modes [Figs. 4(c)–4(g)]. Additionally, we compare the experimental results for the mode with highest intensity at 6.1 GHz with micromagnetic simulations [38] in Fig. 4(b) (for details please see Supplemental Material [24]). The first thing to realize is that all of the split modes show a clear azimuthal character and confirm the analytical calculations and the selection rules imposed by the rotational symmetry: pure radial modes with $(n, 0)$ split in modes with $m_1 = -m_2$ and $n_1 \neq n_2$. As far as possible, we label the modes according to their radial and azimuthal mode numbers $(n, m)$. We resolve azimuthal mode numbers up

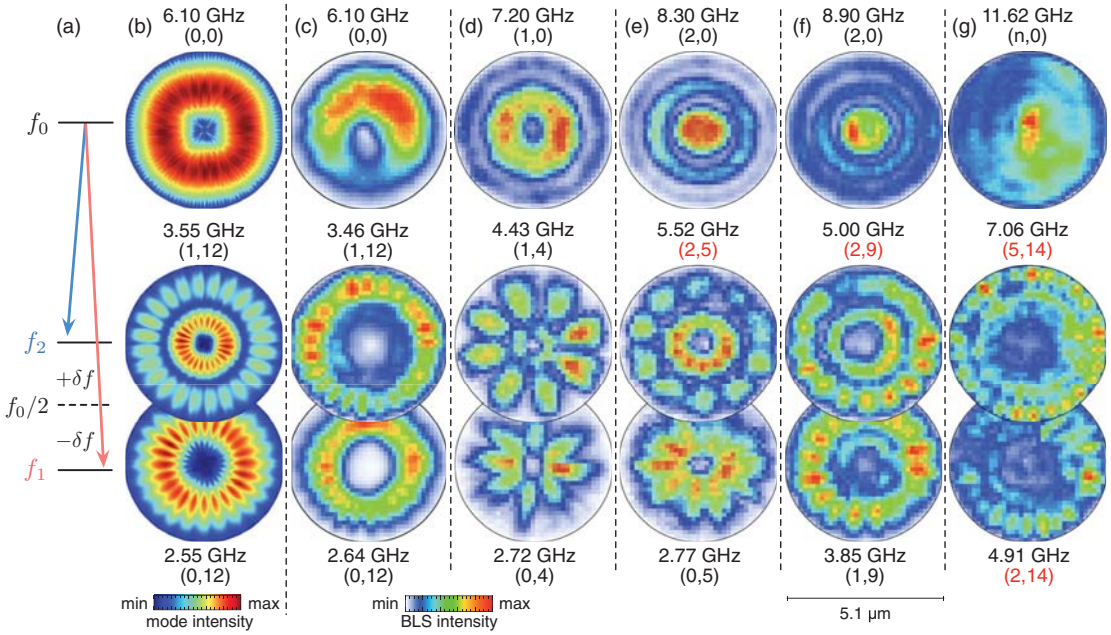


FIG. 4. (a) Energy levels for 3-magnon splitting. (b) Micromagnetic simulation of the 3-magnon splitting for the excitation frequency of 6.1 GHz. (c)–(g) Spatial intensity distributions of the direct excitation (upper line) as well as the split modes (middle and bottom line) for various excitation frequencies. Each magnon mode has been identified regarding its radial and azimuthal order ($n$, $m$). Numbers in red are derived by comparing the experimentally detected magnon frequency to analytical calculations [Fig. 1(b)].

to 14, to our knowledge the first time to observe vortex modes with such high $m$. For higher $n$, an unambiguous identification of the modes was not possible due to limited spatial resolution. However, the radial mode number can still be retrieved by comparing the measured frequencies to the analytic calculations in Fig. 1(b). We counted the azimuthal mode numbers and plotted the measured frequencies as black dots in the calculated spectrum. From this comparison we then determined the radial mode numbers (red labels in Fig. 4).

In Fig. 4(b), the micromagnetic simulation for excitation at 6.1 GHz reveals the splitting into magnons with the same mode numbers as in the experiment, however, with slightly different frequencies of the split modes. This frequency shift may be attributed to variations in the strength and symmetry of the exciting magnetic field or the material parameters. For further details please see Supplemental Material [24].

Note that we only measure stationary mode profiles which implies that, essentially, all split modes are a superposition of modes counterpropagating in the azimuthal direction. Therefore, we conclude that the two splitting processes $(n_0, 0) \rightarrow (n_1, m) + (n_2, -m)$ and $(n_0, 0) \rightarrow (n_1, -m) + (n_2, m)$ occur with equal probability.

It is remarkable, that the higher $m$ for a given $n$, the stronger the mode is localized at the outer circumference of the disc, resembling intensity distributions of optical whispering gallery modes [39]. The most beautiful example in our dataset is the intensity distribution of the split mode (0,12) at the excitation frequency 6.1 GHz shown in Fig. 3(c). It exhibits a distinct area with zero intensity in its center, similar to higher order optical whispering gallery modes.

In summary, we shed light on the nonlinear conversion of magnons in a confined system with rotational symmetry by analyzing their spectral and spatial characteristics. We showed how this mechanism can be utilized to generate magnons with unprecedented high azimuthal wave vectors and localization at the discs' perimeter, which resembles the character of whispering gallery modes. The underlying 3-magnon scattering processes are highly tunable regarding the frequency and spatial distribution of the split modes. We believe that this advanced control of the generation of whispering gallery magnons is a missing link towards the realization of an efficient hybridization of magnons and other quantum particles as found in circular optical cavities and mechanical quantum resonators.

The authors acknowledge fruitful discussions with S. V. Kusminskiy. Financial support by the Deutsche Forschungsgemeinschaft is gratefully acknowledged within program SCHU2922/1-1. K. S. acknowledges funding within the Helmholtz Postdoc Programme. Samples were fabricated at the Nanofabrication Facilities (NanoFaRo) at the Institute of Ion Beam Physics and Materials Research at HZDR. We thank B. Scheumann for film deposition and L. Bischoff for the thickness measurement.

*Corresponding author.
k.schultheiss@hzdr.de

[1] G. Mie, Ann. Phys. (N.Y.) **330**, 377 (1908).
[2] P. Debye, Ann. Phys. (N.Y.) **335**, 755 (1909).
[3] L. Rayleigh, Philos. Mag. **27**, 100 (1914).
[4] A. N. Oraevsky, Quantum Electron. **32**, 377 (2002).
[5] K. J. Vahala, Nature (London) **424**, 839 (2003).
[6] Y. Tabuchi, S. Ishino, T. Ishikawa, R. Yamazaki, K. Usami, and Y. Nakamura, Phys. Rev. Lett. **113**, 083603 (2014).
[7] A. Osada, R. Hisatomi, A. Noguchi, Y. Tabuchi, R. Yamazaki, K. Usami, M. Sadgrove, R. Yalla, M. Nomura, and Y. Nakamura, Phys. Rev. Lett. **116**, 223601 (2016).
[8] J. A. Haigh, A. Nunnenkamp, A. J. Ramsay, and A. J. Ferguson, Phys. Rev. Lett. **117**, 133602 (2016).
[9] S. V. Kusminskiy, H. X. Tang, and F. Marquardt, Phys. Rev. A **94**, 033821 (2016).
[10] J. Graf, H. Pfeifer, F. Marquardt, and S. V. Kusminskiy, Phys. Rev. B **98**, 241406 (2018).
[11] X. Y. Zhang, C.-L. Zou, N. Zhu, F. Marquardt, L. Jiang, and H. X. Tang, Nat. Commun. **6**, 8914 (2015).
[12] H. Suhl, J. Phys. Chem. Solids **1**, 209 (1957).
[13] C. Ordonez-Romero, B. A. Kalinikos, P. Krivosik, W. Tong, P. Kabos, and C. E. Patton, Phys. Rev. B **79**, 144428 (2009).
[14] H. Schultheiss *et al.*, Phys. Rev. Lett. **103**, 157202 (2009).
[15] R. E. Camley, Phys. Rev. B **89**, 214402 (2014).
[16] T. Shinjo, T. Okuno, R. Hassdorf, K. Shigeto, and T. Ono, Science **289**, 930 (2000).
[17] V. Novosad, M. Grimsditch, K. Y. Guslienko, P. Vavassori, Y. Otani, and S. D. Bader, Phys. Rev. B **66**, 052407 (2002).
[18] K. Y. Guslienko and V. Novosad, J. Appl. Phys. **96**, 4451 (2004).
[19] V. Novosad, F. Y. Fradin, P. E. Roy, K. Buchanan, K. Y. Guslienko, and S. D. Bader, Phys. Rev. B **72**, 024455 (2005).
[20] K. Y. Guslienko, A. N. Slavin, V. Tiberkevich, and S.-K. Kim, Phys. Rev. Lett. **101**, 247203 (2008).
[21] M. Buess, R. Höllinger, T. Haug, K. Perzlmaier, U. Krey, D. Pescia, M. R. Scheinfein, D. Weiss, and C. H. Back, Phys. Rev. Lett. **93**, 077207 (2004).
[22] M. Buess, T. P. J. Knowles, R. Höllinger, T. Haug, U. Krey, D. Weiss, D. Pescia, M. R. Scheinfein, and C. H. Back, Phys. Rev. B **71**, 104415 (2005).
[23] B. A. Kalinikos and A. N. Slavin, J. Phys. C **19**, 7013 (1986).
[24] See Supplemental Material at http://link.aps.org/supplemental/10.1103/PhysRevLett.122.097202 for additional information on sample fabrication, the experimental technique of Brillouin light scattering and an introduction to the theoretical calculations.
[25] V. S. L'vov, *Wave Turbulence Under Parametric Excitation* (Springer-Verlag, New York, 1994).
[26] P. Krivosik and C. E. Patton, Phys. Rev. B **82**, 184428 (2010).
[27] K. Livesey, Nonlinear Behavior in Metallic Thin Films and Nanostructures, in *Handbook of Surface Science*, edited by R. E. Camley, Z. Celinski, and R. L. Stamps (Elsevier, North-Holland, 2015), Vol. 5.
[28] A. Yu. Galkin, B. A. Ivanov, and C. E. Zaspel, Phys. Rev. B **74**, 144419 (2006).
[29] K. Y. Guslienko and A. N. Slavin, J. Appl. Phys. **87**, 6337 (2000).
[30] R. Zivieri and F. Nizzoli, Phys. Rev. B **71**, 014411 (2005).
[31] A. A. Awad, G. R. Aranda, D. Dieleman, K. Y. Guslienko, G. N. Kakazei, B. A. Ivanov, and F. G. Aliev, Appl. Phys. Lett. **97**, 132501 (2010).
[32] B. Taurel, T. Valet, V. V. Naletov, N. Vukadinovic, G. deLoubens, and O. Klein, Phys. Rev. B **93**, 184427 (2016).
[33] T. Sebastian, K. Schultheiss, B. Obry, B. Hillebrands, and H. Schultheiss, Front. Phys. **3**, 35 (2015).
[34] K. Vogt, O. Sukhostavets, H. Schultheiss, B. Obry, P. Pirro, A. A. Serga, T. Sebastian, J. Gonzalez, K. Y. Guslienko, and B. Hillebrands, Phys. Rev. B **84**, 174401 (2011).
[35] H. Schultheiss, K. Vogt, and B. Hillebrands, Phys. Rev. B **86**, 054414 (2012).
[36] H. Suhl, J. Appl. Phys. **31**, 935 (1960).
[37] P. A. Praveen Janantha, B. Kalinikos, and M. Wu, Phys. Rev. B **95**, 064422 (2017).
[38] A. Vansteenkiste, J. Leliaert, M. Dvornik, M. Helsen, F. Garcia-Sanchez, and B. Van Waeyenberge, AIP Adv. **4**, 107133 (2014).
[39] J. J. Yang, M. Huang, J. Yu, and Y. Z. Lan, Europhys. Lett. **96**, 57003 (2011).

ARTICLES
https://doi.org/10.1038/s41565-019-0383-4
nature nanotechnology

# Emission and propagation of 1D and 2D spin waves with nanoscale wavelengths in anisotropic spin textures

Volker Sluka[1*], Tobias Schneider[1], Rodolfo A. Gallardo[2,3], Attila Kákay[1], Markus Weigand[4], Tobias Warnatz[1,10], Roland Mattheis[5], Alejandro Roldán-Molina[6], Pedro Landeros[2,3], Vasil Tiberkevich[7], Andrei Slavin[7], Gisela Schütz[4], Artur Erbe[1], Alina Deac[1], Jürgen Lindner[1], Jörg Raabe[8], Jürgen Fassbender[1,9] and Sebastian Wintz[1,8*]

**Spin waves offer intriguing perspectives for computing and signal processing, because their damping can be lower than the ohmic losses in conventional complementary metal–oxide–semiconductor (CMOS) circuits. Magnetic domain walls show considerable potential as magnonic waveguides for on-chip control of the spatial extent and propagation of spin waves. However, low-loss guidance of spin waves with nanoscale wavelengths and around angled tracks remains to be shown. Here, we demonstrate spin wave control using natural anisotropic features of magnetic order in an interlayer exchange-coupled ferromagnetic bilayer. We employ scanning transmission X-ray microscopy to image the generation of spin waves and their propagation across distances exceeding multiples of the wavelength. Spin waves propagate in extended planar geometries as well as along straight or curved one-dimensional domain walls. We observe wavelengths between 1 μm and 150 nm, with excitation frequencies ranging from 250 MHz to 3 GHz. Our results show routes towards the practical implementation of magnonic waveguides in the form of domain walls in future spin wave logic and computational circuits.**

Spin waves, also referred to as magnons, are the elementary excitations of the order parameter in ferromagnetic materials (Fig. 1a)[1]. They can be used in a similar manner to electrons in CMOS circuitry to transmit information, but with lower losses. Therefore, they are currently attracting a lot of interest as possible information carriers in alternative computing schemes[2–5]. Another substantial advantage of spin wave technology is the fact that, in the gigahertz range, magnon wavelengths are several orders of magnitude shorter than those of electromagnetic waves[6]. Accordingly, significant device miniaturization can be achieved for applications where the wavelength imposes a critical constraint on the device footprint. For such purposes it will be crucial to utilise spin waves with wavelengths in the submicrometre range, where both magnetostatic and exchange effects are relevant (dipole-exchange waves)[3]. While surface acoustic waves are already present as short-wavelength signal carriers in today's communication technology, spin waves offer a superior scalability of wave excitation and propagation at frequencies above 2 GHz as well as a much wider frequency tunability[7,8].

Two challenging aspects of building a magnonic computer are the generation of short-wavelength magnons[9–17] and the construction of suitable waveguides for spin wave transport[17–25]. A standard method to coherently generate spin waves employs the localized Oersted fields from alternating electric currents flowing in metallic antennas that are patterned adjacent to a magnetic medium. The smallest excitable wavelengths that are possible using this method, however, are approximately equal to the patterning sizes involved (Supplementary Section 3). In terms of nanopatterning and microwave impedance matching, it is therefore highly challenging to efficiently scale such an antenna-based excitation to nanoscale wavelengths. While similar restrictions apply from the patterning size, spin-transfer torques are an alternative suitable source for spin wave excitation[26–29], with the possibility of steering spin waves with external magnetic bias fields[29]. More recently, it has also been shown that spin waves can be generated using the internal fields of non-uniform spin textures[11–16,30–33], yet direct observations are limited to wavelengths >1 μm, apart from those in refs. [17,34,35]. Reference [34] demonstrates the emission of high-amplitude nanoscale spin waves from a pair of stacked vortex cores[36] driven by an alternating magnetic field[37,38]. However, in the geometry of ref. [34], where a point-like vortex core source is radiating spin waves into a two-dimensional (2D) propagation medium, spin waves originating from a vortex core and travelling outwards radially experience not only Gilbert damping, but also a purely geometric reduction of amplitude proportional to the inverse square root of the distance from the source, as shown schematically in Fig. 1b. Furthermore, it has been suggested that magnetic domain walls could be harnessed to guide spin waves across the magnonic chip[5,17–21,39–41]. In particular, it has been shown that domain walls can host localized modes excited by alternating magnetic fields[19]. In ref. [19], the lateral position of the excited magnetization amplitudes could be well controlled by tuning the lateral domain wall position, but these modes quickly decayed

[1]Helmholtz-Zentrum Dresden-Rossendorf, Dresden, Germany. [2]Universidad Técnica Federico Santa María, Valparaíso, Chile. [3]Center for the Development of Nanoscience and Nanotechnology (CEDENNA), Santiago, Chile. [4]Max-Planck-Institut für Intelligente Systeme, Stuttgart, Germany. [5]Leibniz Institut für Photonische Technologien, Jena, Germany. [6]Universidad de Aysén, Coyhaique, Chile. [7]Oakland University, Rochester, MI, USA. [8]Paul Scherrer Institut, Villigen, PSI, Switzerland. [9]Technische Universität Dresden, Dresden, Germany. [10]Present address: Uppsala Universitet, Uppsala, Sweden.
*e-mail: v.sluka@hzdr.de; s.wintz@hzdr.de

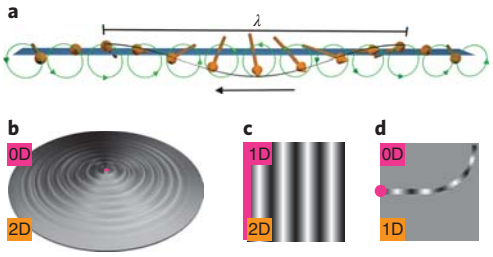


**Fig. 1 | Spin waves in different geometries. a**, Schematic of a spin wave of wavelength $\lambda$ propagating along the direction indicated by the black arrow. The green arrows refer to the precessional motion performed by the magnetization vectors (orange arrows). **b**–**d**, Three different geometries of spin wave propagation explored in this Article. The magenta and orange fields denote the geometric dimensions of the source and propagation medium, respectively. In **b**, spin wave emission is from a point source. In this case, the dimensions of the medium and source differ by two. As a result, in addition to the exponential decay caused by Gilbert damping, there is a geometric decay of the spin wave amplitude. In **c**, plane-wave-like spin wave propagation is shown. Similar to **b**, the waveguide medium is 2D, yet the source has dimension one. In **d**, a 0D source excites a 1D medium (a domain wall).

along the domain wall coordinate with increasing distance from the microwave antenna within subwavelength length scales.

These key issues—short-wavelength spin wave generation and spin wave guidance—are the points we address in this work, where we make use of naturally formed anisotropic spin textures. First, we demonstrate the excitation and propagation of 2D planar spin waves (Fig. 1c) excited by the oscillation of straight domain walls. These excitations can travel distances spanning multiples of the wavelength. Second, we observe excitation and propagation of spin wave modes confined to quasi-1D natural waveguides (straight or curved) formed by domain walls embedded in a 2D host medium (Fig. 1d).

## Anisotropic spin textures

We patterned $Ni_{81}Fe_{19}$/Ru/$Co_{40}Fe_{40}B_{20}$ multilayers (44.9/0.8/46.6 nm thickness) into disk- and square-shaped elements with lateral sizes of several micrometres (Fig. 2a). Each ferromagnetic layer exhibits an in-plane uniaxial anisotropy. The Ru interlayer causes antiferromagnetic coupling between the two ferromagnetic layers[42] (see Methods for further details).

The magnetic ground-state configuration stabilized in this system is a pair of stacked vortices, with opposite vorticity due to the antiferromagnetic interlayer exchange coupling. The influence of the CoFeB uniaxial anisotropy leads to a significant distortion of the vortex magnetization distribution in both magnetic layers. The result in each layer is a state of two homogeneously in-plane magnetized domains with opposite magnetizations. These domains are separated by a narrow, partially perpendicularly oriented, 180° domain wall that contains the vortex cores and spans the lateral extension of the disks. These magnetic configurations are presented in the scanning transmission X-ray microscopy (STXM) images in Fig. 2b,c, which display magnetic information about the in-plane (Fig. 2b) and out-of plane (Fig. 2c) components of the individual layers, where the technique provides a lateral resolution of about 25 nm. As Fig. 2c indicates, the out-of-plane magnetization components of the respective layers couple ferromagnetically to each other via their stray field. In particular, this is true for the polarizations of the vortex cores. Micromagnetic simulations confirm this and reveal that the domain wall formed in the sample is a mixture of Néel and Bloch types of domain wall[43], where the in-plane components couple antiferromagnetically across the Ru interlayer, as in the domains. Figure 2d presents a schematic top view of the domain wall structure in the CoFeB layer, showing the mixed Bloch and Néel components. Figure 2e shows a schematic cross-section across the domain wall, revealing that the out-of-plane magnetization components in the domain wall follow a flux-closing distribution between the two layers.

## Nanoscale spin wave generation

Spin waves can be excited in such anisotropic spin textures by applying an alternating magnetic field, as shown in Fig. 3. The corresponding measurements were made by means of time-resolved (TR) STXM imaging, allowing for a stroboscopic time resolution of ~100 ps. Figure 3a presents a snapshot of the magnetic excitations at an Oersted field frequency of 1.11 GHz, taken at the Ni absorption edge, displaying the out-of-plane contrast. Plane spin waves are visible, with wave fronts parallel to the domain wall and propagating away from the domain wall towards the rim of the elliptical element, as indicated by the green arrow. The oscillating Oersted-field in-plane component is oriented along the minor axis of the ellipse, perpendicular to the domain wall. The main effect of the Oersted field is to excite the dynamics of the domain wall, and the excited domain wall acts as a confined perpendicular source for the observed spin waves[15,17,33]. In more detail, by acting on the full sample volume, the field excites a non-resonant antiphase width oscillation of the walls in the two different layers, which is coherent over the wall length, causing highly localized out-of-plane torques in the wall vicinity. In this way, spin waves are essentially excited via a linear and coherent coupling of the discrete wall mode to the spin wave continuum, similar to the situation with vortex core-driven spin waves, as reported earlier[34,35].

The time-periodic nature of the waves allows us to capture the wave motion at discrete, equi-spaced phases in each scanned pixel, and to compose the recorded data into movie-like arrangements, which show the propagation of these spin excitations (see videos in the Supplementary Information). A comparison of the absorption data taken along the green arrow in Fig. 3a at different time slices yields the wavelength of the wave and its speed of propagation. Three of these time slices are shown in Fig. 3b. Notably, the spin wave amplitude does not visibly decrease across the distance of 2 µm, corresponding to about 7.5 times the wavelength. Taking into account a set of measurements for the given frequency of 1.11 GHz, we obtain a wavelength of 286 ± 20 nm and a phase velocity of 317 ± 22 m $s^{-1}$. Increasing the excitation frequency to 1.46 GHz results in a similar wave pattern, but with shorter wavelength (Fig. 3c). The corresponding values for the wavelength and phase velocity are 211 ± 15 nm and 307 ± 22 m $s^{-1}$, respectively. By comparison with the contrast of the vortex core, the spin wave amplitudes are estimated to reach a precession angle of more than 5°, which can be considered as very high when compared to standard spin wave excitation techniques (cf. ref. [44], which reports an angle of 1.5°).

Around the vortex centre, as shown in the magnified image in Fig. 3d, in addition to the plane waves generated by the oscillating wall, there are radial wave fronts that arise from the motion of the vortex core[34]. As expected, these radially symmetric waves decay faster than the plane waves excited by the domain wall. This difference is a consequence of the relative dimensionality of the source and medium: while the plane waves are excited by a 1D source (the domain wall), for the radial waves the source is 0D (the vortex core). Nevertheless, as the two wave forms are excited simultaneously, interference patterns arise (Fig. 3d).

We can excite planar spin waves for a broad range of frequencies up to 3 GHz. One can expect this process to scale to higher frequencies if the magnetization gradient of the exciting source (domain wall or vortex core) is enhanced as for domain walls in systems with strong perpendicular magnetic anisotropy or if the spin wave dispersion relation is tuned to longer wavelengths by modifying

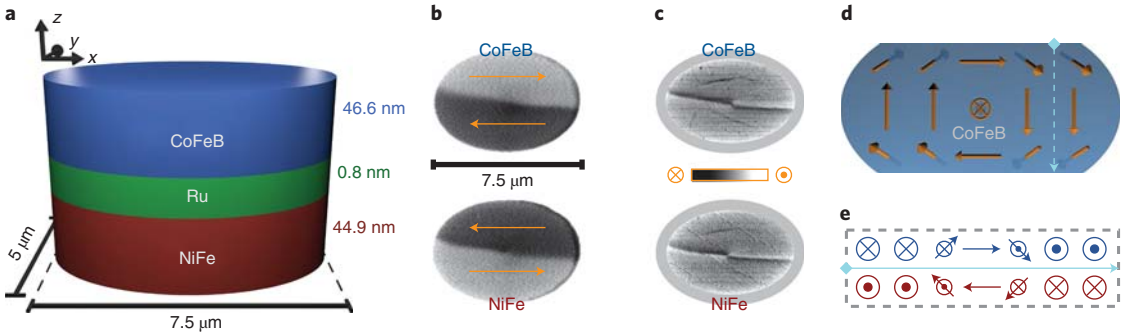


**Fig. 2 | Sample layout and magnetic configuration. a**, The ferromagnetic element is patterned out of an interlayer-exchange-coupled bilayer system consisting of a NiFe layer and a CoFeB layer, coupled antiferromagnetically by a Ru interlayer. **b**,**c**, High-resolution X-ray magnetic circular dichroism (XMCD) STXM images, showing that the magnetic configuration is a pair of stacked vortices, with antiferromagnetically coupled in-plane magnetizations. In **b**, the contrast represents the in-plane magnetic component along the long axis of the elliptic element (orange arrows indicate the magnetic orientation). In **c**, the out-of-plane magnetic contrast is displayed. We find that an additional anisotropy with the easy axis along the long axis of the elliptic element leads to an anisotropic deformation of the vortex patterns, resulting in the formation of a domain wall, which is also visible both in the in-plane and out-of-plane contrast images. Micromagnetic simulations reveal that this domain wall has both Néel and Bloch character, as shown schematically in **d**, where the orange arrows indicate the magnetic orientation. **e**, Cross-section of the domain wall profile, which can be imagined as taken along the blue dashed line in **d**, illustrating the in- and out-of-plane components of the layer magnetizations in and around the domain wall.

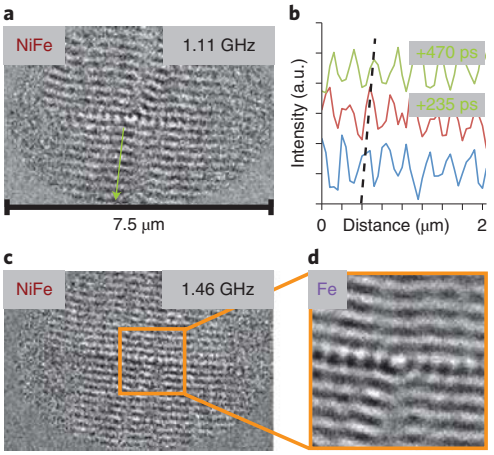


**Fig. 3 | Excitation of spin waves.** TR-STXM snapshots of spin waves (NiFe layer out-of-plane magnetization component), excited using a.c. magnetic fields at different frequencies. **a**, Spin waves generated at an excitation frequency of 1.11 GHz. These plane waves travel from the wall to the rim of the disk, as indicated by the green arrow. **b**, Three time slices of the signal amplitude along the arrow in **a** taken at equidistant time intervals of 235 ps. **c**, Corresponding image of a spin wave excited at 1.46 GHz. **d**, Enlarged image of the region indicated in the centre of **c**.

the magnetic layer stack. A qualitatively different effect, however, appears when going to rather low excitation frequencies, as shown in Fig. 4, which displays excitations at 0.52 GHz and 0.26 GHz (Fig. 4a,b, respectively). At these low frequencies, no visible excitations exist in the domains, yet the data show spin waves propagating confined to the domain wall in the directions away from the vortex cores. The wavelength can again be controlled by tuning the excitation frequency. Note that there is a directional asymmetry in the spin wave emission at 0.52 GHz, which, however, can be attributed to sample imperfections in the exciting core region, as simulations indicate a symmetric emission pattern (Supplementary Video 7). Irrespective of this, the wave amplitude is still significant, even after a propagation distance extending from the vortex core to the rim of the ellipse. This situation is again a consequence of a dimensionality difference of one between source and medium. For waves propagating along the domain wall, the source is of dimension zero, yet the propagation medium is effectively 1D. Hence, geometrical decay of the amplitude is avoided, making the domain wall act as a low-loss waveguide (Supplementary Video 4) of propagating spin waves in the domain walls. The confined waves excited here can be considered a bilayer analogue of the spin wave mode predicted for a single domain wall[40]. The coherent domain wall resonance (or infinite wavelength $k=0$) case of such a bilayer has been theoretically studied[45] (cf. Supplementary Section 2).

To shed light on the underlying physics, we followed a twofold strategy. First, both phenomena—the excitation and propagation of planar spin waves in the domain and 1D waves confined to the domain wall—were investigated and qualitatively confirmed with micromagnetic simulations. To achieve this, the experimental static magnetization distribution was reproduced before excitation by an a.c. magnetic field. Supplementary Video 7 shows the time-dependent perpendicular magnetization of a simulated ellipse yielding a qualitative confirmation of the gapless 1D spin wave mode in the domain wall. To obtain details of the dispersion relation for the planar waves in the domains within a reasonable computation time, the system was modelled by two continuous, homogeneously magnetized coupled layers (see Methods for further details).

## 2D plane spin wave dispersion

In addition to the simulations, we developed a theory (see Supplementary Information for in-depth technical details) for the propagation of spin waves in two exchange-coupled extended ferromagnetic films. The theory allows to compute the spin wave dispersion relation in coupled films whose thicknesses exceed the respective material's exchange length. This is done by considering each magnetic layer as being composed of several coupled thin layers, for which the thin film approximation holds (for details see Methods). In Fig. 5, the measured spin wave dispersion relations $f(k=2\pi/\lambda)$ (where $f$ denotes frequency, $k$ is the wavenumber and $\lambda$ is the wavelength) for waves in the domains and in the domain walls are combined with the analytical and micromagnetic simulation results. We first consider the planar waves propagating through the domains. The theoretical result is found to depend sensitively on the CoFeB in-plane uniaxial anisotropy $K_u$(CoFeB) and the interlayer exchange coupling $J$. For $J=-0.1\,\mathrm{mJ\,m^{-2}}$ and $K_u(\mathrm{CoFeB})=3\,\mathrm{kJ\,m^{-3}}$, we find good agreement with the experimental data. The elevated value of $K_u$(CoFeB) is reasonable, because

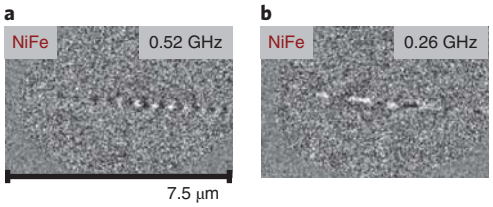


**Fig. 4 | Spin waves in the domain wall. a**,**b**, Spin waves confined to the domain wall (TR-STXM of the NiFe layer magnetization out-of-plane component) excited at 0.52 and 0.26 GHz, respectively, with accordingly changing wavelengths.

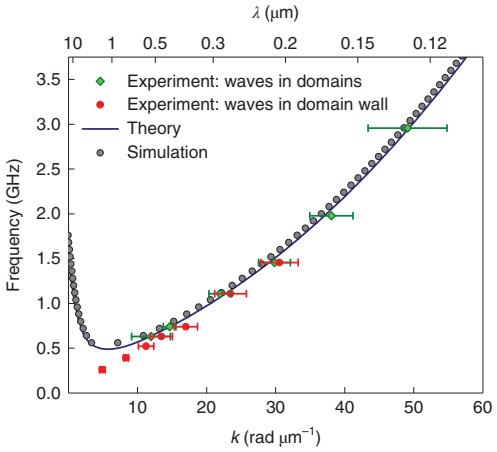


**Fig. 5 | Spin wave dispersion relations.** From the experiment, we obtain the dispersion relations for spin waves propagating in the domains (full green diamonds) and waves confined to the domain wall (red dots) with wavevectors $k = 2\pi/\lambda$. The error bars correspond to the uncertainty in the wavelength determination. In addition, we show the plane wave dispersions calculated using our model (blue continuous line) and micromagnetic simulations (grey dots), which are in good agreement.

we expect the CoFeB to react sensitively to strain exerted by the patterned waveguide microstructure onto the elliptical element[46]. Using the same parameters as in the theory, we also computed the dispersion using micromagnetic simulations (grey dots in Fig. 5), which were found to quantitatively reproduce the results from both the experiment and analytic calculations. Note that the antiparallel bilayer system considered here can in principle host two separate spin wave modes of acoustic and optical character (Supplementary Section 2). However, because the optical mode resides at much higher frequencies and is not accessed by our experiments, we only consider the acoustic mode in the following.

A striking feature of the acoustic plane wave dispersion is the existence of a local minimum at low $k$ around 5 rad μm$^{-1}$ and, accordingly, a frequency gap, below which no spin wave excitations are possible. The local minimum at some finite value of the wavevector in Fig. 5 results from a combination of the non-reciprocity induced by the dipolar coupling between the two antiferromagnetically coupled magnetic layers[34,47] (Supplementary Section 2) and the uniaxial magnetic anisotropy. Namely, when the anisotropy is zero, the collective dispersion in Damon–Eshbach geometry ($\mathbf{k}\perp\mathbf{M}_0$)[48] has a minimum of zero frequency at $k = 0$, while at finite anisotropies this minimum is shifted to finite values of both wavevector and frequency. Such $k$-shifting of the dispersion minimum is somewhat analogous to that induced by the Dzyaloshinskii–Moriya interaction, for example for ferromagnetic–heavy metal interfaces, where the minimum of the dispersion is also shifted[49]. Note that we only observe the slow branch ($k \geq +5$ rad μm$^{-1}$) of the non-reciprocal dispersion relation in our experiment because the wavelengths of the fast branch waves for the given frequencies are of the order of the sample size or even exceed it (cf. Supplementary Section 2). At the same time the spin wave amplitudes predicted for the fast branch are much lower. Hence, spin wave edge reflections are not noticeable in the experiment.

## 1D spin waves along domain walls

Our experimental observations of selective excitation and propagation of spin waves in the domain wall can be explained based on the existence of the frequency gap discussed above. The red circles in Fig. 5 display the dispersion relation of the measured spin waves in the domain wall. In contrast to the planar waves in the domains, the waves confined to the wall exhibit an almost linear dispersion, which runs below its plane wave counterpart and, when extrapolated towards zero, intercepts the $y$ axis close to $f = 0$. Thus, when tuning the excitation frequency to values inside the gap, no propagating magnons are excited in the domains, and only the energetically lower modes existing in the wall are populated. The existence or absence of a gap in the domain and domain wall, respectively, are explained by the Goldstone theorem[50], which states that a system exhibiting a continuous symmetry spontaneously broken by the ground state has a gapless mode. In the case of spin waves in the domains, the corresponding system comprises the two coupled disks. Here, the continuous symmetry is compromised by the uniaxial anisotropy and, accordingly, the planar spin wave dispersion relation exhibits a gap. In the case of the waves confined to the domain wall, there exists a continuous translational symmetry that gives rise to a gapless mode. The presence of defects and the finite size of the sample, in principle, break this symmetry, but the resulting gap is too small to be observed in the experiment.

The idea of using domain walls as waveguides is intriguing, and Fig. 6 shows that the above described phenomenon indeed extends to cases where the walls are curved, that is, lead 'around the corner'. Neither is the concept restricted to continuous wave excitation. Figure 6a displays the static magnetization configuration (out-of-plane contrast) of a domain wall of the same type as above, but curved towards the right-hand rim of the magnetic element. Figure 6b–d displays snapshots of the excitation following a field pulse. Due to the width of the spectral composition of the pulse, spin waves are excited inside and above the frequency gap. The resulting plane wavepacket traverses the domains in the direction away from the wall and makes it easy to optically distinguish the domain wall wave from the remainder of the excitations. At 11.1 ns after the pulse, the wall wavepacket has reached the region in front of the turn (Fig. 6c); 2.5 ns later the wavepacket has travelled around the corner. Remarkably, even after the turn, the wavepacket maintains a detectable amplitude. While the spatial distribution of the domain wall in our experiment is solely a consequence of both dipolar sample confinement fields and magnetostrictive anisotropies, it was shown that further control of the domain wall position can be achieved, for example by exchange bias patterning[20,24], ferroelectric coupling[13,32] or external magnetic fields[19].

## Conclusions

We have addressed several key aspects of magnonic computing by exploiting magnetic anisotropy. The first aspect is related to energy and the signal range. We have demonstrated that textures in a magnetization distribution, like domain walls and vortex cores, can serve as sources for the generation of short-wavelength, dipole-exchange spin waves of a directional nature, that is, planar waves in magnetic domains and waves confined to domain walls. These are, due to their geometry, not subject to a reduction of amplitude

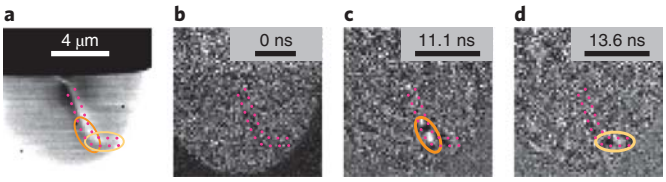


**Fig. 6 | Domain walls as waveguides.** We demonstrate the possibility of harnessing domain walls as waveguides for magnonic excitations by sending a spin wavepacket around a domain wall curving around a corner (TR-STXM images). **a**, An out-of-plane magnetic contrast image of the domain wall, with the position of the wall outlined by the red dotted line. Orange and yellow ellipses mark two regions in front and behind the curve, respectively. **b**–**d**, Snapshots of a spin wavepacket excited by a magnetic field pulse, at different times after the pulse. At 11.1 ns after the pulse (**c**), the wavepacket has reached the region in front of the curve. At 13.6 ns (**d**), the wavepacket has travelled around the corner.

due to the geometric dilution of the energy flow. Such waves minimize the losses occurring during propagation. Indeed, we found that the resulting excitations can travel distances easily spanning several micrometres, that is, significantly exceeding multiples of the nanoscale wavelengths—a necessary condition, for example, for magnon interference-based applications. The second aspect is to identify possible waveguides for magnonic chips. Here, we have shown that domain walls can serve as such waveguides, combining several useful properties. First, due to their inherent symmetry, and consequently their near-gapless dispersion relation, spin waves can be excited selectively in these structures. In addition, we have shown that spin wavepackets can travel along angled domain walls while largely maintaining their amplitude. Such a possibility of angled signal guidance is vital for chip design, and therefore our result may enable new solutions to the development of magnonic circuits.

## Online content

Any methods, additional references, Nature Research reporting summaries, source data, statements of data availability and associated accession codes are available at https://doi.org/10.1038/s41565-019-0383-4.

Received: 2 August 2018; Accepted: 21 January 2019;
Published online: 25 February 2019

## References

1. Bloch, F. Zur theorie des ferromagnetismus. *Z. Phys.* **61**, 206–209 (1930).
2. Kruglyak, V. V., Demokritov, S. O. & Grundler, D. Magnonics. *J. Phys. D* **43**, 264001 (2010).
3. Chumak, A. V., Serga, A. A. & Hillebrands, B. Magnon transistor for all-magnon data processing. *Nat. Commun.* **5**, 4700 (2014).
4. Chumak, A. V., Vasyuchka, V. I., Serga, A. A. & Hillebrands, B. Magnon spintronics. *Nat. Phys.* **11**, 453–461 (2015).
5. Lan, J., Yu, W., Wu, R. & Xiao, J. Spin-wave diode. *Phys. Rev. X* **5**, 041049 (2015).
6. Gurevich, A. G. & Melkov, G. A. *Magnetization Oscillations and Waves* (CRC, New York, 1996).
7. Oliner, A. A. *Acoustic Surface Waves* (Springer, Berlin, 1978).
8. Morgan, D. R. Surface acoustic wave devices and applications: 1. Introductory review. *Ultrasonics* **11**, 121–131 (1973).
9. Lee, K.-S., Choi, S. & Kim, S.-K. Radiation of spin waves from magnetic vortex cores by their dynamic motion and annihilation processes. *Appl. Phys. Lett.* **87**, 192502 (2005).
10. Demokritov, S. O. et al. Bose–Einstein condensation of quasi-equilibirum magnons at room temperature under pumping. *Nature* **443**, 430–433 (2006).
11. Davies, C. S., Poimanov, V. D. & Kruglyak, V. V. Mapping the magnonic landscape in patterned magnetic structures. *Phys. Rev.* **96**, 094439 (2017).
12. Mozooni, B. & McCord, J. Direct observation of closure domain wall mediated spin waves. *Appl. Phys. Lett.* **107**, 042402 (2015).
13. Wiele, B. V., Hämäläinen, S. J., Baláz, P., Montoncello, F. & Dijken, S. V. Tunable short-wavelength spin wave excitation from pinned magnetic domain walls. *Sci. Rep.* **6**, 21330 (2016).
14. Whitehead, N. J., Horsley, S. A. R., Philbin, T. G., Kuchko, A. N. & Kruglyak, V. V. Theory of linear spin wave emission from a Bloch domain wall. *Phys. Rev. B* **96**, 064415 (2017).
15. Hermsdoerfer, S. J. et al. A spin-wave frequency doubler by domain wall oscillation. *Appl. Phys. Lett.* **94**, 223510 (2009).
16. Holländer, R. B., Müller, C., Schmalz, J., Gerken, M. & McCord, J. Magnetic domain walls as broadband spin wave and elastic magnetisation wave emitters. *Sci. Rep.* **8**, 13871 (2018).
17. Sluka, V *et al.*in Stacked topological spin textures as emitters for multidimensional spin wave modes. *IEEE International Magnetics Conference (INTERMAG)* https://doi.org/10.1109/INTMAG.2015.7157029 (IEEE, 2015).
18. Garcia-Sanchez, F. et al. Narrow magnonic waveguides based on domain walls. *Phys. Rev. Lett.* **114**, 247206 (2015).
19. Wagner, K. et al. Magnetic domain walls as reconfigurable spin-wave nanochannels. *Nat. Nanotechnol.* **11**, 432–436 (2016).
20. Albisetti, E. et al. Nanoscale spin-wave circuits based on engineered reconfigurable spin-textures. *Commun. Phys.* **1**, 56 (2018).
21. Aliev, F. G. et al. Localized domain-wall excitations in patterned magnetic dots probed by broadband ferromagnetic resonance. *Phys. Rev. B* **84**, 144406 (2011).
22. Vogt, K. et al. Realization of a spin-wave multiplexer. *Nat. Commun.* **5**, 3727 (2014).
23. Gruszecki, P., Kasprzak, M., Serebryannikov, A. E., Krawczyk, M. & Smigaj, W. Microwave excitation of spin wave beams in thin ferromagnetic films. *Sci. Rep.* **6**, 22367 (2016).
24. Albisetti, E. et al. Nanopatterning reconfigurable magnetic landscapes via thermally assisted scanning probe lithography. *Nat. Nanotechnol.* **11**, 545–551 (2016).
25. Haldar, A., Kumar, D. & Adeyeye, A. O. A reconfigurable waveguide for energy-efficient transmission and local manipulation of information in a nanomagnetic device. *Nat. Nanotechnol.* **11**, 437–443 (2016).
26. Demidov, V. E., Urazhdin, S. & Demokritov, S. O. Direct observation and mapping of spin waves emitted by spin–torque nano-oscillators. *Nat. Mater.* **9**, 984–988 (2010).
27. Madami, M. et al. Direct observation of a propagating spin wave induced by spin-transfer torque. *Nat. Nanotechnol.* **6**, 635–638 (2011).
28. Urazhdin, S. et al. Nanomagnetic devices based on the spin–transfer torque. *Nat. Nanotechnol.* **9**, 509–513 (2014).
29. Bonetti, S. et al. Direct observation and imaging of a spin-wave soliton with p-like symmetry. *Nat. Commun.* **6**, 8889 (2015).
30. Yu, H. et al. Omnidirectional spin-wave nanograting coupler. *Nat. Commun.* **4**, 2702 (2013).
31. Yu, H. et al. Approaching soft X-ray wavelengths in nanomagnet-based microwave technology. *Nat. Commun.* **7**, 11255 (2016).
32. Hämäläinen, S. J., Brandl, F., Franke, K. J. A., Grundler, D. & van Dijken, S. Tunable short-wavelength spin-wave emission and confinement in anisotropy-modulated multiferroic heterostructures. *Phys. Rev. Appl.* **8**, 014020 (2017).
33. Voto, M., Lopez-Diaz, L. & Martinez, E. Pinned domain wall oscillator as tunable direct current spin wave emitter. *Sci. Rep.* **7**, 13559 (2017).
34. Wintz, S. et al. Magnetic vortex cores as tunable spin wave emitters. *Nat. Nanotechnol.* **11**, 948–953 (2016).
35. Dieterle, G. et al. Coherent excitation of heterosymmetric spin waves with ultrashort wavelengths. Preprint at https://arxiv.org/abs/1712.00681 (2017).
36. Shinjo, T., Okuno, T., Hassdorf, R., Shigeto, K. & Ono, T. Magnetic vortex core observation in circular dots of permalloy. *Science* **289**, 930–932 (2000).
37. Thiele, A. A. Steady-state of motion of magnetic domains. *Phys. Rev. Lett.* **30**, 230 (1973).
38. Choe, S.-B. et al. Vortex core-driven magnetization dynamics. *Science* **304**, 420–422 (2004).
39. Xing, X. & Zhou, Y. Fiber optics for spin waves. *NPG Asia Mater.* **8**, e246 (2016).
40. Winter, J. M. Bloch wall excitation. Application to nuclear resonance in a Bloch wall. *Phys. Rev.* **124**, 452 (1961).
41. Stoll, H. et al. High-resolution imaging of fast magnetization dynamics in magnetic nanostructures. *Appl. Phys. Lett.* **84**, 3328 (2004).
42. Grünberg, P., Schreiber, R., Pang, Y., Brodsky, M. B. & Sowers, H. Layered magnetic structures: evidence for antiferromagnetic coupling of Fe layers across Cr interlayers. *Phys. Rev. Lett.* **57**, 2442 (1986).
43. Labrune, M. & Miltat, J. Wall structures in ferro/antiferromagnetic exchange-coupled bilayers: a numerical micromagnetic approach. *J. Magn. Magn. Mater.* **151**, 231–245 (1995).
44. Groß, F. et al. Nanoscale detection of spin wave deflection angles in permalloy. *Appl. Phys. Lett.* **114**, 012406 (2019).
45. Stamps, R. L., Carriço, A. S. & Wigen, P. E. Domain-wall resonance in exchange-coupled magnetic films. *Phys. Rev. B* **55**, 6473–6484 (1997).
46. Wang, D., Nordman, C., Qian, Z., Daughton, J. M. & Myers, J. Magnetostriction effect of amorphous CoFeB thin films and application in spin-dependent tunnel junctions. *J. Appl. Phys.* **97**, 10C906 (2005).

47. Grünberg, P. Magnetostatic spinwave modes of a heterogeneous ferromagnetic double layer. *J. Appl. Phys.* **52**, 6824–6829 (1981).
48. Damon, R. W. & Eshbach, J. R. Magnetostatic modes of a ferromagnetic slab. *J. Phys. Chem. Solids.* **19**, 308–320 (1961).
49. Cho, J. et al. Thickness dependence of the interfacial Dzyaloshinskii–Moriya interaction in inversion symmetry broken systems. *Nat. Commun.* **6**, 7635 (2015).
50. Goldstone, J., Salam, A. & Weinberg, S. Broken symmetries. *Phys. Rev.* **127**, 965–970 (1962).

## Acknowledgements

The authors thank B. Sarafimov, B. Watts and M. Bechtel for experimental support at the STXM beamlines, as well as C. Fowley, K. Kirsch, B. Scheumann and C. Neisser for their help with sample fabrication. Most of the experiments were performed at the Maxymus endstation at BESSY2, HZB, Berlin, Germany. The authors thank HZB for the allocation of synchrotron radiation beamtime. Some experiments were performed at the PolLux endstation at SLS, PSI, Villigen, Switzerland. Pollux is financed by BMBF via contracts 05KS4WE1/6 and 05KS7WE1. Support by the Nanofabrication Facilities Rossendorf at IBC, HZDR, Dresden, Germany is gratefully acknowledged. V.S. and A.D. acknowledge funding from the Helmholtz Young Investigator Initiative under grant VH-N6-1048. R.A.G. acknowledges financial support from FONDECYT Iniciacion 11170736 and 1161403. A.R.M. acknowledges funding from FONDECYT 3170647; funding from the Basal Program for Centers of Excellence, grant FB0807 CEDENNA, CONICYT is also acknowledged. V.T. and A.S. acknowledge support from the US National Science Foundation under grants EFMA-1641989 and ECCS-1708982 and from the DARPA M3IC grant under contract no. W911-17-C-0031. S.W. acknowledges funding from the European Community's Seventh Framework Programme (FP7/2007-2013) under grant agreement no. 290605 (PSI-FELLOW/COFUND).

## Author contributions

S.W. conceived the experiment. V.S., M.W. and S.W. performed the STXM measurements. V.S. and S.W. analysed the data. T.S., T.W., A.K. and S.W. conducted the micromagnetic simulations. R.A.G., A.R.M. and P.L. calculated the spin wave dispersion relation. R.M. and S.W. supervised sample preparation. V.S. and S.W. wrote the manuscript. All authors discussed the results and commented on the manuscript.

## Competing interests

The authors declare no competing interests.

## Additional information

**Supplementary information** is available for this paper at https://doi.org/10.1038/s41565-019-0383-4.

**Reprints and permissions information** is available at www.nature.com/reprints.

**Correspondence and requests for materials** should be addressed to V.S. or S.W.

**Journal peer review information** *Nature Nanotechnology* thanks Ferran Macià, Takuya Satoh and other anonymous reviewer(s) for their contribution to the peer review of this work.

## Methods

**Sample fabrication.** $Ni_{81}Fe_{19}$/Ru/$Co_{40}Fe_{40}B_{20}$/Al multilayers were deposited by magnetron sputtering on X-ray transparent silicon nitride membrane substrates of 200 nm thickness. The 5-nm-thick Al layer is used as capping for oxidation protection. From transmission electron microscopy (TEM) measurements, the NiFe and CoFeB thicknesses were determined to be 44.9 and 46.6 nm, respectively. The two ferromagnetic layers are subject to antiferromagnetic interlayer exchange coupling, mediated by the Ru layer (0.8 nm nominal thickness)[42], as indicated by hard axis magnetization reversal measured by the magneto-optical Kerr effect (MOKE) on extended multilayer films[51]. MOKE measurements performed on corresponding single-layer films of NiFe and CoFeB showed that these films exhibit colinear uniaxial anisotropies. The respective values for NiFe and CoFeB are 0.2 kJ m$^{-3}$ and 1.1 kJ m$^{-3}$. However, a significantly higher uniaxial anisotropy value for CoFeB of about 3 kJ m$^{-3}$ is needed in order to reproduce the experimentally found static magnetization distribution by micromagnetic simulations.

This elevated value for the in-plane uniaxial anisotropy in CoFeB can be attributed to strain, which in our case is caused by the contact with the waveguide. In fact, CoFeB is known for its sensitivity to strain, and the orientation of the experimentally observed magnetic pattern with respect to the waveguide is consistent with this interpretation[46]. The microelements were patterned by electron beam lithography (EBL) and consecutive ion beam etching. Following an initial oxygen plasma treatment for adhesive purposes, a negative resist (MA-N 2910) was spun onto the multilayer films. In a second step, the microelements were exposed by EBL. The samples were then developed for 300 s in MA-D 525 and rinsed in deionized water. Finally, the samples were exposed to an argon ion beam at two different angles (85° and 5°) to physically etch the magnetic microelements out of the continuous films. The remaining resist was removed by acetone and a second oxygen plasma treatment. For magnetic field excitation, a copper strip of 200 nm thickness was fabricated on top of the microelements by EBL, electron beam evaporation deposition and liftoff processing[34], resulting in a patterned microstrip 5 µm in width. The estimated Oersted field arising from a 1 mA electric current flowing through such a strip is about $\mu_0 H = 4\pi \times 10^{-2}$ mT.

**Time-resolved STXM.** Synchrotron STXM[52] was used to image the magnetic orientation in the multilayer microelements. Here, a monochromatic X-ray beam is focused onto the sample by means of a diffractive zone plate. The locally transmitted X-ray intensity is measured by a single-pixel detector, so raster scanning the sample provides a 2D absorption image of the sample with approximately 25 nm lateral resolution. Using circularly polarized X-rays allows XMCD[53] to be exploited, thus obtaining a magnetic contrast. As XMCD only occurs relevantly at the element-specific resonant absorption edges, the magnetic signal from both ferromagnetic layers, NiFe and CoFeB, can be separated by using X-rays of the corresponding $L_3$ energies, Ni $L_3$ ~853 eV and Co $L_3$ ~778 eV, respectively. On the other hand, a collective signal from both layers can be collected from the Fe $L_3$ edge at ~708 eV because both layers contain Fe. The acquired magnetic contrast scales with the projection of the magnetic orientation $\mathbf{m} = \mathbf{M}/M$ on the direction of photon propagation. Hence, in normal incidence, our STXM set-up is sensitive to the perpendicular magnetization component, while an inclined sample mounting also allows for detecting in-plane magnetization components at the same time.

Time-resolved STXM was used to stroboscopically image the magnetization dynamics of the multilayer microelements. This method utilizes the specific time structure of the incident X-rays, which comprises pulses with a 2 ns repetition rate and ~100 ps effective pulse length. Each incoming probe event (photon transmitted or not transmitted) is routed after every pulse to a periodic counting register of a field programmable gate array. Here, the number of registers ($Q$) sets the maximum non-stroboscopic observation period ($Q \times 2$ ns), while the number of excitation repetitions within this period sets the nominal time resolution as well as the excitation frequency in the case of a continuous sinusoidal excitation. The excitation current was monitored via −20 dB pick-off tees, both in front and behind the sample's signal line.

**Theoretical model.** We developed a theory for the calculation of spin wave dispersion relations in two extended interlayer exchange-coupled ferromagnetic layers.

The core of the theory is described in detail in the Supplementary Information. It considers spin wave modes in thin magnetic films, where the magnetization along the coordinate perpendicular to the film plane can be considered homogeneous. The case of thicker films, as in the experiment, is accounted for by splitting each ferromagnetic layer into a number $N$ of thin films of equal thickness, so that for each of these films the thin film approximation holds. The $N$ thin films of each layer are then coupled to each other by an effective ferromagnetic intralayer exchange coupling, whose strength is determined by estimating the energy of a magnetization distribution subject to homogeneous torsion and by requiring consistency with the continuum limit. The theory thus enables us to quickly compute dispersion relations for spin waves in the interlayer exchange-coupled bilayer system with ferromagnetic layers whose thicknesses exceed the exchange lengths of the respective material.

**Micromagnetic simulations.** Time integration of the Landau–Lifshitz–Gilbert[54,55] equation was carried out using the MuMax$^3$ code[56] for a spatially discretized, interacting lattice. The simulations were performed to compute the spin wave dispersion relations in the coupled layer system. The ferromagnetic layers are homogeneously magnetized and the dispersion relations are calculated in a thin film approach. Therefore, the system was discretized into (4096, 16, 115) ($x$,$y$,$z$) cells and periodic boundary conditions were applied along the $y$ direction, which corresponds to the direction of equilibrium magnetization. The thickness of the individual layers and the spacer were chosen according to TEM measurements. This resulted in a cell size along the $z$ axis of 0.8 nm. The material parameters used in the micromagnetic simulations are as follows. For NiFe, the respective values of saturation magnetization, exchange stiffness and uniaxial in-plane anisotropy are $M_s^{Py} = 800$ kA m$^{-1}$, $A_{xc}^{Py} = 7.5$ pJ m$^{-1}$ (ref. [57]) and $K_u^{Py} = 200$ J m$^{-3}$. For the CoFeB layer, we used $M_s^{CoFeB} = 1{,}250$ kA m$^{-1}$, $A_{xc}^{CoFeB} = 12$ pJ m$^{-1}$ (ref. [58]) and $K_u^{CoFeB} = 3{,}000$ J m$^{-3}$. The interlayer exchange coupling is $J = -0.1$ mJ m$^{-2}$. The Gilbert damping constants $\alpha$ for CoFeB and NiFe were chosen to be 0.008 and 0.01, respectively. To prevent reflection of spin waves from the edges, the damping was increased linearly to 0.065 for both layers.

An out-of-plane sinusoidal excitation field with a fixed frequency was applied in a 100-nm-wide region in the centre of the system. After the system reached dynamic equilibrium, the magnetization configuration was stored. To extract the wave number for each frequency a spatial fast-Fourier transform along the $x$ direction of the system was performed. The corresponding dispersion relations are shown in Fig. 5 as grey full dots and are in good agreement with the results from the model calculations. Additional simulations were performed to compare the effects of oscillatory magnetic fields applied in-plane and out-of-plane, in each case perpendicular to the magnetization. The simulations clearly show that the bilayer system is more susceptible to out-of-plane field perturbations. This result can be understood taking into account the fact that the excited collective mode exhibits an in-phase oscillation of the perpendicular, yet anti-phase oscillation of the in-plane magnetization component (acoustic mode), and thus couples more efficiently to driving fields oriented perpendicular to the sample plane. There exists another type of collective mode in the system (optical mode), which exhibits an in-phase oscillation of the in-plane component; however, this mode resides at higher frequency values than the measured ones.

Due to the absence of domain walls, the thin film approach above cannot reproduce the observed 1D spin-wave dispersion within the walls and the emission of planar waves from them. To gain insight into these phenomena an elliptical bilayer with short and long axes of 2.16 µm and 3.24 µm, respectively, was simulated at a discretization of 648 × 432 × 115 cells. The material parameters were chosen to be the same as for the thin film approach, but for the slightly modified constants $A_{xc}^{Py} = 10.5$ pJ m$^{-1}$, $A_{xc}^{CoFeB} = 13$ pJ m$^{-1}$, $K_u^{CoFeB} = 5$ kJ m$^{-3}$ and $J = -0.3$ mJ m$^{-2}$. To simulate the excitation of spin wave dynamics a spatially homogeneous sinc($t$) pulse with a cutoff frequency of 10 GHz was utilized. To obtain the dynamic response the magnetization data was Fourier-transformed and filtered afterwards to extract the desired frequency.

## Data availability

The data that support the plots within this paper and other findings of this study are available from the corresponding authors upon reasonable request.

## References

51. Wintz, S. et al. Control of vortex pair states by post-deposition interlayer exchange coupling modification. *Phys. Rev. B* **85**, 134417 (2012).
52. Raabe, J. et al. PolLux: a new facility for soft X-ray spectromicroscopy at the Swiss Light Source. *Rev. Sci. Instrum.* **79**, 113704 (2008).
53. Schütz, G. et al. Absorption of circularly polarized X rays in iron. *Phys. Rev. Lett.* **58**, 737–740 (1987).
54. Landau, L. & Lifshits, E. On the theory of the dispersion of magnetic permeability in ferromgnetic bodies. *Phys. Z. Sow.* **8**, 135 (1935).
55. Gilbert, T. L. A Lagrangian formulation of the gyromagnetic equation of the magnetization field. *Phys. Rev.* **100**, 1243 (1955).
56. Vansteenkiste, A. et al. The design and verification of MuMax3. *AIP Adv.* **4**, 107133 (2014).
57. Wei, J. et al. Annealing influence on the exchange stiffness constant of permalloy films with stripe domains. *J. Phys. D* **49**, 265002 (2016).
58. Conca, A. et al. Annealing influence on the Gilbert damping parameter and the exchange constant of CoFeB films. *Appl. Phys. Lett.* **104**, 182407 (2014).

# Statistics

Image: HZDR / R. Podlipec, G. Hlawacek

# User facilities and services

## Ion Beam Center (IBC)

The Ion Beam Center (IBC) at HZDR combines various machines (electrostatic accelerators, ion implanters, low-energy and focused ion beam systems) into a unique facility used for ion beam modification and ion beam analysis of materials. The available energy range spans from a few eV to 60 MeV with a respective interaction depth in solids between 0.1 nm to 10 µm. In addition to standard broad beams also focused (down to 1 nm) and highly-charged (charge state up to 45+) ion beams are available. In combination with an allocated ion beam experiment, users can also profit from structural analysis (electron microscopy and spectroscopy, X-ray scattering techniques) and sample or device processing under clean-room conditions. At the 6 MV tandem accelerator, the IBC operates the DREAMS (DREsden AMS = accelerator mass spectrometry) facility, which is used for the determination of long-lived radionuclides, like $^{7,10}$Be, $^{26}$Al, $^{35}$Cl, $^{41}$Ca, $^{129}$I, and others. A schematic overview of the IBC including the description of the main beam lines and experimental stations is given on page 75 of this Annual Report. In 2019, about 17.000 beam time hours were delivered for about 340 users from 23 countries worldwide performing experiments at IBC or using the capabilities for ion beam services.

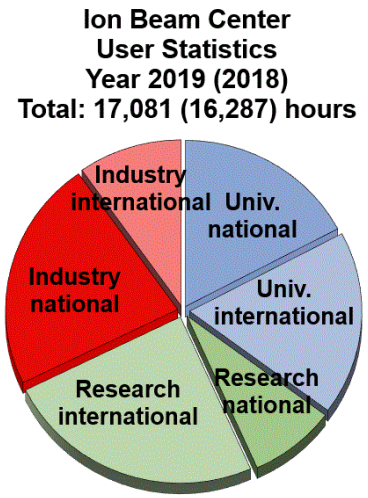


The IBC has provided ion beam technology as a user and competence center for ion beam applications for more than 30 years. With respect to user beam time hours, the IBC is internationally leading and has been supported by numerous national and European grants and by industry.

The research activities cover both ion beam modification and ion beam analysis (IBA).

The operation of IBC is accompanied by a strong in-house research at the affiliated host “Institute of Ion Beam Physics and Materials Research”, both in experiment and theory. Furthermore, the IBC strongly supports the commercial exploitation of ion beam technology of partners from industry, which is essential for materials science applications. For ion beam services, the HZDR Innovation GmbH (spin-off of the HZDR) – www.hzdr-innovation.de – provides a direct and fast access to the IBC facilities based on individual contracts.

Recently, new ion beam tools and end-stations have been commissioned which will attract new users by state-of-the-art experimental instrumentation. The basically upgraded ion microprobe station at the 3 MV machine is now in routine and user-friendly operation mode, delivering the possibility to use – in parallel or sequentially – several IBA techniques with a spatial resolution of about 3 µm. An ion microscope *ORION NanoFab* (He/Ne ions, 10 – 40 keV) provides unique possibilities for surface

imaging, nano-fabrication, and for the first time, elemental analysis based on ion beam techniques. The cluster tool at the 6 MV accelerator allows *in-situ* deposition and analysis investigations at temperatures of up to 800 °C. Recently, first instruments for the new low-energy ions nano-engineering laboratory have been commissioned, including the installation of a 100 kV accelerator, a medium-energy ion scattering (MEIS) setup, and a new low-energy electron microscope (LEEM) aiming to study low-energy ion interactions at surfaces.

IBC activities are efficiently integrated into various Helmholtz programmes within the research field “Matter”, but also in the Helmholtz cross-programme activities “Mineral Resources”, “Materials Research for Energy Technologies”, and “Helmholtz Energy Materials Foundry”. Since 2013, the IBC has been recognized as a large-scale facility within the “BMBF Verbundforschung” promoting long-term collaborations with universities. In addition, as of 2019 the IBC is coordinating the EU Integrated Infrastructure Initiative (I3) project RADIATE, which provides trans-national access to the largest ion beam centers in Europe (www.ionbeamcenters.eu).

Following the rules of a European and national user facility, access for scientific experiments to IBC is provided on the basis of a proposal procedure (www.hzdr.de/IBC) via the common HZDR user facility portal **HZDR-GATE** (gate.hzdr.de), and for RADIATE via www.ionbeamcenters.eu. IBC users from EU countries are eligible to receive support through the RADIATE initiative. Due to the availability of multiple machines and versatile instrumentation, IBC proposals can be submitted continuously. The scientific quality of the proposals is evaluated and ranked by an external international User Selection Panel. For successfully evaluated proposals, users get free access to IBC facilities for their experiments. The use of the IBC facilities includes the scientific and technical support during planning, execution and evaluation of the experiments. For AMS samples preparation, two chemical laboratories are available.

For more detailed information, please contact Dr. Stefan Facsko (s.facsko@hzdr.de) or Dr. Johannes von Borany (j.v.borany@hzdr.de), and visit the IBC webpage: www.hzdr.de/IBC.

## Free Electron Laser FELBE

FELBE is an acronym for the free-electron laser (FEL) at the Electron Linear accelerator with high Brilliance and low Emittance (ELBE) located at the Helmholtz-Zentrum Dresden-Rossendorf. The heart of ELBE is a superconducting linear accelerator operating in continuous-wave (cw) mode with a pulse repetition rate of 13 MHz. The electron beam (40 MeV, 1 mA max.) is guided to several laboratories where secondary beams (particle and electromagnetic) are generated. Two free-electron lasers (U37-FEL and U100-FEL) produce intense, coherent electromagnetic radiation in the mid and far infrared, which is tunable over a wide wavelength range (5 –250 µm) by changing the electron energy or the undulator magnetic field. Main parameters of the infrared radiation produced by FELBE are as follows:

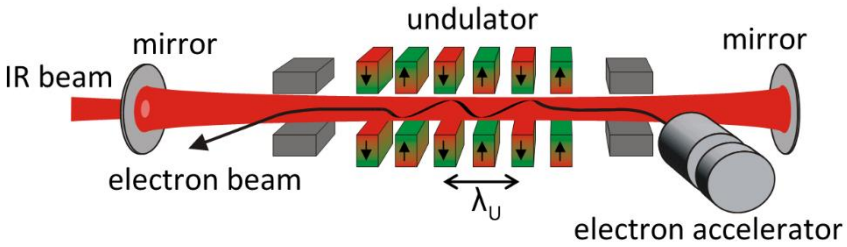


| | | |
|---|---|---|
| Wavelength λ | 5 – 40 µm<br>18 – 250 µm | FEL with undulator U37<br>FEL with undulator U100 |
| Pulse energy | 0.01 – 2 µJ | depends on wavelength |
| Pulse length | 1 – 25 ps | depends on wavelength |
| Repetition rate | 13 MHz | 3 modes: • cw<br>• macropulsed (> 100 µs, < 25 Hz)<br>• single pulsed (Hz … kHz) |

In addition, there is the THz beamline TELBE that is run by the Institute of Radiation Physics. TELBE delivers high-power pulses (up to 10 µJ) in the low THz range (0.1 to 1.5 THz) at a repetition rate of 100 kHz. ELBE is a user facility and applications for beam time can be submitted twice a year, typically by April 15 and October 15. FELBE and TELBE users from EU countries are eligible to receive support through the HORIZON 2020 Integrated Infrastructure Initiative (I3) CALIPSOplus (**C**onvenient **A**ccess to **Li**ght Sources O**p**en to Innovation, **S**cience and to the W**o**rld) which started in May 2017.

Typical applications are picosecond pump-probe spectroscopy (also in combination with several other femtosecond lasers, which are synchronized to the FEL), near-field microscopy, and nonlinear optics. The FELBE facility also serves as a far-infrared source for experiments at the Dresden High Magnetic Field Laboratory (HLD) involving pulsed magnetic fields up to 70 T.

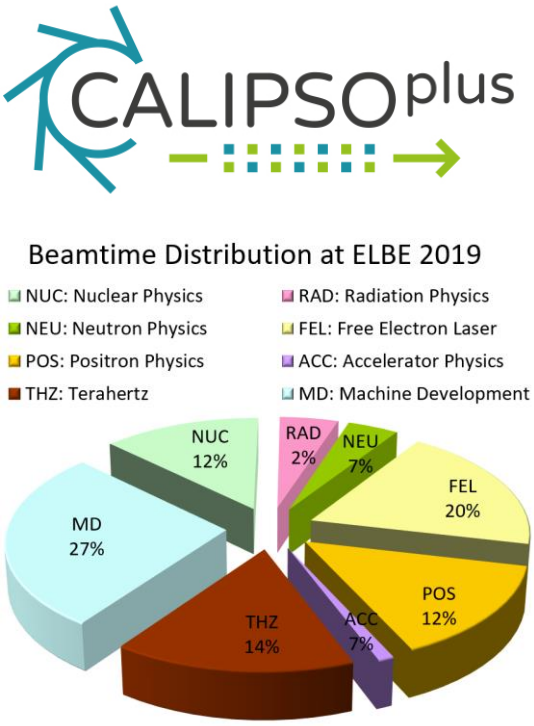


The statistics shows that the FEL used 1104 hours beam time of the ELBE accelerator. This corresponds to 20 % of total beam time, which is again distributed among internal and external users.

For further information, please contact Prof. Manfred Helm (m.helm@hzdr.de) or visit the FELBE webpage www.hzdr.de/FELBE.

# Experimental equipment

## Accelerators, ion implanters, and other ion processing tools

| | | |
|---|---|---|
| Van de Graaff Accelerator (VdG) | 2 MV | *TuR Dresden, DE* |
| Tandetron Accelerator (T1) | 3 MV | *HVEE, NL* |
| Tandetron Accelerator (T2) | 6 MV | *HVEE, NL* |
| Low-Energy Ion Implanter | 0.1 – 40 kV | *Danfysik, DK* |
| Low-Energy Ion Platform | 20 – 130 kV | *HVEE, NL* |
| High-Energy Ion Implanter | 20 – 500 kV | *HVEE, NL* |
| Mass-Separated Focused Ion Beam (FIB) (15 nm, variable ions) | 10 – 30 keV<br>>10 A/cm$^2$ | *Orsay Physics, FR* |
| ORION NanoFab FIB Tool (including GIS and Nanopatterning, RBS, SIMS) | He, Ne ions,<br>10 – 35 kV,<br>Resolution < 2 nm | *Carl Zeiss Microscopy, DE* |
| Highly-Charged Ion Facility | 25 eV – 6 keV × Q<br>Q = 1 … 40 (Xe) | *DREEBIT, DE;*<br>*PREVAC, PL* |
| Surface Modifications by Low-Energy Ion Irradiation | 200 – 1200 eV | *Home-built* |
| UHV Ion Irradiation (Ar, He, etc.) | 0 – 5 kV<br>Scan 10 × 10 mm$^2$ | *Cremer, DE; VG, USA* |

## Ion beam analysis (IBA)

A wide variety of advanced IBA techniques are available at the MV accelerators (see figure).

| | | | |
|---|---|---|---|
| RBS | Rutherford Backscattering Spectrometry | (A1), (A2), (5), (9), (11), (14) | *VdG, T1, T2, HIM* |
| RBS/C | RBS – Channeling | (A1) | *VdG* |
| Liquid-RBS | Liquid Rutherford Backscattering Spectrometry | (A2) | *VdG* |
| MEIS | Medium Energy Ion Scattering | MEIS | |
| ERDA | Elastic Recoil Detection Analysis | (2), (9) | *T2* |
| PIXE | Particle-Induced X-ray Emission | (A1), (A2), (5), (14) | *VdG, T1, T2* |
| PIGE | Particle-Induced gamma Emission | (5), (14) | *T1, T2* |
| NRA | Nuclear Reaction Analysis | (1), (14) | *T1, T2* |
| NMP | Nuclear Microprobe | (14) | *T1* |
| AMS | Accelerator Mass Spectrometry (focused to long-lived radionuclides: $^{7}$Be, $^{10}$Be, $^{26}$Al, $^{36}$Cl, $^{41}$Ca, $^{129}$I) | (B2) | *T2* |

Some stations are equipped with additional process facilities enabling *in-situ* IBA investigations during ion irradiation, sputtering, deposition, annealing, investigations at solid-liquid interfaces, etc.

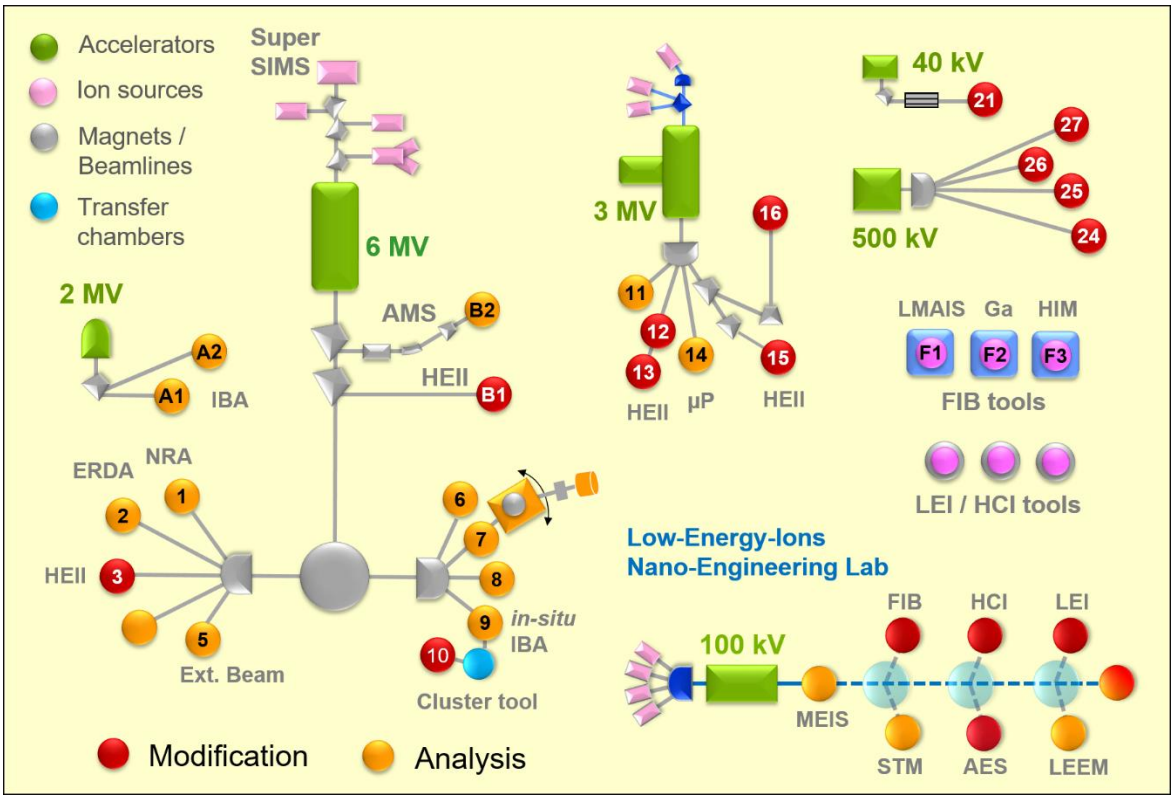


*Schematic overview of the HZDR Ion Beam Center*

## Other particle-based analytical techniques

| | | | |
|---|---|---|---|
| SEM | Scanning Electron Microscope (S4800 II) | 1 – 30 keV<br>+ EDX | *Hitachi, JP* |
| TEM | Transmission Electron Microscope<br>(Titan 80-300 with Image Corrector) | 80 – 300 keV<br>+ EDX, EELS | *FEI, NL* |
| TEM | Transmission Electron Microscope<br>(Talos F200X) | 20 – 200 keV<br>+ SuperX EDX | *FEI, NL* |
| FIB/SEM | Focused Ion/Electron Cross Beam<br>(NVision 40 with Elphy Plus Litho) | 0.5 – 30 keV<br>+ EDX, EBSD | *Carl Zeiss Microscopy, DE* |
| AES | Auger Electron Spectroscopy | + SAM, SEM, XPS, EDX, CL | *Scienta Omicron, DE* |
| LEEM | Low-Energy Electron Microscope<br>(Spec-LEEM-III) | 0 eV – 4.5 keV<br>Resolution < 6 nm<br>+ AES | *Elmitec, DE* |

## Photon-based analytical techniques

| | | | |
|---|---|---|---|
| XRD/XRR | X-Ray Diffractometers | Cu-Kα | |
| | θ-θ Powder D8<br>θ-2θ 4-Circle D5005<br>θ-θ 4-Circle Empyrean<br>θ-2θ 4+2-Circle SEIFERT XRD3003-HR | | *Bruker, DE*<br>*Siemens, DE*<br>*PANalytical, NL*<br>*General Electric, US* |
| SE | Angle Dependent Spectroscopic Ellipsometry | 250 – 1700 nm | *Woollam, US* |
| UV-Vis | Solid Spec 3700 DUV | 190 – 3300 nm | *Shimadzu, JP* |
| FTIR | Fourier-Transform Infrared Spectrometer | 50 – 15000 $cm^{-1}$ | *Bruker, DE* |
| | Ti:Sapphire Femtosecond Laser | 78 MHz | *Spectra Physics, US* |
| | Femtosecond Optical Parametric Osci. | | *APE, DE* |
| | Ti:Sapphire Femtosecond Amplifier | 1 kHz, 250 kHz | *Coherent, US* |
| | Femtosecond Optical Parametric Amplifier | | *Light Conversion, LT* |
| THz-TDS | Terahertz Time-Domain Spectroscopy | 0.1 – 4 THz | *Home-built* |
| Raman | Raman Spectroscopy | > 10 $cm^{-1}$ | *Jobin-Yvon-Horiba, FR* |
| | In-situ Raman Spectroscopy | > 100 $cm^{-1}$ | *Jobin-Yvon-Horiba, FR* |
| PL | Photoluminescence (10 – 300 K) | 405 – 1550 nm | *Jobin-Yvon-Horiba, FR* |
| | Micro-Photoluminescence | < 0.5 µm | *Jobin-Yvon-Horiba, FR* |
| TRPL | Time-Resolved Photoluminescence | $\tau$ = 3 ps – 2 ns<br>$\tau$ > 5 ns | *Hamamatsu Phot., JP*<br>*Stanford Research, US* |
| EL | Electroluminescence | 300 – 1600 nm | *Jobin-Yvon-Horiba, FR* |
| | Optical Split-Coil Supercond. Magnet | 7 T | *Oxford Instr., UK* |
| PR | Photomodulated Reflectivity | 300 – 1600 nm | *Jobin-Yvon-Horiba, FR* |
| PLE | Photoluminescence Excitation | 300 – 1600 nm | *Jobin-Yvon-Horiba, FR* |
| OES | Optical Emission Spectroscopy | 250 – 800 nm | *Jobin-Yvon-Horiba, FR* |
| Confocal | Confocal scanning photoluminescence microscope | ~1 µm resol.<br>5 – 300 K | *Attocube, DE* |
| SSPD | Superconducting single photon detectors | 800 – 1500 nm | *Single Quantum, NL* |

## Magnetic thin film deposition and analysis

| | | | |
|---|---|---|---|
| PLD | Pulsed Laser Deposition | | *SURFACE, DE* |
| MFM | Magnetic Force Microscope | ~ 50 nm resol. | *VEECO; DI, US* |
| AFM/MFM | Magnetic Force Microscope | ~ 50 nm resol. | *BRUKER ICON tool, US* |
| SQUID MPMS | Superconducting Quantum Interference Device | ± 7 T | *Quantum Design, US* |
| SQUID VSM | Vibrating Sample Magnetometer | ± 7 T | *Quantum Design, US* |
| Vector-VSM | Vibrating Sample Magnetometer | ± 2 T | *Quantum Design, US* |
| MOKE | Magneto-Optic Kerr Effect (in-plane) | ± 0.35 T | *Home-built* |
| MOKE | Magneto-Optic Kerr Effect (perpend.) | ± 2 T | *Home-built* |
| FR-MOKE | Frequency-Resolved Magneto-Optic KE | ± 1.1 T | *Home-built* |
| SKM | Scanning Kerr Microscope | | *Home-built* |
| | Kerr Microscope | | *Evico Magnetics, DE* |
| TR-MOKE | Time-Resolved MOKE (Pump-Probe) | | *Home-built* |
| VNA-FMR | Vector Network Analyzer Ferromagnetic Resonance | 50 GHz | *Agilent, DE; Home-built* |
| Cryo-FMR | Variable-Temperature Ferromagnetic Resonance | 3 – 300 K | *Attocube, DE; Home-built* |
| ME | Magnetoellipsometer | | *LOT, DE; AMAC, US* |
| µBLS | Brillouin Light Scattering Microscope | ± 0.8 T, 491 & 532 nm | *Home-built* |
| SKM | Scanning Kerr Microscope with RF Detection (Spectrum Analyzer) | ± 0.5 T, 40 GHz | *Home-built* |
| MT-50G | High Frequency Magneto-Transport Setup | ± 1.5 T, 50 GHz 250 ps | *Home-built* |

## Other analytical and measuring techniques

| | | | |
|---|---|---|---|
| STM/AFM | UHV Scanning Probe Microscope (variable T) | | *Omicron, DE* |
| AFM | Atomic Force Microscope (Contact, Tapping, Spreading) | | *Bruker, US* |
| AFM | Atomic Force Microscope (with c-AFM, SCM-Module) | | *Bruker, US* |
| | Dektak Surface Profilometer | | *Bruker, US* |
| | Micro Indenter/Scratch Tester | | *Shimatsu, JP* |
| MPMS | Mechanical Properties Measurement System – Stretcher | | *Home-built* |
| MS | Mass Spectrometers (EQP-300, HPR-30) | | *HIDEN, UK* |
| | Wear Tester (pin-on disc) | | *Home-built* |
| LP | Automated Langmuir Probe | | *Impedans, IE* |
| HMS | Hall Measurement System | 2 – 400 K, ≤ 9 T | *LakeShore, US* |
| | Van-der-Pauw HMS Ecopia | 300 K & LNT, 0.5 T | *Bridge Technol., US* |
| MTD | Magneto-Transport Device | 300 K, ≤ 3 T | *Home-built* |
| RS | Sheet-Rho-Scanner | | *AIT, KR* |
| RMAG | Redmag Tensormeter System | 240 – 350 K, 1.5 T | *Home-built* |
| GMAG | Greymag Tensormeter System | 300 K, 0.7 T | *Home-built* |
| IV / CV | I-V and C-V Analyzer | | *Keithley, US* |
| IV / CV | I-V and C-V Semi-Automatic Prober | -60 – 300 °C | *Süss, DE; Keithley, US* |
| IV | I-V Prober | 4.2 – 600 K | *LakeShore, Agilent, US* |
| GC | Gas Chromatography (GC-2010) | | *Shimadzu, JP* |
| ECW | Electrochemical workstation (CHI 760e) | | *CH instruments, US* |
| FDA | Force-displacement analysis machine | | *Sauter, DE* |
| IV / VNA | I-V and VNA Prober for VHF, LCR and frequency analysis measurements | 20-120 MHz | *Süss, DE; Cascade, US; Keysight, US* |
| OSCI | 4-channel real time oscilloscope | 1,5 GHz (BW), 5 GSa/s | *Keysight, US* |
| IR-Cam | TrueIR Thermal Imager | -20 – 350 °C | *Keysight, US* |
| CM | Confocal Microscope (Smartproof 5) | 405 nm LED, z drive res. ~ 1 nm | *Carl Zeiss, DE* |
| FAS | Fluidic Analytic Setup – microscope, high speed camera, and fluidic pumps | 2 GB 120 kfps, 5 modules | *Zeiss, DE; Photron, US; Cetoni, DE* |

## Deposition and processing techniques

| | | |
|---|---|---|
| Physical Deposition | Sputtering DC/RF, Evaporation | *Nordiko, UK* |
| | Electron Beam Evaporation System | *Leybold Optics, DE* |
| | Thermal Evaporation | *Bal-Tec, LI* |
| | DC/RF magnetron sputter system, 4x 3'' + 4x 2'' magnetrons, substrate heating: RT – 950 °C, up to 4" wafers | *BESTEC, DE* |
| | DC/RF magnetron sputter system, 6x 2'' confocal magnetrons, substrate heating: RT – 650 °C, up to 3" wafers | *AJA International, US* |
| | High Power Impulse Magnetron Sputtering | *Melec, DE* |
| Molecular Beam Epitaxy | III-V Semiconductors | *Riber, FR* |
| Chemical Vapour Deposition | Plasma Enhanced CVD: a-Si, a-Ge, $SiO_2$, SiON, $Si_3N_4$ | *Oxford Instr., UK* |
| Atomic Layer Deposition | $Al_2O_3$, $HfO_2$, $SiO_2$ | *Ultratech, US* |
| Dry Etching | ICP-RIE: $CF_4$, $SF_6$, $C_4F_8$ | *Sentech, DE* |
| | RIBE, ∅ 6": Ar, $CF_4$ | *Roth & Rau, DE* |
| | Barrel reactor, ∅ 4": $O_2$, $SF_6$ | *Diener electronic, DE* |
| Etching/Cleaning | incl. Anisotropic Selective KOH Etching | |
| Photolithography | Mask-Aligner MJB3, 2 µm accur.; ∅ 3" | *Süss, DE* |
| | Direct Laser Writer DWL 66FS, 2 µm accuracy, ∅ 8"x8" | *Heidelberg Instr., DE* |
| | Laser Micro Writer ML, 10 µm accuracy | *Durham Magneto Optics, UK* |
| Electron Beam Lithography | Raith 150-TWO: ∅ 6", 10 nm resol. | *Raith, DE* |
| | e-Line Plus: ∅ 4", 10 nm resol. | *Raith, DE* |
| Thermal Treatment | Room Temperature – 2000 °C | |
| Furnace | | *InnoTherm, DE* |
| Rapid Thermal Annealing JETFIRST 100 | | *JIPELEC, FR* |
| Rapid Thermal Annealing AW 610 | | *Allwin21, USA* |
| Flash-Lamp Units (0.5 – 20 ms) | | *Home-built;FHR/DTF, DE* |
| Combined Flash Lamp Sputter Tool (Magnetron sputtering plus flash lamp annealing 0.3 – 3 ms, up to 10 Hz) | | *ROVAK GmbH, DE* |
| RF Heating (Vacuum) | | *JIPELEC, FR* |
| Laser Annealing (CW, 808 nm, 450 W) | | *LIMO, DE* |
| Laser Annealing (30 ns pulse,10 Hz, 308 nm, 500 mJ) | | *COHERENT, USA* |
| CVD Tube furnace (RT– 1200 °C, three channel gas) | | *NBD, CN* |
| Vacuum oven (RT – 250 °C, Vacuum < 133 Pa) | | *LAB-KITS, CN* |
| Bonding Techniques | Ultrasonic Wire Bonding | *Kulicke & Soffa, US* |
| | Semi-automatic Wire-bonder: Gold-ball and wedge-wedge bonding Ultrasonic generator: 60 kHz, 140 kHz Wire deformation control software | *F & S Bondtec, AT* |
| Cutting, Grinding, Polishing | | *Bühler, DE* |
| TEM Sample Preparation | Plan View and Cross Section incl. Ion Milling Equipment | *Gatan, US* |
| Disperse and mixer | Mixer for pastes and emulsions | *IKA, DE* |
| Centrifuge | Max. 17850 rpm, -10 – 40 °C | *Thermo Scientific, US* |

# Doctoral training programme

## International Helmholtz Research School NANONET

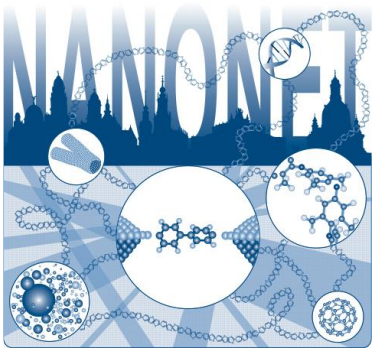


The Institute of Ion Beam Physics and Materials Research is coordinating the International Helmholtz Research School for Nanoelectronic Networks (IHRS NANONET) supported by the Initiative and Networking Fund of the Helmholtz Association. The project started in October 2012. The total funding is 1.2 Mio. € for a period of 8 years.

The IHRS NANONET is an international, interdisciplinary and thematically focused doctoral programme in the field of molecular electronics. The research school aims at attracting and promoting excellence by educating promising doctoral candidates with backgrounds in physics, chemistry, materials science and electrical engineering. During a period of three years, PhD candidates benefit from well-structured, comprehensive training curricula and multiple mentorship, while performing cutting edge research projects within one of the 15 NANONET research groups. The doctoral candidates have the unique opportunity to contribute to the advancement of molecular electronics by developing strategies for the integration of single nano-sized building blocks into large interconnected networks.

The IHRS NANONET fosters not only professional qualification but also personal development by equipping young graduates with competencies for successful careers in a wide variety of positions in academia and industry. The NANONET International Conference 2019 was held in Dresden downtown and was attended by 61 participants of 20 nationalities.

Three senior students concluded their PhD degrees in 2019: Congratulations to Dr. Julian Schütt, Dr. Dmitry Skidin and Dr. Panpan Zhang (all at TU Dresden).

**The consortium**

- Helmholtz-Zentrum Dresden-Rossendorf (HZDR)
- Technische Universität (TU) Dresden
- Leibniz Institute of Polymer Research (IPF) Dresden
- Fraunhofer Institute for Ceramic Technologies and Systems (IKTS) Dresden
- Nanoelectronic Materials Laboratory (NaMLab) gGmbH Dresden

For further information, please contact the NANONET coordinator, Dr. Peter Zahn (nanonet@hzdr.de), or visit the IHRS NANONET website: www.hzdr.de/nanonet.

# Publications and patents

## Books and Chapters

1. Hlawacek, G.
**Ion Microscopy**
in Hawkes,P.; Spence, J.C.H. (eds.): Springer Handbook of Microscopy, Heidelberg: Springer (2019), ISBN 978-3030000684, pp. 677-714

2. Rebohle, L.; Prucnal, S.; Reichel, D.
**Flash Lamp Annealing: From Basics to Applications**
Springer Series in Materials Science **288**, Cham: Springer (2019), ISBN 978-3030232986

3. Sluka, V.; Wintz, S.;
**Spin Textures as Sources for Magnons with Short Wavelengths and 3D Mode Profiles**
in Gubbiotti, G. (ed.): Three-Dimensional Magnonics, Singapur: Jenny Stanford Publishing (2019), ISBN 978-9814800730, pp. 219-259

## Publications in journals

1. Arora, H.; Jung, Y.; Venanzi, T.; Watanabe, K.; Taniguchi, T.; Schneider, H.; Hone, J.; Helm, M.; Erbe, A.; Hübner, R.
**Effective Hexagonal Boron Nitride Passivation of Few-Layered InSe and GaSe to Enhance Their Electronic and Optical Properties**
ACS Applied Materials and Interfaces **11**, 43480 (2019)

2. Balaghi, L.; Bussone, G.; Grifone, R.; Hübner, R.; Grenzer, J.; Ghorbani-Asl, M.; Krasheninnikov, A.; Schneider, H.; Helm, M.; Dimakis, E.
**Widely tunable GaAs bandgap via strain engineering in core/shell nanowires with large lattice mismatch**
Nature Communications **10**, 2793 (2019)

3. Ge, J.; Wang, X.; Drack, M.; Volkov, O.M.; Liang, M.; Cañón Bermúdez, G.S.; Illing, R.; Wang, C.; Zhou, S.; Fassbender, J.; Kaltenbrunner, M.; Makarov, D.
**A bimodal soft electronic skin for tactile and touchless interaction in real time**
Nature Communications **10**, 4405 (2019)

4. Joseph, T.; Ghorbani Asl, M.; Kvashnin, A.G.; Larionov, K.V.; Popov, Z.I.; Sorokin, P.B.; Krasheninnikov, A.
**Nonstoichiometric Phases of Two-Dimensional Transition-Metal Dichalcogenides: From Chalcogen Vacancies to Pure Metal Membranes**
Journal of Physical Chemistry Letters **10**, 6492 (2019)

5. Prucnal, S.; Heera, V.; Hübner, R.; Wang, M.; Mazur, G.P.; Grzybowski, M.J.; Qin, X.; Yuan, Y.; Voelskow, M.; Skorupa, W.; Rebohle, L.; Helm, M.; Sawicki, M.; Zhou, S.
**Superconductivity in single-crystalline aluminum- and gallium-hyperdoped germanium**
Physical Review Materials **3**, 054802 (2019)

6. Schultheiss, K.; Verba, R.; Wehrmann, F.; Wagner, K.; Körber, L.; Hula, T.; Hache, T.; Kákay, A.; Awad, A.A.; Tiberkevich, V.; Slavin, A.N.; Fassbender, J.; Schultheiss, H.
**Excitation of whispering gallery magnons in a magnetic vortex**
Physical Review Letters **122**, 097202 (2019)

7. Sluka, V.; Schneider, T.; Gallardo, R.A.; Kakay, A.; Weigand, M.; Warnatz, T.; Mattheis, R.; Roldan-Molina, A.; Landeros, P.; Tiberkevich, V.; Slavin, A.; Schütz, G.; Erbe, A.; Deac, A.; Lindner, J.; Fassbender, J.; Raabe, J.; Wintz, S.
**Emission and propagation of 1D and 2D spin waves with nanoscale wavelengths in anisotropic spin textures**
Nature Nanotechnology **14**, 328 (2019)

8. Abbe, E.; Renger, T.; Sznajder, M.; Klemmed, B.; Sachse, E.; Hübner, R.; Schüler, T.; Bärtling, Y.; Muchow, B.; Tajmar, M.; Schmiel, T.
**A material experiment for small satellites to characterise the behaviour of carbon nanotubes in space – development and ground validation**
Advances in Space Research **63**, 2312 (2019)

9. Ai, W.; Kou, L.; Hu, X.; Wang, Y.; Krasheninnikov, A.; Sun, L.; Shen, X.
**Enhanced sensitivity of $MoSe_2$ monolayer for gas adsorption induced by electric field**
Journal of Physics: Condensed Matter **31**, 445301 (2019)

10. Appel, P.; Shields, B.J.; Kosub, T.; Hedrich, N.; Hübner, R.; Fassbender, J.; Makarov, D.; Maletinsky, P.
**Nanomagnetism of Magnetoelectric Granular Thin-Film Antiferromagnets**
Nano Letters **19**, 1682 (2019)

11. Aumayr, F.; Ueda, K.; Sokell, E.; Schippers, S.; Sadeghpour, H.; Merkt, F.; Gallagher, T.F.; Dunning, F.B.; Scheier, P.; Echt, O.; Kirchner, T.; Fritzsche, S.; Surzhykov, A.; Ma, X.; Rivarola, R.; Fojon, O.; Tribedi, L.; Lamour, E.; Crespo López-Urrutia, J.R.; Litvinov, Y.A.; Shabaev, V.; Cederquist, H.; Zettergren, H.; Schleberger, M.; Wilhelm, R.A.; Azuma, T.; Boduch, P.; Schmidt, H.T.; Stöhlker, T.
**Roadmap on photonic, electronic and atomic collision physics: III. Heavy particles: with zero to relativistic speeds**
Journal of Physics B **52**, 171003 (2019)

12. Baghban Khojasteh Mohammadi, N.; Apelt, S.; Bergmann, U.; Facsko, S.; Heller, R.
**Revealing the Formation Dynamics of the Electric Double Layer by means of in-situ Rutherford Backscattering Spectrometry**
Review of Scientific Instruments **90**, 085107 (2019)

13. Bardeleben, H.; Zhou, S.; Gerstmann, U.; Skachkov, D.; Lambrecht, W.; Ho, Q.; Deák, P.
**Proton irradiation induced defects in β-$Ga_2O_3$: A combined EPR and theory study**
APL Materials **7**, 022521 (2019)

14. Beljakowa, S.; Pichler, P.; Kalkofen, B.; Hübner, R.
**Diffusion of Phosphorus and Boron from Atomic Layer Deposition Oxides into Silicon**
Physica Status Solidi (A) **216**, 1900306 (2019)

15. Berencén, Y.; Xie, Y.; Wang, M.; Prucnal, S.; Rebohle, L.; Zhou, S.
**Structural and optical properties of pulsed-laser deposited crystalline β-$Ga_2O_3$ thin films on silicon**
Semiconductor Science and Technology **34**, 035001 (2019)

16. Blasetti, C.; Andrian, I.; Billè, F.; Coghetto, E.; Deiuri, S.; Favretto, D.; Turcinovich, M.; Pugliese, R.; Osmenaj, E.; Appleby, G.; Froideval, A.; Pietsch, U.; Sanchez, A.; Valls Vidal, N.; Mitchell, E.; Rabhi, N.; Aogaki, S.; Kasik, Z.; Canova, F.; Gliksohn, F.; Stozno, D.; Michel, J.; Normand, D.; Brancaleon, R.; Paro, G.; Tinta, M.; Zotti, D.
**Wayforlight: The Catalogue of European Light Sources**
Synchrotron Radiation News **32**, 35 (2019)

17. Boeltzig, A.; Best, A.; Pantaleo, F.R.; Imbriani, G.; Junker, M.; Aliotta, M.; Balibrea-Correa, J.; Bemmerer, D.; Broggini, C.; Bruno, C.G.; Buompane, R.; Caciolli, A.; Cavanna, F.; Chillery, T.; Ciani, G.F.; Corvisiero, P.; Csedreki, L.; Davinson, T.; Deboer, R.J.; Depalo, R.; Di Leva, A.; Elekes, Z.; Ferraro, F.; Fiore, E.M.; Formicola, A.; Fülöp, Z.; Gervino, G.; Guglielmetti, A.; Gustavino, C.; Gyürky, G.; Kochanek, I.; Lugaro, M.; Marigo, P.; Menegazzo, R.; Mossa, V.; Munnik, F.; Paticchio, V.; Perrino, R.; Piatti, D.; Prati, P.; Schiavulli, L.; Stöckel, K.; Straniero, O.; Strieder, F.; Szücs, T.; Takács, M.P.; Trezzi, D.; Wiescher, M.; Zavatarelli, S.
**Direct measurements of low-energy resonance strengths of the $^{23}Na(p,\gamma)^{24}Mg$ reaction for astrophysics**
Physics Letters B **795**, 122 (2019)

18. Böhm, B.; Fallarino, L.; Pohl, D.; Rellinghaus, B.; Nielsch, K.; Kiselev, N.S.; Hellwig, O.
**Antiferromagnetic domain wall control via surface spin flop in fully tunable synthetic antiferromagnets with perpendicular magnetic anisotropy**
Physical Review B **100**, 140411 (2019)

19. Böttger, S.; Wagner, C.; Lorkowski, F.; Hartmann, M.; Schuster, J.; Hermann, S.
**Sensitivity control of carbon nanotube based piezoresistive sensors by drain-induced barrier lowering**
Sensors and Actuators A **295**, 288 (2019)

20. Bredemeier, D.; Walter, D.C.; Heller, R.; Schmidt, J.
**Impact of Hydrogen-Rich Silicon Nitride Material Properties on Light-Induced Lifetime Degradation in Multicrystalline Silicon**
Physica Status Solidi (RRL) **13**, 1900201 (2019)

21. But, D.B.; Mittendorff, M.; Consejo, C.; Teppe, F.; Mikhailov, N.N.; Dvoretskii, S.A.; Faugeras, C.; Winnerl, S.; Helm, M.; Knap, W.; Potemski, M.; Orlita, M.
**Suppressed Auger scattering and tunable light emission of Landau-quantized massless Kane electrons**
Nature Photonics **13**, 783 (2019)

22. Cañón Bermudez, G.S.; Kruv, A.; Voitsekhivska, T.; Hochnadel, I.; Lebanov, A.; Potthoff, A.; Fassbender, J.; Yevsa, T.; Makarov, D.
**Implantable highly compliant devices for heating of internal organs: towards cancer treatment**
Advanced Engineering Materials **21**, 1900407 (2019)

23. Cansever, H.; Lindner, J.; Huebner, T.; Niesen, A.; Reiss, G.; Faßbender, J.; Deac, A.M.
**Characterization of Continuous Wave Laser-Induced Thermal Gradients in Magnetic Tunnel Junctions Integrated Into Microresonators via COMSOL Simulations**
IEEE Transactions on Magnetics **55**, 7401505 (2019)

24. Chen, C.; Wang, C.; Cai, X.; Xu, C.; Li, C.; Zhou, J.; Luo, Z.; Fan, Z.; Qin, M.; Zeng, M.; Lu, X.; Gao, X.; Kentsch, U.; Yang, P.; Zhou, G.; Wang, N.; Zhu, Y.; Zhou, S.; Chen, D.; Liu, J.
**Controllable defect driven symmetry change and domain structure evolution in $BiFeO_3$ with enhanced tetragonality**
Nanoscale **11**, 8110 (2019)

25. Ciubotariu, O.; Semisalova, A.; Lenz, K.; Albrecht, M.
**Strain-induced perpendicular magnetic anisotropy and Gilbert damping of $Tm_3Fe_5O_{12}$ thin films**
Scientific Reports **9**, 17474 (2019)

26. Coelho, P.M.; Komsa, H.-P.; Lasek, K.; Kalappattil, V.; Karthikeyan, J.; Phan, M.-H.; Krasheninnikov, A.; Batzill, M.
**Room temperature ferromagnetism in $MoTe_2$ by post-growth incorporation of vanadium impurities**
Advanced Electronic Materials **5**, 1900044 (2019)

27. Cornelius, S.; Colombi, G.; Nafezarefi, F.; Schreuders, H.; Heller, R.; Munnik, F.; Dam, B.
**Oxyhydride Nature of Rare-Earth-Based Photochromic Thin Films**
The Journal of Physical Chemistry Letters **10**, 1342 (2019)

28. Creutzburg, S.; Schmidt, E.; Kutza, P.; Loetzsch, R.; Uschmann, I.; Undisz, A.; Rettenmayr, M.; Gala, F.; Zollo, G.; Boulle, A.; Debelle, A.; Wendler, E.
**Defects and mechanical properties in weakly damaged Si ion implanted GaAs**
Physical Review B **99**, 245205 (2019)

29. Das, K.S.; Makarov, D.; Gentile, P.; Cuoco, M.; van Wees, B.J.; Ortix, C.; Vera-Marun, I.J.
**Independent Geometrical Control of Spin and Charge Resistances in Curved Spintronics**
Nano Letters **19**, 6839 (2019)

30. Das, P.; Raibhar, M.K.; Elliman, R.G.; Möller, W.; Facsko, S.; Chatterjee, S.
**Nanoscale modification of one-dimensional single-crystalline cuprous oxide**
Nanotechnology **30**, 365304 (2019)

31. Dieterle, G.; Förster, J.; Stoll, H.; Semisalova, A.S.; Finizio, S.; Gangwar, A.; Weigand, M.; Noske, M.; Fähnle, M.; Bykova, I.; Bozhko, D.A.; Musiienko-Shmarova, H.Y.; Tiberkevich, V.; Slavin, A.N.; Back, C.H.; Raabe, J.; Schütz, G.; Wintz, S.
**Coherent excitation of heterosymmetric spin waves with ultrashort wavelengths**
Physical Review Letters **122**, 117202 (2019)

32. Dollinger, F.; Lim, K.-G.; Li, Y.; Guo, E.; Formánek, P.; Hübner, R.; Fischer, A.; Kleemann, H.; Leo, K.
**Vertical Organic Thin-Film Transistors with an Anodized Permeable Base for Very Low Leakage Current**
Advanced Materials **31**, 1900917 (2019)

33. Du, R.; Fan, X.; Jin, X.; Hübner, R.; Hu, Y.; Eychmüller, A.
**Emerging Noble Metal Aerogels: State of the Art and a Look Forward**
Matter **1**, 39 (2019)

34. Du, R.; Hu, Y.; Hübner, R.; Joswig, J.-O.; Fan, X.; Schneider, K.; Eychmüller, A.
**Specific ion effects directed noble metal aerogels: Versatile manipulation for electrocatalysis and beyond**
Science Advances **5**, eaaw4590 (2019)

35. Du, R.; Jin, X.; Hübner, R.; Fan, X.; Hu, Y.; Eychmüller, A.
**Engineering Self-Supported Noble Metal Foams Toward Electrocatalysis and Beyond**
Advanced Energy Materials **10**, 1901945 (2020)

36. Duan, J.; Wang, M.; Vines, L.; Böttger, R.; Helm, M.; Zeng, Y.J.; Zhou, S.; Prucnal, S.
**Formation and characterization of shallow junctions in GaAs made by ion implantation and ms-range flash lamp annealing**
Physica Status Solidi (A) **216**, 1800618 (2019)

37. Ehrler, J.; Liedke, M.O.; Cizek, J.; Boucher, R.; Butterling, M.; Zhou, S.; Böttger, R.; Hirschmann, E.; Trinh, T.T.; Wagner, A.; Lindner, J.; Fassbender, J.; Leyens, C.; Potzger, K.; Bali, R.
**The role of open-volume defects in the annihilation of antisites in a B2-ordered alloy**
Acta Materialia **176**, 167 (2019)

38. El-Said, A.S.; Wilhelm, R.A.; Heller, R.; Facsko, S.
**Creation of Surface Nanostructures in Lanthanum Fluoride Single Crystals by Irradiation with Slow Highly Charged Ions**
Nuclear Instruments and Methods in Physics Research B **460**, 137 (2019)

39. Fallarino, L.; Oelschlägel, A.; Arregi, J.A.; Bashkatov, A.; Samad, F.; Böhm, B.; Chesnel, K.; Hellwig, O.
**Control of domain structure and magnetization reversal in thick Co/Pt multilayers**
Physical Review B **99**, 024431 (2019)

40. Fan, X.; Cai, B.; Du, R.; Hübner, R.; Georgi, M.; Jiang, G.; Li, L.; Samadi Khoshkhoo, M.; Sun, H.; Eychmüller, A.
**Ligand-Exchange-Mediated Fabrication of Gold Aerogels Containing Different Au(I) Content with Peroxidase-like Behavior**
Chemistry of Materials **31**, 10094 (2019)

41. Fang, X.; Zheng, F.; Drachenko, O.; Zhou, S.; Zheng, X.; Chen, Z.; Wang, P.; Ge, W.; Shen, B.; Feng, J.; Wang, X.
**Determination of electron effective mass in InN by cyclotron resonance spectroscopy**
Superlattices and Microstructures **136**, 106318 (2019)

42. Faye, D.N.A.; Biquard, X.B.; Nogales, E.C.; Felizardo, M.A.; Peres, M.A.; Redondo-Cubero, A.A.; Auzelle, T.B.; Daudin, B.; Tizei, L.H.G.; Kociak, M.; Ruterana, P.; Möller, W.; Méndez, B.; Alves, E.; Lorenz, K.
**Incorporation of Europium into GaN Nanowires by Ion Implantation**
The Journal of Physical Chemistry C **123**, 11874 (2019)

43. Fenker, M.; Julin, J.; Petrikowski, K.; Richter, A.
**Physical and electrical properties of nitrogen-doped hydrogenated amorphous carbon films**
Vacuum **162**, 8 (2019)

44. Finizio, S.; Wintz, S.; Zeissler, K.; Sadovnikov, A.V.; Mayr, S.; Nikitov, S.A.; Marrows, C.H.; Raabe, J.
**Dynamic Imaging of the Delay-and Tilt-Free Motion of Neel Domain Walls in Perpendicularly Magnetized Superlattices**
Nano Letters **19**, 375 (2019)

45. Finizio, S.; Zeissler, K.; Wintz, S.; Mayr, S.; Weßels, T.; Huxtable, A.J.; Burnell, G.; Marrows, C.H.; Raabe, J.
**Deterministic field-free skyrmion nucleation at a nano-engineered injector device**
Nano Letters **19**, 7246 (2019)

46. Flacke, L.; Liensberger, L.; Althammer, M.; Huebl, H.; Geprägs, S.; Schultheiß, K.; Buzdakov, A.; Hula, T.; Schultheiß, H.; Edwards, E.R.J.; Nembach, H.T.; Shaw, J.M.; Gross, R.; Weiler, M.
**High spin-wave propagation length consistent with low damping in a metallic ferromagnet**
Applied Physics Letters **115**, 122402 (2019)

47. Förster, J.; Wintz, S.; Bailey, J.; Finizio, S.; Josten, E.; Dubs, C.; Bozhko, D.A.; Stoll, M.; Dieterle, G.; Träger, N.; Raabe, J.; Slavin, A.N.; Weigand, M.; Gräfe, U.; Schütz, G.
**Nanoscale X-Ray Imaging of Spin Dynamics in Yttrium Iron Garnet**
Journal of Applied Physics **126**, 173909 (2019)

48. Fotev, I.; Balaghi, L.; Schmidt, J.; Schneider, H.; Helm, M.; Dimakis, E.; Pashkin, A.
**Electron dynamics in $In_xGa_{1-x}As$ shells around GaAs nanowires probed by terahertz spectroscopy**
Nanotechnology **30**, 244004 (2019)

49. Frenzel, P.; Preuß, A.; Bankwitz, J.; Georgi, C.; Ganss, F.; Mertens, L.; Schulz, S.; Hellwig, O.; Mehring, M.; Lang, H.
**Synthesis of Mg and Zn diolates and their use in metal oxide deposition**
RSC Advances **9**, 10657 (2019)

50. Fuchs, F.; Gemming, S.; Schuster, J.
**Electron transport through $NiSi_2$-Si contacts and their role in reconfigurable field-effect transistors**
Journal of Physics: Condensed Matter **31**, 355002 (2019)

51. Fuchs, F.; Gemming, S.; Schuster, J.
**Radially resolved electronic structure and charge carrier transport in silicon nanowires**
Physica E **108**, 181 (2019)

52. Gacka, E.; Lindner, A.A.; Mazurkiewicz-Pawlicka, M.; Malolepszy, A.; Stobiński, L.; Kubas, A.; Hug, G.L.; Marciniak, B.; Lewandowska-Andralojc, A.
**Noncovalent Porphyrin–Graphene Oxide Nanohybrids: The pH-Dependent Behavior**
Journal of Physical Chemistry C **123**, 3368 (2019)

53. Gago, R.; Prucnal, S.; Hübner, R.; Munnik, F.; Esteban-Mendoza, D.; Jiménez, I.; Palomares, J.
**Phase Selectivity in Cr and N Co-Doped $TiO_2$ Films by Modulated Sputter Growth and Post-Deposition Flash-Lamp-Annealing**
Coatings **9**, 448 (2019)

54. Gallardo, R.A.; Alvarado-Seguel, P.; Schneider, T.; Gonzalez-Fuentes, C.; Roldán-Molina, A.; Lenz, K.; Lindner, J.; Landeros, P.
**Spin-wave nonreciprocity on magnetization-graded ferromagnetic films**
New Journal of Physics **21**, 033026 (2019)

55. Gallardo, R.A.; Cortés-Ortuno, D.; Schneider, T.; Roldán-Molina, A.; Ma, F.; Lenz, K.; Fangohr, H.; Lindner, J.; Landeros, P.
**Flat Bands, Indirect Gaps, and Unconventional Spin-Wave Behavior Induced by a Periodic Dzyaloshinskii-Moriya Interaction**
Physical Review Letters **122**, 067204 (2019)

56. Gallardo, R.A.; Schneider, T.; Chaurasiya, A.K.; Oelschlägel, A.; Arekapudi, S.S.P.K.; Roldán-Molina, A.; Hübner, R.; Lenz, K.; Barman, A.; Fassbender, J.; Lindner, J.; Hellwig, O.; Landeros, P.
**Reconfigurable spin-wave non-reciprocity induced by dipolar interaction in a coupled ferromagnetic bilayer**
Physical Review Applied **12**, 034012 (2019)

57. Galle, T.; Kazes, M.; Hübner, R.; Lox, J.; Khoshkhoo, M.S.; Sonntag, L.; Tietze, R.; Sayevich, V.; Oron, D.; Koitzsch, A.; Lesnyak, V.; Eychmüller, A.
**Colloidal Mercury-Doped CdSe Nanoplatelets with Dual Fluorescence**
Chemistry of Materials **31**, 5065 (2019)

58. Gandy, A.S.; Jim, B.; Coe, G.; Patel, D.; Hardwick, L.; Akhmadaliev, S.; Reeves-Mclaren, N.; Goodall, R.
**High Temperature and Ion Implantation-Induced Phase Transformations in Novel Reduced Activation Si-Fe-V-Cr (-Mo) High Entropy Alloys**
Frontiers in Materials **6**, 146 (2019)

59. Gogoi, P.K.; Lin, Y.-C.; Senga, R.; Komsa, H.-P.; Liang, S.; Chi, W.D.; Krasheninnikov, A.V.; Li, L.-J.; Breese, M.B.H.; Pennycook, S.J.; Wee, A.T.S.; Suenaga, K.
**Layer Rotation-Angle-Dependent Excitonic Absorption in van der Waals Heterostructures Revealed by Electron Energy Loss Spectroscopy**
ACS Nano **13**, 9541 (2019)

60. Gómez-Ferrer, B.; Heintze, C.; Pareige, C.
**On the role of Ni, Si and P on the microstructural evolution of FeCr alloys under irradiation**
Journal of Nuclear Materials **517**, 35 (2019)

61. Granell, P.; Wang, G.; Canon Bermudez, G.S.; Kosub, T.; Golmar, F.; Steren, L.; Fassbender, J.; Makarov, D.
**Highly compliant planar Hall effect sensor with sub 200 nT sensitivity**
npj Flexible Electronics **3**, 3 (2019)

62. Gräning, T.; Klimenkov, M.; Rieth, M.; Heintze, C.; Möslang, A.
**Long-term stability of the microstructure of austenitic ODS steel rods produced with a carbon-containing process control agent**
Journal of Nuclear Materials **523**, 111 (2019)

63. Hache, T.; Weinhold, T.; Schultheiss, K.; Stigloher, J.; Vilsmeier, F.; Back, C.; Arekapudi, S.S.P.K.; Hellwig, O.; Fassbender, J.; Schultheiss, H.
**Combined frequency and time domain measurements on injection-locked, constriction-based spin Hall nano-oscillators**
Applied Physics Letters **114**, 102403 (2019)

64. Hammerath, F.; Bali, R.; Hübner, R.; Brandt, M.R.D.; Rodan, S.; Potzger, K.; Böttger, R.; Sakuraba, Y.; Büchner, B.; Wurmehl, S.
**Structure-property relationship of $Co_2MnSi$ thin films in response to He+-irradiation**
Scientific Reports **9**, 2766 (2019)

65. Hartley, N.; Grenzer, J.; Lu, W.; Huang, L.; Inubushi, Y.; Kamimura, N.; Katagiri, K.; Kodama, R.; Kon, A.; Lipp, V.; Makita, M.; Matsuoka, T.; Medvedev, N.; Nakajima, S.; Ozaki, N.; Pikuz, T.; Rode, A.V.; Rohatsch, K.; Sagae, D.; Schuster, A.; Tono, K.; Vorberger, J.; Yabuuchi, T.; Kraus, D.
**Ultrafast Anisotropic Disordering in Graphite Driven by Intense Hard X-ray Pulses**
High Energy Density Physics **32**, 63 (2019)

66. Hashemi, A.; Krasheninnikov, A.; Puska, M.; Komsa, H.
**Efficient method for calculating Raman spectra of solids with impurities and alloys and its application to two-dimensional transition metal dichalcogenides**
Physical Review Materials **3**, 023806 (2019)

67. He, S.; Zhang, Z.; Liu, H.; Akhmadaliev, S.; Zhou, S.; Wang, X.; Wu, P.
**Spatial solitons in $KTa_xNb_{1-x}O_3$ waveguides produced by swift carbon ion irradiation and femtosecond laser ablation**
Applied Physics Express **12**, 076502 (2019)

68. He, Y.; Zhang, P.; Wang, M.; Wang, F.; Tan, D.; Li, Y.; Zhuang, X.; Zhang, F.; Feng, X.
**Nano-sandwiched metal hexacyanoferrate/graphene hybrid thin films for in-plane asymmetric micro-supercapacitors with ultrahigh energy density**
Materials Horizons **6**, 1041 (2019)

69. Higley, D.; Reid, A.; Chen, Z.; Le Guyader, L.; Hellwig, O.; Lutman, A.; Liu, T.; Shafer, P.; Chase, T.; Dakovski, G.; Mitra, A.; Yuan, E.; Schlappa, J.; Dürr, H.; Schlotter, W.; Stöhr, J.
**Femtosecond X-ray induced changes of the electronic and magnetic response of solids from electron redistribution**
Nature Communications **10**, 5289 (2019)

70. Hoffmann, M.; Sharma, A.; Matthes, P.; Okano, S.; Hellwig, O.; Ecke, R.; Zahn, D.; Salvan, G.; Schulz, S.
**Spectroscopic ellipsometry and magneto-optical Kerr effect spectroscopy study of thermally treated $Co_{60}Fe_{20}B_{20}$ thin films**
Journal of Physics: Condensed Matter **32**, 055702 (2019)

71. Huang, Q.; Jia, Q.; Feng, J.; Huang, H.; Yang, X.; Grenzer, J.; Huang, K.; Zhang, S.; Lin, J.; Zhou, H.; You, T.; Yu, W.; Facsko, S.; Jonnard, P.; Wu, M.; Giglia, A.; Zhang, Z.; Liu, Z.; Wang, Z.; Wang, X.; Ou, X.
**Realization of wafer-scale nanogratings with sub-50 nm period through vacancy epitaxy**
Nature Communications **10**, 1 (2019)

72. Huang, X.-P.; Chen, K.; Qi, M.-X.; Zhang, P.-F.; Li, Y.; Winnerl, S.; Schneider, H.; Yang, Y.; Zhang, S.
**Plasmonic field guided patterning of ordered colloidal nanostructures**
Nanophotonics **8**, 505 (2019)

73. Iastremskyi, I.; Volkov, O.M.; Kopte, M.; Kosub, T.; Stienen, S.; Lenz, K.; Lindner, J.; Faßbender, J.; Ivanov, B.A.; Makarov, D.
**Thermodynamics and determination of the exchange stiffness of asymmetrically sandwiched ultrathin ferromagnetic films with perpendicular anisotropy**
Physical Review Applied **12**, 064038 (2019)

74. Jadidi, M.M.; Daniels, K.M.; Myers-Ward, R.L.; Gaskill, D.K.; König-Otto, L.C.; Winnerl, S.; Sushkov, A.B.; Drew, H.D.; Murphy, T.E.; Mittendorff, M.
**Optical Control of Plasmonic Hot Carriers in Graphene**
ACS Photonics **6**, 302 (2019)

75. Jäger, N.; Klima, S.; Hruby, H.; Julin, J.; Keckes, J.F.; Mitterer, C.; Daniel, R.
**Evolution of structure and residual stress of a fcc/hex-AlCrN multi-layered system upon thermal loading revealed by cross-sectional X-ray nano-diffraction**
Acta Materialia **162**, 55 (2019)

76. Jagerová, A.; Malinský, P.; Mikšová, R.; Nekvindová, P.; Cajzl, J.; Akhmadaliev, S.; Holý, V.; Macková, A.
**Distinct defect appearance in Gd implanted polar and nonpolar ZnO surfaces in connection to ion channeling effect**
Journal of Vacuum Science & Technology A **37**, 061406 (2019)

77. Jakubowski, M.M.; Liedke, M.O.; Butterling, M.; Dynowska, E.; Sveklo, I.; Milińska, E.; Kurant, Z.; Böttger, R.; von Borany, J.; Maziewski, A.; Wagner, A.; Wawro, A.
**On defects' role in enhanced perpendicular magnetic anisotropy in Pt/Co/Pt, induced by ion irradiation**
Journal of Physics: Condensed Matter **31**, 185801 (2019)

78. Jolie, W.; Murray, C.; Weiß, P.S.; Hall, J.; Portner, F.; Atodiresei, N.; Krasheninnikov, A.; Busse, C.; Komsa, H.-P.; Rosch, A.; Michely, T.
**Tomonaga-Luttinger liquid in a box: electrons confined within $MoS_2$ mirror twin boundaries**
Physical Review X **9**, 011055 (2019)

79. Juhász, R.; Kelling, J.; Ódor, G.
**Critical dynamics of the Kuramoto model on sparse random networks**
Journal of Statistical Mechanics: Theory and Experiment **5**, 053403 (2019)

80. Karthikeyan, J.; Komsa, H.-P.; Batzill, M.; Krasheninnikov, A.V.
**Which transition metal atoms can be embedded into two-dimensional molybdenum dichalcogenides and add magnetism?**
Nano Letters **19**, 4581 (2019)

81. Kern, F.; Linck, M.; Wolf, D.; Niermann, T.; Arora, H.; Alem, N.; Erbe, A.; Gemming, S.; Lubk, A.
**Direct Correction of Residual Symmetric Aberrations in Electron Holograms of Weak Phase Objects**
Microscopy and Microanalysis **25**, 98 (2019)

82. Khan, M.B.; Deb, D.; Kerbusch, J.; Fuchs, F.; Löffler, M.; Banerjee, S.; Mühle, U.; Weber, W.M.; Gemming, S.; Schuster, J.; Erbe, A.; Georgiev, Y.
**Towards reconfigurable electronics: silicidation of top down fabricated Silicon nanowires**
Applied Sciences **9**, 3462 (2019)

83. Kiani, M.; Du, N.; Vogel, M.; Raff, J.; Hübner, U.; Skorupa, I.; Bürger, D.; Schulz, S.E.; Schmidt, O.G.; Schmidt, H.
**P-N Junction-Based Si Biochips with Ring Electrodes for Novel Biosensing Applications**
Biosensors **9**, 120 (2019)

84. Kinyanjui, M.K.; Björkman, T.; Lehnert, T.; Köster, J.; Krasheninnikov, A.; Kaiser, U.
**Effects of electron beam generated lattice defects on the periodic lattice distortion structure in 1T-$TaS_2$ and 1T-$TaSe_2$ thin layers**
Physical Review B **99**, 024101 (2019)

85. Klingner, N.; Heller, R.; Hlawacek, G.; Facsko, S.; von Borany, J.
**Time-of-flight secondary ion mass spectrometry in the helium ion microscope**
Ultramicroscopy **198**, 10 (2019)

86. Koll, D.; Korschinek, G.; Faestermann, T.; Gómez-Guzmán, J.; Kipfstuhl, S.; Merchel, S.; Welch, J.M.
**Interstellar $^{60}$Fe in Antarctica**
Physical Review Letters **123**, 072701 (2019)

87. Kowalska, E.; Fukushima, A.; Sluka, V.; Fowley, C.; Kákay, A.; Aleksandrov, Y.; Lindner, J.; Fassbender, J.; Yuasa, S.; Deac, A.M.
**Tunnel magnetoresistance angular and bias dependence enabling tuneable wireless communication**
Scientific Reports **9**, 9541 (2019)

88. Kowalska, E.; Kákay, A.; Fowley, C.; Sluka, V.; Lindner, J.; Fassbender, J.; Deac, A.M.
**Zero-field dynamics stabilized by in-plane shape anisotropy in MgO-based spin-torque oscillators**
Journal of Applied Physics **125**, 083902 (2019)

89. Kozubek, R.; Tripathi, M.; Ghorbani-Asl, M.; Kretschmer, S.; Madauß, L.; Pollmann, E.; O'Brien, M.; Mcevoy, N.; Ludacka, U.; Susi, T.; Duesberg, G.S.; Wilhelm, R.A.; Krasheninnikov, A.V.; Kotakoski, J.; Schleberger, M.Y.
**Perforating Freestanding Molybdenum Disulfide Monolayers with Highly Charged Ions**
The Journal of Physical Chemistry Letters **10**, 904 (2019)

90. Krupinski, M.; Bali, R.; Mitin, D.; Sobieszczyk, P.; Gregor-Pawlowski, J.; Zarzycki, A.; Böttger, R.; Albrecht, M.; Potzger, K.; Marszałek, M.
**Ion induced ferromagnetism combined with self-assembly for large area magnetic modulation of thin films**
Nanoscale **11**, 8930 (2019)

91. Lammel, M.; Schlitz, R.; Geishendorf, K.; Makarov, D.; Kosub, T.; Fabretti, S.; Reichlova, H.; Huebner, R.; Nielsch, K.; Thomas, A.; Goennenwein, S.T.B.
**Spin Hall magnetoresistance in heterostructures consisting of noncrystalline paramagnetic YIG and Pt**
Applied Physics Letters **114**, 252402 (2019)

92. Lang, D.; Balaghi, L.; Winnerl, S.; Schneider, H.; Hübner, R.; Kehr, S.C.; Eng, L.M.; Helm, M.; Dimakis, E.; Pashkin, A.
**Nonlinear plasmonic response of doped nanowires observed by infrared nanospectroscopy**
Nanotechnology **30**, 084003 (2019)

93. Langer, M.; Gallardo, R.A.; Schneider, T.; Stienen, S.; Roldán-Molina, A.; Yuan, Y.; Lenz, K.; Lindner, J.; Landeros, P.; Fassbender, J.
**Spin-Wave Modes in Transition from a Thin Film to a Full Magnonic Crystal**
Physical Review B **99**, 024426 (2019)

94. Larowska, D.; Lindner, A.A.; Mazurkiewicz-Pawlicka, M.; Malolepszy, A.; Stobiński, L.; Marciniak, B.; Lewandowska-Andralojc, A.
**Cationic Porphyrin-Graphene Oxide Hybrid: Donor-Acceptor Composite for Efficient Photoinduced Electron Transfer**
ChemPhysChem **20**, 1054 (2019)

95. Lehnert, T.; Ghorbani Asl, M.; Köster, J.; Lee, Z.; Krasheninnikov, A.; Kaiser, U.
**Electron-Beam-Driven Structure Evolution of Single-Layer $MoTe_2$ for Quantum Devices**
ACS Applied Nano Materials **2**, 3262 (2019)

96. Lenz, K.; Narkowicz, R.; Wagner, K.; Reiche, C.F.; Körner, J.; Schneider, T.; Kákay, A.; Schultheiss, H.; Suter, D.; Büchner, B.; Fassbender, J.; Mühl, T.; Lindner, J.
**Magnetization Dynamics of an Individual Single-Crystalline Fe-Filled Carbon Nanotube**
Small **15**, 1904315 (2019)

97. Li, C.; Gusev, V.; Dimakis, E.; Dekorsy, T.; Hettich, M.
**Broadband photo-excited coherent acoustic frequency combs and mini-Brillouin-zone modes in a MQW-SESAM structure**
Applied Sciences **9**, 289 (2019)

98. Li, H.; Wang, C.; Li, D.-Y.; Pereira, L.M.C.; Homm, P.; Menghini, M.; Locquet, J.-P.; Temst, K.; Vantomme, A.; van Haesendonck, C.; van Bael, M.J.; Ruan, S.; Zeng, Y.-J.
**Magnetic Orders and Origin of Exchange Bias in Co Clusters Embedded Oxide Nanocomposite Films**
Journal of Physics: Condensed Matter **31**, 155301 (2019)

99. Li, K.; Jin, S.; Guo, J.; Xu, Y.; Su, Y.; Feng, E.; Liu, Y.; Zhou, S.; Ying, T.; Li, S.; Wang, Z.; Chen, G.; Chen, X.
**Double-peak specific heat and spin freezing in the spin-2 triangular lattice antiferromagnet $FeAl_2Se_4$**
Physical Review B **99**, 054421 (2019)

100. Li, L.; Xu, C.; Yuan, Y.; Zhou, S.
**Equiatomic quinary rare-earth rich amorphous ribbons with excellent magnetocaloric performance**
Materialia **3**, 74 (2019)

101. Li, R.; Pang, C.; Li, Z.; Dong, N.; Wang, J.; Ren, F.; Akhmadaliev, S.; Zhou, S.; Chen, F.
**Monolithic waveguide laser mode-locked by embedded Ag nanoparticles operating at 1 μm**
Nanophotonics **8**, 859 (2019)

102. Liu, C.; Hübner, R.; Xie, Y.; Wang, M.; Xu, C.; Jiang, Z.; Yuan, Y.; Li, X.; Yang, J.; Li, L.; Weschke, E.; Prucnal, S.; Helm, M.; Zhou, S.
**Ultra-fast annealing manipulated spinodal nano-decomposition in Mn-implanted Ge**
Nanotechnology **30**, 054001 (2019)

103. Lungwitz, F.; Escobar-Galindo, R.; Janke, D.; Schumann, E.; Wenisch, R.; Gemming, S.; Krause, M.
**Transparent Conductive Tantalum Doped Tin Oxide as Selectively Solar-Transmitting Coating for High Temperature Solar Thermal Applications**
Solar Energy Materials and Solar Cells **196**, 84 (2019)

104. Luxa, J.; Mazánek, V.; Mackova, A.; Malinsky, P.; Akhmadaliev, S.; Sofer, Z.
**Tuning of electrocatalytic properties of $MoS_2$ by chalcogenide ion implantation**
Applied Materials Today **14**, 216 (2019)

105. Ma, J.; Zhang, K.; Schellhammer, S.; Fu, Y.; Komber, H.; Xu, C.; Popov, A.A.; Hennersdorf, F.; Weigand, J.J.; Zhou, S.; Pisula, W.; Ortmann, F.; Berger, R.; Liu, J.; Feng, X.
**Wave-shaped polycyclic hydrocarbons with controlled aromaticity**
Chemical Science **10**, 4025 (2019)

106. Macková, A.; Malinský, P.; Jagerová, A.; Mikšová, R.; Nekvindová, P.; Cajzl, J.; Rinkevičiūtė, E.; Akhmadaliev, S.
**Damage formation and Er structural incorporation in m-plane and a-plane ZnO**
Nuclear Instruments and Methods in Physics Research B **460**, 38 (2019)

107. Macková, A.; Malinský, P.; Jagerová, A.; Mikšová, R.; Sofer, Z.; Klímová, K.; Mikulics, M.; Böttger, R.; Akhmadaliev, S.; Oswald, J.
**Damage accumulation and implanted Gd and Au position in a- and c-plane GaN**
Thin Solid Films **680**, 102 (2019)

108. Macková, A.; Malinský, P.; Jagerová, A.; Mikšová, R.; Nekvindová, P.; Cajzl, J.; Böttger, R.; Akhmadaliev, S.
**Au incorporation into various ZnO crystallographic cuts realised by ion implantation – ZnO damage characterization**
Vacuum **169**, 108892 (2019)

109. Malinský, P.; Cutroneo, M.; Sofer, Z.; Szőkölová, K.; Böttger, R.; Akhmadaliev, S.; Macková, A.
**Structural and compositional modification of graphene oxide by means of medium and heavy ion implantation**
Nuclear Instruments and Methods in Physics Research B **460**, 201 (2019)

110. Mazalski, P.; Kurant, Z.; Sveklo, I.; Dobrogowski, W.; Fassbender, J.; Wawro, A.; Maziewski, A.
**Ion irradiation driven changes of magnetic anisotropy in ultrathin Co films sandwiched between Au or Pt covers**
Journal of Magnetism and Magnetic Materials **479**, 332 (2019)

111. Mechernich, S.; Dunai, T.J.; Binnie, S.A.; Goral, T.; Heinze, S.; Dewald, A.; Schimmelpfennig, I.; Keddadouche, K.; Aumaître, G.; Bourlès, D.; Marrero, S.M.; Wilcken, K.; Simon, K.; Fink, D.; Phillips, F.M.; Caffee, M.W.; Gregory, L.C.; Phillips, R.; Freeman, S.P.H.T.; Shanks, R.P.; Sarıkaya, M.A.; Pavetich, S.; Rugel, G.; Merchel, S.; Akçar, N.; Yesiyurt, S.; Ivy-Ochs, S.; Vockenhuber, C.
**Carbonate and silicate intercomparison materials for cosmogenic $^{36}$Cl measurements**
Nuclear Instruments and Methods in Physics Research B **455**, 250 (2019)

112. Merchel, S.; Gärtner, A.; Beutner, S.; Bookhagen, B.; Chabilan, A.
**Attempts to understand potential deficiencies in chemical procedures for AMS: Cleaning and dissolving quartz for $^{10}$Be and $^{26}$Al analysis**
Nuclear Instruments and Methods in Physics Research B **455**, 293 (2019)

113. Merchel, S.; Gurlit, S.; Opel, T.; Rugel, G.; Scharf, A.; Tiessen, C.; Weiß, S.; Wetterich, S.
**Attempts to understand potential deficiencies in chemical procedures for AMS**
Nuclear Instruments and Methods in Physics Research B **456**, 186 (2019)

114. Meyer, M.; Gliganic, L.A.; May, J.-H.; Merchel, S.; Rugel, G.; Schlütz, F.; Aldenderfer, M.; Krainer, K.
**Landscape dynamics and human-environment interactions in the northern foothills of Cho Oyu and Mount Everest (southern Tibet) during the Late Pleistocene and Holocene**
Quaternary Science Reviews **229**, 106127 (2020)

115. Mingchao, W.; Marco, B.; Wang, M.; Hung-Hsuan, L.; Bishnu, P.B.; Xiaocang, H.; Silvia, P.; Eike, B.; Pan, L.; Mingwei, C.; Mischa, B.; Heine, T.; Zhou, S.; Enrique, C.; Renhao, D.; Xinliang, F.
**Unveiling Electronic Properties in Metal−Phthalocyanine-Based Pyrazine-Linked Conjugated Two-Dimensional Covalent Organic Frameworks**
Journal of the American Chemical Society **141**, 42 (2019)

116. Mousley, M.; Eswara, S.; de Castro, O.; Bouton, O.; Klingner, N.; Koch, C.T.; Hlawacek, G.; Wirtz, T.
**Stationary beam full-field transmission helium ion microscopy using sub-50 keV $He^+$: Projected images and intensity patterns**
Beilstein Journal of Organic Chemistry **10**, 1648 (2019)

117. Nadarajan, R.; Devaraj, M.; Satyanarayana, S.V.M.; Posselt, M.
**First principles calculations of the thermodynamic stability of Ba, Zr, and O vacancies in $BaZrO_3$**
RSC Advances **9**, 34158 (2019)

118. Nasdala, L.; Akhmadaliev, S.; Chanmuang N., C.; Zowalla, A.; Csato, C.; Rüb, M.
**$^4$He irradiation of zircon, $ZrSiO_4$, using a micro-patterned, Si-based energy filter**
Nuclear Instruments and Methods in Physics Research B **443**, 38 (2019)

119. Nekić, N.; Šarić, I.; Salamon, K.; Basioli, L.; Sancho-Parramon, J.; Grenzer, J.; Hübner, R.; Bernstorff, S.; Petravić, M.; Mičetić, M.
**Preparation of non-oxidized Ge quantum dot lattices in amorphous $Al_2O_3$, $Si_3N_4$ and SiC matrices**
Nanotechnology **30**, 335601 (2019)

120. Neumann, M.; Strobel, A.; Al-Saadawi, Y.; Steinbach, G.; Erbe, A.; Gemming, S.
**A Two-Parameter Model for Colloidal Particles with an Extended Magnetic Cap**
Physica Status Solidi (A) **216**, 1900506 (2019)

121. Nord, M.; Semisalova, A.; Kákay, A.; Hlawacek, G.; MacLaren, I.; Liersch, V.; Volkov, O.M.; Makarov, D.; Paterson, G.W.; Potzger, K.; Lindner, J.; Faßbender, J.; McGrouther, D.; Bali, R.
**Strain Anisotropy and Magnetic Domains in Embedded Nanomagnets**
Small **15**, 1904738 (2019)

122. Novak, E.V.; Pyanzina, E.S.; Sánchez, P.A.; Kantorovich, S.S.
**The structure of clusters formed by Stockmayer supracolloidal magnetic polymers**
European Physical Journal E **42**, 158 (2019)

123. Ódor, G.; Kelling, J.
**Critical synchronization dynamics of the Kuramoto model on connectome and small world graphs**
Scientific Reports **9**, 19621 (2019)

124. Pan, X.; Shuai, Y.; Wu, C.; Luo, W.; Sun, X.; Zeng, H.; Guo, H.; Yuan, Y.; Zhou, S.; Böttger, R.; Cheng, H.; Zhang, J.; Zhang, W.; Schmidt, H.
**Compliance-current-modulated resistive switching with multi-level resistance states in single-crystalline $LiNbO_3$ thin film**
Solid State Ionics **334**, 1 (2019)

125. Panizo-Laiz, M.; Díaz-Rodríguez, P.; Rivera, A.; Valles, G.; Martín-Bragado, I.; Perlado, J.M.; Munnik, F.; González-Arrabal, R.
**Experimental and computational studies of the influence of grain boundaries and temperature on the radiation-induced damage and hydrogen behavior in tungsten**
Nuclear Fusion **59**, 086055 (2019)

126. Pavetich, S.; Wallner, A.; Martschini, M.; Akhmadaliev, S.; Dillmann, I.; Fifield, K.; Halfon, S.; Heftrich, T.; Käppeler, F.; Lederer-Woods, C.; Merchel, S.; Paul, M.; Reifarth, R.; Rugel, G.; Steier, P.; Tessler, M.; Tims, S.; Weigand, M.; Weissman, L.
**Accelerator mass spectrometry measurement of the reaction $^{35}Cl(n,\gamma)^{36}Cl$ at keV energies**
Physical Review C **99**, 015801 (2019)

127. Pilz, W.; Mazarov, P.; Klingner, N.; Bauerdick, S.; Bischoff, L.
**Lithium Ion Beams from Liquid Metal Alloy Ion Sources**
Journal of Vacuum Science & Technology B **37**, 021802 (2019)

128. Poshakinskiy, A.V.; Astakhov, G.
**Optically detected spin-mechanical resonance in silicon carbide membranes**
Physical Review B **100**, 094104 (2019)

129. Prucnal, S.; Berencen, Y.; Wang, M.; Georgiev, Y.; Erbe, A.; Khan, M.B.; Böttger, R.; Hübner, R.; Schönherr, T.; Kalbacova, J.; Vines, L.; Facsko, S.; Engler, M.; Zahn, D.R.T.; Knoch, J.; Helm, M.; Skorupa, W.; Zhou, S.
**Nanoscale $n^{++}$-p junction formation in GeOI probed by tip-enhanced Raman spectroscopy and conductive atomic force microscopy**
Journal of Applied Physics **125**, 245703 (2019)

130. Prucnal, S.; Berencén, Y.; Wang, M.; Rebohle, L.; Kudrawiec, R.; Polak, M.; Zviagin, V.; Schmidt-Grund, R.; Grundmann, M.; Grenzer, J.; Turek, M.; Droździel, A.; Pyszniak, K.; Zuk, J.; Helm, M.; Skorupa, W.; Zhou, S.
**Band gap renormalization in n-type GeSn alloys made by ion implantation and flash lamp annealing**
Journal of Applied Physics **125**, 203115 (2019)

131. Prüfer, T.; Möller, W.; Heinig, K.-H.; Wolf, D.; Engelmann, H.-J.; Xu, X.; von Borany, J.
**Computer Modeling of Single-layer Nanocluster Formation in a Thin $SiO_2$ Layer Buried in Si by Ion Mixing and Thermal Phase Decomposition**
Journal of Applied Physics **125**, 225708 (2019)

132. Qarra, H.H.; Knowles, K.M.; Vickers, M.E.; Akhmadaliev, S.; Lambrinou, K.
**Heavy ion irradiation damage in $Zr_2AlC$ MAX phase**
Journal of Nuclear Materials **523**, 1 (2019)

133. Radic, D.; Hilke, S.; Peterlechner, M.; Posselt, M.; Bracht, H.
**Fluctuation electron microscopy on silicon amorphized at varying self ion-implantation conditions**
Journal of Applied Physics **126**, 095707 (2019)

134. Rahaman, M.; Wagner, C.; Mukherjee, A.; Lopez-Rivera, A.; Gemming, S.; Zahn, D.R.T.
**Probing Interlayer Excitons in a Vertical van der Waals p-n Junction using Scanning Probe Microscopy Technique**
Journal of Physics: Condensed Matter **31**, 114001 (2019)

135. Rajbhar, M.; Das, P.; Satpati, B.; Möller, W.; Facsko, S.; Böttger, R.; Ramgir, N.; Chatterjee, S.
**Joining of two different ceramic nanomaterials for bottom-up fabrication of heterojunction devices**
Applied Surface Science **478**, 651 (2019)

136. Rana, R.; Klopf, J.M.; Grenzer, J.; Schneider, H.; Helm, M.; Pashkin, A.
**Nonthermal nature of photo-induced insulator-to-metal transition in $NbO_2$**
Physical Review B **99**, 041102(R) (2019)

137. Rastei, M.V.; Pierron-Bohnes, V.; Toulemon, D.; Bouillet, C.; Kákay, A.; Hertel, R.; Tetsi, E.; Begin-Colin, S.; Pichon, B.P.
**Defect-Driven Magnetization Configuration of Isolated Linear Assemblies of Iron Oxide Nanoparticles**
Advanced Functional Materials **29**, 1903927 (2019)

138. Rayapati, V.R.; Bürger, D.; Du, N.; Patra, R.; Skorupa, I.; Blaschke, D.; Stöcker, H.; Matthes, P.; Schulz, S.E.; Schmidt, H.
**Electroforming-free resistive switching in yttrium manganite thin films by cationic substitution**
Journal of Applied Physics **126**, 074102 (2019)

139. Regensburger, S.; Winnerl, S.; Klopf, J.M.; Lu, H.; Gossard, A.C.; Preu, S.
**Picosecond-scale Terahertz pulse characterization with field-effect transistors**
IEEE Transactions on Terahertz Science and Technology **9**, 262 (2019)

140. Reichlova, H.; Janda, T.; Godinho, J.; Markou, A.; Kriegner, D.; Schlitz, R.; Zelezny, J.; Soban, Z.; Bejarano, M.; Schultheiß, H.; Nemec, P.; Jungwirth, T.; Felser, C.; Wunderlich, J.; Goennenwein, S.T.B.
**Imaging and writing magnetic domains in the non-collinear antiferromagnet $Mn_3Sn$**
Nature Communications **10**, 5459 (2019)

141. Reissig, F.; Hübner, R.; Steinbach, J.; Pietzsch, H.-J.; Mamat, C.
**Facile preparation of radium-doped, functionalized nanoparticles as carriers for targeted alpha therapy**
Inorganic Chemistry Frontiers **6**, 1341 (2019)

142. Saha, S.; Zelent, M.; Finizio, S.; Mruczkiewicz, M.; Tacchi, S.; Suszka, A.K.; Wintz, S.; Bingham, N.S.; Raabe, J.; Krawczyk, M.; Heyderman, L.J.
**Formation of Néel Type Skyrmions in an Antidot Lattice with Perpendicular Magnetic Anisotropy**
Physical Review B **100**, 144435 (2019)

143. Salikhov, R.; Alekhin, A.; Parpiiev, T.; Pezeril, T.; Makarov, D.; Abrudan, R.; Meckenstock, R.; Radu, F.; Farle, M.; Zabel, H.; Temnov, V.V.
**Gilbert damping in NiFeGd compounds: Ferromagnetic resonance versus time-resolved spectroscopy**
Physical Review B **99**, 104412 (2019)

144. Sánchez, P.A.; Vögele, M.; Smiatek, J.; Qiao, B.; Sega, M.; Holm, C.
**Atomistic simulation of PDADMAC/PSS oligoelectrolyte multilayers: overall comparison of tri- and tetra-layer systems**
Soft Matter **15**, 9437 (2019)

145. Saringer, C.; Kickinger, C.; Munnik, F.; Mitterer, C.; Schalk, N.; Tkadletz, M.
**Thermal expansion of magnetron sputtered $TiC_xN_{1-x}$ coatings studied by high-temperature X-ray diffraction**
Thin Solid Films **688**, 137307 (2019)

146. Sato, N.; Schultheiß, K.; Körber, L.; Puwenberg, N.; Mühl, T.; Awad, A.A.; Arekapudi, S.S.P.K.; Hellwig, O.; Faßbender, J.; Schultheiß, H.
**Domain wall-based spin-Hall nano-oscillators**
Physical Review Letters **123**, 057204 (2019)

147. Schaffers, T.; Feggeler, T.; Pile, S.; Meckenstock, R.; Buchner, M.; Spoddig, D.; Ney, V.; Farle, M.; Wende, H.; Wintz, S.; Weigand, M.; Ohldag, H.; Ollefs, K.; Ney, A.
**Extracting the Dynamic Magnetic Contrast in Time-Resolved X-ray Transmission Microscopy**
Nanomaterials **9**, 940 (2019)

148. Schlitz, R.; Helm, T.; Lammel, M.; Nielsch, K.; Erbe, A.; Goennenwein, S.T.B.
**Focused ion beam modification of non-local magnon-based transport in yttrium iron garnet/platinum heterostructures**
Applied Physics Letters **114**, 252401 (2019)

149. Schneider, T.; Lenz, K.; Semisalova, A.; Gollwitzer, J.; Heitler-Klevans, J.; Potzger, K.; Fassbender, J.; Lindner, J.; Bali, R.
**Tuning Ferromagnetic Resonance via Disorder/Order Interfaces**
Journal of Applied Physics **125**, 195302 (2019)

150. Schwestka, J.; Niggas, A.; Creutzburg, S.; Kozubek, R.; Heller, R.; Schleberger, M.; Wilhelm, R.A.; Aumayr, F.
**Charge-Exchange-Driven Low-Energy Electron Splash Induced by Heavy Ion Impact on Condensed Matter**
The Journal of Physical Chemistry Letters **2019**, 4805 (2019)

151. Sheremet, E.; Meszmer, P.; Blaudeck, T.; Hartmann, S.; Wagner, C.; Ma, B.; Hermann, S.; Wunderle, B.; Schulz, S.E.; Hietschold, M.; Rodriguez, R.D.; Zahn, D.R.T.
**Advanced characterization methods for electrical and sensoric components and devices at the micro and nanoscale**
Physica Status Solidi (A) **216**, 1900106 (2019)

152. Singh, A.; Welsch, M.; Winnerl, S.; Helm, M.; Schneider, H.
**Improved electrode design for interdigitated large-area photoconductive terahertz emitters**
Optics Express **27**, 13108 (2019)

153. Slobodianiuk, D.V.; Melkov, G.A.; Schultheiß, K.; Schultheiß, H.; Verba, R.V.
**Nonlinear ferromagnetic resonance in the presence of 3-magnon scattering in magnetic nanostructures**
IEEE Magnetics Letters **10**, 6103405 (2019)

154. Smith, T.; Merchel, S.; Pavetich, S.; Rugel, G.; Scharf, A.; Leya, I.
**The constancy of galactic cosmic rays as recorded by cosmogenic nuclides in iron meteorites**
Meteoritics & Planetary Science **54**, 2951 (2019)

155. Solina, D.; Schmidt, W.; Kaltofen, R.; Krien, C.; Lai, C.-H.; Schreyer, A.
**The magnetic structure of $L1_0$ ordered MnPt at room temperature determined using polarized neutron diffraction**
Materials Research Express **6**, 076105 (2019)

156. Spindlberger, L.; Prucnal, S.; Aberl, J.; Brehm, M.
**Thermal Stability of Defect-Enhanced Ge on Si Quantum Dot Luminescence upon Millisecond Flash Lamp Annealing**
Physica Status Solidi (A) **216**, 1900307 (2019)

157. Steier, P.; Martschini, M.; Buchriegler, J.; Feige, J.; Lachner, J.; Merchel, S.; Michlmayr, L.; Priller, A.; Rugel, G.; Schmidt, E.; Wallner, A.; Wild, E.M.; Golser, R.
**Comparison of methods for the detection of $^{10}$Be with AMS and a new approach based on a silicon nitride foil stack**
International Journal of Mass Spectrometry **444**, 116175 (2019)

158. Steinbach, G.; Schreiber, M.; Nissen, D.; Albrecht, M.; Novak, E.; Sánchez, P.A.; Kantorovich, S.S.; Gemming, S.; Erbe, A.
**Field-responsive colloidal assemblies defined by magnetic anisotropy**
Physical Review E **100**, 012608 (2019)

159. Steiner, A.M.; Mayer, M.; Schletz, D.; Wolf, D.; Formanek, P.; Hübner, R.; Dulle, M.; Förster, S.; König, T.A.F.; Fery, A.
**Silver Particles with Rhombicuboctahedral Shape and Effective Isotropic Interactions with Light**
Chemistry of Materials **31**, 2822 (2019)

160. Stolle, A.; Schwanghart, W.; Andermann, C.; Bernhardt, A.; Wittmann, H.; Merchel, S.; Rugel, G.; Fort, M.; Adhikari, B.R.; Korup, O.
**Protracted river response to medieval earthquakes**
Earth Surface Processes and Landforms **44**, 331 (2019)

161. Stor, T.; Schaller, M.; Merchel, S.; Martínek, K.; Rittenour, T.; Rugel, G.; Scharf, A.
**Quaternary evolution of the Ploučnice River system (Bohemian Massif) based on fluvial deposits dated with optically stimulated luminescence and in situ-produced cosmogenic nuclides**
Geomorphology **329**, 152 (2019)

162. Šujan, M.; Braucher, R.; Šujan, M.; Hók, J.; Povinec, P.P.; Šipka, F.; Rugel, Georg; Scharf, A.
**The tectono-sedimentary evolution of a major seismogenic zone with low slip rate activity: A geochronological and sedimentological investigation of the Dobrá Voda Depression (Western Carpathians)**
Sedimentary Geology **383**, 248 (2019)

163. Suschke, K.; Gupta, P.; Williams, G.V.M.; Hübner, R.; Markwitz, A.; Kennedy, J.
**Observation of multiple magnetic phases and complex nanostructures in Co implanted amorphous carbon films**
Journal of Physics and Chemistry of Solids **127**, 158 (2019)

164. Tiessen, C.; Bemmerer, D.; Rugel, G.; Querfeld, R.; Scharf, A.; Steinhauser, G.; Merchel, S.
**Accelerator mass spectrometry (AMS) for beryllium-7 measurements in smallest rainwater samples**
Journal of Radioanalytical and Nuclear Chemistry **319**, 965 (2019)

165. Titova, A.; Fowley, C.; Clifford, E.; Lau, Y.-C.; Borisov, K.; Betto, D.; Atcheson, G.; Hübner, R.; Xu, C.; Stamenov, P.; Coey, M.; Rode, K.; Lindner, J.; Fassbender, J.; Deac, A.M.
**Effect of insertion layer on electrode properties in magnetic tunnel junctions with a zero-moment half-metal**
Scientific Reports **9**, 4020 (2019)

166. Tsai, H.-S.; Liu, F.-W.; Liou, J.-W.; Chi, C.-C.; Tang, S.-Y.; Wang, C.; Ouyang, H.; Chueh, Y.-L.; Liu, C.; Zhou, S.; Woon, W.-Y.
**Direct Synthesis of Large-Scale Multilayer $TaSe_2$ on $SiO_2$/Si Using Ion Beam Technology**
ACS Omega **4**, 17536 (2019)

167. Tyschenko, I.E.; Voelskow, M.; Mikhaylov, A.N.; Tetelbaum, D.I.
**Diffusion and Interaction of In and As Implanted into $SiO_2$ Films**
Semiconductors **53**, 1004 (2019)

168. Ueda, M.; Silva, C.; de Souza, G.B.; Pichon, L.; Reuther, H.
**High temperature plasma immersion ion implantation using hollow cathode discharges in small diameter metal tubes**
Journal of Vacuum Science & Technology B **37**, 042902 (2019)

169. Vallinayagam, M.; Posselt, M.; Faßbender, J.
**Investigation of structural models for O-Y and O-Y-Ti clusters in bcc Fe: A DFT study**
Journal of Physics: Condensed Matter **31**, 095701 (2019)

170. Vallinayagam, M.; Posselt, M.; Faßbender, J.
**Interaction of O-Y and O-Y-Ti clusters embedded in bcc Fe with He, vacancies and self-interstitial atoms**
Journal of Physics: Condensed Matter **31**, 485702 (2019)

171. Vegesna, S.V.; Bürger, D.; Patra, R.K.; Dellith, J.; Abendroth, B.; Skorupa, I.; Schmidt, O.G.; Schmidt, H.
**Tunable large field magnetoconductance of ZnO, ZnMnO, and ZnCoO thin films**
Journal of Applied Physics **125**, 215305 (2019)

172. Venanzi, T.; Arora, H.; Erbe, A.; Pashkin, O.; Winnerl, S.; Helm, M.; Schneider, H.
**Exciton localization in $MoSe_2$ monolayer induced by adsorbed gas molecules**
Applied Physics Letters **114**, 172106 (2019)

173. Volkov, O.M.; Kakay, A.; Florian, K.; Mönch, J.I.; Mohamad-Assaad, M.; Faßbender, J.; Makarov, D.
**Experimental Observation of Exchange-Driven Chiral Effects in Curvilinear Magnetism**
Physical Review Letters **123**, 077201 (2019)

174. Volkov, O.M.; Kronast, F.; Mönch, I.; Mawass, M.-A.; Kákay, A.; Fassbender, J.; Makarov, D.
**Experimental and Theoretical Study of Curvature Effects in Parabolic Nanostripes**
Physica Status Solidi (RRL) **13**, 1800309 (2019)

175. Volkov, O.M.; Rößler, U.K.; Faßbender, J.; Makarov, D.
**Concept of artificial magnetoelectric materials via geometrically controlling curvilinear helimagnets**
Journal of Physics D: Applied Physics **52**, 345001 (2019)

176. Wagner, C.; Meszmer, P.; Blaudeck, T.; Böttger, S.; Fuchs, F.; Hermann, S.; Schuster, J.; Wunderle, B.; Schulz, S.E.
**Carbon nanotubes for mechanical sensor applications**
Physica Status Solidi (A) **216**, 1900584 (2019)

177. Wagner, C.; Schuster, J.; Schleife, A.
**Strain and screening: Optical properties of a small-diameter carbon nanotube from first principles**
Physical Review B **99**, 075140 (2019)

178. Wallner, A.; Bichler, M.; Coquard, L.; Dillmann, I.; Forstner, O.; Golser, R.; Heil, M.; Käppeler, F.; Kutschera, W.; Martschini, M.; Mengoni, A.; Merchel, S.; Michlmayr, L.; Priller, A.; Steier, P.; Wiescher, M.
**Stellar and thermal neutron capture cross section of $^9$Be**
Physical Review C **99**, 015804 (2019)

179. Wang, C.; Chang, C.-H.; Huang, A.; Wang, P.-C.; Wu, P.-C.; Yang, L.; Xu, C.; Pandey, P.; Zeng, M.; Böttger, R.; Jeng, H.-T.; Zeng, Y.-J.; Helm, M.; Chu, Y.-H.; Ganesh, R.; Zhou, S.
**Tunable disorder and localization in the rare-earth nickelates**
Physical Review Materials **3**, 053801 (2019)

180. Wang, C.; Zhang, H.; Deepak, K.; Chen, C.; Fouchet, A.; Duan, J.; Hilliard, D.; Kentsch, U.; Chen, D.; Zeng, M.; Gao, X.; Zeng, Y.-J.; Helm, M.; Prellier, W.; Zhou, S.
**Tuning the metal-insulator transition in epitaxial $SrVO_3$ films by uniaxial strain**
Physical Review Materials **3**, 115001 (2019)

181. Wang, M.; Debernardi, A.; Berencen, Y.; Heller, R.; Xu, C.; Yuan, Y.; Xie, Y.; Böttger, R.; Rebohle, L.; Skorupa, W.; Helm, M.; Prucnal, S.; Zhou, S.
**Breaking the Doping Limit in Silicon by Deep Impurities**
Physical Review Applied **11**, 054039 (2019)

182. Wang, M.; Hübner, R.; Xu, C.; Xie, Y.; Berencen, Y.; Heller, R.; Rebohle, L.; Helm, M.; Prucnal, S.; Zhou, S.
**Thermal stability of Te-hyperdoped Si: Atomic-scale correlation of the structural, electrical, and optical properties**
Physical Review Materials **3**, 044606 (2019)

183. Wang, X.; Faßbender, J.; Posselt, M.
**Efficient calculation methods for the diffusion coefficient of interstitial solutes in dilute alloys**
Materials **12**, 1491 (2019)

184. Wang, Y.; Zhang, N.; Hübner, R.; Tan, D.; Löffler, M.; Facsko, S.; Zhang, E.; Ge, Y.; Qi, Z.; Wu, C.
**Enzymes Immobilized on Carbon Nitride ($C_3N_4$) Cooperating with Metal Nanoparticles for Cascade Catalysis**
Advanced Materials Interfaces **6**, 1801664 (2019)

185. Wehmeier, L.; Lang, D.; Liu, Y.; Zhang, X.; Winnerl, S.; Eng, L.M.; Kehr, S.C.
**Polarization-dependent near-field phonon nanoscopy of oxides: $SrTiO_3$, $LiNbO_3$, and $PbZr_{0,2}Ti_{0,8}O_3$**
Physical Review B **100**, 035444 (2019)

186. Wilhelm, R.A.; Grande, P.L.
**Unraveling energy loss processes of low energy heavy ions in 2D materials**
Communications Physics **2**, 89 (2019)

187. Willig, L.; von Reppert, A.; Deb, M.; Ganss, F.; Hellwig, O.; Bargheer, M.
**Finite-size effects in ultrafast remagnetization dynamics of FePt**
Physical Review B **100**, 224408 (2019)

188. Wu, H.; Böttger, R.; Couffignal, F.; Gutzmer, J.; Krause, J.; Munnik, F.; Renno, A.; Hübner, R.; Wiedenbeck, M.; Ziegenrücker, R.
**'Box-Profile' Ion Implants as Geochemical Reference Materials for Electron Probe Microanalysis and Secondary Ion Mass Spectrometry**
Geostandards and Geoanalytical Research **43**, 531 (2019)

189. Xu, C.; Wang, M.; Yuan, Y.; Larkin, G.; Helm, M.; Zhou, S.
**Hole compensation effect in III-Mn-V dilute ferromagnetic semiconductors**
Journal of Physics D: Applied Physics **52**, 355301 (2019)

190. Xu, C.; Wang, M.; Zhang, X.; Yuan, Y.; Zhou, S.
**Ferromagnetic (In,Ga,Mn)As films prepared by ion implantation and pulsed laser melting**
Nuclear Instruments and Methods in Physics Research B **442**, 31 (2019)

191. Xu, C.; Zhang, C.; Wang, M.; Xie, Y.; Hübner, R.; Heller, R.; Yuan, Y.; Helm, M.; Zhang, X.; Zhou, S.
**p-type codoping effect in (Ga,Mn)As: Mn lattice location versus magnetic properties**
Physical Review Materials **3**, 084604 (2019)

192. Xu, K.; Gabourie, A.J.; Hashemi, A.; Fan, Z.; Wei, N.; Farimani, A.B.; Komsa, H.-P.; Krasheninnikov, A.; Pop, E.; Ala-Nissila, T.
**Thermal Transport in $MoS_2$ from Molecular Dynamics using Different Empirical Potentials**
Physical Review B **99**, 054303 (2019)

193. Xu, M.; Liu, X.; Li, M.; Liu, K.; Qu, G.; Wang, V.; Hu, L.; Schneider, H.
**Transient Characteristics of Interdigitated GaAs Photoconductive Semiconductor Switch at 1-kHz Excitation**
IEEE Electron Device Letters **40**, 1136 (2019)

194. Yang, C.; Dong, R.; Wang, M.; Petkov, P.S.; Zhang, Z.; Wang, M.; Han, P.; Ballabio, M.; Bräuninger, S.A.; Liao, Z.; Zhang, J.; Schwotzer, F.; Zschech, E.; Klauss, H.-H.; Cánovas, E.; Kaskel, S.; Bonn, M.; Zhou, S.; Heine, T.; Feng, X.
**A semiconducting layered metal-organic framework magnet**
Nature Communications **10**, 3260 (2019)

195. Zhang, C.; Yuan, Y.; Wang, M.; Li, P.; Zhang, J.; Wen, Y.; Zhou, S.; Zhang, X.X.
**Critical behavior of intercalated quasi-van der Waals ferromagnet $Fe_{0.26}TaS_2$**
Physical Review Materials **3**, 114403 (2019)

196. Zhang, W.; Wang, M.; Wang, L.; Liu, C.H.; Chang, H.; Yang, J.J.; Liao, J.L.; Yang, Y.Y.; Liu, N.
**Interface stability, mechanical and corrosion properties of AlCrMoNbZr/(AlCrMoNbZr)N high-entropy alloy multilayer coatings under helium ion irradiation**
Applied Surface Science **485**, 108 (2019)

197. Zhang, X.; Xu, M.; Li, Q.; Wang, M.; Akhmadaliev, S.; Zhou, S.; Wu, Y.; Guo, B.
**Optical properties of $ZnS_xTe_{1-x}$ synthesized by sulfur implantation**
Nuclear Instruments and Methods in Physics Research B **442**, 24 (2019)

198. Zhou, S.; Chen, X.
**Defect-induced magnetism in SiC**
Journal of Physics D: Applied Physics **52**, 393001 (2019)

199. Zhu, J.; Xia, Y.; Li, G.; Zhou, S.; Wimmer, S.; Springholz, G.; Pashkin, O.; Helm, M.; Schneider, H.
**Absorption edge, Urbach tail, and electron-phonon interactions in topological insulator $Bi_2Se_3$ and band insulator $(Bi_{0.89}In_{0.11})_2Se_3$**
Applied Physics Letters **114**, 162105 (2019)

200. Zinovieva, A.F.; Zinovyev, V.A.; Stepina, N.P.; Katsuba, A.V.; Dvurechenskii, A.V.; Gutakovskii, A.K.; Kulik, L.V.; Bogomyakov, A.S.; Erenburg, S.B.; Trubina, S.V.; Voelskow, M.
**Electron Paramagnetic Resonance in Ge/Si Heterostructures with Mn-Doped Quantum Dots**
JETP Letters **109**, 270 (2019)

## Publications in conference proceedings

201. Braun, J.M.; Schneider, H.; Helm, M.; Mirek, R.; Boatner, L.A.; Marvel, R.E.; Haglund, R.F.; Pashkin, A.
**Optical Pump – THz Probe Response of $VO_2$ under High Pressure**
XXI International Conference on Ultrafast Phenomena, 15.–20.07.2018, Hamburg, Germany
EPJ Web of Conferences **205**, 04003 (2019)

202. Campillo, G.; Figueroa, A.I.; Arnache, O.; Osorio, J.; Marín Ramírez, J.M.; Fallarino, L.
**A brief discussion of the magnetocaloric effect in thin films of manganite doped with chromium**
VI Congreso Nacional de Ingeniería Física, 22.–26.10.2018, Bucaramanga, Colombia
Journal of Physics: Conference Series **1247**, 012013 (2019)

203. Ciano, C.; Montanari, M.; Persichetti, L.; Di Gaspare, L.; Virgilio, M.; Bagolini, L.; Capellini, G.; Zoellner, M.; Skibitzki, O.; Stark, D.; Scalari, G.; Faist, J.; Rew, K.; Paul, D.J.; Grange, T.; Birner, S.; Pashkin, O.; Helm, M.; Baldassarre, L.; Ortolani, M.; de Seta, M.
**Electron-doped SiGe Quantum Well Terahertz Emitters pumped by FEL pulses**
2019 44th International Conference on Infrared, Millimeter, and Terahertz Waves (IRMMW-THz), 01.–06.09.2019, Paris, France, DOI: 10.1109/IRMMW-THz.2019.8873894

204. Fotev, I.; Balaghi, L.; Shan, S.; Hübner, R.; Schmidt, J.; Schneider, H.; Helm, M.; Dimakis, E.; Pashkin, O.
**Pump – Probe THz Spectroscopy Study of Electronic Properties of Semiconductor Nanowires**
2019 44th International Conference on Infrared, Millimeter, and Terahertz Waves (IRMMW-THz), 01.–06.09.2019, Paris, France, DOI: 10.1109/IRMMW-THz.2019.8874068

205. Meng, F.; Thomson, M.D.; Klug, B.; Ul-Islam, Q.; Pashkin, O.; Schneider, H.; Roskos, H.G.
**Cavity enhanced third-harmonic generation in Si:B pumped with intense terahertz pulses**
2019 44th International Conference on Infrared, Millimeter, and Terahertz Waves (IRMMW-THz), 01.–06.09.2019, Paris, France, DOI: 10.1109/IRMMW-THz.2019.8874582

206. Mitteramskogler, T.; Haslinger, M.J.; Wennberg, A.; Fernandez Martínez, I.; Muehlberger, M.; Krause, M.; Guillén, E.
**Preparation and Characterization of Solar Thermal Absorbers by Nanoimprint Lithography and Sputtering**
2019 MRS Spring Meeting & Exhibition, 22.–26.04.2019, Phoenix, USA
MRS Advances **4**, 1905 (2019)

207. Pereira, P.H.; Penello, G.M.; Pires, M.P.; Helm, M.; Schneider, H.; Souza, P.L.
**Effect of the dopant location and the number of Bragg mirrors on the performance of superlattice infrared photodetectors**
2019 34th Symposium on Microelectronics Technology and Devices (SBMicro), 26.–30.08.2019, São Paulo, Brazil, DOI: 10.1109/SBMicro.2019.8919485

208. Rana, R.; Balaghi, L.; Fotev, I.; Schneider, H.; Helm, M.; Dimakis, E.; Pashkin, O.
**Plasmonic nonlinearity in GaAs/$In_{0.20}Ga_{0.80}As$ core/shell nanowires**
2019 44th International Conference on Infrared, Millimeter, and Terahertz Waves (IRMMW-THz), 01.–06.09.2019, Paris, France, DOI: 10.1109/IRMMW-THz.2019.8874085

209. Rana, R.; Klopf, J.M.; Grenzer, J.; Schneider, H.; Helm, M.; Pashkin, A.
**Ultrafast metallization in $NbO_2$ studied by pump-probe THz spectroscopy**
2019 44th International Conference on Infrared, Millimeter, and Terahertz Waves (IRMMW-THz), 01.–06.09.2019, Paris, France, DOI: 10.1109/IRMMW-THz.2019.8873838

210. Singh, A.; Pashkin, O.; Winnerl, S.; Helm, M.; Schneider, H.
**Filling the 5-10 THz gap using Ge-based photoconductive emitter**
2019 Conference on Lasers and Electro-Optics (CLEO), 05.–10.05.2019, San José, USA, DOI: 10.1364/CLEO_SI.2019.STu3F.3

211. Singh, A.; Welsch, M.; Winnerl, S.; Helm, M.; Schneider, H.
**Scalable Large-Area Terahertz Emitters with Improved Electrode Design**
2019 44th International Conference on Infrared, Millimeter, and Terahertz Waves (IRMMW-THz), 01.–06.09.2019, Paris, France, DOI: 10.1109/IRMMW-THz.2019.8874010

## Patents

1. Samad, F.; Koch, L.; Arekapudi, S.S.P.K.; Schultheiß, H.; Hellwig, O.
**Magnetische Streufeld-Struktur, magnonisches Bauelement und Verfahren zur Herstellung einer magnetischen Streufeld-Struktur, DE 10 2019 129 203.4**
submitted to Deutsches Patent- und Markenamt (DPMA): 29.10.2019

# Concluded scientific degrees

## PhD theses

1. Baghban Khojasteh Mohammadi, Nasrin
   **Chemical analysis of solid-liquid interfaces by Liquid-Rutherford Backscattering Spectrometry**
   *TU Dresden, 10.09.2019*
2. Blaschke, Daniel
   **Memristive Eigenschaften von Hafniumdioxid- und Titandioxid-Dünnschichten**
   *TU Chemnitz, 12.06.2019*
3. Braun, Johannes
   **Ultrafast response of photoexcited carriers in transition metal oxides under high pressure**
   *TU Dresden, 21.05.2019*
4. Canon Bermudez, Gilbert Santiago
   **Magnetosensitive e-skins for interactive electronics**
   *TU Dresden, 08.11.2019*
5. Cansever, Hamza
   **Spin-transfer torque induced by thermal gradients in magnetic tunnel junctions investigated using micro cavity ferromagnetic resonance**
   *TU Dresden, 05.04.2019*
6. Lang, Denny
   **Infrared nanospectroscopy at cryogenic temperatures and on semiconductor nanowires**
   *TU Dresden, 16.09.2019*
7. Schmidt, Johannes
   **THz pump-probe spectroscopy of the intersubband AC-Stark effect in a GaAs quantum well**
   *TU Dresden, 11.11.2019*
8. Schneider, Tobias
   **Spin dynamics and transport in magnetic heterostructures**
   *TU Chemnitz, 15.03.2019*
9. Tauchnitz, Tina
   **Novel methods for controlled growth of GaAs nanowires and GaAs/$Al_xGa_{1-x}As$ axial nanowire heterostructures on Si substrates by molecular beam epitaxy**
   *TU Dresden, 13.12.2019*
10. Titova, Alexandra
    **Spin-transport in magnetic tunnel junctions with a zero-moment half-metallic electrode**
    *TU Dresden, 17.12.2019*
11. Wang, Mao
    **Silicon hyperdoped with tellurium: Physical structure, electrical transport and infrared photoresponse**
    *TU Dresden, 07.10.2019*
12. Xu, Chi
    **Application of ion beams on fabricating and manipulating III-Mn-V dilute ferromagnetic semiconductors**
    *TU Dresden, 30.10.2019*

## Bachelor/Master/Diploma theses

1. Fekri, Zahra
   **Fabrication and characterization of $MoS_2$ based field effect transistor**
   *TU Dresden (M.Sc.), 26.09.2019*

2. Jagtap, Nagesh
   **Fabrication and characterization of string resonator structures in silicon carbide for hybrid spin-mechanical systems**
   *TU Dresden (M.Sc.), 11.12.2019*

3. Kateel, Vaishnavi
   **Fabrication and characterization of two-dimensional van der Waals heterostructures**
   *TU Dresden (M.Sc.), 25.09.2019*

4. Körber, Lukas
   **Theory and simulation on nonlinear spin-wave dynamics in magnetic vortices**
   *TU Dresden (M.Sc.), 22.10.2019*

5. Preis, Kevin
   **Theoretische Untersuchung der komplexen Bandstruktur konjugierter Polymere mit der dichtefunktionalbasierten Tight-Binding Methode**
   *TU Chemnitz (B.Sc.), 09.09.2019*

6. Roscher, Willi
   **Statistische Untersuchung zufälliger Konfigurationen des SiGe:C Kristalls mit Dichtefunktionaltheorie**
   *TU Chemnitz (M.Sc.), 29.04.2019*

7. Weinhold, Tillmann
   **Comparison of different approaches of wave vector resolved Brillouin light scattering spectroscopy for investigating interfacial Dzyaloshinskii–Moriya interaction**
   *TU Dresden (M.Sc.), 16.10.2019*

8. Welsch, Malte
   **Optimization of broadband photoconductive terahertz emitters**
   *TU Dresden (M.Sc.), 14.11.2019*

# Awards and honors

1. **Duan, Juanmei**

   PhD student in the department “Semiconductor Materials” won the **Graduate Student Award** of the E-MRS Fall Meeting 2019 for her presentation "Tunable plasmonics in heavily doped GaAs fabricated by ion implantation and sub-second annealing", Warsaw, Poland, Sept. 16 – 19, 2019.

2. **Hache, Toni**

   PhD student in the Emmy-Noether group “Magnonics” received the **Mentor-Prize** of the FH Zwickau (WSHZ) in the Category 'Technik' for his Master’s Thesis “Preparation and Characterization of Spin-Hall Effect-based nano Microwave Oscillators”.

3. **König-Otto, Jacob**

   Former PhD student of the department “Spectroscopy“ won the **HZDR PhD Award 2019** for his dissertation “Ladungsträgerdynamik in Graphen unterhalb der optischen Phononenergie”.

4. **Kosub, Tobias**

   Member of the department “Intelligent Materials and Systems” received a Helmholtz Enterprise Funding Grant “Tensormeter” between 02/2019 – 06/2020.

5. **Krasheninnikov, Arkady**

   Head of the group “Atomistic Simulations of Irradiation-induced Phenomena” was announced as Highly Cited Researcher 2019 by Clarivate Analytics (Web of Science), Philadelphia, PA, USA.

6. **Makarov, Denys**

   Head of the department “Intelligent Materials and Systems” was awarded the **HZDR Research Prize 2019** for his work in the field of magnetic sensor technology for microfluidics and augmented reality. Furthermore, he received a **Fudan Fellow Grant**. He was invited to the Department of Material Science at the Fudan University, China, to carry out studies on shapeable magnetoelectronics and active soft matter.

7. **Singh, Abhishek**

   Postdoc in the department "Spectroscopy" was selected by the International Union of Radio Science (Union Radio-Scientifique Internationale, URSI) for a **URSI Young Scientist Award** for his remarkable achievements in the field of photoconductive terahertz emitters on the occasion of the 2019 URSI Asia-Pacific Radio Science Conference, New Delhi, India, March 9 – 15, 2019.

8. **Wagner, Kai**

Former PhD student in the Emmy-Noether group “Magnonics” received the **Dresdner Promotionspreis Physik 2019** of the Faculty of Physics, TU Dresden for his dissertation ”Spin-wave generation and transport in magnetic microstructures”.

9. **Wang, Mao**

PhD student in the department “Semiconductor Materials” won the **Graduate Student Award** at the E-MRS Spring Meeting 2019 for her presentation "Breaking the doping limit in silicon by deep-level impurities”, Nice, France, May 27 – 31, 2019.

# Invited conference contributions

1. Akhmadaliev, S.
**Commercial applications of research institute Tandem accelerators: the Rossendorf example**
NUSPRASEN Workshop on Nuclear Science Applications, 25.–27.11.2019, Helsinki, Finland

2. Astakhov, G.
**Engineering and coherent control of defect qubits in SiC at room temperature**
1st Sino-German Symposium on "Defect Engineering in SiC Device Manufacturing – Atomistic Simulations, Characterization and Processing", 10.-14.11.2019, Beijing, China

3. Astakhov, G.
**Room temperature coherent control of spin qudit modes in SiC**
Colloquium on Quantum Technology: Quantum Sensing, Quantum-IT, Quantum Computing, Simulation, Industrialization, 09.10.2019, Esslingen, Germany

4. Astakhov, G.V.
**Coherent control of qudit modes in SiC at room temperature**
4th International Conference on Metamaterials and Nanophotonics METANANO 2019, Special Symposium QuantuMetanano, 14.–19.07.2019, Saint Petersburg, Russia

5. Astakhov, G.V.
**Effect of irradiation on defect coherence properties in silicon carbide**
Ion Beams for Future Technologies 2019, 01.–03.04.2019, Dubrovnik, Croatia

6. Awari, N.; Ilaykov, I.; Fowley, C.; Rode, K.; Lau, Y.-C.; Betto, D.; Thiyagarajah, N.; Green, B.W.; Yildrim, O.; Lindner, J.; Faßbender, J.; Coey, M.; Deac, A.M.; Gensch, M.; Kovalev, S.
**Narrow band tunable spintronic THz emission from ferrimagnetic nano-films**
International Conference on Optics and Electro-Optics 2019, 19.–22.10.2019, Dehradun, India

7. Bali, R.; Schmeink, A.H.; Eggert, B.; Ehrler, J.; Liersch, V.; Semisalova, A.; Hlawacek, G.; Potzger, K.; Faßbender, J.; Thomson, T.; Wende, H.; Lindner, J.
**Nanoscale Ferromagnetism in Alloy Thin Film via Lattice Disordering**
Symposium ”Spins, Waves and Interactions“, 03.–05.09.2019, Greifswald, Germany

8. Bali, R.; Schmeink, A.H.; Eggert, B.; Ehrler, J.; Liersch, V.; Semisalova, A.; Hlawacek, G.; Potzger, K.; Faßbender, J.; Thomson, T.; Wende, H.; Lindner, J.
**Nanoscale Ferromagnetism in Alloy Thin Film via Lattice Disordering**
6th International Conference “From Nanoparticles and Nanomaterials to Nanodevices and Nanosystems” (6th IC4N), 30.06.–03.07.2019, Corfu, Greece

9. Bischoff, L.; Mazarov, P.; Pilz, W.; Klingner, N.; Gierak, J.
**Ion Sources for Focused Ion Beams – Present Status and Prospective Developments**
European FIB Network, 3rd EuFN Workshop 2019, 12.–14.06.2019, Dresden, Germany

10. Cansever, H.; Lenz, K.; Narkowicz, R.; Kowalska, E.; Faßbender, J.; Deac, A.M.; Lindner, J.
**Ferromagnetic resonance detection in magnetic single objects via a novel microresonator and microantenna approach**
9th APMAS 2019 - International Advances in Applied Physics & Materials Science Congress & Exhibition, 20.–28.10.2019, Fethiye, Turkey

11. Facsko, S.
**Emergence of nanoscale patterns under ion induced non-equilibrium conditions**
23rd International Workshop on Inelastic Ion-Surface Collisions, 17.–22.11.2019, Matsue, Japan

12. Fuchs, F.; Gemming, S.; Schuster, J.
**Understanding the electron transport through $NiSi_2$-Si interfaces**
International Workshop "Correlations and transport in one-dimensional structures", 04.–07.07.2019, Dresden, Germany

13. Georgiev, Y.
**Junctionless Nanowire Transistors: an Excellent Platform for Ultrasensitive Chemo/Biosensors**
IHRS NanoNet International Conference, 08.–11.10.2019, Dresden, Germany

14. Gierak, J.; Mazarov, P.; Bruchhaus, L.; Jede, R.; Bischoff, L.
**Electro-Hydro Dynamic Ion Sources and Focused Ion Beam Machines**
2019 MRS Fall Meeting, 01.–06.12.2019, Boston, USA

15. Helm, M.
**THz relaxation dynamics and nonlinear optics in graphene**
2D Materials 2019, 30.09.–04.10.2019, Sochi, Russia

16. Hlawacek, G.
**Nanostructure characterization with ions**
8th EU Korea Nanoworkshop, 25.11.2019, Brüssel, Belgien

17. Hlawacek, G.
**Focused ion beam materials modification with noble gas ions**
23rd International Workshop on Inelastic Ion-Surface Collisions, 20.11.2019, Matsue, Japan

18. Hlawacek, G.
**Spatially resolved materials modification using Helium Ion Microscopy**
63rd International Conference on Electron, Ion, and Photon Beam Technology and Nanofabrication (EIPBN), 30.05.2019, Minneapolis, USA

19. Hlawacek, G.
**High resolution materials modification with low fluence Helium Ion Microscopy**
1st Sino-German Symposium on "Defect Engineering in SiC Device Manufacturing - Atomistic Simulations, Characterization and Processing" DESiC 2019, 12.11.2019, Beijing, China

20. Hlawacek, G.
**In-situ experiments and characterization in the Helium Ion Microscope**
Ion beams for future technologies 2019, 02.04.2019, Dubrovnik, Croatia

21. Hlawacek, G.; Klingner, N.; Veligura, V.; Xu, X.; Serralta Hurtado De Menezes, E.; Schmeink, A.H.; Borany, J.; Facsko, S.
**Analytic approaches for Helium Ion Microscopy**
Zakopane School of Physics, 24.05.2019, Zakopane, Poland

22. Kelling, J.; Ódor, G.; Gemming, G.
**Solving the Kuramoto Oscillator Model on Random Graphs**
GPU Day 2019, 11.–12.07.2019, Budapest, Hungary

23. Makarov, D.
**Compliant magnetic field sensors for flexible electronics**
FFlexCom Meeting 2019; DFG Priority Programme “High Frequency Flexible Bendable Electronics for Wireless Communication Systems”, SPP 1796, 07.10.2019, Dresden, Germany

24. Makarov, D.
**Curved magnetic thin films: fundamentals and applications**
Joint European Magnetic Symposia (JEMS), 26.–30.08.2019, Uppsala, Sweden

25. Makarov, D.
**Application of Magnetism on Curved Surfaces**
European Forum for Science, Research and Innovation, 24.–25.06.2019, Dresden, Germany

26. Makarov, D.
**Flexible magnetoelectronics**
Nanoforum 2019, 17.05.2019, Linz, Austria

27. Makarov, D.
**Droplet-based magnetofluidic platforms for detection and analytics**
The 2019 Joint MMM-Intermag Conference, 14.–18.01.2019, Washington DC, USA

28. Makarov, D.
**Mechanical compliancy for magnetic field sensors**
Magnetic Frontiers 2019: Magnetic Sensors, 24.–27.06.2019, Lisbon, Portugal

29. Makarov, D.
**Curvilinear magnetism**
6th International Conference 'From Nanoparticles and Nanomaterials to Nanodevices and Nanosystems', 30.06.–03.07.2019, Corfu, Greece

30. Makarov, D.
**Flexible electronics: from interactive on-skin devices to bio/medical applications**
Workshop on Active and Passive Materials for Tissue Engineering and Biomedical Applications, 30.10.2019, Shanghai, China

31. Mazarov, P.; Bruchhaus, L.; Nadzeyka, A.; Richter, T.; Jede, R.; Yu, Y.; Sanabia, J.E.; Bischoff, L.; Pilz, W.; Klingner, N.; Hlawacek, G.
**New light and heavy ion beams from liquid metal alloy ion sources for advanced nanofabrication and ion implantation**
2019 MRS Fall Meeting, 01.–06.12.2019, Boston, USA

32. Mazarov, P.; Richter, T.; Bruchhaus, L.; Jede, R.; Yu, Y.; Sanabia, J.E.; Bischoff, L.; Gierak, J.
**Light and Heavy Ions from New Non-classical Liquid Metal Ion Sources for Advanced Nanofabrication**
AVS 66th International Symposium & Exhibition, 20.–25.10.2019, Columbus, OH, USA

33. Merchel, S.; Rugel, G.; DREAMS-Users; DREAMS-Friends
**Chemistry first, Accelerator Mass Spectrometry (AMS) second**
52nd Annual conference of the German Society for Mass Spectrometry (DGMS), 10.–13.03.2019, Rostock, Germany

34. Merchel, S.; Rugel, G.; Wallner, A.; DREAMS-Friends/Users
**Bedtime stories from space - Cosmogenic nuclides investigated by accelerator mass spectrometry**
Colloquium Analytische Atomspektroskopie 2019 (canas 2019), 23.–26.09.2019, Freiberg, Germany

35. Pashkin, O.; Singh, A.; Winnerl, S.; Helm, M.; Schneider, H.
**Photoconductive germanium antenna emitting broadband THz pulses**
Advanced Electromagnetics Symposium AES 2019, 24.–26.07.2019, Lisbon, Portugal

36. Rugel, G.; Tiessen, C.J.; Bemmerer, D.; Querfeld, R.; Scharf, A.; Steinhauser, G.; Merchel, S.
**Ultrasensitive (<1 mBq), cheap, and fast detection method for $^{7}$Be allowing high sample throughput**
2nd International Conference on Radioanalytical and Nuclear Chemistry (RANC 2019), 05.–10.05.2019, Budapest, Hungary

37. Schneider, H.
**Nonlinear terahertz spectroscopy of III-V semiconductor quantum wires and quantum wells using a free-electron laser**
Light Conference 2019, 16.–18.07.2019, Changchun, China

38. Schultheiss, H.
**Magnon Transport in Spin Textures**
MLZ Conference: Neutrons for Information and Quantum Technologies, 04.06.2019, Lenggries, Germany

39. Schultheiss, H.
**Magnon Transport in Spin Textures**
Magnonics 2019, 28.07.2019, Carovigno, Italy

40. Schultheiss, K.; Verba, R.; Wehrmann, F.; Wagner, K.; Körber, L.; Hula, T.; Hache, T.; Kákay, A.; Awad, A.A.; Tiberkevich, V.; Slavin, A.N.; Fassbender, J.; Schultheiss, H.
**Excitation of whispering gallery magnons in a magnetic vortex**
APS March Meeting, 04.03.2019, Boston, USA

41. Schultheiss, K.; Verba, R.; Wehrmann, F.; Wagner, K.; Körber, L.; Hula, T.; Hache, T.; Kákay, A.; Awad, A.A.; Tiberkevich, V.; Slavin, A.N.; Fassbender, J.; Schultheiss, H.
**Excitation of whispering gallery magnons in a magnetic vortex**
Magnetics and Optics Research International Symposium, 24.06.2019, Prague, Czech Republic

42. Schultheiss, K.; Verba, R.; Wehrmann, F.; Wagner, K.; Körber, L.; Hula, T.; Hache, T.; Kákay, A.; Awad, A.A.; Tiberkevich, V.; Slavin, A.N.; Fassbender, J.; Schultheiss, H.
**Excitation of whispering gallery magnons in a magnetic vortex**
Conference on Magnetism and Magnetic Materials (MMM), 06.11.2019, Las Vegas, USA

43. Skorupa, W.; Quade, A.; Schäfer, J.; Schumann, T.; Eule, D.
**Antikorrosive Wirkung nanoskaliger Schichten auf metallischen Legierungen im Orgelbau**
BDO-Workshop Bleikorrosion (Bund Deutscher Orgelbaumeister e.V.), 24.–25.10.2019, Ludwigsburg, Germany

44. Sluka, V.; Schneider, T.; Gallardo, R.A.; Kakay, A.; Weigand, M.; Warnatz, T.; Mattheis, R.; Roldan-Molina, A.; Landeros, P.; Tiberkevich, V.; Slavin, A.; Schütz, G.; Erbe, A.; Deac, A.; Lindner, J.; Fassbender, J.; Raabe, J.; Wintz, S.
**Emission and Propagation of Multi-Dimensional Spin Waves in Anisotropic Spin Textures**
11th Joint BER II and BESSY II User Meeting, 04.–06.12.2019, Berlin, Germany

45. Titova, A.; Fowley, C.; Lau, Y.-C.; Borisov, K.; Atcheson, G.; Stamenov, P.; Coey, M.; Rode, K.; Lindner, J.; Faßbender, J.; Deac, A.M.
**Spin-transport in magnetic tunnel junctions with a zero-moment half-metallic electrode**
11th International Workshop on nanomagnetism and its novel applications SpinS-2019, 02.–04.10.2019, Duisburg/Mülheim an der Ruhr, Germany

46. Volkov, O.
**Experimental observation of exchange-driven chiral effects in parabolic nanostripes**
International Workshop “Curvilinear Magnetism”, 23.–24.05.2019, Kyiv, Ukraine

47. Wagner, C.; Gemming, S.
**Calculation of defect- and interface-induced electronic states in 2D materials**
International Symposium on Epi-Graphene, 25.–28.08.2019, Chemnitz, Germany

48. Wagner, C.; Rahaman, M.; Zahn, D.R.T.; Gemming, S.
**Interlayer excitons in van-der-Waals heterostructures from ab-initio perspective - the case of $MoS_2$ on GaSe**
Holzhau-2019 meeting, 25.–27.09.2019, Holzhau, Germany

49. Wilhelm, R.A.
**Ion Beam Spectroscopy with 2D Materials**
International Workshop on Inelastic Ion Surface Collisions, 17.–22.11.2019, Matsue, Japan

50. Wilhelm, R.A.
**Interaction of highly charged ions with 2D materials**
Nanopatterning Workshop, 07.–10.07.2019, Guildford, United Kingdom

51. Wilhelm, R.A.
**Ultrafast neutralization dynamics of highly charged ions upon impact on 2D materials**
Towards Reality in Nanoscale Materials X, 12.–14.02.2019, Levi, Finnland

52. Wilhelm, R.A.
**Collisions of highly charged ions with 2D materials - What we learn from ion transmission spectroscopy**
XXXI International Conference on Photonic, Electronic and Atomic Collisions (ICPEAC), 23.–30.07.2019, Deauville, France

53. Winnerl, S.
**Ultrafast Mid-Infrared and Terahertz Phenomena in Graphene**
Sino-German Bilateral Symposium on Low Dimensional Semiconductors and Opto-electronics Integration, 14.–17.11.2019, Changsha, China

54. Winnerl, S.; Jadidi, M.M.; Chin, M.; Seidl, A.; Schneider, H.; Helm, M.; Drew, H.D.; Murphey, T.E.; Mittendorff, M.
**Nonlinear THz resoponse of graphene plasmonic structures**
10th International Conference on Metamaterials, Photonic Crystals and Plasmonics META 2019, 23.–26.07.2019, Lisbon, Portugal

55. Winnerl, S.; Schmidt, J.; König-Otto, J.; Mittendorff, M.; Schneider, H.; Helm, M.
**Nonlinear THz spectroscopy in low-dimensional semiconductors using a free-electron laser**
Photonics & Electromagnetics Research Symposium (PIERS), 17.–20.06.2019, Rome, Italy

56. Wintz, S.
**Topological spin textures as spin-wave emitters**
6th International Conference from Nanoparticles and Nanomaterials to Nanodevices and Nanosystems (6th IC4N), 30.06.–03.07.2019, Corfu, Greece

57. Wintz, S.
**Spin textures and spin waves as seen by x-ray microscopy**
9th International Conference on Nanomaterials: Applications & Properties (NAP) 2019, 15.–20.09.2019, Odessa, Ukraine

58. Wintz, S.
**Spin textures and spin waves as seen by x-ray microscopy**
Challenges & Opportunities in X-Ray Microscopy, 11.–15.02.2019, Kreuth (Schloss Ringberg), Germany

59. Wintz, S.
**Spin textures and spin waves as seen by x-ray microscopy**
SpinS-2019, 02.–04.10.2019, Duisburg/Mülheim an der Ruhr, Germany

60. Wolff, A.; Klingner, N.; Thompson, W.; Zhou, Y.; Lin, J.; Peng, Y.Y.; Ramshaw, J.A.M.; Xiao, Y.
**Focused ion beams in biology: How the Helium Ion Microscope and FIB/SEMs help reveal nature's tiniest structures**
Microscience Microscopy Congress 2019, 01.–04.07.2019, Manchester, United Kingdom

61. Zhou, S.
**Extended room-temperature infrared photoresponse in hyperdoped Si by ion implantation**
2nd International Conference on Radiation and Emission in Materials, 15.–18.12.2019, Bangkok, Thailand

62. Zhou, S.
**Extended room-temperature infrared photoresponse in hyperdoped Si by ion implantation**
14th National Conference on Laser Technology and Optoelectronics, 17.–20.03.2019, Shanghai, China

63. Zhou, S.; Wang, Y.; Liu, Y.; Gemming, S.; Helm, M.
**Defect induced magnetism in SiC**
1st Sino-German Symposium on "Defect Engineering in SiC Device Manufacturing – Atomistic Simulations, Characterization and Processing", 10.-14.11.2019, Beijing, China

# Conferences, workshops, colloquia and seminars

## Organization of conferences and workshops

1. Bittencourt, C.; Foster, A.; Hynninen, T.; Krasheninnikov, A.
**Towards reality in nanoscale materials X: Energy materials, defects, transport, methods, tools**
*12. – 14.02.2019, Levi, Finland*

2. Chesnel, K.; Hellwig, O.
**Exploring Nanomagnetism in Thin Films**
*12. – 14.11.2019, Brigham Young University, Provo, UT, USA*

3. Engelmann, H.-J.; Hlawacek, G.; Bischoff, L.; Klingner, N.
**3rd European FIB Network Workshop**
*12. – 14.06.2019, HZDR, Dresden, Germany*

4. Escobar Galindo, R.; Ambrossini, A.; Guillén, E.; Krause, M.
**Materials Challenges in Surfaces and Coatings for Solar Thermal Technologies, Symposium ES08 at 2019 MRS Spring Meeting & Exhibit**
*22.04. – 26.04.2019, Phoenix, Arizona, USA*

5. Erbe, A. et al.
**Physics of Self-Organization in DNA Nanostructures, Interdivisional Symposium SYDN at the Annual Spring Meeting of the German Physical Society (DPG)**
*31.03. – 05.04.2019, Regensburg, Germany*

6. Erbe, A.; Zahn, P.
**NanoNet International Conference**
*08. – 11.10.2019, Dresden, Germany*

7. Facsko, S.; Heller, R.
**Ion Beam Physics Workshop**
*24. – 26.06.2019, HZDR, Dresden, Germany*

8. Hellwig, O.
**Control of Magnetic Microstructure in Thin Film Systems via Ion Beam Irradiation, Session at the Workshop "Spins, Waves and Interactions"**
*03. – 06.09.2019, Alfried Krupp College, Greifswald, Germany*

9. Hellwig, O.
**Physics and Applications of Synthetic Antiferromagnets (SAFs), Symposium at the MMM Conference**
*04. – 08.11.2019, Las Vegas, USA*

10. Krasheninnikov, A.V.; Komsa, H.-P.
**Atomic structure of nanosystems from first-principles simulations and microscopy experiments, International workshop**
*28. – 30.05.2019, Helsinki, Finland*

11. Krause, M.
**Idea Workshop: Intelligent Layers and Nano Technologies**
*24. – 25.07.2019, HZDR, Dresden, Germany*

12. Makarov, D.; Ortix, C.
**Geometry, topology, and condensed matter, Interdivisional Symposium SYGT at the Annual Spring Meeting of the German Physical Society (DPG)**
*31.03. – 05.04.2019, Regensburg, Germany*

13. Makarov, D.
**Curvilinear magnetism: fundamentals and applications, Focused Session of the Magnetism Division at the Annual Spring Meeting of the German Physical Society (DPG)**
*31.03. – 05.04.2019, Regensburg, Germany*

14. Makarov, D.; Sheka, D.
**Curvilinear Micromagnetism, Workshop**
22. – 25.05.2019, Kiev, Ukraine

15. Oswald, S. et al.
**18th European Conference on Applications of Surface and Interface Analysis - ECASIA19**
*15. – 20.09.2019, Dresden, Germany*

16. Skorupa, W., Donchev, A.
**Sitzung des AiF projektbegleitenden Ausschusses „Nickel für Hochtemperatur-anwendungen“**
*03.12.2019, HZDR, Dresden, Germany*

## Colloquia

1. Mittleman, D. M.
Brown University, Providence, RI, USA
**Laser terahertz emission nanoscopy**
*25.06.2019*

2. Ropers, C.
IV. Physikalisches Institut, Georg-August-Universität Göttingen, Germany
**Ultrafast Electron Diffraction and Microscopy**
*14.11.2019*

3. Suenaga, K.
National Institute of Advanced Industrial Science and Technology (AIST), Tsukuba, Japan
**Electron microscopy and spectroscopy of low-dimensional materials**
*13.05.2019*

4. Srikanth, H.
University of South Florida, Tampa, FL, USA
**Tuning magnetic anisotropy in nanostructures for biomedical and electromagnetic applications**
*24.04.2019*

5. Yang, D.
State Key Lab of Silicon Materials and School of Material Science and Engineering, Zhejiang University, Hangzhou, China
**Defects in cast quasi-single crystalline silicon for solar cells**
*19.09.2019*

6. Yang, H.
Department of Electrical and Computer Engineering, National University of Singapore
**Spin-Orbit Technologies: From Magnetic Memory to Terahertz Generation**
*30.09.2019*

## Seminars

1. Auerbach, K.
Vienna University of Technology, Austria
**Understanding nonlinear magnetization dynamics in magnetic read heads: RF characterization and micromagnetic modelling**
*09.01.2019*

2. Baraban, L.
Institute for Materials Science and Max Bergmann Center of Biomaterials, TU Dresden, Germany
**Nanoscale sensor devices for life science applications**
*27.05.2019*

3. Bastard, G.
École Normale Supérieure, Paris, France
**Investigations of IV-VI topological superlattices**
*26.09.2019*

4. Cao, L.
Forschungszentrum Jülich, Germany
**Controlling structural and physical properties of epitaxial transition metal oxide films through oxygen stoichiometry**
*29.04.2019*

5. Chen, F.
Shandong University of Science and Technology, Shandong, China
**Ion beam modification of 2D materials for photonic applications**
*23.08.2019*

6. Coey, M.
Trinity College Dublin, Ireland
**Anomalous magnetism due to quantum fluctuations of the vacuum**
*16.12.2019*

7. de la Rosa, N.
Lund University, Sweden
**Investigation of lithium and fluorine content in geological materials using Nuclear Reaction Analysis (NRA)**
*19.12.2019*

8. Efremov, D.
Leibniz-Institut für Festkörper- und Werkstoffforschung Dresden, Germany
**Impurity effects in interaction driven topological insulators**
*05.02.2019*

9. Gladii, O.
CEA Grenoble, France
**Spin pumping as a generic probe for linear spin fluctuations**
*23.01.2019*

10. Grande, P.L.
Ion Implantation Laboratory, Institute of Physics, Federal University of Rio Grande do Sul, Porto Alegre, Brazil
**Medium energy ion scattering for characterization of the advanced materials: fundamentals and applications**
*29.01.2019*

11. Iurchuk, V.
Univ. Grenoble Alpes, CEA, CNRS, Spintec, Grenoble, France
**Spin torque driven oscillations of the reference layer in fully perpendicular magnetic tunnel junctions**
*29.03.2019*

12. Ishioka, K.
National Institute for Materials Science, Tsukuba, Ibaraki, Japan
**Ultrafast Carrier and Phonon Dynamics at Semiconductor Hetero-interfaces**
*27.09.2019*

13. Kalbac, M.
J. Heyrovsky Institute of Physical Chemistry of the ASCR, Prague, Czech Republic
**Identification and Quantification of Defects in 2D Materials**
*10.10.2019*

14. Kiselev, N.S.
Institute for Advanced Simulation and Peter Grünberg Institut, Forschungszentrum Jülich, Germany
**Topological magnetic textures with particle-like properties**
*08.10.2019*

15. Komander, K.
Uppsala University, Sweden
**Hydrogen site occupation in thin films directly investigated by ion beam analysis**
*05.09.2019*

16. Kostylev, M.
Department of Physics and Astrophysics, The University of Western Australia, Perth, Australia
**Applied Magnonics**
*09.09.2019*

17. Langer, M.
Paul Scherrer Institut, Swiss Light Source, Villigen, Switzerland
**Development of a new soft x-ray ptychography spectro-microscope at the Swiss Light Source (SLS)**
*29.01.2019*

18. Li, Y.
City University of Hong Kong
**Synthetic strategies, shape control and optoelectronic applications of lead halide perovskite nanocrystals**
*07.11.2019*

19. Matthus, C.
Fraunhofer-Institut für Integrierte Systeme und Bauelementetechnologie IISB, Erlangen, Germany
**UV light detection and temperature measurements using 4H-SiC sensor devices**
*16.01.2019*

20. Nadarajan, R.
Pondicherry University, Puducherry, India
**Thermodynamics of divacancies in $BaZrO_3$**
*19.06.2019*

21. Navarro, J.
Universidad de Zaragoza, Spain
**Development and optimization of 3D functional ferromagnetic nanostructures grown by focused electron beam induced deposition**
*13.06.2019*

22. Neugebauer, N.
Fachgebiet Physik, Justus-Liebig-Universität Gießen, Germany
**Investigation of the dipole interaction in and between ordered arrangements of magnetic nanoparticles**
*28.08.2019*

23. Nguyen-Le, T.
TU Dresden, Germany, and Katholieke Universiteit Leuven, Belgium
**Development of a platform for inspection of bacteria co-existance in gel micro-beads**
*16.08.2019*

24. Piskarev, E.
École Polytechnique Fédérale de Lausanne (EPFL), Institute of Mechanical Engineering, Lausanne, Switzerland
**Soft technologies based on electroactive polymers**
*11.12.2019*

25. Poshakinskiy, A.
Ioffe Institute St. Petersburg, Russia
**Membrane optomechanics and spin-mechanics**
*08.04.2019*

26. Radic, D.
Universität Münster, Germany
**Fluctuation electron microscopy on silicon amorphized at varying self ion-implantation conditions**
*29.11.2019*

27. Ravelosona, D.
Centre de Nanosciences et de Nanotechnologies (C2N), Université Paris Sud, France
**Dzyaloshinskii-Moryia Interaction at disordered interfaces in ultra-thin films with perpendicular anisotropy**
*16.10.2019*

28. Rigler, M.
AEROSOLL d.o.o., Ljubljana, Slowenia
**Measurements of carbonaceous aerosols**
*04.11.2019*

29. Scheuner, C.
Felix-Bloch-Institut für Festkörperphysik, Universität Leipzig, Germany
**Development of nano apertures for ion beam collimation**
*06.09.2019*

30. Shaw, J.M.
National Institute of Standards and Technology, Boulder, CO, USA
**Broadband ferromagnetic resonance spectroscopy: The "Swiss Army Knife" for understanding spin-orbit phenomena**
*21.05.2019*

31. Togawa, Y.
Department of Physics and Electronics, Graduate School of Engineering, Osaka Prefecture University, Japan
**Wonders of Chiral Magnetic Materials**
*05.07.2019*

32. Vaez Allaei, M.
University of Tehran, Iran
**Phononic heat transport and thermal rectification in low dimensional heterostructures**
*29.01.2019*

33. Valez, S.
ETH Zurich, Switzerland
**Probing and manipulating magnetic domains and domain walls in magnetic insulators by spin currents**
*29.04.2019*

34. Valtiner, M.
Vienna University of Technology, Austria
**Angstrom-resolved characterization of electrochemical interfaces in real time during polarization**
*22.01.2019*

35. van der Sar, T.
Kavli Institute of Nanoscience, Delft University of Technology, Netherlands
**Probing condensed-matter physics using single-spin magnetometry**
*28.01.2020*

36. van Houselt, A.
University of Twente, Enschede, Netherlands
**Growth of hBN on Ir(111)**
*15.05.2019*

37. Varvaro, G.
CNR, Istituto di Struttura della Materia, Monterotondo Scalo, Rome, Italy
**Synthetic antiferromagnets for biomedical and flexible spintronic applications**
*25.11.2020*

38. Veremchuk, I.
Max-Planck-Institut für Chemische Physik fester Stoffe, Dresden, Germany
**"Structural imperfections" in transition metal oxides: SPS synthesis and thermoelectricity**
*09.09.2019*

39. Wunderlich, J.
Hitachi Cambridge Laboratory/University of Cambridge, United Kingdom
**Domain wall nucleation and supermagnonic dynamics of domain walls driven by Spin-Orbit Fields in an antiferromagnet**
*14.05.2019*

40. Yu, H.
Spintronics Interdisciplinary Research Center Beihang University, Beijing, China
**Strong interlayer magnon-magnon coupling in magnetic hybrid nanostructures**
*17.04.2019*

# Exchange of researchers

## Guests at our institute

1. Andriyevska, O.
   *York University, Toronto, Canada; 01.07. - 27.09.2019*

2. Arias, R.
   *Universidad de Chile, Santiago, Chile; 14.07. - 27.07.2019*

3. Cardos Tisnado, K. L.
   *Universidad Nacional Autonoma de Mexico, Ensenada, Mexico; 15.11.2019 - 12.02.2020*

4. Cullen, E.
   *Dublin Institute of Technology, Dublin, Ireland; 21.01. - 31.08.2019*

5. El-Said, A. S.
   *Mansoura University, Mansoura, Egypt; 15.06. - 15.08.2019*

6. Escobar-Galindo, R.
   *Cadiz University, Puerto Real, Spain; 15.07. - 26.07.2019*

7. Gallardo, R.
   *Universidad Técnica Federico Santa Maria, Valparaiso, Chile; 23.05. - 21.07.2019*

8. Granell, P.
   *Universidad Nacional de San Martin, San Martin, Argentina; 28.06. - 31.08.2019*

9. Guardia Arce, V.
   *Universität Madrid, Madrid, Spain; 02.10. - 20.12.2019*

10. Hu, L.
    *Shenzen University, Shenzen, P. R. China; 01.05.2019 - 30.04.2020*

11. Iastremskyi, I.
    *Kyiv University, Kyiv, Ukraine; 10.01. - 09.02.2019*

12. Kaleniuk, O.
    *Institute for Metal Physics, Kyiv, Ukraine; 22.02. - 15.03.2019*

13. Kobya, E. D.
    *Pamukkale University, Denizli, Turkey; 11.06. - 10.09.2019*

14. Kordyuk, A.
    *Institute for Metal Physics, Kyiv, Ukraine; 18.02. - 03.03.2019*

15. Korniienko, A.
    *Kyiv University, Kyiv, Ukraine; 01.06. - 31.08.2019*

16. Kysliuk, V.
    *Institute for Metal Physics, Kyiv, Ukraine; 08.03. - 16.03.2019*

17. Lao, Y.
    *Nanning Normal University, Nanning, P. R. of China; 01.12.2019 - 30.11.2020*

18. Li, J.
    *Institute of Fluid Physics, Mianyang, P. R. China; 01.06.2019 - 31.05.2021*

19. Li, Y.
*University Cleveland, OH, USA; 15.05. - 02.08.2019*

20. Liu, J.
*North Carolina State University, Raleigh, NC, USA; 06.06. - 22.08.2019*

21. Makushko, P.
*Institute for Metal Physics, Kyiv, Ukraine; 01.06. - 31.07.2019*

22. Mensah, P. A.
*KNUST, Kumasi, Ghana; 01.06. - 31.08.2019*

23. Mystkowski, A.
*Bialystok University, Bialystok, Poland; 01.07. - 30.09.2019*

24. Nadarajan, R.
*University Pondicherry, Puducherry, India; 15.05. - 14.08.2019*

25. Oguz, O.
*Ankara University, Ankara, Turkey; 29.06. - 26.09.2019*

26. Pereira, P.
*Pontificia Universidade Católica do Rio de Janeiro, Brazil; 01.03.2018 - 30.06.2019*

27. Pylypovskyi, O.
*Kyiv University, Kyiv, Ukraine; 07.01. - 03.02.2019*

28. Qu, D.
*Southeast University, Nanjing, P. R. China; 11.06.2018 - 10.11.2019*

29. Ruiz Arce, D. D.
*Universidad Nacional Autonoma de Mexico, Ensenada, Mexico; 15.11.2019 - 12.02.2020*

30. Shapovalov, A.
*Institute for Metal Physics, Kyiv, Ukraine; 22.02. - 15.03.2019*

31. Sheka, D.
*Kyiv University, Kyiv, Ukraine; 07.01. - 03.02.; 01.07. - 22.07.; 05. - 26.08.2019*

32. Sing, P.
*Indian Institute of Technology, Delhi, India; 03.06. - 03.07.2019*

33. Suvorov, O.
*Institute for Metal Physics, Kyiv, Ukraine; 18.02. - 11.03.2019*

34. Tomilo, A.
*Kyiv University, Kyiv, Ukraine; 07.01. - 19.01.2019*

35. Tracy, J.
*North Caroline State University, Raleigh, USA; 06.06. - 22.08.2019*

36. Wojewoda, O.
*Brno University of Technology, Brno, Czech Republic; 19.02. - 30.08.2019*

37. Wu, D.
*Institute of Applied Electronics, Mianyang, P. R. China; 02.08. – 30.10.2019*

38. Yastremskyi, I.
*Kyiv University, Kyiv, Ukraine; 01.07. - 30.09.2019*

39. Yi, A.
*Shanghai University, Shanghai, P. R. China; 02.08. - 30.09.2019*

40. Zabila, Y.
*Institute of Nuclear Physics, Krakow, Poland; 23.08. - 27.09.2019*

41. Zaiets, O.
*Kyiv University, Kyiv, Ukraine; 25.02. - 23.03.2019*

# Projects

The projects are listed by funding institution and project starting date. In addition, the institute has several bilateral service collaborations with industrial partners and research institutions. These activities are not included in the following overview.

## European Projects

1. 02/2016 – 07/2020 European Union EU
**IONS4SET – Single Electron Transistor**
*Dr. J. v. Borany* *Phone: 0351 260 3378* *j.v.borany@hzdr.de*

2. 01/2017 – 12/2020 European Union EU
**TRANSPIRE –Terahertz Radio Communication**
*Dr. A. Deac* *Phone: 0351 260 3709* *a.deac@hzdr.de*

3. 01/2017 – 12/2020 European Union EU
**npSCOPE – Nanoparticle Characterization**
*Dr. G. Hlawacek* *Phone: 0351 260 3409* *g.hlawacek@hzdr.de*

4. 05/2017 – 04/2021 European Union EU
**CALIPSOplus – Coordinated Access to Lightsources**
*Prof. M. Helm* *Phone: 0351 260 2260* *m.helm@hzdr.de*

5. 09/2017 – 02/2019 European Union EU
**Analytics – All-electrical analytic platform for digital fluidics**
*Dr. D. Makarov* *Phone: 0351 260 3273* *d.makarov@hzdr.de*

6. 01/2019 – 12/2022 European Union EU
**RADIATE – Research And Development with Ion Beams - Advancing Technology in Europe**
*Prof. J. Fassbender* *Phone: 0351 260 3096* *j.fassbender@hzdr.de*

## Helmholtz Association Projects

1. 10/2012 – 12/2020 Helmholtz-Gemeinschaft HGF
**NANONET – International Helmholtz Research School on Nanoelectronics**
*Dr. A. Erbe* *Phone: 0351 260 2366* *a.erbe@hzdr.de*

2. 01/2013 – 12/2019 Helmholtz-Gemeinschaft HGF
**W3-Professorship TU Chemnitz**
*Prof. S. Gemming* *Phone: 0351 260 2470* *s.gemming@hzdr.de*

3. 11/2014 – 12/2019 Helmholtz-Gemeinschaft HGF
**Magnetism – HGF Postdoc Dr. K. Schultheiß**
*Prof. J. Fassbender* *Phone: 0351 260 3096* *j.fassbender@hzdr.de*

4. 05/2016 – 08/2019 Helmholtz-Gemeinschaft HGF
**THz Spectroscopy – HGF Postdoc Dr. A. Singh**
*Prof. M. Helm* *Phone: 0351 260 2260* *m.helm@hzdr.de*

5. 10/2017 – 08/2020 Helmholtz-Gemeinschaft HGF
**Helmholtz Exzellenznetzwerk – cfaed 2 + 3**
*Dr. A. Erbe* *Phone: 0351 260 2366* *a.erbe@hzdr.de*

6. 10/2017 – 02/2020 Helmholtz-Gemeinschaft HGF
**Helmholtz ERC Recognition Award**
*Dr. H. Schultheiß* *Phone: 0351 260 3243* *h.schultheiss@hzdr.de*

7. 01/2019 – 09/2020 Helmholtz-Gemeinschaft HGF
**Helmholtz Exzellenznetzwerk – DCM-MatDNA Phase 3**
*Prof. S. Gemming Phone: 0351 260 2470 s.gemming@hzdr.de*

8. 01/2019 – 12/2021 Helmholtz-Gemeinschaft HGF
**CROSSING – Crossing borders and scales - an interdisciplinary approach**
*Dr. J. v. Borany Phone: 0351 260 3378 j.v.borany@hzdr.de*

9. 02/2019 – 06/2020 Helmholtz-Gemeinschaft HGF
**Helmholtz Enterprise – Tensormeter**
*Dr. T. Kosub Phone: 0351 260 2900 t.kosub@hzdr.de*

10. 07/2019 – 06/2020 Helmholtz-Gemeinschaft HGF
**Helmholtz Enterprise Plus – Tensormeter**
*Dr. T. Kosub Phone: 0351 260 2900 t.kosub@hzdr.de*

11. 12/2019 – 11/2024 Helmholtz-Gemeinschaft HGF
**Helmholtz Innovation Lab – FlexiSens**
*Dr. D. Makarov Phone: 0351 260 3273 d.makarov@hzdr.de*

## German Science Foundation Projects

1. 05/2014 – 01/2021 Deutsche Forschungsgemeinschaft DFG
**Emmy Noether Junior Research Group – Magnonics**
*Dr. H. Schultheiß Phone: 0351 260 3243 h.schultheiss@hzdr.de*

2. 03/2017 – 08/2020 Deutsche Forschungsgemeinschaft DFG
**MUMAGI – Disorder induced magnetism**
*Dr. R. Bali Phone: 0351 260 2919 r.bali@hzdr.de*

3. 07/2017 – 06/2020 Deutsche Forschungsgemeinschaft DFG
**HELEX2D – Interaction of highly charged ions with 2D materials**
*Dr. R. Wilhelm Phone: 0351 260 3378 r.wilhelm@hzdr.de*

4. 08/2017 – 07/2020 Deutsche Forschungsgemeinschaft DFG
**FlexCom – Magnetic field sensitive flexible communication system**
*Dr. D. Makarov Phone: 0351 260 3273 d.makarov@hzdr.de*

5. 09/2017 – 08/2020 Deutsche Forschungsgemeinschaft DFG
**Lane Formation**
*Dr. A. Erbe Phone: 0351 260 2366 a.erbe@hzdr.de*

6. 11/2017 – 10/2020 Deutsche Forschungsgemeinschaft DFG
**ULTRACRITICAL – High-temperature superconductors**
*Dr. A. Pashkin Phone: 0351 260 3287 o.pashkin@hzdr.de*

7. 04/2018 – 03/2021 Deutsche Forschungsgemeinschaft DFG
**Confined Microswimmers**
*Dr. A. Erbe Phone: 0351 260 2366 a.erbe@hzdr.de*

8. 04/2018 – 03/2021 Deutsche Forschungsgemeinschaft DFG
**IMASTE – Graphene encapsulated quasi-2D materials**
*Dr. A. Krasheninnikov Phone: 0351 260 3148 a.krasheninnikov@hzdr.de*

9. 10/2018 – 09/2020 Deutsche Forschungsgemeinschaft DFG
**Doping by ALD and FLA**
*Dr. L. Rebohle Phone: 0351 260 3368 l.rebohle@hzdr.de*

10. 03/2018 – 02/2019 Deutsche Forschungsgemeinschaft DFG
**Magnetic Landscapes – Spin Dynamics**
*Dr. A. Semisalova Phone: 0203 37 92474 anna.semisalova@uni-due.de*

11. 01/2019 – 09/2019 Deutsche Forschungsgemeinschaft DFG
**Cluster of Excellence – Center for Advancing Electronics Dresden (cfaed)**
*Dr. A. Erbe Phone: 0351 260 2366 a.erbe@hzdr.de*

12. 01/2019 – 05/2021 Deutsche Forschungsgemeinschaft DFG
**Quantum control of single spin centers in silicon carbide coupled to optical microcavities**
*Dr. G. Astakhov Phone: 0351 260 3894 g.astakhov@hzdr.de*

13. 01/2019 – 01/2022 Deutsche Forschungsgemeinschaft DFG
**Printable giant magnetoresistive sensors with high sensitivity at small magnetic fields**
*Dr. D. Makarov Phone: 0351 260 3273 d.makarov@hzdr.de*

14. 06/2019 – 06/2022 Deutsche Forschungsgemeinschaft DFG
**Interacting Magnonic Currents and Chiral Spin Textures for Energy Efficient Spintronics**
*Dr. H. Schultheiß Phone: 0351 260 3243 h.schultheiss@hzdr.de*

15. 07/2019 – 06/2022 Deutsche Forschungsgemeinschaft DFG
**3D tailoring of all-oxide heterostructures by ion beams**
Dr. S. *Zhou Phone: 0351 260 2484 s.zhou@hzdr.de*

16. 07/2019 – 06/2022 Deutsche Forschungsgemeinschaft DFG
**Lab-on-chip Systems Carrying Artificial Motors for Multiplexed and Multiparametric Biochemical Assays**
*Dr. D. Makarov Phone: 0351 260 3273 d.makarov@hzdr.de*

17. 10/2019 – 11/2022 Deutsche Forschungsgemeinschaft DFG
**3D transport of spin waves in curved nano-membranes**
*Dr. A. Kakay Phone: +49 351 260 2689 a.kakay@hzdr.de*

18. 11/2019 – 10/2022 Deutsche Forschungsgemeinschaft DFG
**Functionalization of Ultrathin $MoS_2$ by Defect Engineering**
*Dr. A. Krasheninnikov Phone: 0351 260 3148 a.krasheninnikov@hzdr.de*

## Federally and Saxony State Funded Projects

1. 04/2017 – 03/2019 Bundesministerium für Bildung und Forschung BMBF
**German-Ukrainian Center for Large Scale Experiment**
*Dr. D. Makarov Phone: 0351 260 3273 d.makarov@hzdr.de*

2. 08/2017 – 11/2019 Sächsische Aufbaubank SAB
**PlatMOS – Atmospheric plasma treatment for corrosion suppression at organ pipes**
*Dr. W. Skorupa Phone: 0351 260 3612 w.skorupa@hzdr.de*

3. 09/2017 – 12/2019 Sächsische Aufbaubank SAB
**SiNergy – Si based battery electrodes**
*Dr. S. Prucnal Phone: 0351 260 2065 s.prucnal@hzdr.de*

4. 10/2017 – 03/2019 Bundesministerium für Bildung und Forschung BMBF
**Resistance-Tensormeter**
*Dr. T. Kosub Phone: 0351 260 2900 t.kosub@hzdr.de*

5. 11/2017 – 12/2019 Arbeitsgemeinschaft industrielle Forschung AiF
**Liquid metal ion source**
*Dr. L. Bischoff Phone: 0351 260 2866 l.bischoff@hzdr.de*

6. 01/2018 – 10/2020 DECHEMA e.V. DECHEMA
**High temperature oxidation resistance for nickel-based alloys by fluorine implantation**
*Dr. W. Skorupa Phone: 0351 260 3612 w.skorupa@hzdr.de*

7. 11/2018 – 10/2020 Bundesministerium für Bildung und Forschung BMBF
**Metal-germanium interface: Schottky barrier and ohmic contacts**
*Dr. S. Prucnal Phone: 0351 260 2065 s.prucnal@hzdr.de*

8. 03/2019 – 08/2020 Arbeitsgemeinschaft industrielle Forschung AiF
**Improvement of the dynamic properties of GaAs power diodes by proton irradiation**
*Dr. J. v. Borany Phone: 0351 260 3378 j.v.borany@hzdr.de*

9. 03/2019 – 08/2020 Bundesministerium für Wirtschaft und Energie BMWi
**Electrostatically functionalized materials with bio-sensitive adsorption properties**
*Dr. L. Rebohle Phone: 0351 260 3368 l.rebohle@hzdr.de*

10. 05/2019 – 10/2020 Bundesministerium für Wirtschaft und Energie BMWi
**Magnetoelectrical detector**
*Dr. D. Makarov Phone: 0351 260 3273 d.makarov@hzdr.de*

11. 07/2019 – 01/2022 Sächsische Aufbaubank SAB
**Innovative product platform for space-based Global Navigation Satellite Systems (GNSS)**
*Dr. J. v. Borany Phone: 0351 260 3378 j.v.borany@hzdr.de*

12. 10/2019 – 09/2023 Bundesministerium für Bildung und Forschung BMBF
**Group IV-heterostructures for most advanced nanoelectronics devices**
*Dr. Y. Georgiev Phone: 0351 260 2321 y.georgiev@hzdr.de*
*Dr. S. Prucnal Phone: 0351 260 2065 s.prucnal@hzdr.de*

13. 10/2019 – 09/2023 Bundesministerium für Bildung und Forschung BMBF
**Black phosphorus in sensitive, selective and stable sensors**
*Dr. A. Erbe Phone: 0351 260 2366 a.erbe@hzdr.de*

## Personnel Exchange Projects and Society Chairs

1. 06/2016 – 05/2019 Alexander-von-Humboldt-Stiftung AvH
**Humboldt fellowship Dr. Berencen**
*Dr. L. Rebohle Phone: 0351 260 3368 l.rebohle@hzdr.de*

2. 05/2017 – 12/2020 Institute of Electrical and Electronics Engineers IEEE
**Magnetics Society German Chapter Chair**
*Dr. H. Schultheiß Phone: 0351 260 3243 h.schultheiss@hzdr.de*

3. 07/2017 – 08/2020 Alexander-von-Humboldt-Stiftung AvH
**Humboldt fellowship Prof. Sheka**
*Dr. D. Makarov Phone: 0351 260 3273 d.makarov@hzdr.de*

4. 04/2018 – 03/2020 Deutscher Akademischer Austauschdienst DAAD
**ULTIMAT – Superlattices of ultra-thin $In_xGa_{1-x}N$/GaN quantum wells**
*Dr. E. Dimakis Phone: 0351 260 2765 e.dimakis@hzdr.de*

5. 09/2018 – 08/2019 Deutscher Akademischer Austauschdienst DAAD
**Leonhard Euler Grant: Curvature induced effects in nanowires**
*Dr. D. Makarov Phone: 0351 260 3273 d.makarov@hzdr.de*

6. 07/2019 – 09/2019 Deutscher Akademischer Austauschdienst DAAD
**Visit Dr. Yastremskyi**
*Dr. D. Makarov Phone: 0351 260 3273 d.makarov@hzdr.de*

7. 07/2019 – 10/2019 Deutscher Akademischer Austauschdienst DAAD
**Visit Dr. Mystkowski**
*Dr. D. Makarov Phone: 0351 260 3273 d.makarov@hzdr.de*

8. 11/2019 – 02/2020 Deutscher Akademischer Austauschdienst DAAD
**Visit Karen Lizbeth Cardos Tisnado**
*Dr. A. Erbe Phone: 0351 260 2366 a.erbe@hzdr.de*

# Organization chart

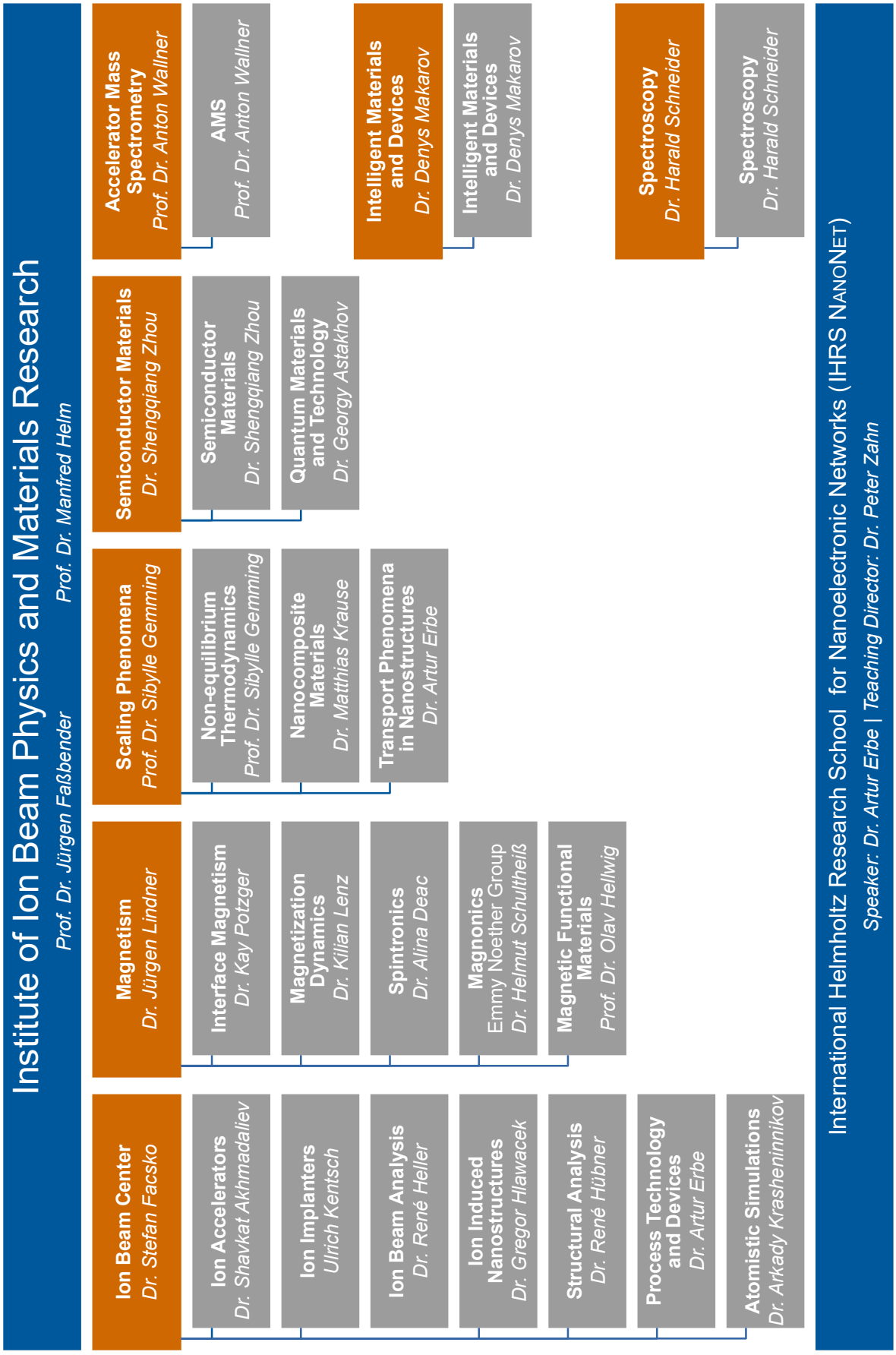

# List of personnel 2019

| DIRECTORS | OFFICE |
|---|---|
| Prof. Dr. M. Helm, Prof. Dr. J. Faßbender | S. Gebel, S. Kirch |

## SCIENTIFIC STAFF

### Permanent staff

Dr. C. Akhmadaliev
Dr. G. Astakhov
Dr. L. Bischoff
Dr. J. von Borany
Dr. A. Deac
Dr. E. Dimakis
Dr. A. Erbe
Dr. S. Facsko
Dr. C. Fowley
Prof. Dr. S. Gemming
Dr. Y. Georgiev
Dr. J. Grenzer
Dr. R. Heller
Dr. G. Hlawacek
Dr. R. Hübner
Dr. A. Krasheninnikov
Dr. M. Krause
Dr. J. Lachner
Dr. K. Lenz
Dr. J. Lindner
Dr. D. Makarov
Dr. S. Merchel
Dr. F. Munnik
Dr. A. Pashkin
Dr. M. Posselt
Dr. K. Potzger
Dr. S. Prucnal
Dr. L. Rebohle
Dr. G. Rugel
Dr. H. Schneider
Prof. Dr. A. Wallner
Dr. S. Winnerl
Dr. P. Zahn
Dr. S. Zhou

### Non-permanent

Dr. R. Bali
Dr. Y. Berencén (P)
Dr. D. Blaschke (P)
Dr. H. Cansever
Dr. A. Eichler-Volf (P)
Dr. H.-J. Engelmann (P)
Dr. D. Erb
Dr. L. Fallarino
Dr. A. Froideval (P)
Dr. J. Ge (P)
Dr. M. Ghorbani Asl
Dr. O. Gladii (P)
Dr. F. Goncalves (P)
Dr. M. Grobosch (P)
Dr. M. Ha (P)
Dr. K.-H. Heinig (P)
Prof. Dr. O. Hellwig
Dr. R. Illing
Dr. V. Iurchuk (P)
Dr. J. Julin
Dr. A. Kákay (P)
R. Kaltofen (P)
Dr. N. Klingner (P)
T. Köhler (P)
Dr. T. Kosub
Dr. E. Kowalska
Dr. C. Lei (P)
Dr. A. Lindner (P)
Prof. Dr. W. Möller (P)
Dr. I. Mönch (P)
Dr. M. Neubert (P)
Dr. N. Nishida (P)
Dr. R. Podlipec (P)
Dr. O. Pylypovskyi
Dr. A. Quade (P)
Dr. R. Rana
Dr. R. Salikhov
Dr. P.A. Sanchez Romero (P)
Dr. H. Schultheiß (P)
Dr. K. Schultheiß (P)
Dr. J. Schütt (P)
Dr. A. Semisalova
Dr. A. Singh (P)
Dr. W. Skorupa (P)
Dr. S. Stienen
Dr. T.T. Trinh
Dr. O. Volkov (P)
Dr. C. Wagner (P)
Dr. K. Wagner (P)
Dr. M. Wang
Dr. R. Wilhelm
Dr. R. Yankov

(P) Projects

## TECHNICAL STAFF

### Permanent staff

Rb. Aniol
Rm. Aniol
E. Christalle
S. Eisenwinder
B. Gebauer
A. Gerner
H. Gude
J. Haufe
A. Henschke
H. Hilliges
S. Klare
J. Kreher
A. Kunz
K. Lang
H. Lange
U. Lucchesi
F. Ludewig
R. Mester
Dr. R. Narkovic
C. Neisser
F. Nierobisch
T. Putzke
A. Reichel
B. Scheumann
G. Schnabel
A. Schneider
A. Scholz
T. Schönherr
T. Schumann
I. Skorupa
M. Steinert
A. Thiel
K. Thiemig
J. Wagner
A. Weise
A. Weißig
J. Winkelmann
R. Ziegenrücker
L. Zimmermann
J. Zscharschuch

### Non-permanent

A. Berens
J. Heinze
U. Kentsch
A. Legrand
T. Naumann
L. Ramasubramanian (P)
J. Schulz
T. Tarnow
T. Voitsekhivska (P)

(P) Projects

## PhD STUDENTS

Y. Alsaadawi
H. Arora
N. Baghban Khojasteh
L. Balaghi
T. Bayrak
V. Begeza
M. Bejarano
G.S. Canon Bermudez
P. Chava
S. Creutzburg
J. Duan
A. Echresh
I. Fotev
S. Ghaderzadeh
T. Hache
D. Hilliard
M. Hollenbach
T. Hula
D. Janke
S. Jazavandi Ghamsari
T. Joseph
M.B. Khan
F. Kilibarda
L. Körber
S. Kretschmer
D. Lang
Zi. Li Lokamani
E.S. Oliveros Mata
T. Prüfer
F. Samad
A. Schmeink
R. de Schulz
A. Seidl
E. Serralta Hurtado
Z. Shang
S. Sorokin
A. Strobel
T. Tauchnitz
A. Titova
M. Vallinayagam
T. Venanzi
C. Wang
X. Wang
Y. Wei
Y. Xie
C. Xu
X. Xu
N. Yuan

## STUDENTS (Diploma / MSc / BSc)

Z. Fekri
Y. Gao
S. Ghosh
M. Hoppe
N. Jagtap
A. Jain
V. Kateel
F. Moebus
A. Oelschlägel
W. Roscher
M.S. Shaik
D. Sharma
S. Skakeel
J. Sonnenberg
Y. Vekariya
T. Weinhold
M. Welsch

Wissenschaftlich-Technische Berichte
HZDR-109 | 2020 | ISSN 2191-8708

HELMHOLTZ ZENTRUM
DRESDEN ROSSENDORF

Institute of Ion Beam Physics and Materials Research
Bautzner Landstrasse 400
01328 Dresden/Germany
Phone +49 351 260-2345
Fax +49 351 260-3285
https://www.hzdr.de

Member of the Helmholtz Association